Doctoral Dissertation

博士論文

Search for Proton Decay via $p \to e^+\pi^0$ and $p \to \mu^+\pi^0$ with an Enlarged Fiducial Mass of the Super-Kamiokande Detector

(スーパーカミオカンデ検出器の拡張有効質量を用いた陽子崩壊$p \to e^+\pi^0$と$p \to \mu^+\pi^0$の探索)

A Dissertation Submitted for the Degree of Doctor of Philosophy
December 2020

令和2年12月博士(理学)申請

Department of Physics, Graduate School of Science,
The University of Tokyo

東京大学大学院理学系研究科物理学専攻

Akira Takenaka

竹中 彰

Abstract

We have searched for proton decay via $p \to e^+\pi^0$ and $p \to \mu^+\pi^0$ modes using all Super-Kamiokande data until May 2018, in total 450 kton·years exposure. In this analysis, we have enlarged the Super-Kamiokande fiducial mass from 22.5 kton to 27.2 kton, and the 78 kton·years of enlarged fiducial mass region data has been analyzed for the first time. No candidates are found for $p \to e^+\pi^0$ with 0.59 of expected atmospheric neutrino backgrounds, and one candidate is found for $p \to \mu^+\pi^0$ with 0.94 of expected atmospheric neutrino backgrounds. The results are consistent with the expected number of backgrounds. Lower limits on the proton partial lifetime are set to be $\tau/B(p \to e^+\pi^0) > 2.4 \times 10^{34}$ years and $\tau/B(p \to \mu^+\pi^0) > 1.6 \times 10^{34}$ years at 90% confidence level. They are the wolrd's most stringent constraints for these decay modes.

Contents

List of Figures

List of Tables

Chapter 1

Introduction

In this thesis, the results of a proton decay search via $p \to e^+\pi^0$ and $p \to \mu^+\pi^0$ modes with the Super-Kamokande detector are presented.

A motivation for this study is to test Grand Unified Theories (GUTs) which are briefly described in Chapter 2. A summary of the Super-Kamiokande detector and its calibration is presented in Chapter 3. Basic detector components and calibration methods are explained. In this analysis, an event simulator to produce proton decay Monte Carlo (MC) events and atmospheric neutrino MC events is used. Details of the event simulator are described in Chapter 4. Chapters 5 and 6 describe an event data set and event reconstruction algorithm used for this analysis, respectively. In order to improve the proton decay search sensitivity, it is crucial to accumulate a larger detector exposure. Therefore, we have enlarged the detector fiducial mass from 22.5 kton to 27.2 kton and searched for $p \to e^+\pi^0$ and $p \to \mu^+\pi^0$ using the enlarged fiducial mass for the first time. In Chapter 5, an external background contamination level in the 4.7 kton additional fiducial mass region, which we have never used, is discussed. Event reconstruction performance in the additional fiducial mass region as well as improvements of the particle identification algorithm are detailed in Chapter 6. One of the most important systematic uncertainties in the proton decay search is the energy scale uncertainty, and it is estimated for the 22.5 kton conventional fiducial mass region and 4.7 kton additional fiducial mass region separately in the same chapter. Proton decay search performances and results are summarized in Chapter 7. Proton decay signal selection criteria as well as the evaluated signal selection efficiency and expected number of background events are described. The search sensitivity improvement by enlarging the fiducial mass is also mentioned. As no proton decay signal has been found, calculation of the lifetime limits is presented in this chapter. At last, this thesis is concluded in Chapter 8. Appendix A describes an additional study to validate PMT response modeling in our detector simulation for enlarging the fiducial mass. The main contents of this work are summarized in [1].

Chapter 2

Physics Motivation

The standard model (SM) [2] of particle physics has succeeded in predicting almost all experimental results; however, it still leaves important questions about the universe, and it is believed that a new physics paradigm beyond the standard model exists. Grand Unified Theory (GUT) [3] is one of the most prospective frameworks beyond the SM, and experimental observation of proton decay would become strong evidence for it. In this Chapter, these theories and previous proton decay search results are introduced.

2.1 Standard Model (SM)

The SM contains quarks, leptons, gauge bosons, and the Higgs boson. It is based on the gauge symmetry:

$$\mathrm{G_{SM}} = \mathrm{SU(3)}_C \times \mathrm{SU(2)}_L \times \mathrm{U(1)}_Y. \tag{2.1}$$

As proved by Noether's theorem, each of them has a conserved quantity. The group $\mathrm{SU(3)}_C$ denotes the color conservation of the strongly-interacting quarks and their gauge particles, gluons. The group $\mathrm{SU(2)}_L$ is associated with the weak interaction with L indicating that only left-handed particles participate in this interaction. The third component of weak isospin is conserved in this interaction. At last, $\mathrm{U(1)}_Y$ conserves the weak hypercharge (Y), and it has the following relation with the third component of weak isospin (T_3) and the electric charge (Q):

$$Y = 2Q - 2T_3. \tag{2.2}$$

Table 2.1 shows the correspondence between the fermion particles and their gauge group representation.

Table 2.1: Fermion particles and their gauge group representation and the weak hypercharge $(N_{\mathrm{SU(3)}}, N_{\mathrm{SU(2)}}, Y)$.

representation and the weak hypercharge	quarks (3,2,1/3)	quarks (3,1,4/3)	quarks (3,1,-2/3)	leptons (1,2,-1)	leptons (1,1,-2)
first generation	$\begin{pmatrix} u \\ d \end{pmatrix}_L$	u_R	d_R	$\begin{pmatrix} \nu_e \\ e^- \end{pmatrix}_L$	e^-_R
second generation	$\begin{pmatrix} c \\ s \end{pmatrix}_L$	c_R	s_R	$\begin{pmatrix} \nu_\mu \\ \mu^- \end{pmatrix}_L$	μ^-_R
third generation	$\begin{pmatrix} t \\ b \end{pmatrix}_L$	t_R	b_R	$\begin{pmatrix} \nu_\tau \\ \tau^- \end{pmatrix}_L$	τ^-_R

A complex scalar Higgs doublet, Φ, is added to generate the weak gauge boson mass through

spontaneous symmetry breaking. The Lagrangian for the Higgs field is as follows:

$$L = |D^{\mu}\Phi|^2 - V(\Phi), \tag{2.3}$$

$$V(\Phi) = -\mu^2|\Phi|^2 + \lambda|\Phi|^4 \ (\mu^2 > 0). \tag{2.4}$$

This Lagrangian is gauge-invariant for the $\mathrm{SU}(2)_L \times \mathrm{U}(1)_Y$ transformation. After spontaneous symmetry breaking, a vacuum expectation value of Φ can be taken as:

$$\langle 0|\Phi|0\rangle = \frac{1}{\sqrt{2}} \begin{pmatrix} 0 \\ v \end{pmatrix}. \tag{2.5}$$

With this vacuum expectation value, the Lagrangian becomes:

$$\begin{aligned} L = \frac{1}{2}\left(\partial_\mu \phi\right)^2 + \frac{1}{8}g^2\left((A^1_\mu)^2 + (A^2_\mu)^2\right)(v+\phi)^2 \\ + \frac{1}{8}\left(gA^3_\mu - g'B_\mu\right)^2(v+\phi)^2 + \frac{\mu^2}{2}(v+\phi)^2 - \frac{\lambda}{4}(v+\phi)^4, \end{aligned} \tag{2.6}$$

where ϕ is the perturbation term, A (B) is the SU(2) (U(1)) gauge field, and g (g') is its coupling constant. In order to clarify the meaning of the Lagrangian, the following terms are introduced:

$$W_\mu = \frac{1}{\sqrt{2}}\left(A^1_\mu - iA^2_\mu\right), \tag{2.7}$$

$$W^\dagger_\mu = \frac{1}{\sqrt{2}}\left(A^1_\mu + iA^2_\mu\right), \tag{2.8}$$

$$\begin{pmatrix} Z_\mu \\ A_\mu \end{pmatrix} = \begin{pmatrix} \cos\theta_W & -\sin\theta_W \\ \sin\theta_W & \cos\theta_W \end{pmatrix} \begin{pmatrix} A^3_\mu \\ B_\mu \end{pmatrix}, \tag{2.9}$$

$$\cos\theta_W = \frac{g}{\sqrt{g^2 + g'^2}}, \tag{2.10}$$

$$\sin\theta_W = \frac{g'}{\sqrt{g^2 + g'^2}}, \tag{2.11}$$

$$M_W = \frac{1}{2}gv, \tag{2.12}$$

$$M_Z = \frac{M_W}{\cos\theta_W}, \tag{2.13}$$

$$M_H = \sqrt{2\lambda}v, \tag{2.14}$$

where W_μ ($W^\dagger_\mu$), Z_μ, and A_μ correspond to the W^+ (W^-) gauge boson, Z^0 gauge boson, and photon, respectively. The mixing angle, θ_W, is so-called the Weinberg angle. As a consequence, non-zero gauge boson mass terms (M_W, M_Z) and the Higgs mass (M_H) term are derived from Eq. (2.6):

$$\begin{aligned} L = \frac{1}{2}M^2_W W^\dagger_\mu W^\mu + \frac{1}{2}M^2_Z Z_\mu Z^\mu \\ + \left(\frac{g^2}{4}\phi^2 + gM_W\phi\right)\left(W^\dagger_\mu W^\mu + \frac{1}{2\cos^2\theta_W}Z_\mu Z^\mu\right) \\ + \frac{1}{2}\left(\left(\partial_\mu\phi\right)^2 - M^2_H\phi^2\right) - \frac{1}{\sqrt{2}}M_H\sqrt{\lambda}\phi^3 - \frac{\lambda}{4}\phi^4 + \text{ const.} \end{aligned} \tag{2.15}$$

In 2012, the Higgs boson was discovered by the ATLAS and CMS collaborations [4], and the SM was completed. However, there are several unresolved issues in the SM, which make it hard to believe that the SM is the ultimate theory of particle physics, and some examples of the unresolved issues are listed as follows:

- Neutrino mass is assumed to be zero in the SM, but neutrino oscillations were discovered by several experiments [5], and non-zero neutrino mass was proved.
- The SM gives no explanations about the gravity [6], a mechanism to generate the baryon asymmetry of the universe [7], dark matter candidate [8] and strong CP problem [9], etc...
- There are too many free parameters and arbitrarinesses in the SM. This model does not give any explanations about each coupling constant and complicated assignments of the gauge group representations as well as the quantization of electric charge between quarks and leptons.

We believe that a new physics paradigm beyond the SM exists, and it solves the above important open questions.

2.2 Grand Unified Theories (GUTs)

Grand Unified Theories are the extensions of the SM and provide hints of the modern particle physics problems suggested in the last section. The SM gauge symmetry (G_{SM}) can be embedded in some larger gauge symmetry assumed in GUTs, and GUTs predict a single coupling constant for all three interactions at the super high energy scale, $\sim 10^{16}$ GeV, GUT scale. There are a variety of proposed GUT models based on different gauge symmetries, such as SU(5) [10], SO(10) [11], E6 [12], etc... In GUT models, quarks and leptons are basically incorporated into common multiplets, and they generically predict proton decay, which is a direct transition between the quarks and leptons without conserving the baryon number.

2.2.1 Minimal SU(5) GUT model

The minimal choice for unification in a simple group is SU(5). In the SU(5) GUT model, the SM gauge symmetry can be embedded in this larger gauge symmetry, and $U(1)_Y$ hypercharge is automatically quantized. One SM generation particles come from the following **10** and $\bar{\mathbf{5}}$ representations,

$$\mathbf{10}: \begin{pmatrix} 0 & u_b^c & -u_g^c & u_r & d_r \\ -u_b^c & 0 & u_r^c & u_g & d_g \\ u_g^c & -u_r^c & 0 & u_b & d_b \\ -u_r & -u_g & -u_b & 0 & e^c \\ -d_r & -d_g & -d_b & -e^c & 0 \end{pmatrix}, \tag{2.16}$$

$$\bar{\mathbf{5}}: \begin{pmatrix} d_r^c \\ d_g^c \\ d_b^c \\ e \\ -\nu_e \end{pmatrix}. \tag{2.17}$$

The top left 3×3 and bottom right 2×2 blocks in the first matrix correspond to $SU(3)_C$ and $SU(2)_L$ fermions, respectively. Since in the SU(5) symmetry there are 24 generators, 12 new gauge bosons (X,Y bosons) are introduced in addition to those in the SM. They can be written in the following matrix form,

$$\begin{pmatrix} G_1^1 - \frac{2A}{\sqrt{30}} & G_2^1 & G_3^1 & \bar{X}_1 & \bar{Y}_1 \\ G_1^2 & G_2^2 - \frac{2A}{\sqrt{30}} & G_3^2 & \bar{X}_2 & \bar{Y}_2 \\ G_1^3 & G_2^3 & G_3^3 - \frac{2A}{\sqrt{30}} & \bar{X}_3 & \bar{Y}_3 \\ X_1 & X_2 & X_3 & \frac{W^3}{\sqrt{2}} + \frac{3A}{\sqrt{30}} & W^+ \\ Y_1 & Y_2 & Y_3 & W^- & -\frac{W^3}{\sqrt{2}} + \frac{3A}{\sqrt{30}} \end{pmatrix}, \tag{2.18}$$

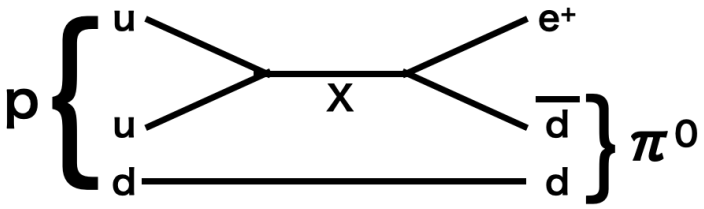

Figure 2.1: Proton decay ($p \to e^+\pi^0$) diagram.

where G represents the SU(3) gauge field. The top right 3×2 and bottom left 2×3 blocks correspond to X and Y bosons, which mediate interactions between quarks and leptons, thus violating the lepton and baryon number conservations and leading proton decays. The dominant proton decay mode is predicted to be $p \to e^+\pi^0$ (Fig. 2.1).

However, the predicted partial lifetime of protons in this model, ($\tau/B(p \to e^+\pi^0) \sim 10^{31\pm1}$ years [3]), is too short and is already excluded by several experiments [13]. Furthermore, there is still no space for the right-handed neutrino helicity state, and neutrinos must be massless in this model.

2.2.2 Extensions of SU(5) GUT model

In the SO(10) GUT model [11], an extra singlet, which could represent a right-handed neutrino helicity state, as well as one SM generation particles can be incorporated into a single **16** representation. From this feature, this model could explain the neutrino mass generation mechanism through the seesaw model [14].

This gauge symmetry, SO(10), can break directly to the SM gauge symmetry, while there are two inequivalent breaking patterns into the SM gauge symmetry, SO(10) $\to$ SU(5) $\times$ U(1) and SO(10) $\to$ SU(4) $\times$ SU(2) $\times$ SU(2). In the first case, $\mathrm{U(1)}_Y$ hypercharge is a linear combination of the U(1) charge inside the SU(5) and one outside, leading to a "flipped" relation for the right-handed leptons and quarks relative to the standard SU(5) model. Accordingly, right-handed quark and lepton assignments in **10** and $\bar{\mathbf{5}}$ representations are flipped. This model is called the flipped SU(5) model and could enhance $p \to \mu^+\pi^0$ decays [15]. In the latter breaking pattern, the intermediate gauge symmetry, SU(4) $\times$ SU(2) $\times$ SU(2), is the historically first proposed GUT model called the Pati-Salam model [16], and the quantization of electric charge can be also explained in this model. The predicted proton lifetime in the SO(10) GUT model is at the same scale or longer than the current lifetime limit (from 10^{34} to 10^{39}) [17].

Further extension of the SO(10) GUT model is also proposed, an exceptional group $\mathrm{E_6}$ [12]. In this model, the **16** representation in SO(10) is embedded in the **27** representation in $\mathrm{E_6}$.

2.2.3 Supersymmetric GUT

Supersymmetric (SUSY) models postulate a symmetry between fermions and bosons, requiring each fermion to have a boson partner and vice versa. Table 2.2 shows SM particles and their SUSY partners. They are expected to exist with a mass of around $1 \sim 10$ TeV and have been searched for in experiments in the LHC. So far, there is no positive result of the existence of SUSY particles but this model is still quite prospective.

Originally, SUSY is introduced to solve the fine-tuning problem (or naturalness problem) [18]. In the SM, the Higgs mass correction term (Δm_H) can be in the order of $\Lambda \sim 10^{19}$ GeV, Planck scale, while the observed Higgs mass is about 125 GeV/c^2. It means that the 10^{-17} order of fine-tuning is needed and suggests an underlying mechanism. In SUSY theories, SUSY partners yield the opposite loop contribution to cancel the mass correction term, and therefore this super precise tuning is no longer needed.

Table 2.2: SM particles and SUSY partners.

SM particles		Spin	SUSY partners		Spin
q	quark	$\frac{1}{2}$	$\tilde{q}$	squark	0
l	lepton	$\frac{1}{2}$	$\tilde{l}$	slepton	0
g	gluon	1	$\tilde{g}$	gluino	$\frac{1}{2}$
W	W boson	1	$\tilde{W}$	wino	$\frac{1}{2}$
Z	Z boson	1	$\tilde{Z}$	zino	$\frac{1}{2}$
γ	photon	1	$\tilde{\gamma}$	photino	$\frac{1}{2}$
H	higgs	0	$\tilde{H}$	higgsino	$\frac{1}{2}$

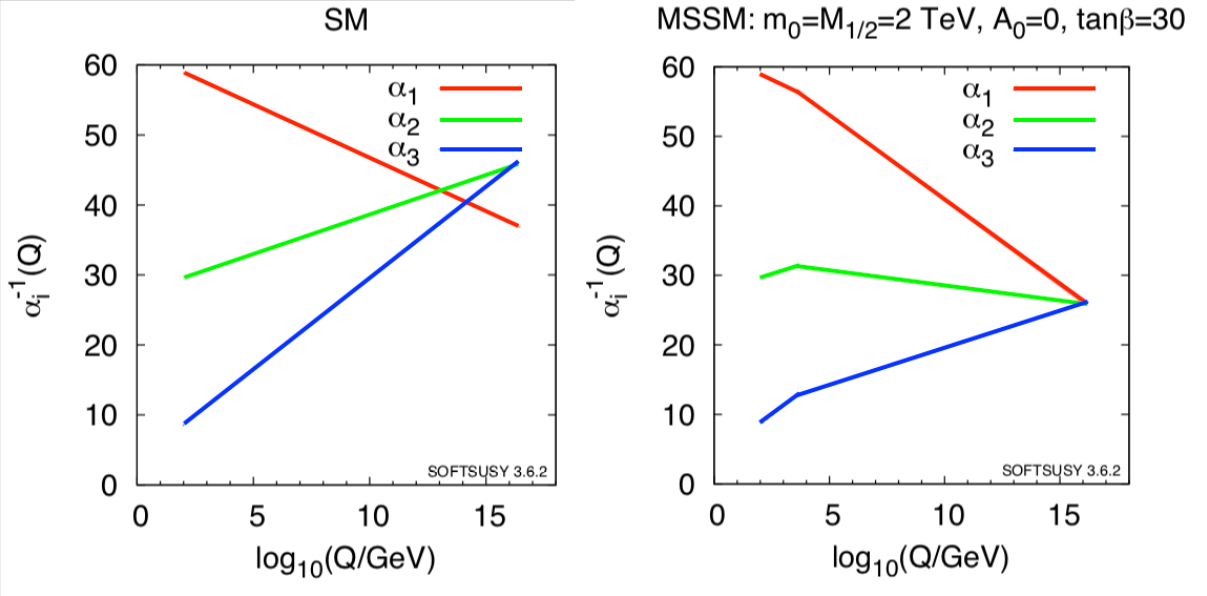

Figure 2.2: Inverse of running coupling constants as a function of the logarithm of the energy scale. Taken from [3, 19].

Another interesting feature in SUSY models is that they can realize single point unification of the coupling constants for the three interactions. Running coupling constants can be calculated using renormalization group equations (RGE) with appropriate inputs from experimental results. In the SM, extrapolated running coupling constants would not meet in a single point, while in the minimal SUSY standard model (MSSM), coefficients in RGE are modified after the SUSY breaking scale, and a single unification point can be realized. Figure 2.2 shows the running coupling constants as a function of the logarithm of the energy scale.

In the MSSM, the predicted partial lifetime of protons via $p \to e^+\pi^0$ is generically longer than that in non-SUSY models because the GUT unification energy scale is shifted to the larger side. On the other hand, SUSY models favor another decay mode, $p \to \nu K^+$, mediated by SUSY particles (Fig. 2.3). For this mode, the predicted partial lifetime depends on SUSY particle parameters, and it is in the order of 10^{33} years or longer [21].

2.3 Proton Decay Searches

In the last section, GUT models and their proton lifetime predictions are briefly reviewed. Historically, the first attempt to search for proton decay was conducted in 1954 by F. Reines *et al.* before these GUT models were proposed. They searched for proton decays in a plastic scintillator and set the lower lifetime limit of $\tau_p > 10^{22}$ years [22]. Thereafter, various proton

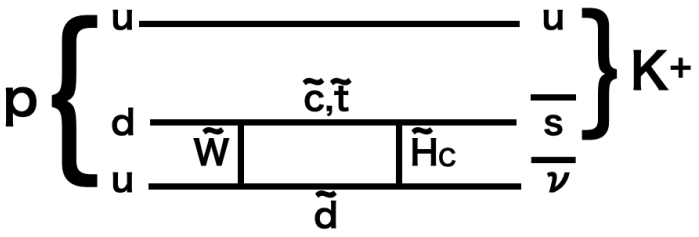

Figure 2.3: Proton decay ($p \to \nu K^+$) diagram. In the diagram, $\tilde{H}_C$ stands for color-triplet higgs.

decay searches have been conducted in the past several decades using different types of detectors, such as plastic scintillator detectors [23], fine-grained iron calorimeters [24], and water Cherenkov detectors [13]. Among such different detector types, a water Cherenkov detector is relatively easy to scale up at a low cost.

This thesis presents proton decay search results via $p \to e^+\pi^0$ and $p \to \mu^+\pi^0$ using the world's largest underground water Cherenkov detector, Super-Kamiokande. Theoretically, the ratio of the two decay rates, $\Gamma(p \to \mu^+\pi^0)/\Gamma(p \to e^+\pi^0)$, could be important to identify the GUT model among SU(5), SO(10), and E_6 [25]. Figure 2.4 shows the relation between the ratio of the two decay rates and each decay mode's lifetime with varying model parameters. This ratio could be also used to differentiate between GUT models, SU(5) and flipped SU(5), through the potential connection with the neutrino oscillation parameters, the PMNS matrix [5, 26]. Figure 2.5 shows the prediction of $\Gamma(p \to \mu^+\pi^0)/\Gamma(p \to e^+\pi^0)$ in case of unflipped (standard) SUSY SU(5) and flipped SUSY SU(5) with normal and inverted neutrino mass ordering assumptions. In the flipped SU(5) with inverted neutrino mass ordering case, the proton decay mode $p \to \mu^+\pi^0$ is enhanced compared to the $p \to e^+\pi^0$ mode. In this way, the discovery of the proton decay would provide not only strong evidence of GUTs but also further physics implications. Therefore, it is quite important to search for these modes comprehensively.

From the experimental point of view, they are the most prospective modes in Super-Kamokande because all final state particles can be reconstructed, and from their unique (back-to-back) event topologies, proton decay signal and atmospheric neutrino background events can be clearly discriminated. Moreover, hydrogen nuclei (free protons) in water are suitable targets for these searches because they are free from the Fermi motion and other nuclear effects. The previous most stringent constraints on these partial lifetimes are $\tau/B(p \to e^+\pi^0) > 1.6 \times 10^{34}$ years and $\tau/B(p \to \mu^+\pi^0) > 7.7 \times 10^{33}$ years at 90% confidence level using the 306 kton·years of Super-Kamiokande data [27].

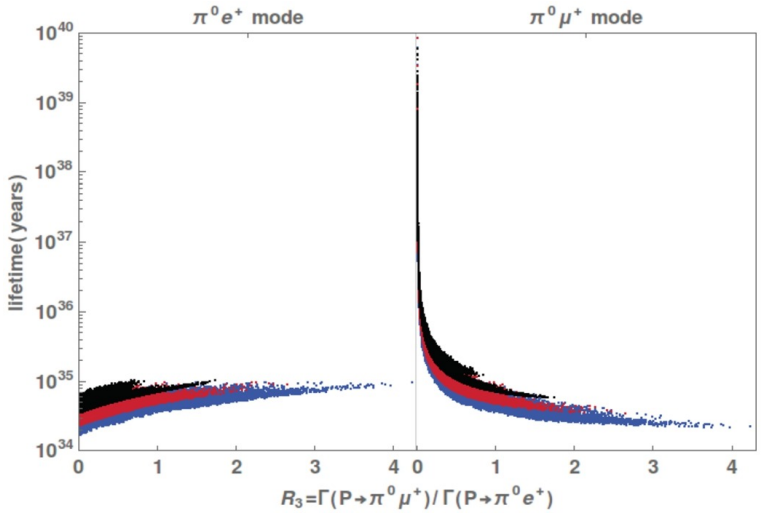

Figure 2.4: Relation between $\Gamma(p \to \mu^+\pi^0)/\Gamma(p \to e^+\pi^0)$ and each decay mode's lifetime. Different gauge group, SU(5), SO(10) and E_6, predictions are plotted in black, red and blue, respectively. Taken from [25].

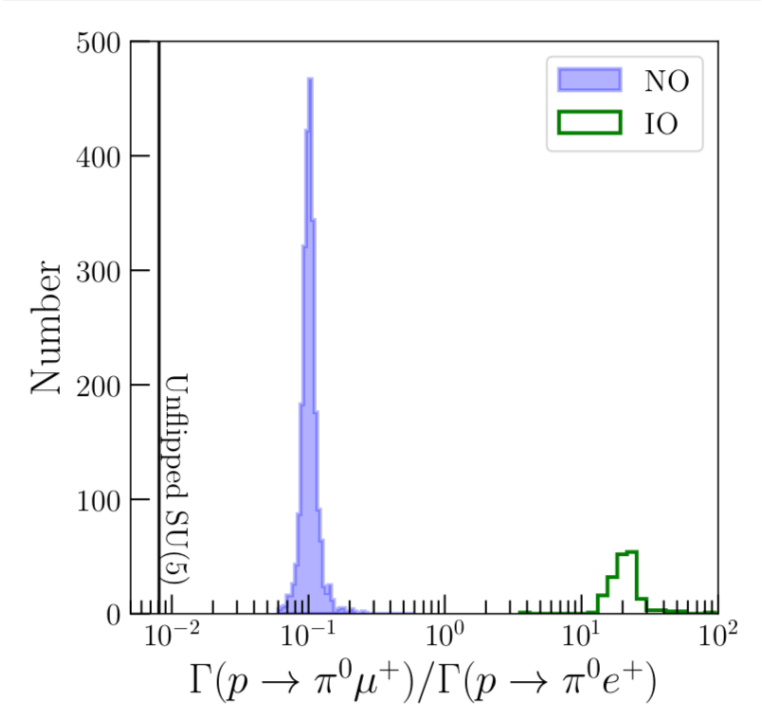

Figure 2.5: Prediction of $\Gamma(p \to \mu^+\pi^0)/\Gamma(p \to e^+\pi^0)$ in case of unflipped (standard) SUSY SU(5) (black line) and flipped SUSY SU(5) with normal (blue histogram) and inverted (green histogram) neutrino mass ordering. Taken from [26].

Chapter 3

The Super-Kamiokande Detector

In this chapter, an overview of the Super-Kamiokande (SK) detector, each detector component, and detector calibration are described.

3.1 Cherenkov Light

Cherenkov light is emitted when a charged particle passes through a dielectric medium at a speed greater than the light velocity in the medium, and it is emitted in a cone shape with a half opening angle (Cherenkov angle, θ_C) from the particle's momentum direction. The Cherenkov angle is given by:

$$\cos\theta_C = \frac{1}{n\beta}, \tag{3.1}$$

$$\beta = \frac{v}{c}, \tag{3.2}$$

where n stands for the refractive index of the medium. In water, n is about 1.34, and the Cherenkov angle is about 42 degrees for a particle with $\beta \sim 1$. The number of emitted photons depends on the wavelength of the emitted photon (λ):

$$\frac{dN}{dxd\lambda} = 2\pi\alpha\left(1 - \frac{1}{n^2\beta^2}\right)\frac{1}{\lambda^2}, \tag{3.3}$$

where x stands for the path length of the particle, and α is the fine structure constant. The number of emitted photons integrated from 300 to 600 nm with respect to λ (SK photomultiplier tube (PMT) sensitive wavelength region) is about 340 photons/cm. The momentum threshold (p_C) of the Cherenkov light emission in a medium is given by the refractive index of the medium and charged particle's mass (m):

$$p_C = \frac{m}{n^2 - 1}. \tag{3.4}$$

The momentum thresholds of charged particles in water are summarized in Table 3.1.

Table 3.1: Charged particles often observed in SK and their Cherenkov threshold.

Particle type	Electron	Muon	Charged Pion	Proton
Cherenkov (momentum) threshold [MeV/c]	0.57	118	156	1052

3.2 Detector

3.2.1 Overview

Super-Kamiokande is the world's largest underground water Cherenkov detector [28]. It is an upright cylinder in shape, 39.3 m in diameter, and 41.4 m in height, containing a total

of 50 kton of ultrapure water. The detector is located about 1,000 m (2,700 meters water equivalent) under Mt. Ikenoyama in Japan. It is optically separated into two regions, an inner detector (ID) and an outer detector (OD). The ID has a diameter of 33.8 m and a height of 36.2 m. More than 11,000 50 cm diameter photomultiplier tubes (PMTs) are mounted on the ID wall facing inwards. The photocathode coverage in the ID is about 40%. 1,885 20 cm diameter PMTs are mounted on the OD behind the ID PMTs facing outwards. The SK data taking period used for the present analysis is divided into four phases with different detector configurations, SK-I, -II, -III, and -IV. The SK-I period began in April 1996 and ended in July 2001. In November 2001, a chain reaction implosion accident destroyed more than half of the PMTs. Using 5,182 ID PMTs to obtain about 19% of photocathode coverage, SK-II operated from October 2002 to October 2005. Between SK-II and SK-III, newly manufactured ID PMTs were installed and SK-III began in July 2006 with recovered 40% of photocathode coverage. In September 2008, front-end electronics and data acquisition systems were upgraded [29, 30], and a new phase named SK-IV lasted for almost 10 years until May 2018. Table 3.2 summarizes each detector phase configuration. A detector side view is shown in Fig. 3.1, and the detector coordinates are defined as shown in Fig. 3.2.

Table 3.2: SK data taking phase and detector configuration.

Phase	SK-I	SK-II	SK-III	SK-IV
Start	Apr./1996	Oct./2002	July/2006	Sep./2008
End	July/2001	Oct./2005	Aug./2008	May/2018
Analysis livetime [days]	1489.2	798.6	518.1	3244.4
The number of ID PMTs	11146	5182	11129	11129
The number of OD PMTs	1885	1885	1885	1885
PMT cover	no	yes	yes	yes
Front-end electronics	ATM	ATM	ATM	QBEE

3.2.2 Inner and Outer Detector

The boundary of the ID and OD is a stainless steel frame structure. A unit of the frame structure is called "supermodule", and it is 2.1 m in height, 2.8 m in width, and 0.55 m in thickness. 12 ID PMTs and 2 OD PMTs are mounted on each supermodule as shown in Fig. 3.3. The gaps between the ID PMTs are covered by opaque black sheets on the ID surface. They work as an optical separation between the ID and OD, and also reduce indirect light contributions, which degrade event reconstruction performance.

A wavelength shifting plate is attached to each OD PMT, and the OD volume is covered by reflective Tyvek sheets. Both instruments help to enhance the light collection efficiency in the OD, working for rejecting external backgrounds such as cosmic-ray muons and gamma rays from radioactive products around the detector.

50 cm Diameter PMT

The 50 cm diameter PMT was originally developed by Hamamatsu Photonics with the cooperation of the Kamiokande collaborators [31]. Based on the original 50 cm diameter PMT, the bleeder circuit and dynode structure were improved to obtain better charge and timing resolution [32]. Its dynode structure is the venetian-blind type. A schematic view of the 50 cm diameter PMT is shown in Fig. 3.4, and basic characteristics are summarized in Table 3.3. The photocathode is coated with Bialkali (Sb-K-Cs), and the sensitive wavelength is from 300 nm to 600 nm. The peak quantum efficiency is about 22% at $\lambda = 390$ nm. The quantum efficiency as a function of incident photon wavelength is shown in Fig. 3.5. A typical single photoelectron distribution and timing distribution are shown in Figures 3.6 and 3.7. Because of the larger

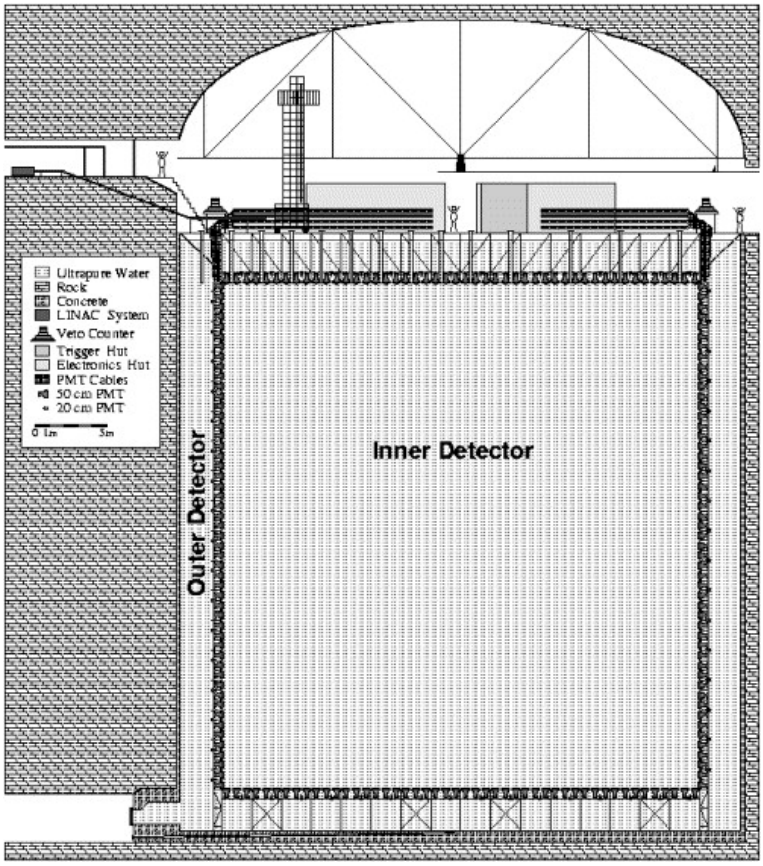

Figure 3.1: Super-Kamikoande detector side view. Taken from [28].

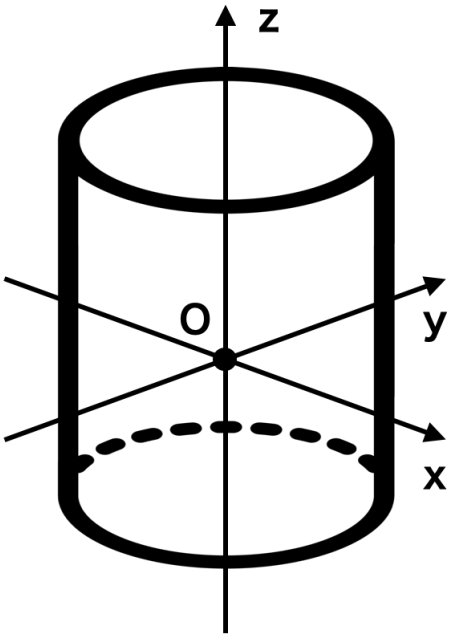

Figure 3.2: Super-Kamikoande detector coordinates. The origin of the coordinates axes is set at the center of the detector.

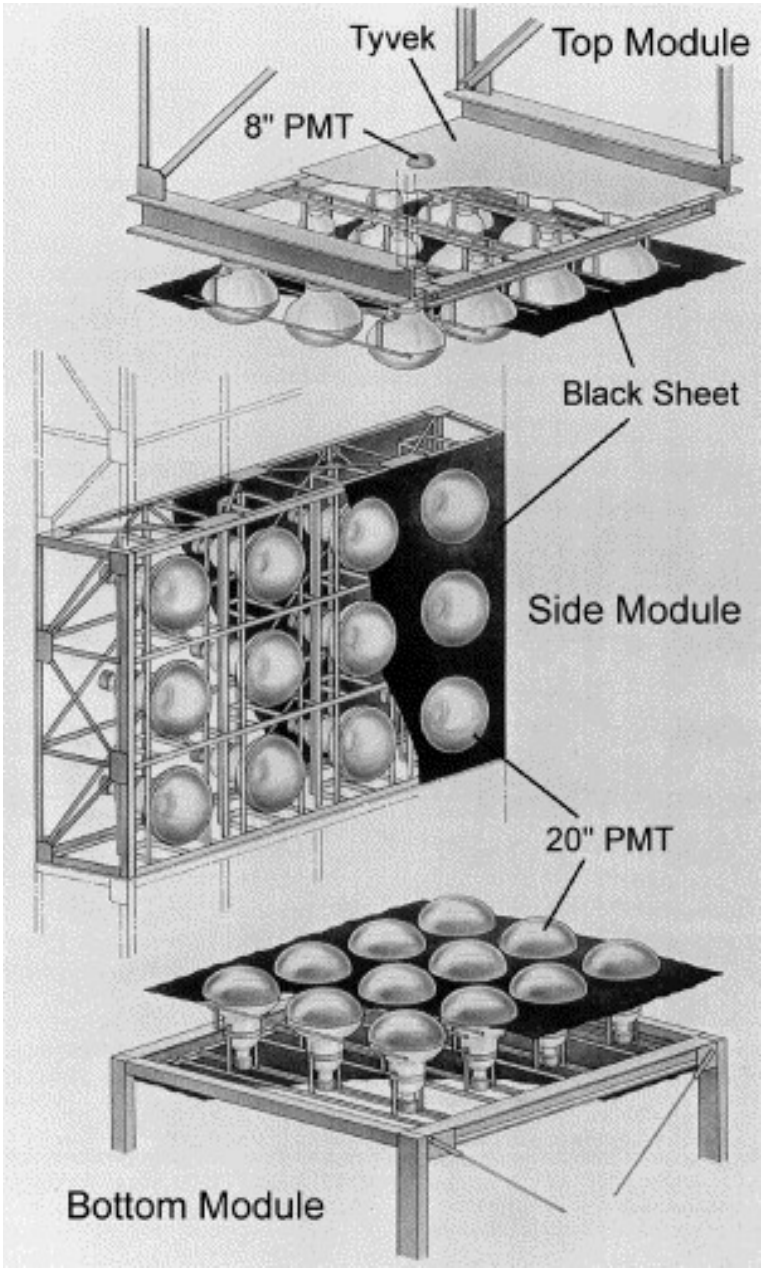

Figure 3.3: Schematic view of the frame structure ("supermodule"). 12 ID PMTs and 2 OD PMTs are mounted on one supermodule. Taken from [28].

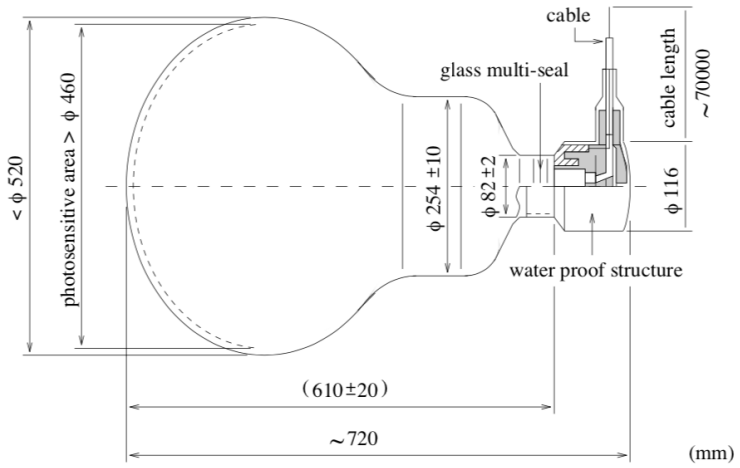

Figure 3.4: Schematic view of the 50 cm diameter PMT. Taken from [28].

diameter of the SK PMT, the PMT response depends on the photon incident position on the photocathode. Such dependence has been measured more detailedly than the previous measurement [32] and is described in Section A.1. From SK-II, the ID PMTs are covered with fiber-reinforced plastic (FRP) and acrylic cases to prevent a chain reaction implosion.

Table 3.3: Characteristics of the 50 cm diameter PMT [28, 32].

Photocathode area	50 cm in diameter
Shape	Hemisherical
Window material	Pyrex glass
Photocathode material	Bialkali
Dynode	Venetian blind type, 11 stages
Pressure tolerance	6 kg/cm^2 water proof
Quantum efficiency	22% at $\lambda = 390$ nm
Gain	10^7 at 2000 Volt
Dark current	200 nA at gain = 10^7
Dark noise rate	~3 kHz at gain = 10^7
Transit time	90 nsec typical at gain = 10^7
Transit time spread	2.2 nsec at single photoelectron

Cherenkov Ring Image

The ID PMTs detect Cherenkov light emitted from charged particles in the ID, and a Cherenkov ring image is projected on the ID wall (Fig. 3.8). Events occurring in the ID are reconstructed using ID PMT charge and timing information as well as their Cherenkov ring image pattern. Figures 3.9 and 3.10 show event displays of an electron and muon generated by our detector simulation (MC). An electron ring has a fuzzy edge due to overlapping rings produced by its electromagnetic cascade, while a muon ring has a crisp edge since its mass is much larger and it does not make any cascades.

Compensation Coils

Due to the large diameter of the SK PMT and the longer electron trajectory distance inside the PMT bulb, the geomagnetic field (about 450 mG) deteriorates the PMT performance. Impacts on a single PMT response by an ambient magnetic field have been measured and are

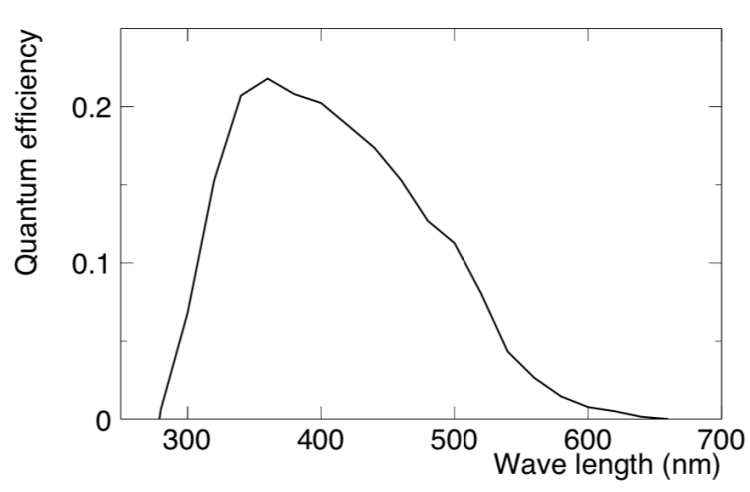

Figure 3.5: Quantum efficiency as a function of incident photon wavelength. Taken from [28].

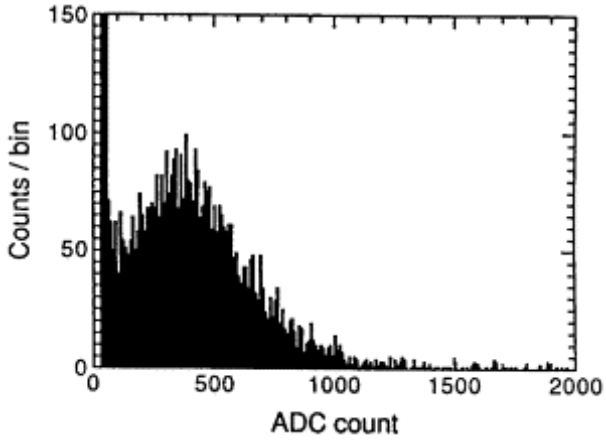

Figure 3.6: Single photoelectron distribution of the 50 cm diameter PMT. Taken from [28].

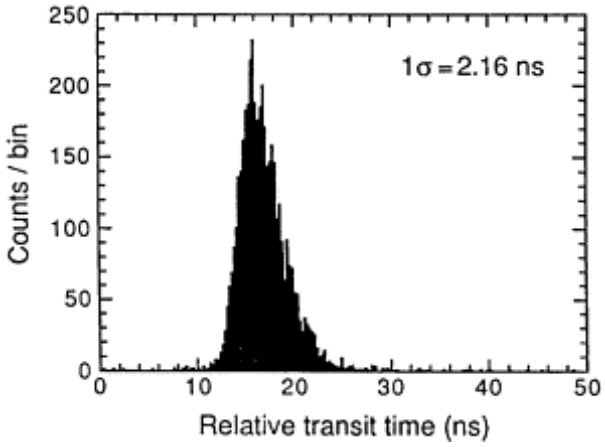

Figure 3.7: Transit time distribution of the 50 cm diameter PMT. Taken from [28].

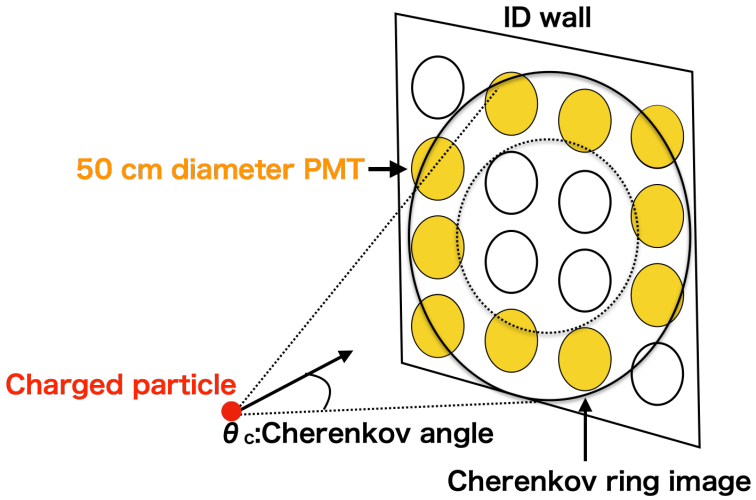

Figure 3.8: Cherenkov ring image.

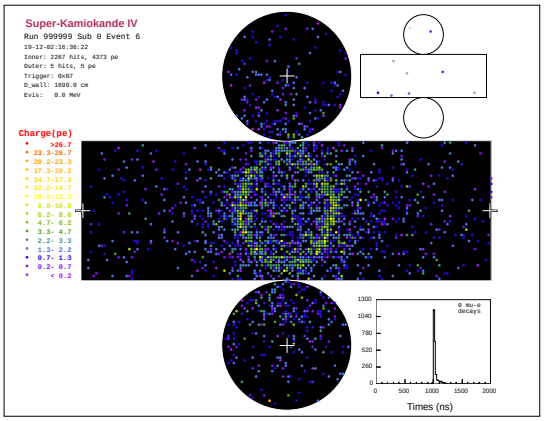

Figure 3.9: Cherenkov ring image produced by an electron.

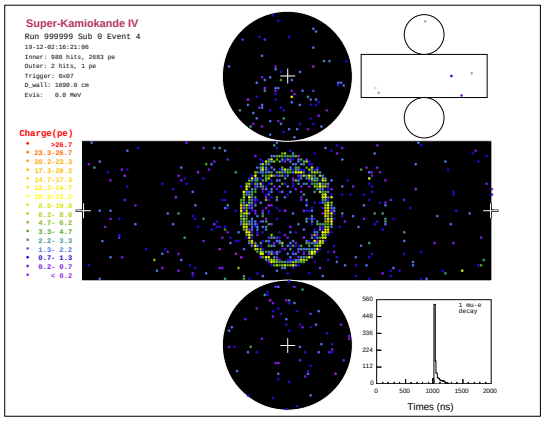

Figure 3.10: Cherenkov ring image produced by a muon.

described in Section A.1. To avoid the deterioration of the PMT performance, magnetic field compensation coils are deployed outside the water tank to suppress the magnetic field inside the detector. A schematic view of the compensation coils is shown in Fig. 3.11. The residual magnetic field inside the ID has been measured. The mean residual magnetic filed strength inside the detector has been estimated to be less than 40 mG with a standard deviation of 16 mG, and the details are described in Section A.2.2.

3.2.3 Water Purification System

The detector is filled with ultrapure water, and its origin is spring water in the Kamioka mine. In order to remove radioactive impurities, dust, and bacteria which produce low energy background events and degrade the transparency of water, a water purification system nearby the detector circulates the water with a flow rate of about 60 ton/hour. The PMT dark noise rate is sensitive to the water temperature, and therefore the system also maintains the water temperature at about 13°C. Over the 20 years of operation, the system has been continuously upgraded. Figure 3.12 shows a schematic diagram of the water purification system as of SK-IV [34, 35]. Specific processes are as follows:

1. 1 μm filter
   A 1 μm filter removes dust larger than 1 μm since they often contain radioactive impurities.

2. Heat exchanger
   Pumps, which are used to circulate the water, and PMTs generate heat and increase the water temperature. Under the higher temperature condition, the growth of bacteria becomes rapid and the PMT dark noise rate becomes higher. To prevent both, a heat exchanger cools the water and keeps it about 13°C.

3. Ion exchanger
   An ion exchanger removes high molecular and heavy ions including the radioactive contaminations.

4. UV sterilizer
   An ultraviolet radiation sterilizer removes bacteria remaining in the water.

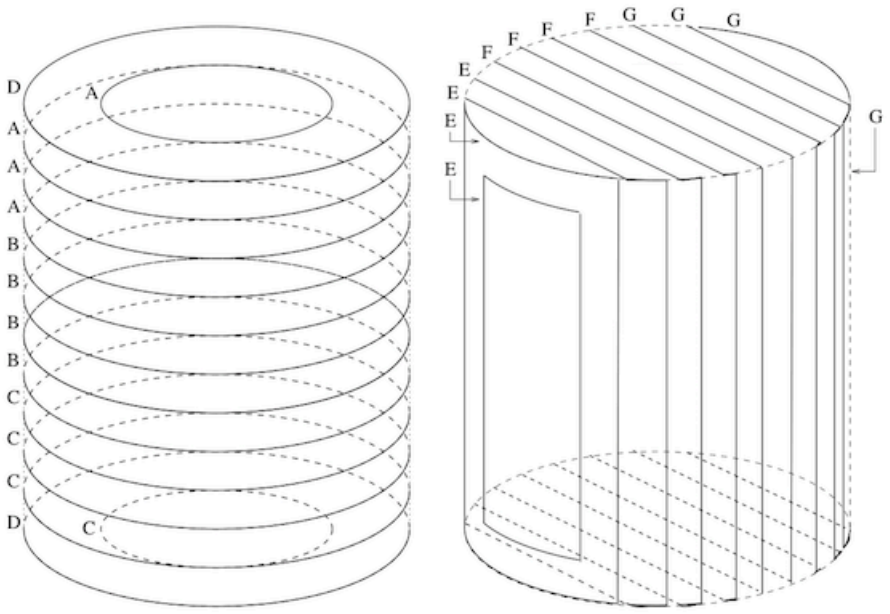

Figure 3.11: Schematic view of the compensation coils. They are composed of 26 sets of coils deployed outside the water tank. Taken from [33].

5. Radon-less air dissolving system
   Radon-less air is dissolved in the water, and it improves the radon removal efficiency in the following vacuum degasifier step.

6. Reverse osmosis filter
   A reverse osmosis filter removes particulates in the water.

7. Vacuum degasifier system
   Radon and air gases are contained in the water. Dissolved oxygen encourages the growth of bacteria. A vacuum degasifier removes gases dissolved in the water. The removal efficiency for radon and oxygen gas is estimated to be about 96% and 99%, respectively.

8. Cartridge ion exchanger
   Cartridge ion exchanger (polisher) further reduces ions in the water.

9. Ultra filter
   An ultrafilter, which consists of hollow fiber membrane filters, removes particulates whose size is greater than $\sim$ 10 nm in diameter.

10. Membrane degasifier
    A membrane degasifier further reduces radon gas dissolved in the water. The removal efficiency for radon gas at this step is estimated to be about 83%.

After these processes, the radon concentration in the supply water is estimated to be 1.74 $\pm$ 0.14 mBq/m^3, and in the return water, it is 9.06 $\pm$ 0.58 mBq/m^3 [35]. Locations of the water inlets and outlets in the SK tank are shown in Fig. 3.13.

3.2.4 Air Purification System

The radon concentration level in the air in the mine is about 100 times higher than outside. This "radon rich" air contaminates the water in the detector. Therefore, an air purification system is located outside the mine, and radon reduced air is sent to the experimental site as

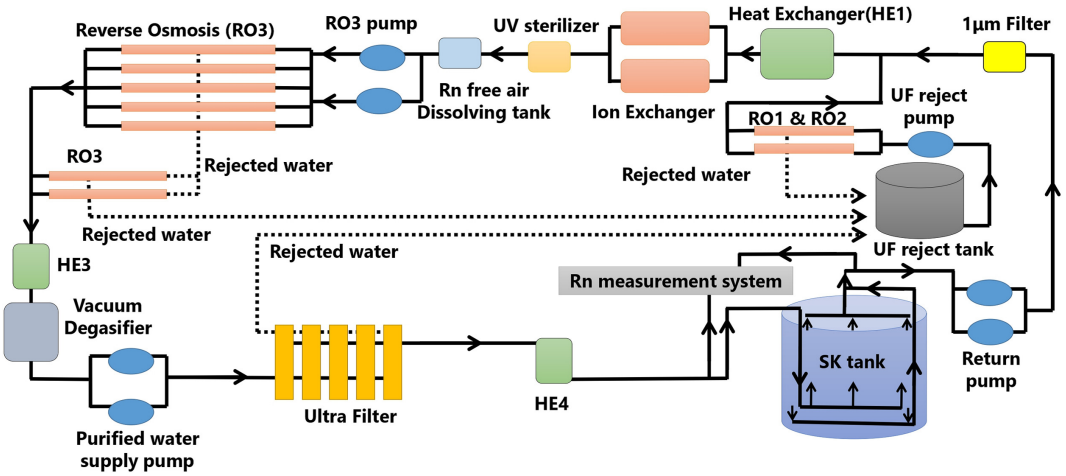

Figure 3.12: Schematic diagram of the water purification system as of SK-IV. Each component is described in the text. Taken from [35].

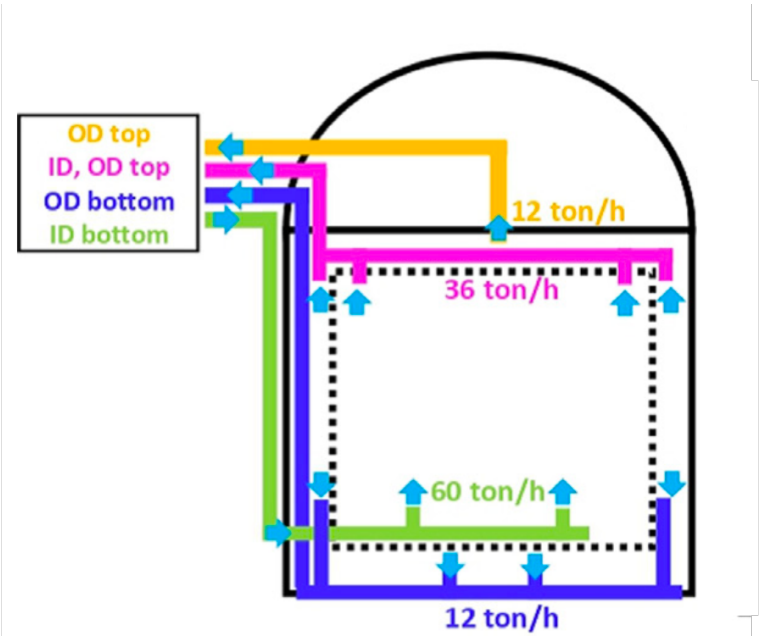

Figure 3.13: Schematic view of the water circulation paths in the SK tank. Taken from [35].

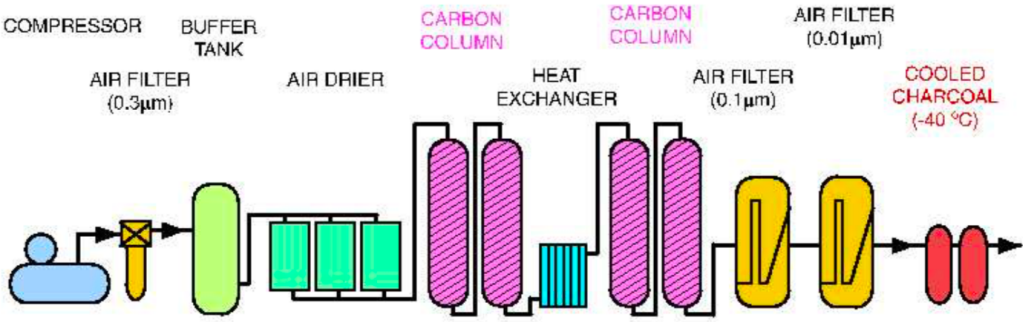

Figure 3.14: Schematic diagram of the air purification system. Each component is described in the text. Taken from [28].

well as inside the tank. A schematic diagram of the air purification system is shown in Fig. 3.14. Specific processes are as follows:

1. Air compressor
   Air is compressed up to about 8 atm.

2. Air filter
   There are three filters, whose mesh size is 0.3 μm, 0.1 μm, and 0.01 μm, and they remove dust in the air.

3. Air drier
   Moisture in the air is removed.

4. Carbon column
   Radon gas in the air is absorbed by a carbon column.

5. Cooled charcoal
   Radon gas in the air is further removed. To improve the radon removal efficiency, the charcoal is cooled.

After these processes, the radon concentration level in the supply air is less than a few mBq/m^3 [36].

3.2.5 Data Acquisition System

Here, data acquisition systems are described. The data acquisition system is different between SK-I to -III and SK-IV. During SK-I to -III, ID PMT signals were processed by custom build TKO (TRISTAN KEK Online) [37] modules called ATM (Analog-Timing-Module) [38, 39]. In 2008, new front-end electronics (QTC-Based Electronics with Ethernet, QBEE [29]) and software trigger system were introduced [30]. There are five electronics huts on the top of the detector tank, one central hut, and four-quadrant huts. The central hut contains electronics and related computers for triggering and GPS. Each quadrant hut contains front-end electronics for all PMTs in one quadrant of the detector. Each PMT is connected to a high voltage supply and front-end electronics. A signal from each PMT is sent to the front-end electronics board through a coaxial cable.

Data Acquisition System for SK-I to -III Inner Detector

A schematic diagram of the ID data acquisition system for SK-I to -III is shown in Fig. 3.15. When a signal from a PMT is sent to an ATM channel, and its amplitude is greater than

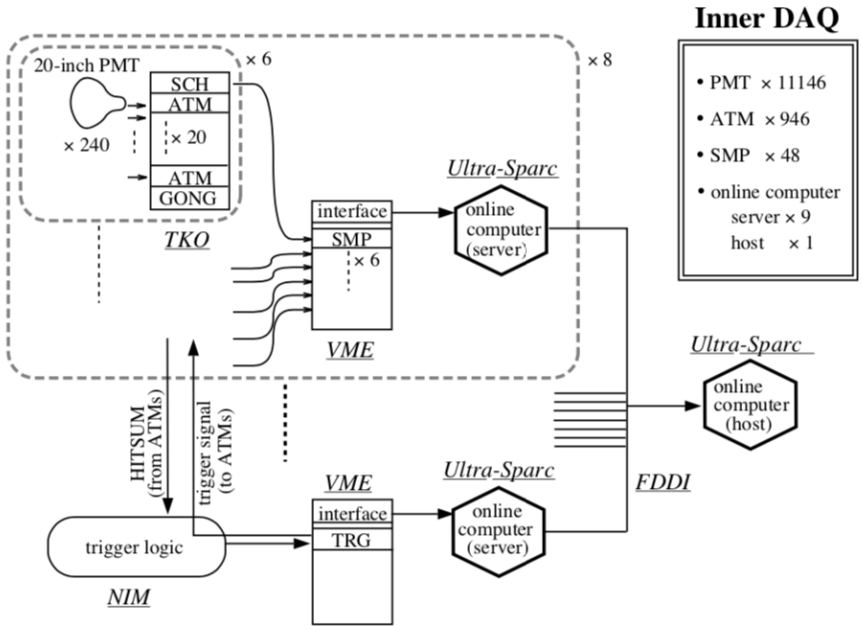

Figure 3.15: Schematic diagram of the ID data acquisition system for SK-I to -III. The data flow is described in the text. Taken from [28].

1/4 photoelectrons, the ATM channel converts its signal amplitude and detection time to an analog charge and keeps it. Simultaneously, the ATM board sends an analog signal whose amplitude is proportional to the number of hit channels (HITSUM signal, a square wave with a width of 200 nsec and height of -15×(number of hit channels) mV) to the trigger module at the central hut. Here, 200 nsec corresponds to an approximate time duration that a charged particle takes to pass through the entire detector. All HITSUM signals are summed up, and if the total amplitude exceeds a threshold, a global trigger is issued. A schematic diagram of the trigger generation is shown in Fig. 3.16. The global trigger is distributed to all ATMs, and each ATM digitizes the analog charge, which is kept in the previous step, using an analog-to-digital converter (ADC). The digital signals are sent to and stored at SMP (Super Module Partner, a memory module) via SCH (Super Control Head). Finally, these data are sent to the online computers located at the central hut.

In this system, the impedance matching at the ATM input circuit is not perfect, and reflection signals from PMTs are observed 700 nsec after the primary PMT signals (the length of the coaxial cable is about 70 m). Therefore, there is a dead-time not to record these reflected signals, degrading the tagging efficiency of Michel electrons from muon decays.

Data Acquisition System for SK-I to -III Outer Detector

A schematic diagram of the OD data acquisition system for SK-I to -III is shown in Fig. 3.17. High-voltage of the OD PMT is supplied through a coaxial cable, and a signal is sent to the OD electronics through the same cable. A high voltage capacitor picks off signals from each OD PMT. A signal from one OD PMT is sent to a charge-to-timing converter (QTC) module, which converts it to a rectangular pulse whose width is proportional to the input charge. Similarly to the ID, a HITSUM signal is generated at the QTC module and sent to the trigger module. If a global trigger is issued, the leading edge and the width of the rectangular pulse is converted to the timing and charge information of the OD PMT by the TDC module. Finally, these digital signals are sent to the online computer through a VME memory module, DPM (Dual Port Memory).

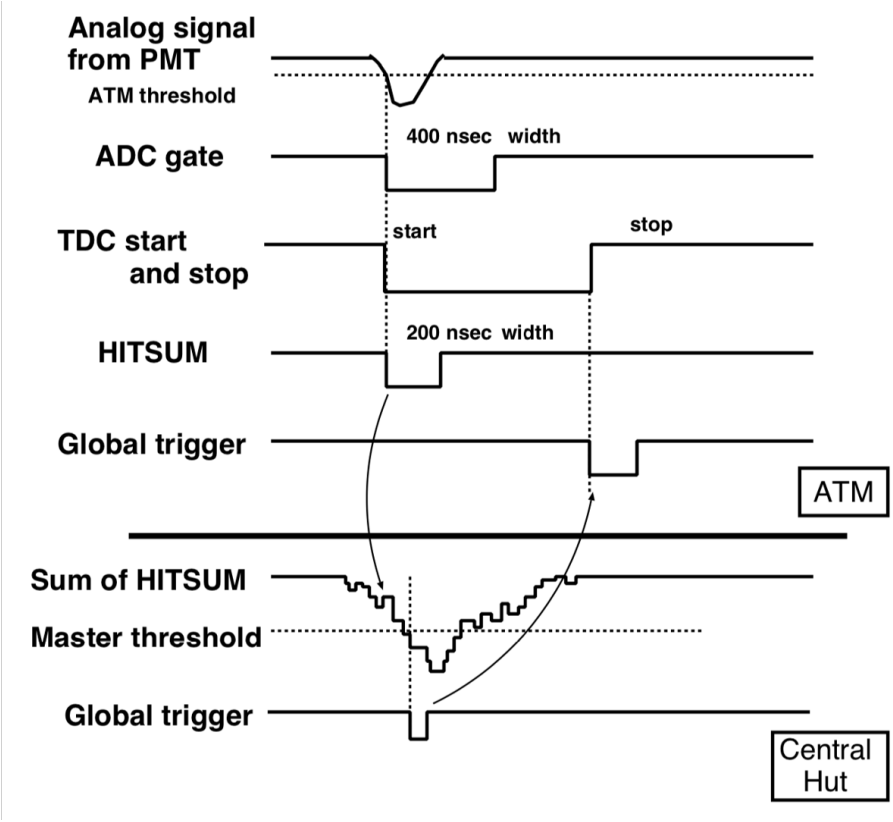

Figure 3.16: Schematic diagram of the trigger generation for SK-I to -III. When the sum of HITSUM exceeds the threshold level, a global trigger is issued. Taken from [41].

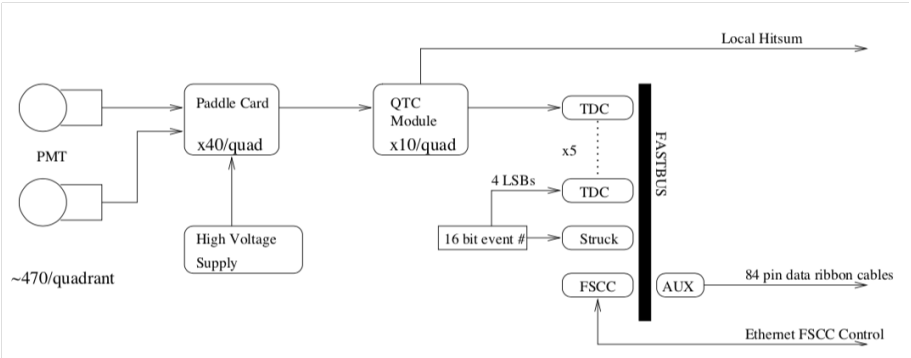

Figure 3.17: Schematic diagram of the OD data acquisition system for SK-I to -III. Taken from [40].

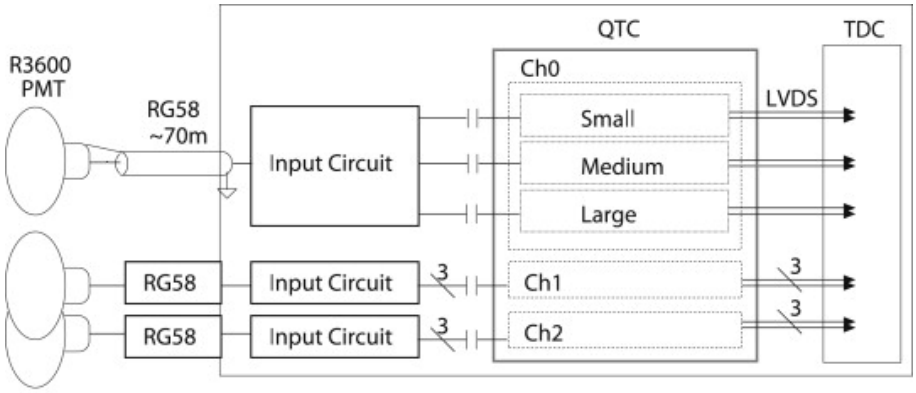

Figure 3.18: Schematic diagram of the QBEE electronics. Taken from [29].

Hardware Trigger

There are three types of global triggers for the ID in SK-I to -III, HE (High Energy), LE (Low Energy), and SLE (Super Low Energy). They have different threshold values for each, and their values are summarized in Table 3.4 including the OD threshold. When the amplitude of the summed HITSUM signal exceeds one of them, the corresponding type of trigger is issued. The HE trigger threshold level roughly corresponds to about 6 MeV of electron equivalent energy deposition in the detector. Among the three, the SLE trigger rate is most sensitive to the detector ambient background level. Therefore, the SLE trigger threshold value was changed many times depending on the background level.

Table 3.4: The global trigger threshold value for each trigger type and SK phase. Since the SLE trigger threshold value was changed many times during SK-I and SK-III, the only initial and last values are shown.

	SK-I	SK-II	SK-III
HE	-340 mV	-180 mV	-320 mV
LE	-320 mV	-152 mV	-302 mV
SLE	$-260 \rightarrow -186$ mV	-110 mV	$-212 \rightarrow -186$ mV
OD	-380 mV	-380 mV	-380 mV

Data Acquisition System for SK-IV

In 2008, the front-end electronics, ATM, was replaced by QBEE. Figures 3.18 and 3.19 show a schematic diagram of the QBEE electronics and a schematic diagram of the entire data acquisition system for SK-IV, respectively. When a signal is sent to a QBEE channel, and its amplitude exceeds the threshold, 1/4 photoelectrons, the QTC module integrates the signal and outputs a rectangular pulse, whose leading-edge represents the signal timing and width represents the integrated charge. There are three gain ranges, small, medium, and large. The gain ratio is set to $1 : \frac{1}{7} : \frac{1}{49}$, and the large range channel can record up to about 2500 pC, which is about five times larger than ATM. The rectangular pulse is sent to the TDC module and digitized. The digitized charge and timing information is sent to the front-end PC through the Ethernet cable after being processed by FPGA. The front-end PCs arrange the received data in a timing order and send them to the merger PCs, where a software trigger is issued. Finally, event information is collected by the organizer PC and recorded on the disk.

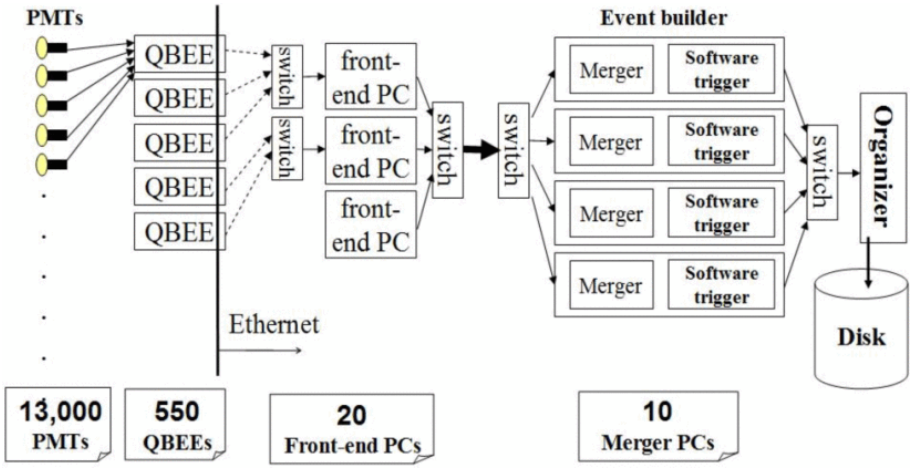

Figure 3.19: Schematic diagram of the data acquisition system for SK-IV. The data flow is described in the text. Taken from [30].

Software Trigger

In this new system, a software trigger is issued if the number of PMT hits in a sliding 200 nsec timing window, N_{200}, exceeds the trigger threshold. There are four trigger types for the ID in SK-IV, SHE (Super High Energy), HE (High Energy), LE (Low Energy), and SLE (Super Low Energy). When a trigger is issued, all hits within -5 μsec to +35 μsec after the trigger timing are recorded for SHE, HE, and LE. This time width is much longer than that in ATM and enables us to tag Michel electrons from muon decays more efficiently. The threshold value and recorded timing width for each trigger type are summarized in Table 3.5. If an SHE trigger is issued without an OD trigger, a special trigger, AFT trigger, is issued, and all of the hits up to 535 μsec after the primary SHE trigger timing are recorded. The AFT trigger information is used for a search for a 2.2 MeV gamma ray emitted from neutron capture on hydrogen (τ_{capture} $\sim$200 μsec). The typical event rate in SK-IV for the data set used in the present work is described in Chapter 5.

Table 3.5: The software trigger threshold value (N_{200}) and recorded timing width for each trigger. The trigger thresholds for SHE and SLE were changed during SK-IV, and the only initial and last values are shown.

	N_{200}	Timing Width
SHE	70 $\rightarrow$ 58	-5 $\sim$ +35 μsec
HE	50	-5 $\sim$ +35 μsec
LE	47	-5 $\sim$ +35 μsec
SLE	34 $\rightarrow$ 31	-0.5 $\sim$ +1.0 μsec
OD	22	-5 $\sim$ +35 μsec

3.3 Detector Calibration

Using various light and radioactive sources, signal outputs of the ID PMTs are calibrated, and water quality inside the detector is measured [42]. Here, these calibration methods are described.

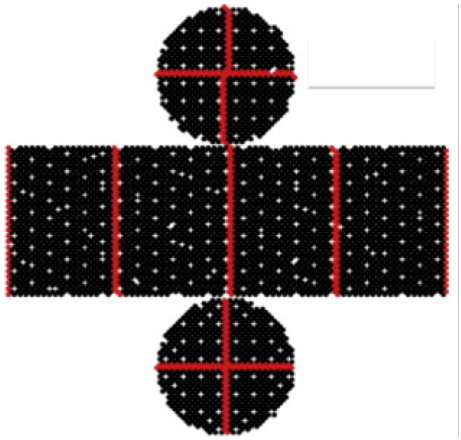

Figure 3.20: Net of the ID. Red points denote the locations of 420 "standard PMTs" in the ID. Taken from [42].

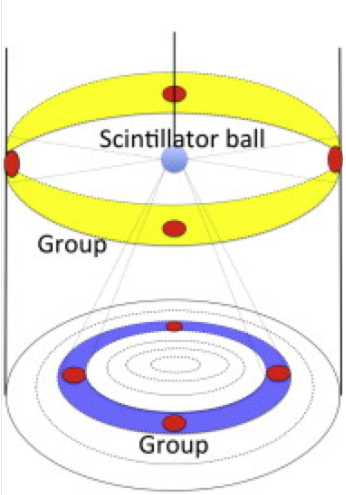

Figure 3.21: Grouping of the ID PMTs for the HV determination. Taken from [42].

3.3.1 High-voltage Determination

Each PMT's applied high-voltage (HV) is set so that all PMTs give the same output charge for the same incident light intensity. Before installing and calibrating them inside the detector, applied HVs were determined for 420 "standard PMTs" using an independent calibration setup to obtain the same output charge among them for the same light intensity. After that "pre-calibration", those 420 standard PMTs were mounted as shown by the red points in Fig. 3.20 and served as "reference PMTs" for other PMTs. PMTs mounted at similar geometrical positions were grouped as shown in Fig. 3.21. A scintillator ball flashing by Xe lamp was placed at the center of the detector (Fig. 3.21), and the HVs of the other PMTs were determined so that their observed charges are matched to the average charge of the reference PMTs in the same group. By doing this, geometrical effects caused by photon absorption and scattering in water can be canceled out. Uniformity of the observed charge compared to the reference PMT value is shown in Fig. 3.22 and its RMS is estimated to be 1.3%.

3.3.2 Relative Gain Calibration

In order to convert the PMT output (observed) charge to the number of photoelectrons (p.e.s), each PMT gain needs to be determined. There were two steps to obtain all PMT gain values. First, the relative difference of the PMT gain was measured, and in the next, the overall average gain was determined. The relative difference of the PMT gain was extracted in the following two measurements using a nitrogen-laser source placed at the center of the detector: the first measurement uses high-intensity flashes so that every PMT detects a sufficient number of photoelectrons, and the second uses low-intensity flashes in which only a few PMTs are fired. Measurement outputs of them, the average charge for the ith PMT, $Q_i^{\rm obs}$, from the first measurement and the number of hits for the ith PMT, $N_i^{\rm obs}$, from the second measurement can be parameterized as follows:

$$Q_i^{\rm obs} \propto I_s \times f(\Theta_i) \times \epsilon_i^{\rm qe} \times G_i, \tag{3.5}$$

$$N_i^{\rm obs} \propto I_w \times f(\Theta_i) \times \epsilon_i^{\rm qe}, \tag{3.6}$$

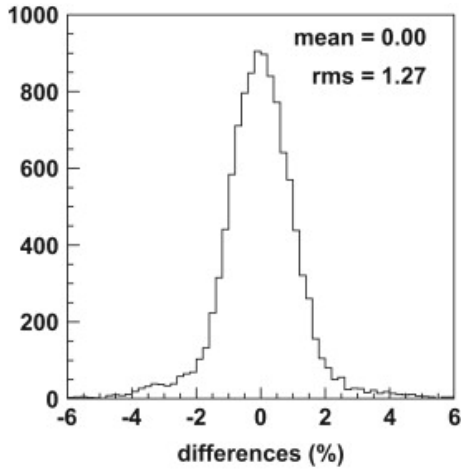

Figure 3.22: Uniformity of the observed charge compared to the reference PMT value. Taken from [42].

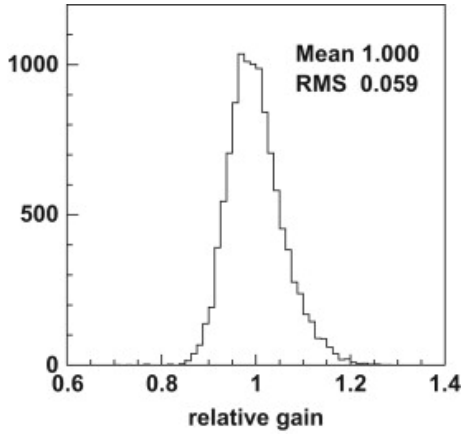

Figure 3.23: Relative gain distribution of the ID PMTs. Values are normalized to their mean value. Taken from [42].

where I_s and I_w are the average intensities of high- and low-intensity flashes, respectively, $f(\Theta_i)$ is the ith PMT acceptance correction factor as a function of photon incident angle (Θ_i), $\epsilon_i^{\rm qe}$ is the ith PMT quantum efficiency (QE), and G_i is the ith PMT gain. Then, each relative PMT gain was extracted by taking the ratio of them. Figure 3.23 shows the distribution of the relative gain of the ID PMTs after being normalized by the overall average gain. The RMS of the distribution is estimated to be 5.9%, and this variation is caused by differences in QE among the ID PMTs since each HV was determined so that all PMTs give the same output charge ("gain" times "QE") for the same incident light intensity. These relative gain values are tabulated and used to correct each PMT's observed charge to the number of photoelectrons in data.

3.3.3 Absolute Gain Calibration

In this calibration, a NiCf source was used (Fig. 3.24) and deployed at the center of the detector. A gamma ray with an energy of about 9 MeV from thermal neutron capture on nickel emits Cherenkov photons, and the photon yield is about 0.004 p.e.'s/PMT/event, and thus more than 99% signals are considered to be single photoelectron contributions. Neutrons are provided by the ^{252}Cf source inside the "Nickel ball". The observed charge distribution is shown in Fig. 3.25. The mean value of the distribution corresponds to the absolute gain value

Figure 3.24: Picture of the NiCf source, which is made of 6.5 kg of NiO and 3.5 kg of polyethylene. The Cf source is located inside the ball and provides neutrons. Taken from [42].

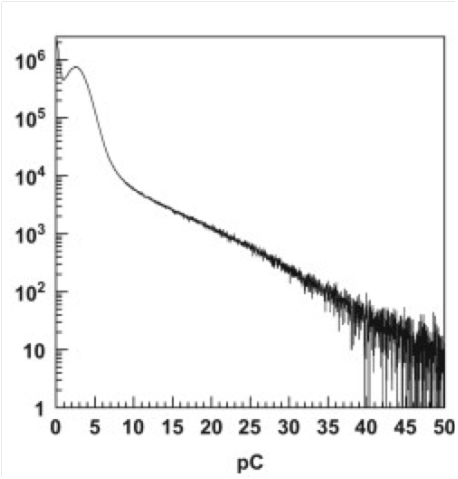

Figure 3.25: Charge distribution in units of pC obtained in the absolute gain calibration in SK-III. Taken from [42].

for the ID PMTs, and it is 2.055 in SK-I, 2.297 in SK-II, 2.243 in SK-III, and 2.645 in SK-IV. The obtained absolute gain factor is also used to convert the observed charge to the number of photoelectrons. The observed charge distribution in this calibration is considered as a single photoelectron distribution and implemented in our detector simulation (MC).

The evolution of the PMT absolute gain over time is monitored using off-timing (dark noise) data. The time variation of the PMT gain is plotted in Fig. 3.26. Since SK-IV, PMTs are divided into five groups depending on their production year. Although its mechanism is unknown, the PMT gain keeps increasing over time, and it is corrected in the present analysis.

3.3.4 Relative Quantum Efficiency Calibration

As pointed out in the previous section, quantum efficiency (QE) differs from one PMT to another. The same NiCf source used in the absolute gain calibration was used for the relative QE calibration because with this low-intensity light source, the observed hit probability for each PMT should be proportional to its QE. When this calibration was conducted, the water was convected in the entire detector to make its quality uniform and to mitigate the geometrical effects. Since it is difficult to estimate the number of photons arriving at each PMT, MC was used for predicting it. The position dependence of the photon detection probability in the detector is shown in Fig. 3.27. In this plot, the number of observed hits is corrected with the distance between the NiCf source and each PMT position, r_i, as well as the PMT effective area,

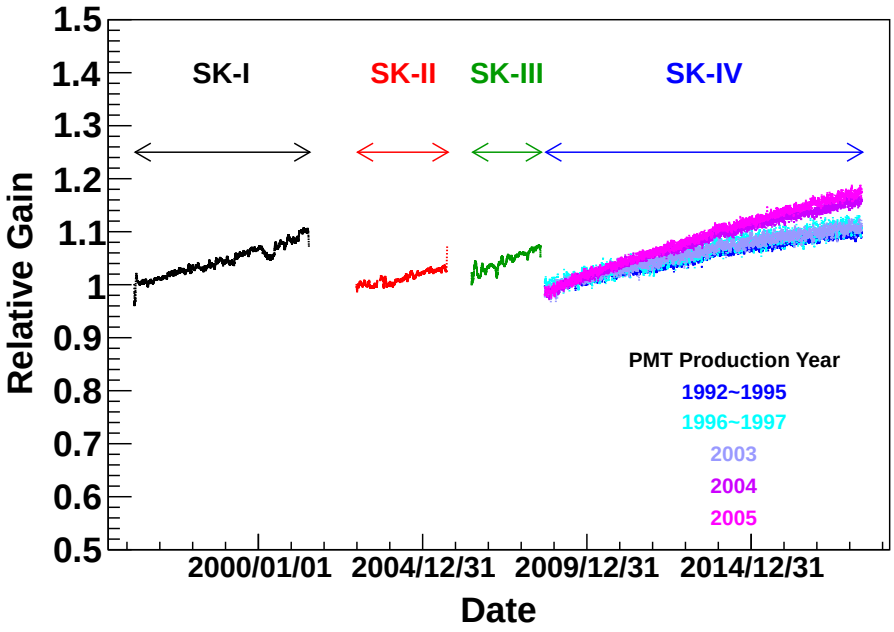

Figure 3.26: Time variation of the PMT gain. Data points for SK-I to -III are normalized by the first data point value in each period, and for SK-IV, they are normalzied by the average value in Apr./2009. In SK-IV, PMTs are divided into five groups depending on their production year.

$f(\Theta_i)$:

$$N_i^{\rm obs} \times r_i^2 / f(\Theta_i), \tag{3.7}$$

where $f(\Theta_i)$ is the PMT acceptance correction factor as a function of photon incident angle, Θ_i. When MC models the water quality (photon absorption, scattering) in the detector, as well as photon reflection on the surfaces of the PMTs and the black sheet, the remaining difference between data and MC should correspond to the QE of individual PMTs. By taking the ratio of the number of observed hits in data to MC, the QE of individual PMTs was obtained. After being tabulated, they are used in MC.

3.3.5 Timing Calibration

The time response of each readout channel is calibrated by taking into account differences in the transit time of the PMT, length of the coaxial cable, and the "time-walk" effect. This was calibrated by injecting various intensities of light into PMTs. A schematic diagram of the timing calibration system is shown in Fig. 3.28. A nitrogen laser light source whose wavelength is shifted to 398 nm by a dye was used. Considering Cherenkov spectrum, light absorption in water, and wavelength dependence of the PMT QE, 398 nm is an optimal wavelength. The pulse width of the nitrogen laser and dye laser is 0.2 nsec and 0.4 nsec in FWHM, respectively. The laser output was monitored by a fast-response 7.5 cm diameter PMT, and it was used to measure the laser light injection time. The laser light intensity to the SK detector was tuned by a variable optical filter so that the dynamic range of the front-end electronics can be covered. The filtered light was distributed into the whole ID PMTs through a diffuser ball (Fig. 3.29). From this calibration, two-dimensional, timing versus pulse height (charge), correlation distributions called "TQ-distributions" were obtained. A typical TQ distribution for one readout channel is shown in Fig. 3.30. By fitting this TQ distribution with three polynomial functions for each

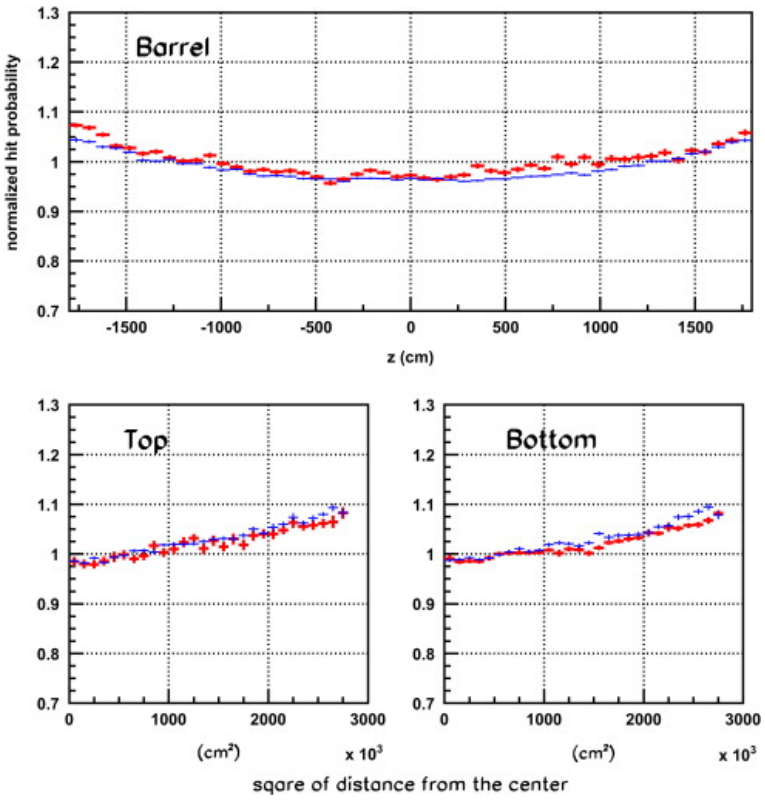

Figure 3.27: Position dependence of the photon detection probability in the detector in the relative QE calibration. The vertical axis values are normalized by the average value of all PMTs. The top plot shows the barrel (side) PMTs, and the horizontal axis is the Z position of PMTs in cm. The bottom left (right) plot shows the top (bottom) PMTs, and the horizontal axis is the square of the distance from the detector center in cm^2. Data points are plotted in red, and MC points are plotted in blue. In MC points, the obtained QE of individual PMTs is not reflected. Taken from [42].

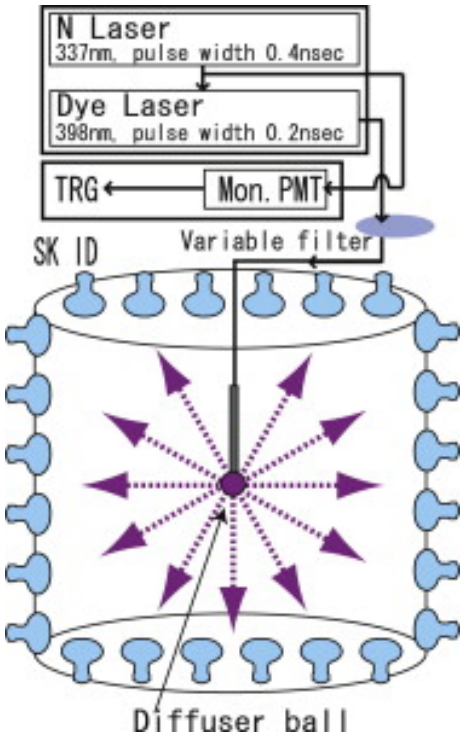

Figure 3.28: Schematic diagram of the timing calibration system. Taken from [42].

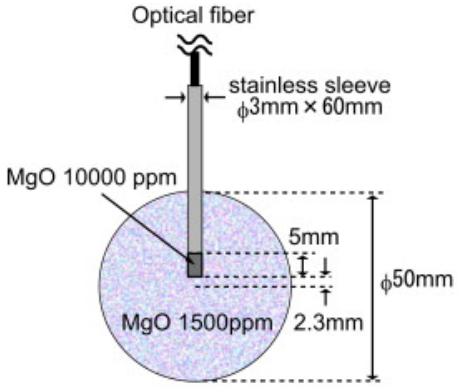

Figure 3.29: Cross-section of the diffuser ball. Taken from [42].

readout channel, correlation tables between charge and timing, called "TQ-map", were obtained for all the ID readout channels and used to correct each readout channel's detection time in data.

The timing resolution of each readout channel was extracted using the same calibration data. This was conducted by fitting the timing distribution for each charge region with an asymmetric Gaussian:

$$f(t) = A_1 \exp\left(-\frac{(t - T_{peak})^2}{\sigma_t^2}\right) + B_1 \quad (t > T_{peak}), \tag{3.8}$$

$$f(t) = A_2 \exp\left(-\frac{(t - T_{peak})^2}{\sigma_t'^2}\right) + B_2 \quad (t < T_{peak}), \tag{3.9}$$

where $A_{1,2}, B_{1,2}$, σ_t, and σ_t' are fit parameters. A typical timing distribution for a certain charge region and fit functions are shown in Fig. 3.31. The obtained timing resolutions (σ_t and σ_t') are plotted as a function of observed charge in Fig. 3.32. They are also tabulated and implemented in MC.

3.3.6 Light Absorption and Scattering in Water

Water absorption and scattering coefficients are also important quantities to be calibrated. A collimated laser beam injector is installed on the top of the ID as shown in Fig. 3.33. The detector side region is divided into five regions, B1 to B5, and photons arriving in the side region are considered as scattered photons. The absorption coefficient was estimated using the number of observed photons in the detector bottom region. Since these coefficients have wavelength dependence, four different laser light sources with a wavelength of 337 nm, 365 nm, 400 nm, and 420 nm are prepared. The wavelength was changed in 2009; from 365 nm to 375 nm, from

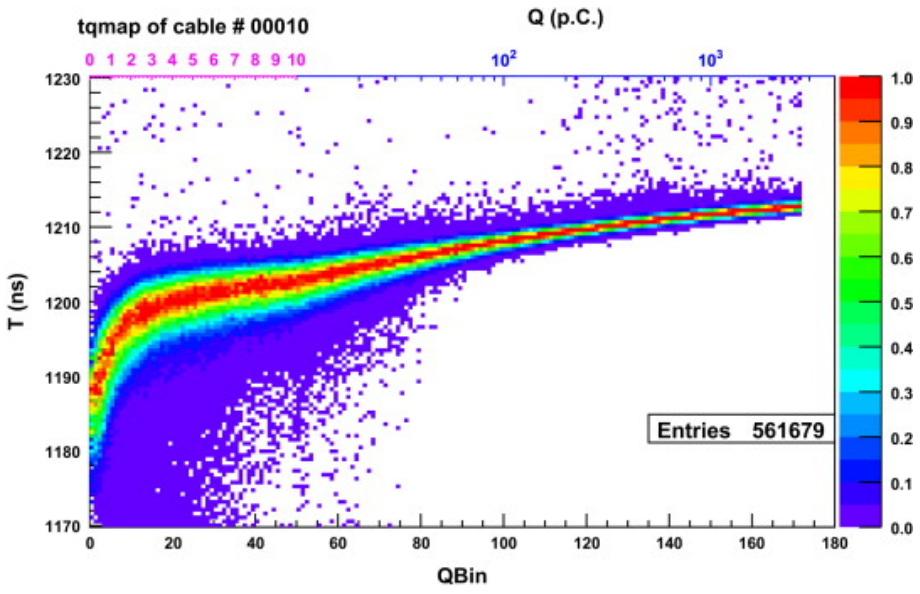

Figure 3.30: Typical TQ distribution for one readout channel (PMT No.10). The horizontal axis corresponds to observed charge and the vertical axis is detection timing. Larger value in the vertical axis corresponds to earlier hits in this plot. Taken from [42].

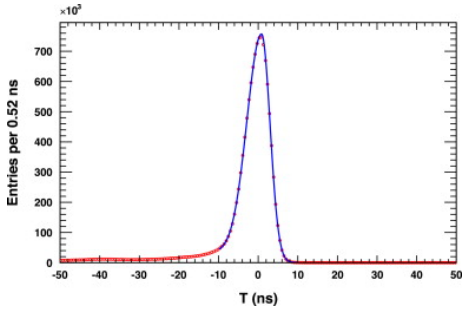

Figure 3.31: Timing distribution added over all the readout channels (red points) and the fitted asymmetric Gaussian function (solid blue curve). The observed charge region used in the distribution is about 3 pC (1 photoelectron level). Here again larger value in the horizontal axis corresponds to earlier hits. Taken from [42].

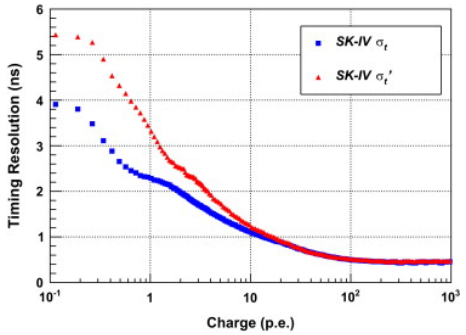

Figure 3.32: Timing resolution as a function of observed charge. Taken from [42].

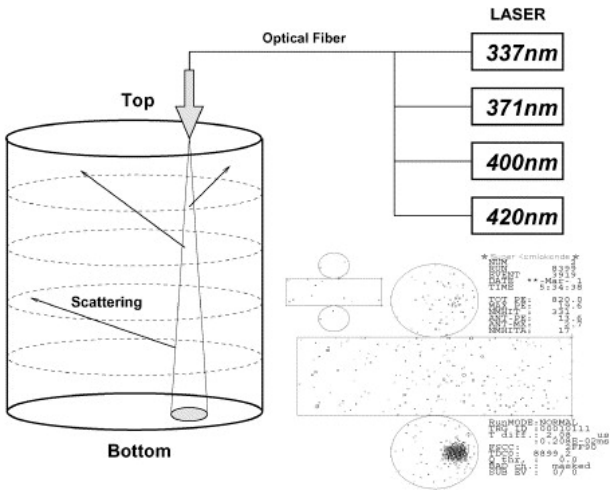

Figure 3.33: Schematic view of the water laser system. A typical event display of the "laser" event is shown in bottom right. The wavelength was changed in 2009; from 365 nm to 375 nm, from 400 nm to 405 nm, and from 420 nm to 445 nm and 473 nm. Taken from [42].

400 nm to 405 nm, and from 420 nm to 445 nm and 473 nm. The number of scattered photons and the shape of the timing distribution were compared between data and MC as shown in Fig. 3.34. Various MC predictions were produced with different coefficients, and the one, which minimizes the χ^2 value for the difference between data and MC, was selected.

Photon scattering and absorption coefficients are parametrized as follows:

$$I(\lambda) = I_0(\lambda) \exp\left(-\frac{l}{L(\lambda)}\right), \tag{3.10}$$

$$L(\lambda) = \frac{1}{a_{\rm abs}(\lambda) + a_{\rm sym}(\lambda) + a_{\rm asy}(\lambda)}, \tag{3.11}$$

$$a_{\rm abs}(\lambda) = P_0 \times \frac{P_1}{\lambda^4} + C, \tag{3.12}$$

$$a_{\rm sys}(\lambda) = \frac{P_4}{\lambda^4} \times \left(1.0 + \frac{P_5}{\lambda^2}\right), \tag{3.13}$$

$$a_{\rm asy}(\lambda) = P_6 \times \left(1.0 + \frac{P_7}{\lambda^4} \times (\lambda - P_8)^2\right), \tag{3.14}$$

where l is the travel length of the light, $I_0(\lambda)$ is the initial light intensity, $I(\lambda)$ is the light intensity at l, $a_{\rm abs}$ is the absorption coefficient, $a_{\rm sym}$ is the symmetric scattering coefficient, $a_{\rm asy}$ is the asymmetric scattering coefficient, and $P_{0\sim8}$ is the constant coefficient. Rayleigh scattering and the symmetric component of Mie scattering contribute to the "symmetric scattering", and the asymmetric component of Mie scattering (forward component) corresponds to "asymmetric scattering". Their wavelength dependence was empirically determined. The obtained coefficient values at each wavelength are shown in Fig. 3.35. They are fitted by polynomial functions written above, and their wavelength dependence is implemented in our MC.

The evolution of the water transparency ("water attenuation length") over time is monitored using cosmic-ray muons entering from the top of the detector and going through the detector bottom. The time variation of water transparency is plotted in Fig. 3.36.

3.3.7 Light Reflection at PMT and Black Sheet

Light reflectivity of the PMT surface was measured using the same laser data as used for the water parameter calibration. There are four layers (refractive indices) from the surface to the

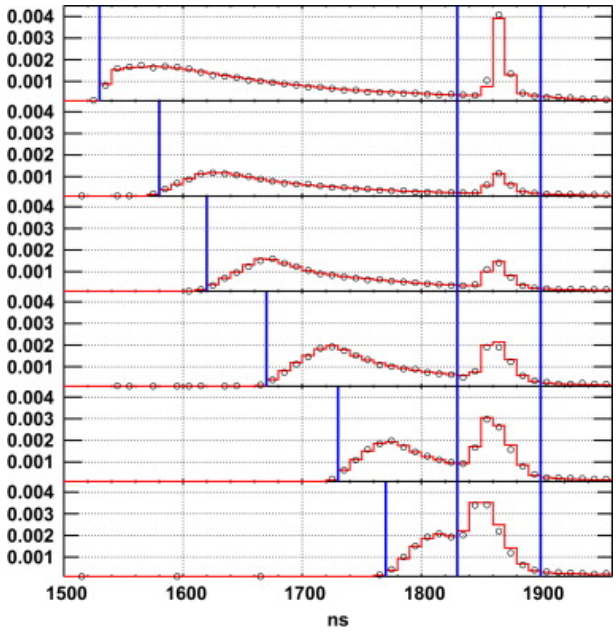

Figure 3.34: Timing distributions after photon time-of-flight (T.O.F.) subtraction (wavelength at 405 nm). The wavelength was changed in the middle of SK-IV from 400 nm to 405 nm. Time-of-flight is calculated based on the distance between the target position of the laser at the detector bottom region and the PMT position. From top to bottom, the detector top region, and B1 to B5 timing distributions are aligned. Entries in left part in each plot indicate scattered photons, and right peaks indicate reflected photons at the detector bottom. Data points are plotted in black dots and MC predictions are plotted in red. Taken from [42].

inside of the PMT: water (1.34), glass ($1.472+\frac{3670}{\lambda^2}$, where λ is the wavelength in units of nm), Bialkali ($n_{\rm real} + in_{\rm img}$, where $n_{\rm real}$ and $n_{\rm img}$ are the real and imaginary parts of the complex refractive index, respectively [43]), and vacuum (1.00). Both two parameters, $n_{\rm real}$ and $n_{\rm img}$, were tuned in the same method as the water parameters, comparison between data and various MC setups as shown in Fig. 3.34. The best fit values are $n_{\rm img} = 1.667$ and $n_{\rm real} = 2.31, 2.69, 3.06$, and 3.24 at λ =337, 365, 400 and 420 nm, respectively. They are also implemented in our MC.

The reflectivity of the black sheet, which covers the gaps between the ID PMTs, was measured using a laser light injector which is set inside the detector as shown in Fig. 3.37. Both the observed charge from reflected light at three incident angles, 35, 45, and 60 degrees, with three wavelengths, 337, 400, 420 nm and the observed charge from direct light without the black sheet were measured. The results of this measurement are shown in Fig. 3.38 and confirm that the reflection component is less than 5% compared to the direct photons as well as good data and MC agreement (about 1% level).

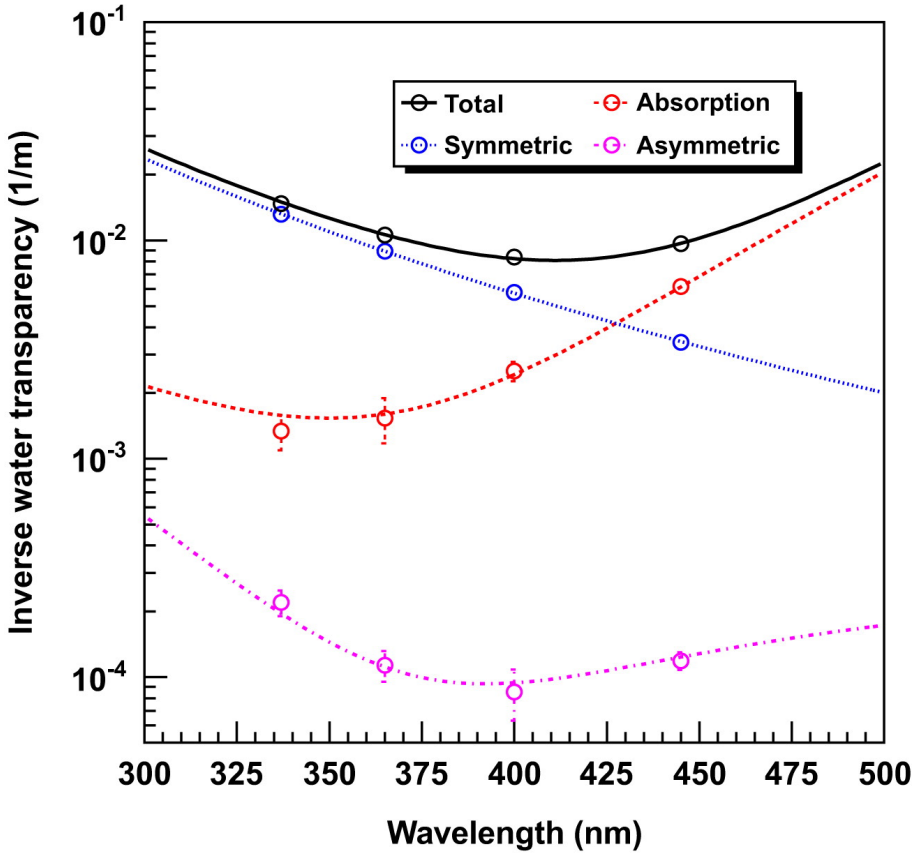

Figure 3.35: Water absorption and scattering coefficients obtained from the water laser data in 2009 are plotted in dots. Curves are the fitted polynomial functions. Taken from [42].

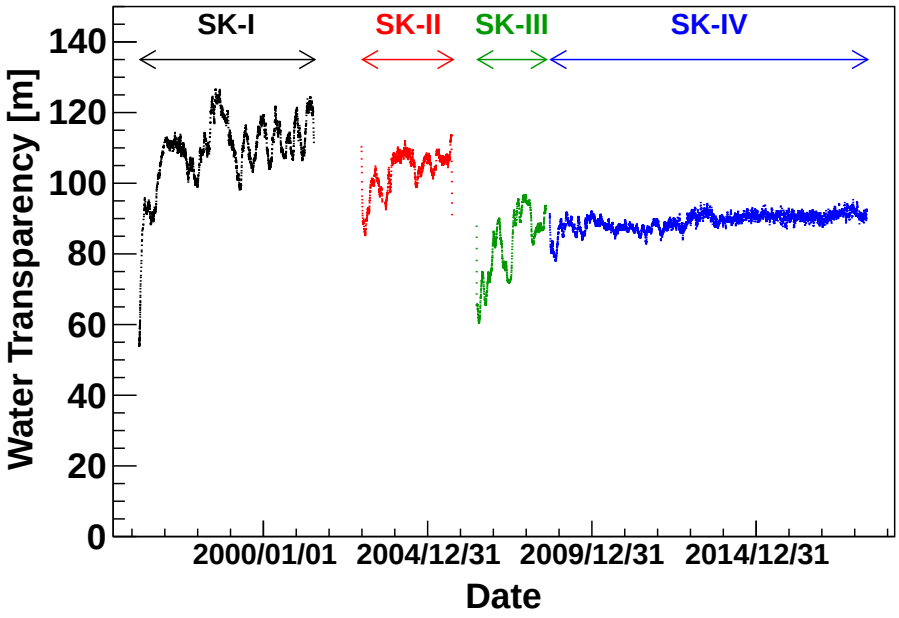

Figure 3.36: Time variation of water transparency (water attenuation length). Absolute values are sensitive to the detector configurations and can not be compared among different detector phases.

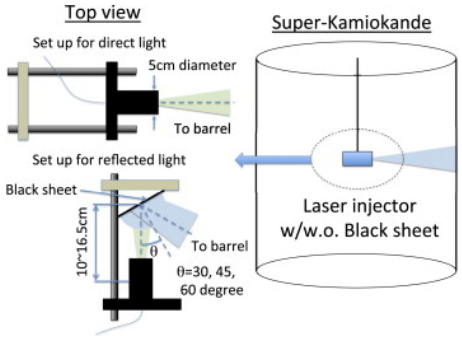

Figure 3.37: Schematic view of the laser light injector system for the reflectivity measurement of the black sheet. Both the reflected and direct light was measured by ID PMTs. Taken from [42].

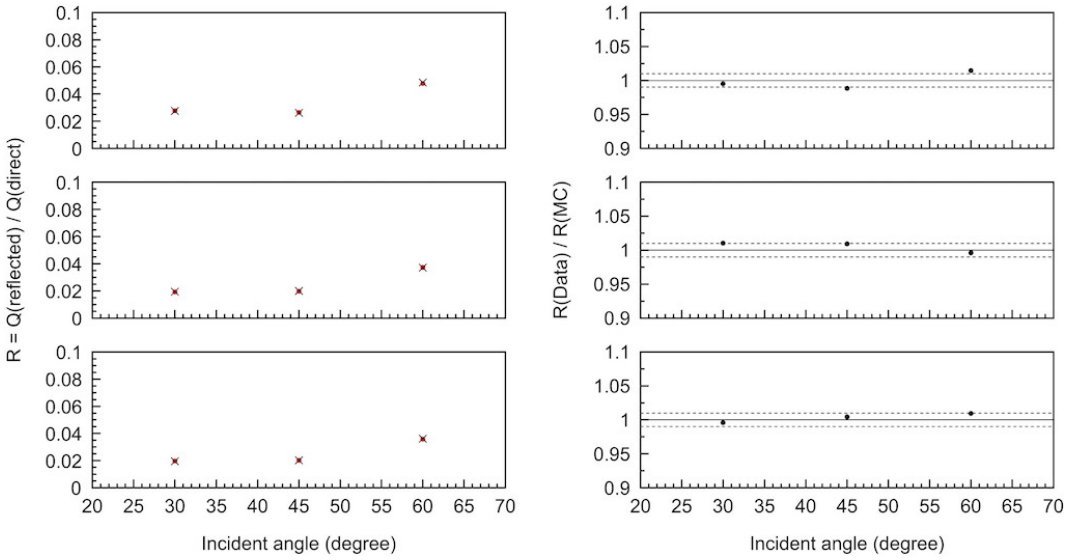

Figure 3.38: The left plot shows the ratio of the observed charge from reflected light to the observed charge from direct light without the black sheet as a function of light incident angle at the black sheet. Data points are plotted in black cross and MC points are in red circle. The right plot shows the ratio between data and MC. The top, middle and bottom plots correspond to the wavelength of 337, 400 and 420 nm, respectively. Taken from [42].

Chapter 4

Simulation

In the present work, proton decay simulation (MC) and atmospheric neutrino simulation are used to estimate the signal selection efficiency and the expected number of atmospheric neutrino background events, respectively. In this chapter, the physics models used in the simulation are described.

4.1 Proton Decay Simulation

In the proton decay MC, the decay is assumed to occur with an equal probability for each proton in the water molecule (H_2O) when producing proton decay events. Hydrogen nuclei (free protons) are stationary and do not interfere with other nucleons, and a positron (anti-muon) and a neutral pion with a momentum of 459 MeV/c (453 MeV/c) are left after free proton $p \to e^+\pi^0$ ($p \to \mu^+\pi^0$) decay. On the other hand, the effects of the Fermi momentum, nuclear binding energy, and correlation with other surrounding nucleons influence protons in oxygen nuclei (bound protons). Furthermore, π nucleon interactions as well as gamma ray and neutron emissions from the remaining ^{15}N nuclei are considered in bound proton decays.

Based on the electron-^{12}C scattering experiment data [44], the Fermi momentum of the nucleon within ^{16}O is simulated, and its distribution is shown in Fig. 4.1 for both the S state and P state. By changing the effective proton mass, $M'_P = M_P - E_b$, where M'_P is the changed proton mass, M_P is the proton rest mass, and E_b is the nuclear binding energy, the effect of the nuclear binding energy is introduced. The nuclear binding energy, E_b, follows a Gaussian distribution with a mean of 39.0 MeV (10.2 MeV) and a standard deviation of 10.2 MeV (3.8 MeV) for the S (P) state. Based on the nuclear shell model [45], the ratio of protons in the S state to those in the P state is set to be 1:3. Proton decay kinematics can be distorted by continuously occurring collisions with a surrounding nucleon during the decay, named "correlated decay", producing broad invariant mass and total momentum spectra. This mechanism is discussed in [46], and the correlated decay probability in bound proton decays is predicted to be about 10%. The proton state, invariant mass, and proton initial momentum distributions are shown in Figures 4.2, 4.3, and 4.4, respectively. In the proton kinetic distributions, the initial proton momentum and mass are calculated with the outgoing charged lepton and pion kinetic information, and effects from pion scattering inside the ^{16}O nucleus, which are described below, are not included. The location of protons within the ^{16}O nucleus is calculated based on the Woods-Saxon nuclear density model [47],

$$\rho(r) = \frac{\rho(0)}{1 + \exp\left(\frac{r-a}{b}\right)}, \tag{4.1}$$

where r is the distance from the center of the ^{16}O nucleus, $\rho(0) = 0.48 m_\pi^3$, a = 2.69 fm, and b = 0.41 fm.

Pions produced in bound proton decays often interact with nucleons via π absorption, elastic scattering, inelastic scattering, and charge exchange. This is so-called final state interaction

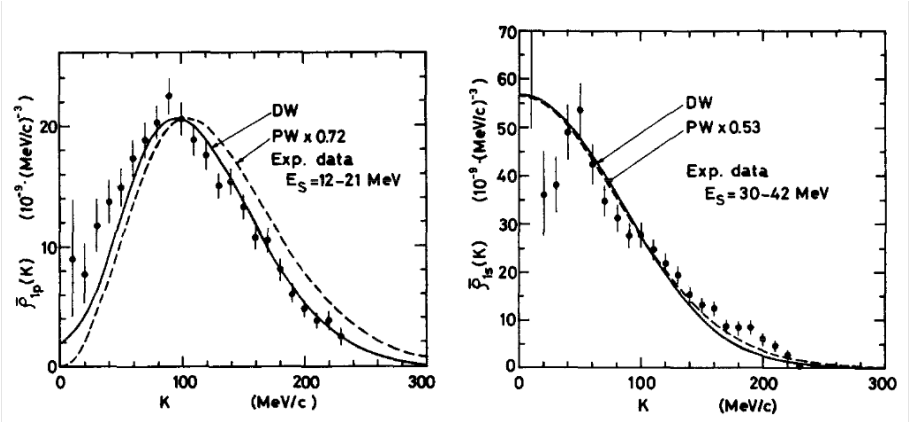

Figure 4.1: Distributions of the Fermi momentum for the P state (left) and S state (right). Data points show electron-^{12}C scattering experiment data and solid lines are theoretical curves. Taken from [44].

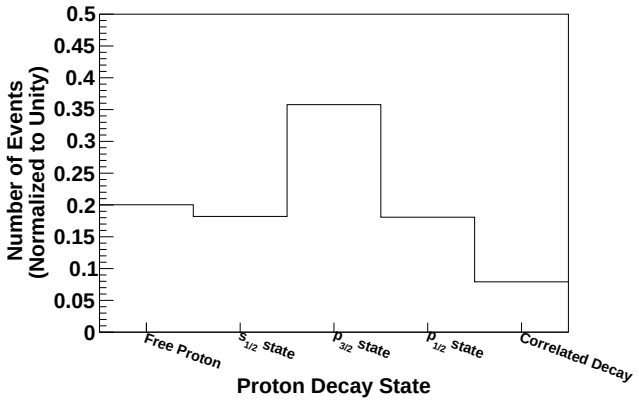

Figure 4.2: Proton state distribution during the decay.

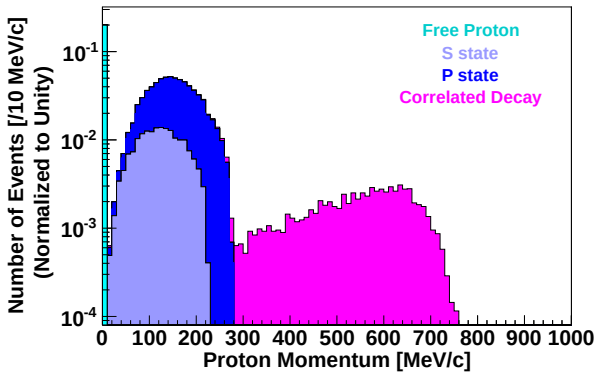

Figure 4.3: Initial proton momentum distribution. Free proton and bound proton decay events are stacked. Pion FSI effects are not included.

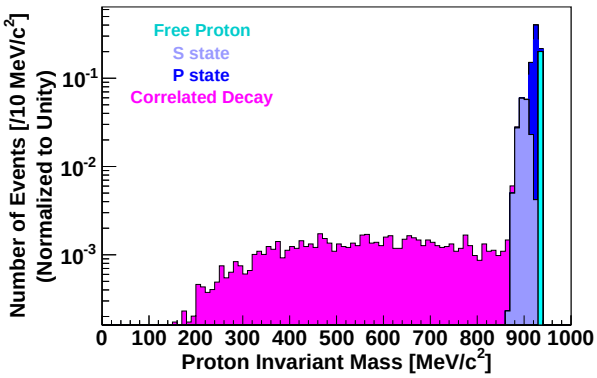

Figure 4.4: Effective proton invariant mass distribution. Free proton and bound proton decay events are stacked. Pion FSI effects are not included.

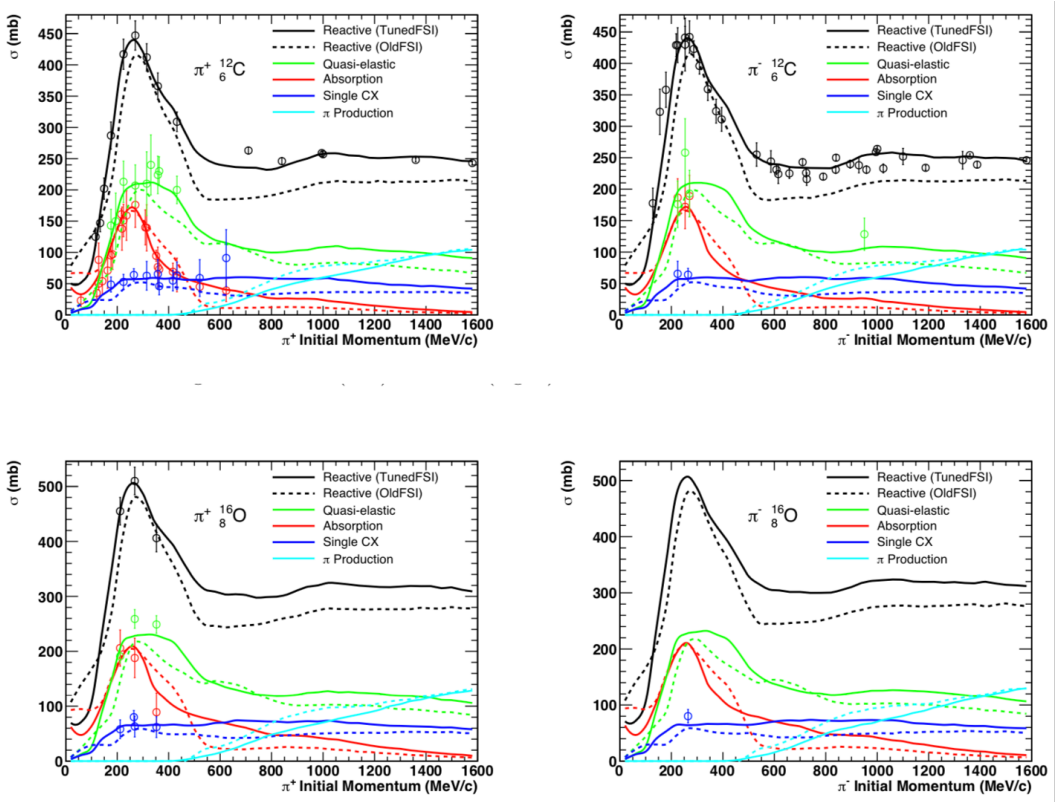

Figure 4.5: Cross-sections of $\pi^{\pm}$-^{12}C scattering (π^+ in top left and π^- in top right) and $\pi^{\pm}$-^{16}O scattering (π^+ in bottom left and π^- in bottom right). Points show experimental data and solid lines are simulation curves. Dashed lines are simulation curves in previous versions. Taken from [49].

(FSI) and is simulated based on the NEUT π FSI cascade model (version 5.3.6) [48, 49]. Pions are propagated classically through a nuclear medium in finite steps in the NEUT π FSI model. This model is tuned by various $\pi^{\pm}$-nucleus experimental data such as $\pi^{\pm}$-C, -O, -Al, and -Fe [50]. The $\pi^{\pm}$-^{12}C and $\pi^{\pm}$-^{16}O cross-sections obtained from different experiments as well as simulated functions are shown in Fig. 4.5. The fraction of π^0 interactions as a function of π^0 momentum is shown in Fig. 4.6. The kinematics of the outgoing pion and nucleon after scattering within the nucleus is simulated based on $\pi^{\pm}$-p scattering data [51] for pions with a momentum less than 500 MeV/c, while it is calculated from the SAID fits [52] for pions with a momentum of larger than 500 MeV/c. The Pauli exclusion principle is taken into account by requiring the momentum of the scattered nucleon is larger than the Fermi surface momentum:

$$p_F(r) = \left(\frac{3}{2}\pi^2\rho(r)\right)^{\frac{1}{3}}, \tag{4.2}$$

where $\rho(r)$ is defined in Eq. (4.1). After escaping the nucleus, the neutral pion immediately decays into two gamma rays.

A gamma ray, neutron, and proton emitted from the remaining ^{15}N nucleus in the excited states after the proton decay are simulated based on [53]. The particle emission probability is summarized in Table 4.1. The probability of neutron emission in proton decay events including free proton decays is predicted to be less than 10%, and no neutrons are produced in hadron secondary interactions in water for the $p \to e^+\pi^0$ and $p \to \mu^+\pi^0$ modes because the remaining particles are gamma rays and position or anti-muon.

At last, a typical event display of the $p \to e^+\pi^0$ event is shown in Fig. 4.7. Since free proton decays are not influenced by any intranuclear effects summarized above, they produce back-to-

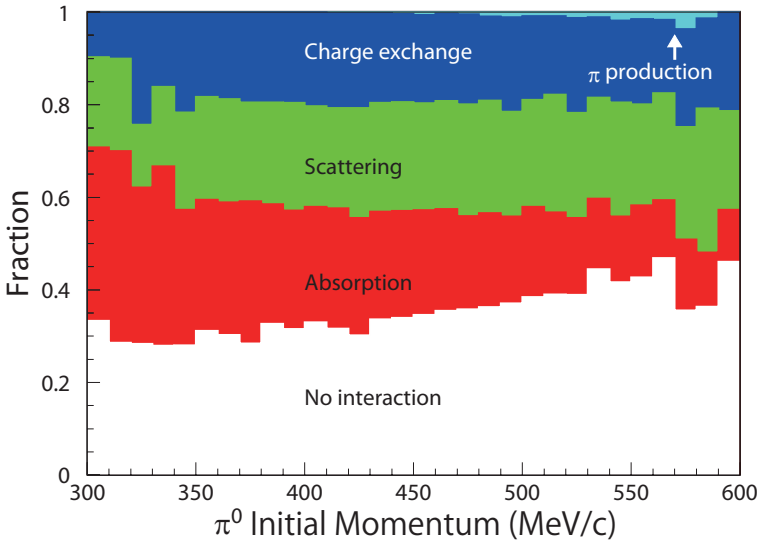

Figure 4.6: Fraction of π^0 interactions as a function of π^0 momentum. Taken from [27].

back event topologies as shown in the figure. Besides, in case the π^0 escapes the remaining nucleus without being affected by π FSI in a bound proton decay, such a event also leaves nearly back-to-back particle tracks and can pass the proton decay signal selection criteria, which are introduced in Section 7.1.1.

Table 4.1: Summary of particle emissions from the remaining ^{15}N nucleus. The residual ^{15}N nucleus is at the ground state after proton decays at the $P_{1/2}$ state, and therefore no particle emission is predicted.

Proton Decay State	Emitted Particle	Probability
$S_{1/2}$	n	1.8%
	γ (7.03 MeV), n	1.8%
	p, n	4.1%
	p	1.8%
	γ (7.01 MeV), p	1.8%
	γ (3.50 MeV), n	4.9%
	γ (3.50 MeV)	9.4%
$P_{3/2}$	γ (6.32 MeV)	43.6%
	γ (9.93 MeV)	3.2%
	p	3.2%
$P_{1/2}$	nothing	25.0%

4.2 Atmospheric Neutrino Flux

In this analysis, atmospheric neutrino events mimic proton decay signal events, and therefore they are considered as background. The atmospheric neutrino flux is simulated based on the calculation by M. Honda *et al.*, the Honda flux model [54], while other models, the Fluka flux model [55] and Bartol flux model [56], are used for the systematic uncertainty estimation.

The Honda model is on the basis of AMS [57] and BESS [58] measurements, and the US-standard atmosphere '76 [59] is used as the model for the atmospheric density structure. DPMJET-III [60] is adopted for simulating the generation of secondary cosmic-ray particles, such as π, μ, in the atmosphere for hadronic interactions above 32 GeV, whereas JAM [61]

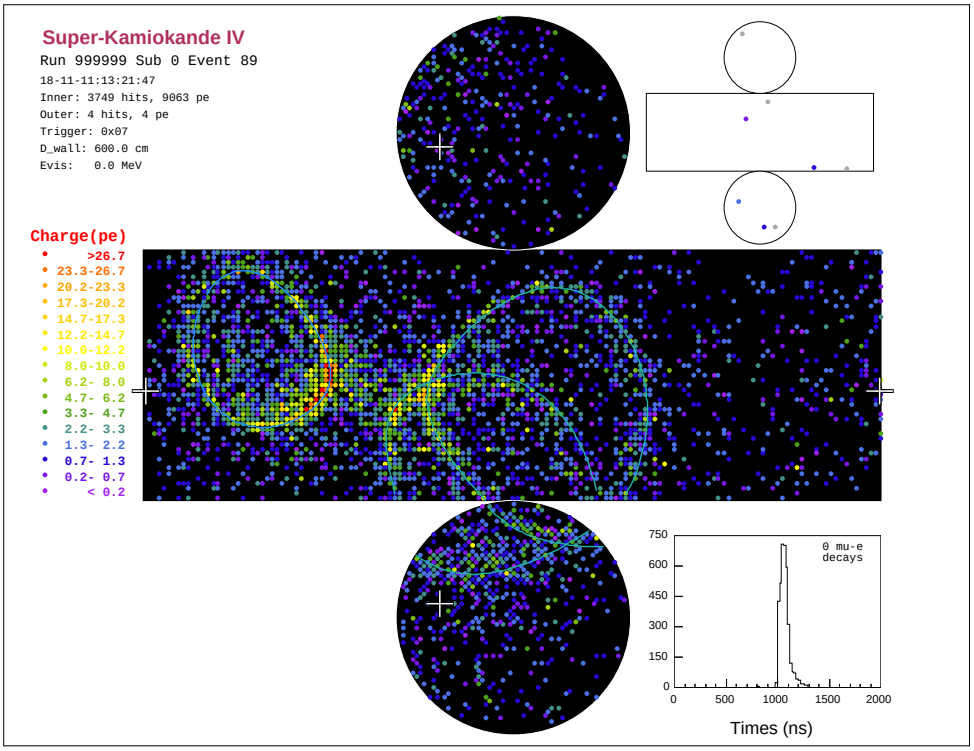

Figure 4.7: Typical event display of a $p \to e^+\pi^0$ event. The ring in the left side is produced by the positron, while the two rings shown in the right side are produced by the gamma rays from the π^0 decay.

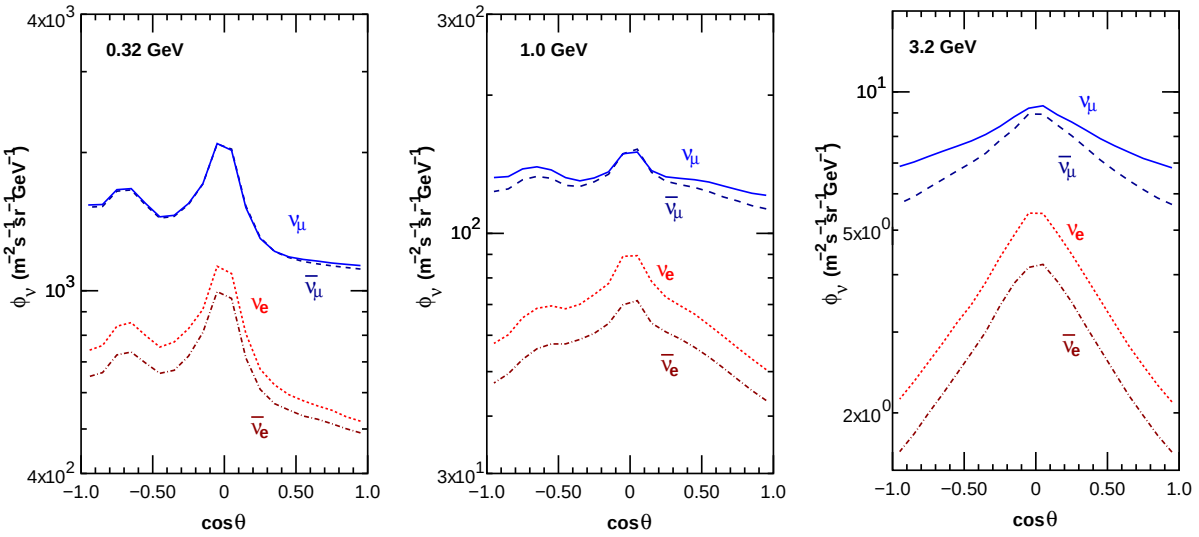

Figure 4.8: Atmospheric neutrino flux distributions at Kamioka as a function of zenith angle, $\cos\theta$. Here θ is the arrival direction of the neutrino, where $\cos\theta = 1$ stands for vertically downward going neutrinos. In these distributions, the azimuth component is averaged out. From left to right, neutrino of 0.32 GeV, 1.0 GeV, and 3.2 GeV cases are shown. Taken from [54].

is adopted for energy below 32 GeV. These hadronic interactions are fine-tuned using various experimental data [58, 62, 63]. The curvatures of charged particles in the geomagnetic field are taken into account when calculating the interaction and propagation of the cosmic-ray particles.

The zenith angle dependence of the atmospheric neutrino flux at Kamioka calculated by the Honda model is shown in Fig. 4.8. The flux is peaked around the horizon because pions and muons travel longer in the atmosphere horizontally than those traveling vertically, allowing more time for the decays. The up-down asymmetry in the lowest energy region in Fig. 4.8 is caused by the geomagnetic field, which affects the track of the cosmic-ray particles. The neutrino flux and flux ratio distributions at Kamioka as a function of neutrino energy are shown in Fig. 4.9. In these distributions, all neutrino directional components are averaged out, and the Honda model and other models are compared.

The atmospheric neutrino MC events have been produced based on the predicted flux at Kamioka, and the neutrino oscillation effect is not considered in this step. It is assumed that all neutrinos produced in the atmosphere reach the SK detector in their original flavor. Then, the neutrino oscillation effect is taken into account by varying the MC event weight at the analysis stage based on the latest oscillation analysis result [64].

The oscillation parameters, which are obtained from [64] and used in this analysis, are as follows:

$$\Delta m^2_{21} = 7.53 \times 10^{-5}\text{eV}^2, \text{ (fixed in fit)} \tag{4.3}$$
$$\Delta m^2_{32} = 2.50 \times 10^{-3}\text{eV}^2, \text{ (fitted)} \tag{4.4}$$
$$\sin^2\theta_{12} = 0.304, \text{ (fixed in fit)} \tag{4.5}$$
$$\sin^2\theta_{13} = 0.0219, \text{ (fixed in fit)} \tag{4.6}$$
$$\sin^2\theta_{23} = 0.588, \text{ (fitted)} \tag{4.7}$$
$$\delta_{CP} = 4.18. \text{ (fitted)} \tag{4.8}$$

Because of the oscillation effects, at most half of the muon neutrinos of O(1) GeV from the $\cos\theta = -1$ direction oscillate into tau neutrinos. In the oscillation fit, flux times cross-sections of the atmospheric neutrinos are also fitted using the total number of observed events used in the oscillation analysis.

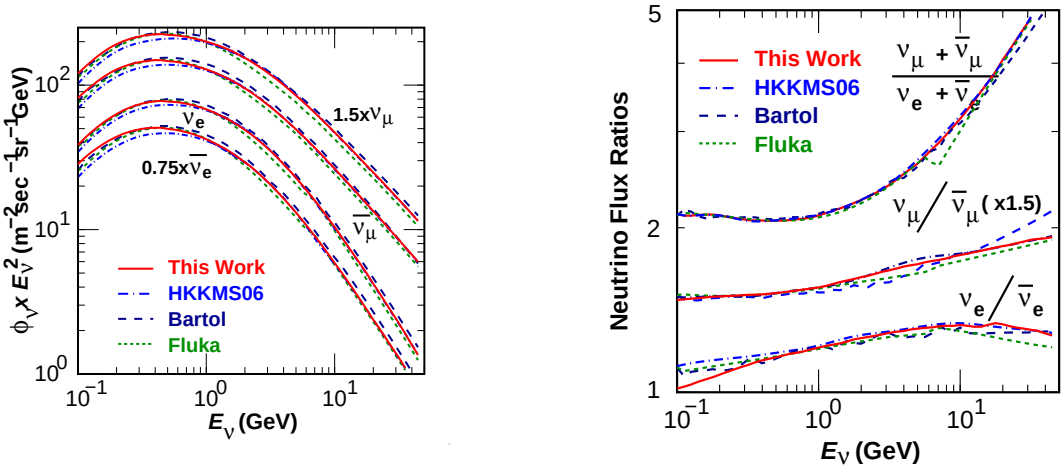

Figure 4.9: Neutrino flux distributions at Kamioka as a function of neutrino energy. The Honda model prediction is shown in red. The previous Honda model prediction is shown in blue. Taken from [54].

4.3 Neutrino Interaction

Atmospheric neutrino interactions inside the detector are simulated based on NEUT [48]. They are classified into two categories, Charged Current (CC) and Neutral Current (NC) interactions. A neutrino exchanges a $W^{\pm}$ boson with the target in the CC interaction. After the interaction, a charged lepton, whose flavor is the same as that of the incoming neutrino, is left in the final state. By distinguishing the flavor of the charged lepton inside the detector, the incoming neutrino flavor can be identified in this interaction. An event reconstruction algorithm to identify the flavor of the charged lepton in SK, whether electron or muon, is described in Section 6.1. In contrast, in the NC interaction, a neutrino interacts with the target mediated by a Z^0 boson. After this NC interaction, no signs of the neutrino flavor are left within the detector because the outgoing lepton is also neutrino.

In the NEUT simulation, the following interactions are considered:

1. CC and NC (quasi-)elastic scattering, CCQE (NCQE): $\nu + N \rightarrow l(\nu) + N'$,
2. CC meson exchange current, CCMEC: $\nu + NN' \rightarrow l + N''N'''$,
3. CC and NC single meson production: $\nu + N \rightarrow l(\nu) + N' + \text{meson}$,
4. CC and NC coherent pion production, CCCOH (NCCOH): $\nu + {}^{16}\text{O} \rightarrow l(\nu) + {}^{16}\text{O} + \pi$,
5. CC and NC deep inelastic scattering, CCDIS (NCDIS): $\nu + N \rightarrow l(\nu) + N' + \text{hadrons}$,

where N, N', N'', and N''' stand for nucleons, l stands for a charged lepton, and ν stands for a neutrino.

4.3.1 (Quasi-)Elastic Scattering

In the neutral current, NC, elastic scattering process, an incoming neutrino scatters off a nucleon target. In this process, no new particles are produced while some momentum transfer occurs. On the other hand, in the charged current, CC, quasi-elastic scattering process, an incoming neutrino is converted into a charged lepton, whose flavor is the same as the neutrino, in the final state. The target nucleon is also converted in this interaction, and thus the total electric charge in the system is conserved.

The Llewellyn-Smith model [65] is adopted in the above two interactions for a hydrogen nucleus target. For a nucleon target in an oxygen nucleus, effects of the Fermi momentum and

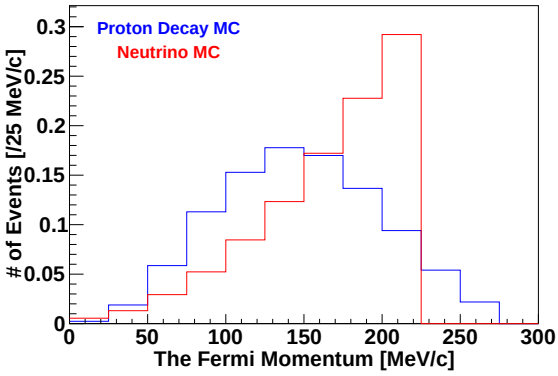

Figure 4.10: The Fermi momentum distributions. The blue histogram shows the Fermi momentum distribution used in the proton decay MC which is based on the shell model [45]. The red histogram shows the one used in the neutrino MC which is based on the relativistic Fermi gas model [66]. In the neutrino MC (NEUT), the Fermi surface momentum is set to 225 MeV/c.

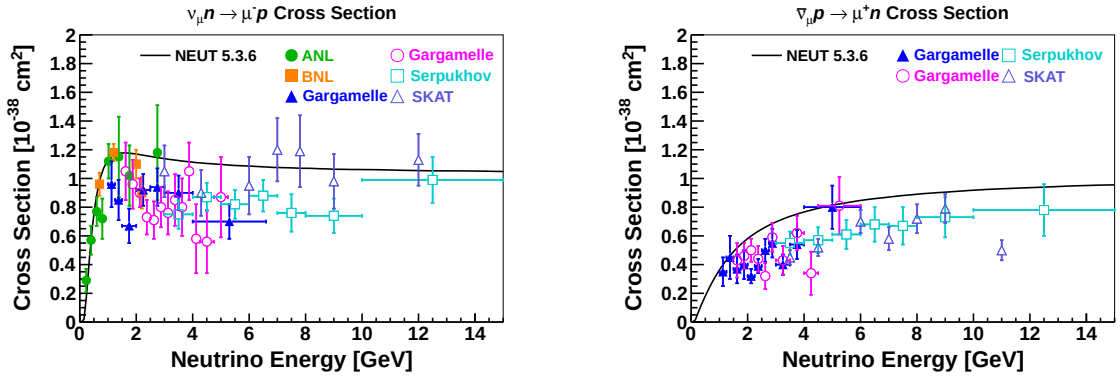

Figure 4.11: Charged current quasi-elastic scattering cross-sections as a function of incoming neutrino energy. The left plot shows the neutrino case and the right shows the anti-neutrino case. The black line is the model prediction used in this analysis (NEUT version 5.3.6). Experimental data points are from: ANL [69], BNL [70], Gargamelle [71], Serpukhov [72], and SKAT [73].

the Pauli exclusion principle are considered based on the relativistic Fermi gas model by Smith and Moniz [66]. The Fermi momentum distribution in the relativistic Fermi gas model is different from the one used in the proton decay simulation described in Section 4.1 and shown in Fig. 4.10. The difference between them is taken into account as a systematic uncertainty on the proton decay signal selection efficiency. The Fermi surface momentum in the atmospheric neutrino MC is set to 225 MeV/c. The differential cross-section for this interaction is formulated as a function of four-momentum transfer, vector and axial-vector form factors [65]. These form factors are parametrized by the vector mass (M_V), which is set to 0.84 GeV, and axial mass (M_A), which is set to 1.21 GeV. They have been determined based on the experimental data from K2K [67] and MiniBooNE [68]. The CCQE cross-sections as a function of incoming neutrino energy in NEUT and various experimental results are shown in Fig. 4.11.

4.3.2 Meson Exchange Current

In the CCQE interaction described above, a neutrino interacts with a single nucleon only, and any correlations between the nucleons in the nucleus are neglected. However, MiniBooNE

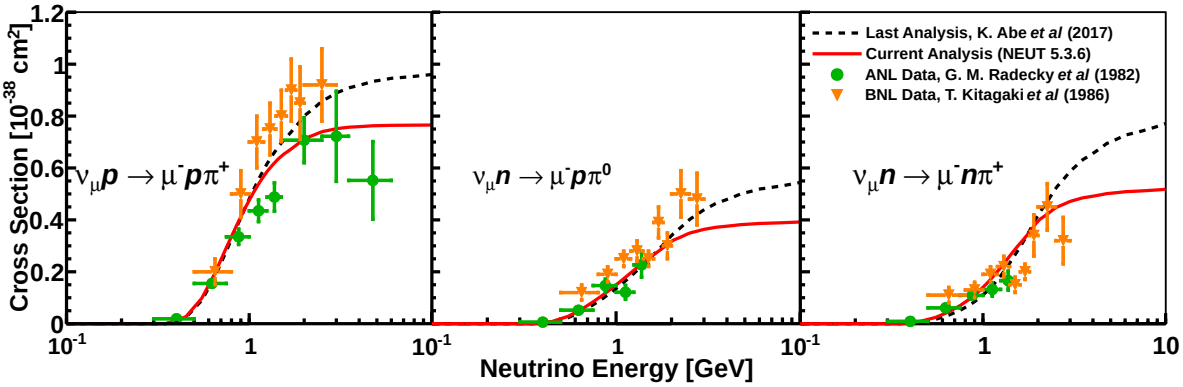

Figure 4.12: Charged current single π production cross-sections as a function of incoming neutrino energy. The dotted black line corresponds to the model used in previous SK proton decay searches [27], NEUT 5.1.4, and the solid red line shows that for the current analysis, NEUT 5.3.6.

data [68] suggests a process in which an incoming neutrino interacts with multiple nucleons in the target nucleus simultaneously. In order to include this interaction, the Meson Exchange Current (MEC) model by Nieves *et al.* [74] has been implemented in NEUT recently.

4.3.3 Single Meson Production

Single meson (such as π, K, and η) production in a neutrino interaction is simulated through a baryon resonance excitation state:

$$\nu + N \rightarrow l(\nu) + N^*, \tag{4.9}$$

$$N^* \rightarrow N' + \text{meson}, \tag{4.10}$$

where N^* is the baryon resonance, and a single meson is produced from N^* in the final state. This interaction is considered for the cases with hadronic invariant mass $W < 2.0$ GeV/c^2, which is the mass of the intermediate resonance (N^*).

The charged current single π production (CC1π) process is the dominant background process for the search for proton decay via $p \rightarrow e^+\pi^0$ and $p \rightarrow \mu^+\pi^0$. In the previous publication about these searches [27], the Rein-Sehgal model [75] has been used. Since then new form factors (Graczyk and Sobczyk) have been obtained from a simultaneous fit [76] to neutrino scattering data from bubble chamber experiments [77], and they are currently used in NEUT. A comparison of the cross-sections as a function of incoming neutrino energy between the previous NEUT version and the current version is shown in Fig. 4.12. Because the dominant neutrino energy range contributing to the proton decay background is about from 1 to 3 GeV, this cross-section change reduces the expected number of atmospheric neutrino backgrounds by about 15%. By this modification, the momentum transfer also becomes smaller as shown in Fig. 4.13, and the outgoing lepton's and total reconstructed momentum becomes higher accordingly. Since the event topology of the proton decay signal event is back-to-back, and only a low total momentum event is allowed as a proton decay signal as described in Section 7.1.1, this momentum transfer change further reduces the expected number of backgrounds by about another 15% compared to the previous version. In total, the reduction of the expected number of backgrounds by the update of NEUT is about 30%.

4.3.4 Coherent Pion Production

Coherent pion production, in which an incoming neutrino coherently interacts with target nucleons in an entire oxygen nucleus and leaves a single pion, is simulated based on the Rein-

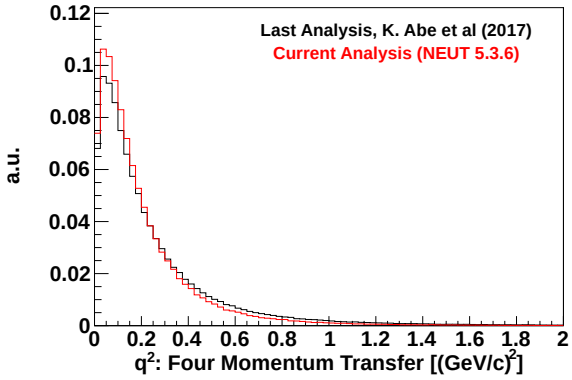

Figure 4.13: Four momentum transfer in the charged current single π production interaction. The black histogram corresponds to the model used in previous SK proton searches [27], NEUT 5.1.4, and the red histogram corresponds that for the current analysis, NEUT 5.3.6.

Sehgal model [75]. Because of the low momentum transfer in this interaction, both the outgoing lepton and pion tend to have forward-going directions. Therefore, events produced in this interaction do not mimic $p \to e^+\pi^0$ and $p \to \mu^+\pi^0$ events.

4.3.5 Deep Inelastic Scattering

In the deep inelastic scattering process, an incoming neutrino interacts with a constituent quark in the target nucleon. In this process, multiple hadrons are produced in the final state. The multiple hadron production is also simulated through a baryon resonance excitation state, but the mass of the intermediate resonance (W) is restricted to be higher than 1.3 GeV/c^2. This interaction becomes dominant in the higher neutrino energy in the NEUT simulation. For interactions with $W < 2.0$ GeV/c^2, only pions are produced as generated hadrons in the final state. The pion multiplicity is modeled based on experimental data in bubble chamber experiments [78]. Since this hadronic invariant mass region ($1.3 < W < 2.0$ GeV/c^2) is overlapped with the region for the single pion production interaction ($W < 2.0$ GeV/c^2), which is described in Section 4.3.3, only the multiple pion production is simulated as the deep inelastic scattering process. Other mesons, such as K and η, can be produced in the final state in interactions with $W > 2.0$ GeV/c^2, and the hadronic final states are modeled based on PYTHIA and JETSET [79]. The nucleon internal structure is modeled based on the GRV98 parton distribution functions [80] with the corrections by Bodek and Yang [81] for the low Q^2 region. The total cross-sections of the charged current interaction including quasi-elastic scattering, single meson production, and deep inelastic scattering are shown in Fig. 4.14. In the region neutrino energy of more than 10 GeV, the deep inelastic scattering interaction becomes increasingly dominant.

4.4 Hadronic Interaction

Neutrons play an important role to separate between a proton decay signal and atmospheric neutrino backgrounds because there are several neutron production processes in atmospheric neutrino events:

1. Primary neutrino interaction, $\bar{\nu} + p \to l^+ + n$,
2. Hadron and meson interactions in a nucleus, FSI, $p + p \to p + n + \pi^+$,
3. Hadron secondary interactions in water, SI, $n + {}^{16}\mathrm{O} \to n + n + {}^{15}\mathrm{O}^*$.

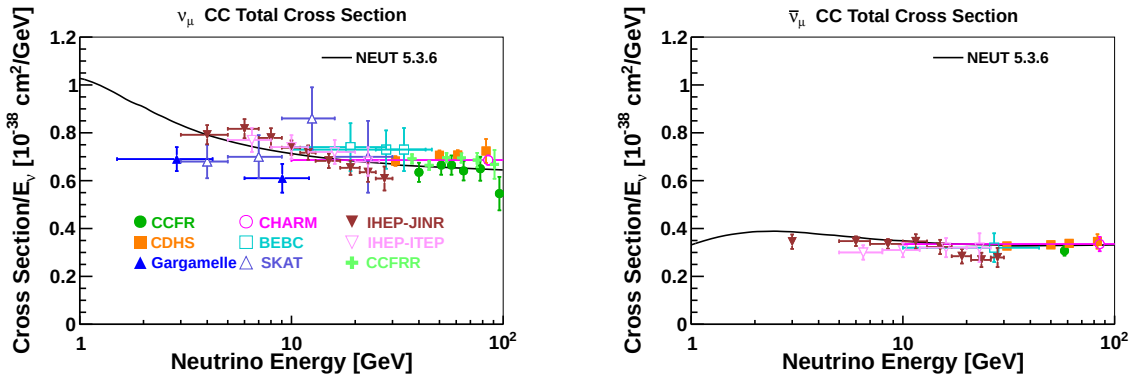

Figure 4.14: Charged current total cross-sections divided by incoming neutrino energy. The left plot shows the neutrino case and the right shows the anti-neutrino case. The black line is the model prediction used in this analysis (NEUT version 5.3.6). Experimental data points are from: CCFR [82], CDHS [83], Gargamelle [84], CHARM [85], BEBC [86], SKAT [87], IHEP-JINR [88], IHEP-ITEP [89], and CCFRR [90].

The dominant neutron production process in atmospheric neutrino events in SK is the hadron secondary interaction in water and its fraction is about 70% [27].

Hadronic interaction processes are simulated by CALOR package [91], which uses HETC [92] for hadrons below 10 GeV, FLUKA [93] for hadrons above 10 GeV, and MICAP [94] for neutrons below 20 MeV.

4.5 Detector Simulation

Produced particles from the above physics processes are fed into a GEANT3-based [95] detector simulation called SKDETSIM [96]. Interactions of the particles in water, particle decays, and production of Cherenkov photons are simulated in SKDETSIM. Detector responses including the water property, optical modeling as well as PMT and electronics responses to the produced photons are simulated based on the detector calibration results described in Chapter 3.

4.5.1 Treatment for Neutron Tagging Process

Neutrons emitted from a primary event thermalize in water and are eventually captured by hydrogen nuclei. After a neutron is captured by a hydrogen nucleus with a capture time constant of about 200 μsec, a 2.2 MeV gamma ray is emitted. Low energy background sources, such as a few MeV gamma rays from radioactive decay products, are not simulated in our detector simulation but they have non-negligible impacts on the 2.2 MeV gamma ray search to count the number of neutrons. Therefore, in the timing region used for this 2.2 MeV gamma ray search, which begins 18 μsec after the primary trigger, the simulated PMT dark noise hits are replaced by the real PMT hit information taken from the random trigger event data (illustration in Fig. 4.15), which include the low energy background activities. This timing region used for the 2.2 MeV gamma ray search is defined to avoid effects from PMT after-pulsing which occurs between 12 and 18 μsec after the primary PMT hit timing as shown in Fig. 4.16. Although the 2.2 MeV gamma ray tagging algorithm is described in Section 6.3 and in [97], the average neutron multiplicity (the number of tagged neutrons per primary neutrino event) distribution is shown in Fig. 4.17 and confirms that the simulated neutron production processes well reproduce the neutron multiplicity in the atmospheric neutrino data in SK.

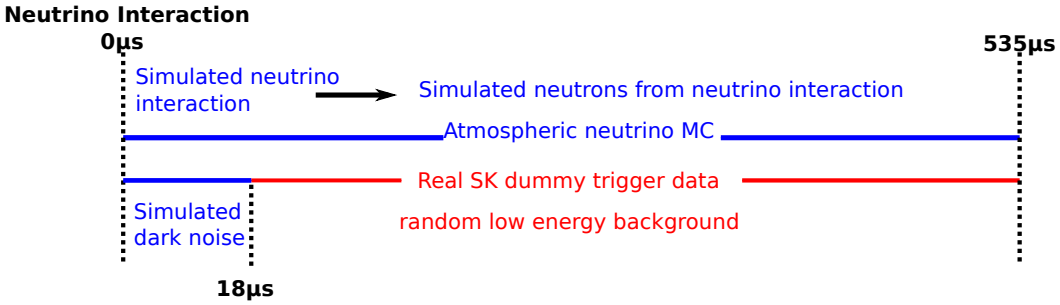

Figure 4.15: Treatment of the PMT simulation. The simulated PMT dark noise hits are replaced by the real PMT hits taken from the random trigger event data for the time region used for neutron tagging, which begins 18 μsec after the primary trigger. Taken from [97].

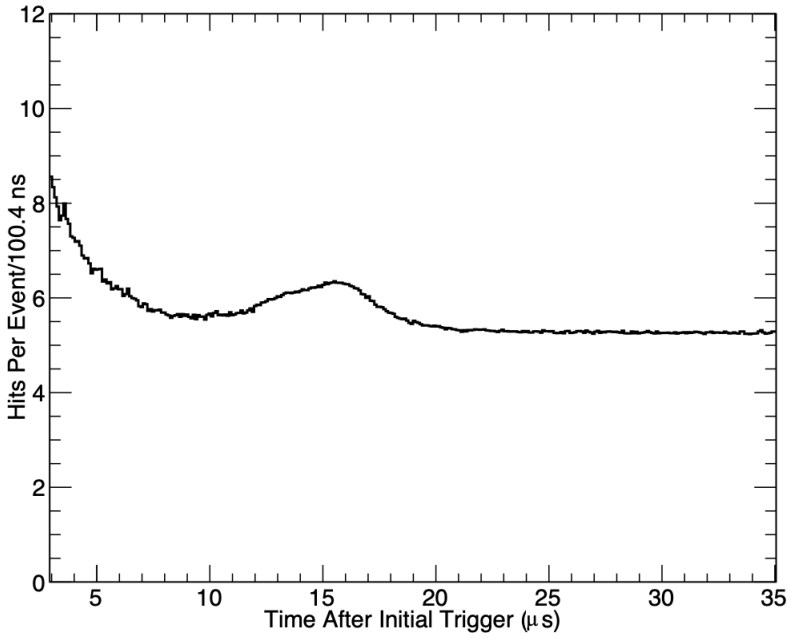

Figure 4.16: PMT hit rate as a function of time after the primary event trigger. The exponential decay within 10 μsec corresponds to hits produced by Michel electrons from muon decays. The bump between 12 and 18 μsec corresponds to hits produced by PMT after-pulsing. Taken from [97].

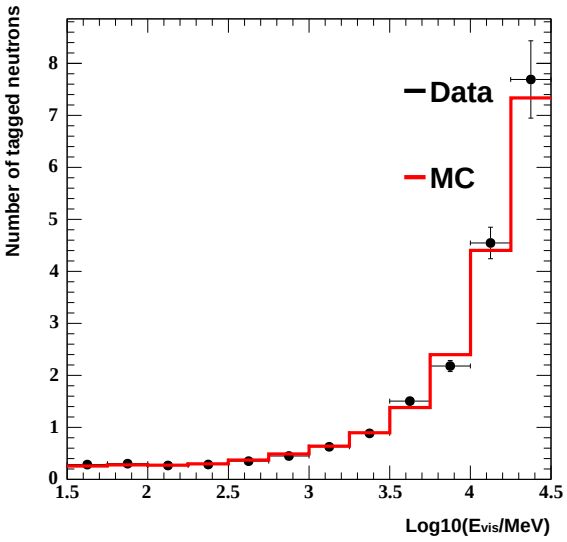

Figure 4.17: Average neutron multiplicity (the number of tagged neutrons per primary neutrino event) as a function of detector deposited energy in SK. The black dots shows the SK-IV data and the red histogram shows the atmospheric neutrino MC events.

Chapter 5

Data Set

The typical SK event rate for this data set is about tens of Hz, 10^6 events per day. Most events are background events such as cosmic-ray muon events, low energy events produced by radioactive products around the detector, and dummy events produced from erroneous discharges in a PMT's dynode, "flasher" events. Event selection criteria to extract proton decay candidates and atmospheric neutrino events are described in this chapter [98].

This analysis uses events termed "fully contained" (FC) whose interaction vertex point is reconstructed within the ID and which have no cluster of hits in the OD. In order to efficiently select FC events from the quite large amount of raw data, the following event selections are applied, and they are composed of five reduction steps:

1, 2. First and second reductions $\cdots$ Loose and simple selection criteria to reject low energy background events and cosmic-ray muons. After the first and second event reduction steps, the event rate is in the order of 10^3 and 10^2 events per day, respectively.

3. Third reduction $\cdots$ More complex criteria to mainly reject cosmic-ray muons and flasher events. The event rate after applying the third reduction is in the order of 10 events per day.

4. Fouth reduction $\cdots$ At the fourth reduction step, a dedicated flasher rejection algorithm is applied.

5. Fifth reduction $\cdots$ Miscellaneous criteria are applied to reject remaining backgrounds.

6. Final event selection $\cdots$ At the analysis stage, criteria using event reconstruction variables are applied. The typical event rate after these criteria is about 8.2 and 1.5 events per day in the 22.5 kton conventional and 4.7 kton additional fiducial mass region, respectively. The definition of the fiducial mass region is introduced in Section 5.7.

An event set passing them, termed "final sample", is commonly used for proton decay searches, atmospheric neutrino analyses, and other exotic searches, such as indirect dark matter searches [99], neutron anti-neutron oscillation searches [100], etc... As for other event categories, "partially contained" (PC) and "Upward-going muon" (UPMU), their event selection criteria can be found elsewhere [98, 101].

5.1 Treatment of OD PMT Hits in SK-IV - ID-OD Crosstalk

In very high energetic events during SK-IV, "fake" OD PMT hits are confirmed, induced by neighbor ID PMTs which detect a large amount of photons. A typical event display is shown in Fig. 5.1. This is an up-going electron event with more than 20 GeV of energy deposition in the detector. In the detector top region, several OD PMTs "detect" low charge hits, less

than 0.2 photoelectrons (p.e.'s), behind the ID PMT hit timing, about 100 nsec late after the ID trigger timing. The same kind of fake OD PMT hits can be seen in laser calibration events described in 3.3.5, which also leave a huge amount of photons in the detector and whose event display is shown in Fig. 5.2. In both events, no particles are thought to exit the ID, and therefore these OD PMT hits should be treated as noises, ID-OD crosstalk.

Figure 5.3 shows the two-dimensional scatter plots of OD PMT charge and hit timing relative to the closest ID PMT hit timing for laser calibration events and partially contained MC events, in which charged particles actually exit the ID and emit Cherenkov photons in the OD. Most OD PMT hits caused by the ID-OD crosstalk are delayed more than 50 nsec with less than 0.2 p.e.'s. Although the mechanism is not fully understood, to reject these fake hits in the event selection, OD PMT hits satisfying the following conditions are not counted in the algorithm for SK-IV:

$$q_{\mathrm{ODPMT}} < 0.2 \text{ p.e.'s}, \tag{5.1}$$

$$50 < t_{\mathrm{ODPMT}} - t_{\mathrm{IDPMT}} < 600 \text{ nsec}, \tag{5.2}$$

where q_{ODPMT} stands for the OD PMT observed charge, t_{ODPMT} stands for the OD PMT hit timing, and t_{IDPMT} for the closest ID PMT hit timing.

5.2 First Reduction

The first event selection criteria are as follows:

FC1-1 $\mathrm{PE}_{300} > 200$ p.e.'s (100 p.e.'s for SK-II),
where PE_{300} is the maximum total ID PMT charge in a sliding 300 nsec timing window.

FC1-2 $\mathrm{NHITA}_{800} < 50$ (55 in SK-IV) or the OD trigger is not issued,
where NHITA_{800} is the number of OD PMT hits within a fixed 800 nsec timing window, from -500 nsec to +300 nsec after the trigger timing.

Criterion **FC1-1** rejects low energy events produced by radioactive products, several MeV scale events. 200 p.e.'s corresponds to about 22 MeV of energy deposition in SK. Criterion **FC1-2** rejects cosmic-ray muons.

5.3 Second Reduction

Events must satisfy the following criteria to pass the second reduction step:

FC2-1 $\mathrm{PE}_{\mathrm{max}}/\mathrm{PE}_{300} < 0.5$,
where $\mathrm{PE}_{\mathrm{max}}$ is the maximum charge in any single ID PMT.

FC2-2 $\mathrm{NHITA}_{800} < 25$ (30 in SK-IV) or $\mathrm{PE}_{\mathrm{total}} > 100000$ p.e.'s or the OD trigger is not issued,
where $\mathrm{PE}_{\mathrm{total}}$ is the total number of p.e.'s in the ID.

In low energy and flasher events, only a single PMT often detects a large amount of p.e.'s. They are rejected by **FC2-1**. Criterion **FC2-2** is to further reject cosmic-ray muons. The $\mathrm{PE}_{\mathrm{max}}/\mathrm{PE}_{300}$ and NHITA_{800} distributions are shown in Figures 5.4 and 5.5, respectively.

5.4 Third Reduction

There are a variety of selection criteria at the third reduction step for each background type.

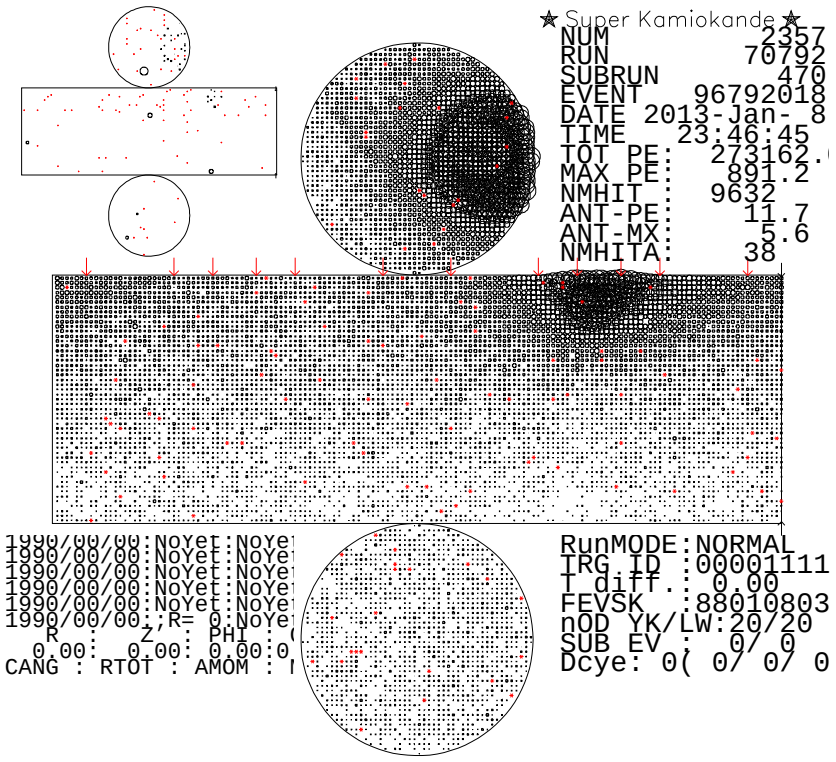

Figure 5.1: Typical event display in which a large amount of photons are observed in the ID and fake OD PMT hits are recorded. The main event display is the ID one and the top left is the OD one. A circle located at each PMT position corresponds to the PMT hit and the size of its radius is proportional to the number of observed photoelectrons. In the detector top region, fake OD PMT hits can be found.

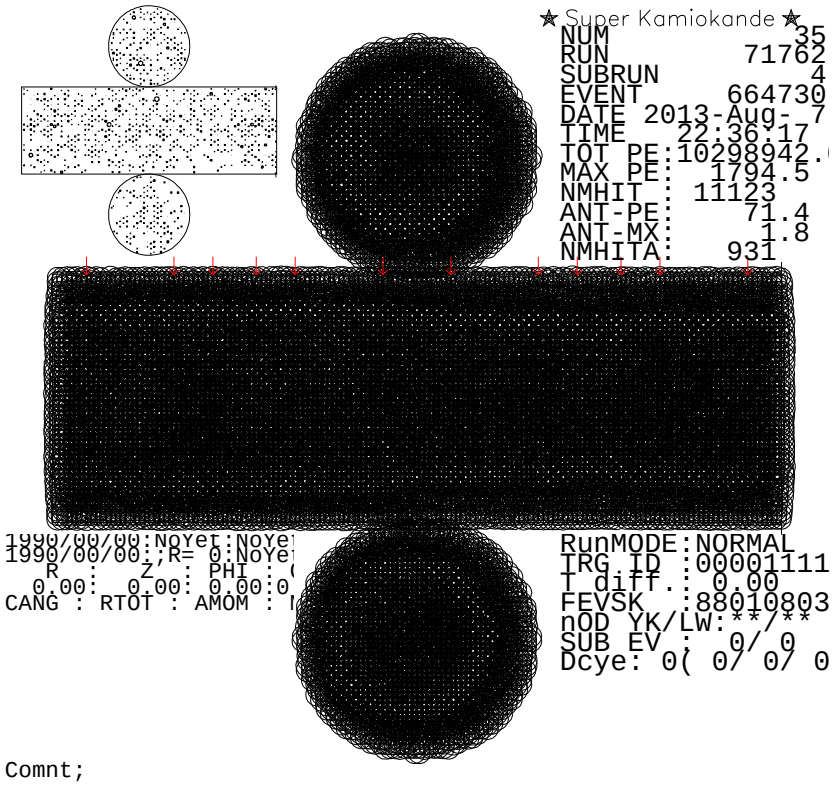

Figure 5.2: Typical laser event display in which a large amount of photons are distributed into the whole ID, and fake OD PMT hits are recorded. In this event, almost all ID PMTs observed more than 1000 p.e.'s.

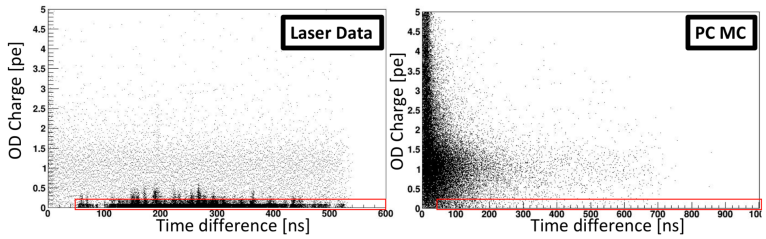

Figure 5.3: Two-dimensional scatter plots of OD PMT charge and hit timing relative to the closest ID PMT hit timing. The laser event plot is in left, and the partially contained MC event plot is in right. In laser calibration event, no charged particles exit the ID, while in the partially contained MC events, charged particles actually exit the ID and emit Cherenkov photons in the OD. Taken from [102].

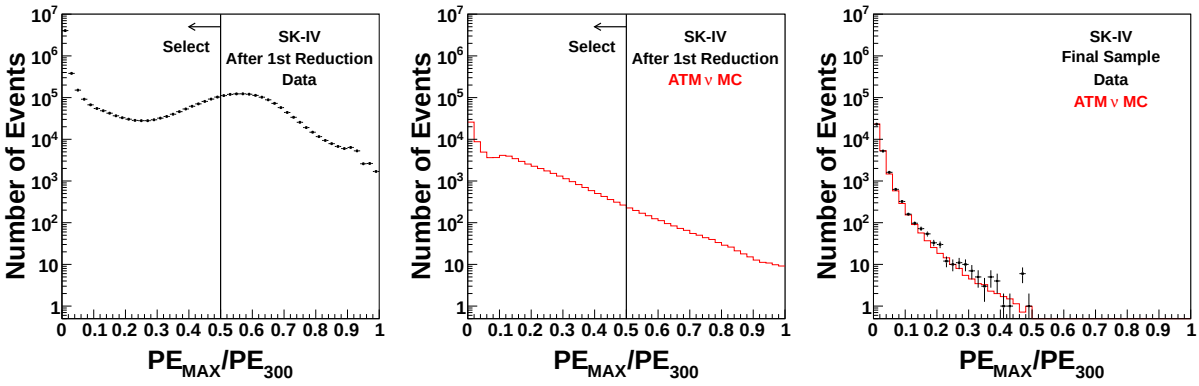

Figure 5.4: Reduction variable $\mathrm{PE_{max}/PE_{300}}$ distributions in SK-IV. The atmospheric neutrino (ATM ν) MC histograms are normalized by SK-IV livetime and the two-flavor oscillation probability ($\Delta m^2 = 2.5 \times 10^{-3}$ eV^2, $\sin^2 2\theta = 1.0$). The term "Final Sample" refers to events after all the FC event selection criteria. Vertical error bars on the data points denote the statistical uncertainty.

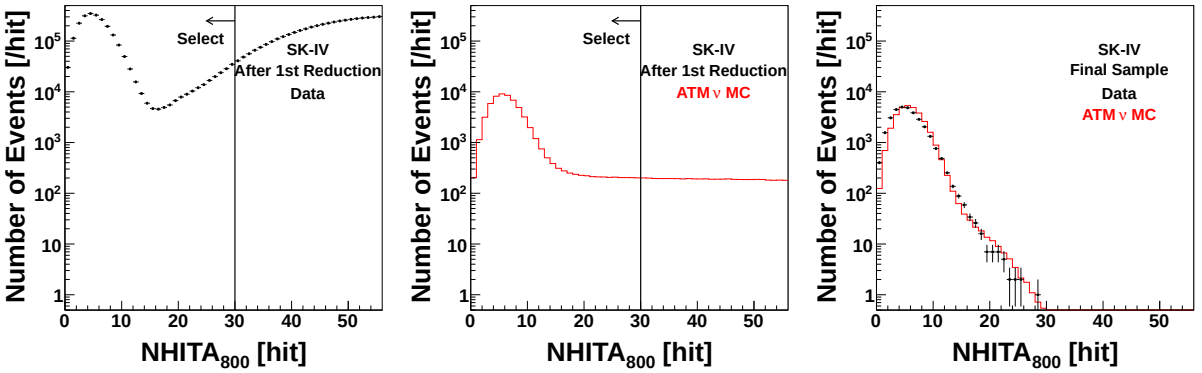

Figure 5.5: Reduction variable $\mathrm{NHITA_{800}}$ distributions in SK-IV. The atmospheric neutrino (ATM ν) MC histograms are normalized by SK-IV livetime and the two-flavor oscillation probability ($\Delta m^2 = 2.5 \times 10^{-3}$ eV^2, $\sin^2 2\theta = 1.0$). The term "Final Sample" refers to events after all the FC event selection criteria. Vertical error bars on the data points denote the statistical uncertainty.

5.4.1 Through-going Muon Rejection

"Through-going" muons are cosmic-ray muons running through the detector and exiting the ID. In order to identify their entering and exiting points in the ID, a special through-going muon fitter is applied to all events which have more than 1000 ID PMT hits with more than 230 p.e.'s deposited therein. The fitter finds them by maximizing the following goodness:

$$\text{goodness} = \frac{1}{\sum_i \frac{1}{\sigma_i^2}} \times \sum_i \frac{1}{\sigma_i^2} \exp\left(-\frac{(t_i' - t_0)^2}{2 \times (\sigma_i \times 1.5)^2}\right), \tag{5.3}$$

where σ_i is the timing resolution of the ith PMT, t_i' is the ith PMT's time-of-flight corrected residual time, and t_0 is chosen so that the goodness is maximal at each tested entering and exiting point. In the photon time-of-flight calculation, the track length of the muon is taken into account.

The number of OD PMT hits around the reconstructed entering and exiting points is also used in the selection. The event rejection criteria are as follows:

FC3-1-1 goodness > 0.75,

FC3-1-2 $\text{NHITA}_{\text{in}}^{\text{thru}} > 10$ or $\text{NHITA}_{\text{out}}^{\text{thru}} > 10$,
where $\text{NHITA}_{\text{in}}^{\text{thru}}$ ($\text{NHITA}_{\text{out}}^{\text{thru}}$) is the number of OD PMT hits located within 8 m from the reconstructed entering (exiting) point in a fixed 800 nsec timing window.

Events satisfying the above criteria are removed from the data set as through-going muons. The two-dimensional $\text{NHITA}_{\text{in}}^{\text{thru}}$ and $\text{NHITA}_{\text{out}}^{\text{thru}}$ scatter plots after applying **FC3-1-1** and one-dimensional distributions of the final sample are shown in Fig. 5.6.

5.4.2 Stopping Muon Rejection

"Stopping" muons are cosmic-ray muons that stop inside the ID and do not have any exiting points. In a similar manner to through-going muons, a special stopping muon fitter identifies a cluster of earliest timing ID PMT hits as a muon entering point from those PMTs' position, and the fitting goodness is evaluated using Eq. (5.3). The event rejection criteria to remove stopping muons are as follows:

FC3-2-1 The stopping muon fit is succeeded, goodness ≥ 0,

FC3-2-2 $\text{NHITA}_{\text{in}} \geq 10$,
where NHITA_{in} is the number of OD PMT hits located within 8 m from the reconstructed entering point in a fixed 800 nsec timing window.

Events satisfying both criteria are rejected. In SK-I, events satisfying the following criterion are additionally rejected.

FC3-2-3 $\text{NHITA}_{\text{in}} \geq 5$ and goodness ≥ 0.5.

The NHITA_{in} distributions are shown in Fig. 5.7.

5.4.3 Cable Hole Muon Rejection

"Cable hole" muons are cosmic-ray muons that pass through cable bundles. Because they do not run in the water, they run through the OD without leaving sufficient light. There are twelve cable holes on the top of the detector through which PMT cables run as shown in Fig. 5.8. Four cable holes out of the twelve have veto counters with a plastic scintillator plate and 50 cm PMT because they are located slightly inner than the other eight cable holes. A schematic view of the veto counter and a typical cable hole muon is shown in Fig. 5.9. Events with both a veto

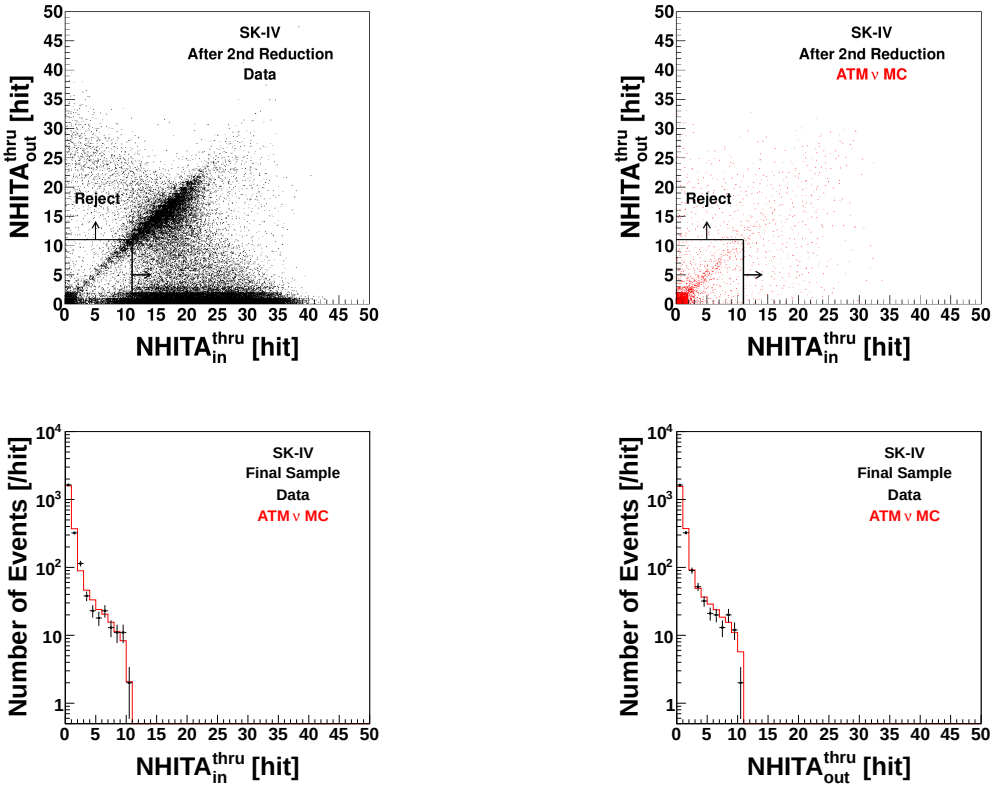

Figure 5.6: The top two plots are the two-dimensional $\mathrm{NHITA}_{\mathrm{in}}^{\mathrm{thru}}$ and $\mathrm{NHITA}_{\mathrm{out}}^{\mathrm{thru}}$ scatter plots in SK-IV. The bottom two plots show the one-dimensional distributions of the final sample in SK-IV. In the bottom plots, the atmospheric neutrino (ATM ν) MC histograms are normalized by SK-IV livetime and the two-flavor oscillation probability ($\Delta m^2 = 2.5 \times 10^{-3}$ eV^2, $\sin^2 2\theta = 1.0$). Vertical error bars on the data points denote the statistical uncertainty.

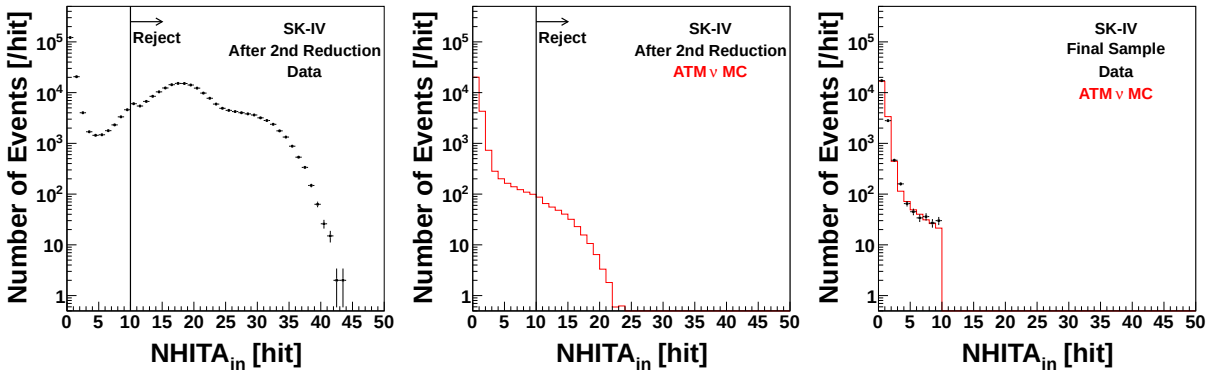

Figure 5.7: Reduction variable $\mathrm{NHITA}_{\mathrm{in}}$ distributions in SK-IV. The atmospheric neutrino (ATM ν) MC histograms are normalized by SK-IV livetime and the two-flavor oscillation probability ($\Delta m^2 = 2.5 \times 10^{-3}$ eV^2, $\sin^2 2\theta = 1.0$). The term "Final Sample" refers to events after all the FC event selection criteria. Vertical error bars on the data points denote the statistical uncertainty.

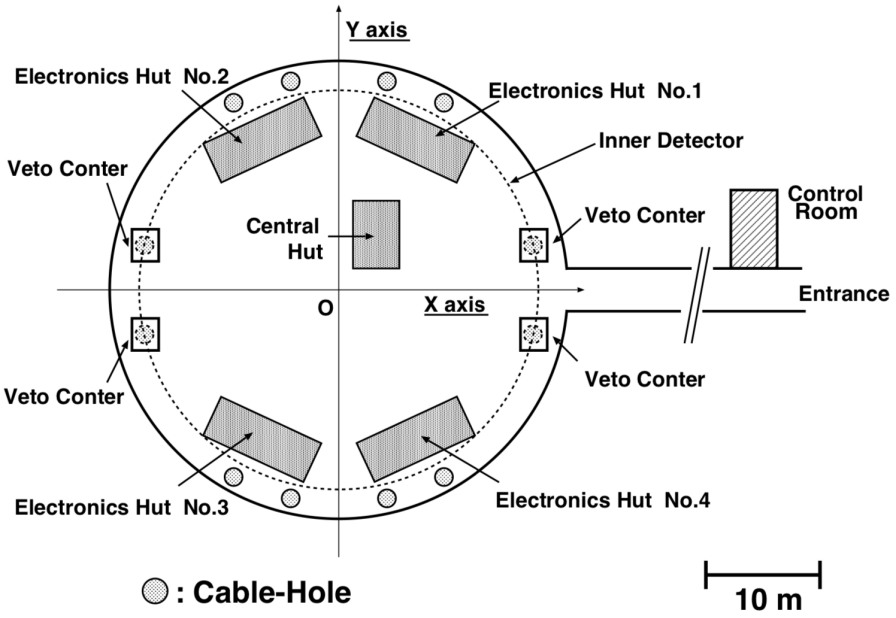

Figure 5.8: Schematic view of the top of the detector. Shaded circles represent the cable holes. Taken from [107].

counter hit and an entering point less than 4 m from the corresponding cable hole have been tagged as cable hole muons and rejected from the data set in previous analyses. Here, again the stopping muon fitter has been used to reconstruct the entering point. In the present analysis, all events with a veto counter hit in the event trigger timing are additionally rejected regardless of the reconstructed entering point.

5.4.4 Low Energy Event Rejection

In order to further reject low energy events, the following rejection criteria are applied:

FC3-3-1 The number of ID PMT hits is less than 500,

FC3-3-2 $N_{50} \leq 50$ (25 for SK-II),
where N_{50} is the maximum number of ID PMT hits in a sliding 50 nsec window after subtracting the photon time-of-flight. The vertex position used for the time-of-flight subtraction is reconstructed with a dedicated low energy event fitter so that the goodness defined in Eq. (5.3) takes maximum.

Events satisfying both criteria are removed. The N_{50} distributions after applying **FC3-3-1** are shown in Fig. 5.10.

5.4.5 Flasher Event Rejection

Flasher events often have a broad timing distribution compared to events produced by charged particles. The minimum number of ID PMT hits in a sliding 100 nsec timing window from +300 nsec to +800 nsec after the trigger timing is defined as $\mathrm{NHIT}_{\mathrm{min100}}$. The flasher event rejection criteria are as follows: For SK-I,

FC3-4-1 $\mathrm{NHIT}_{\mathrm{min100}} \geq 15$,
or

FC3-4-2 The number of ID PMT hits is less than 800 and $\mathrm{NHIT}_{\mathrm{min100}} \geq 10$.

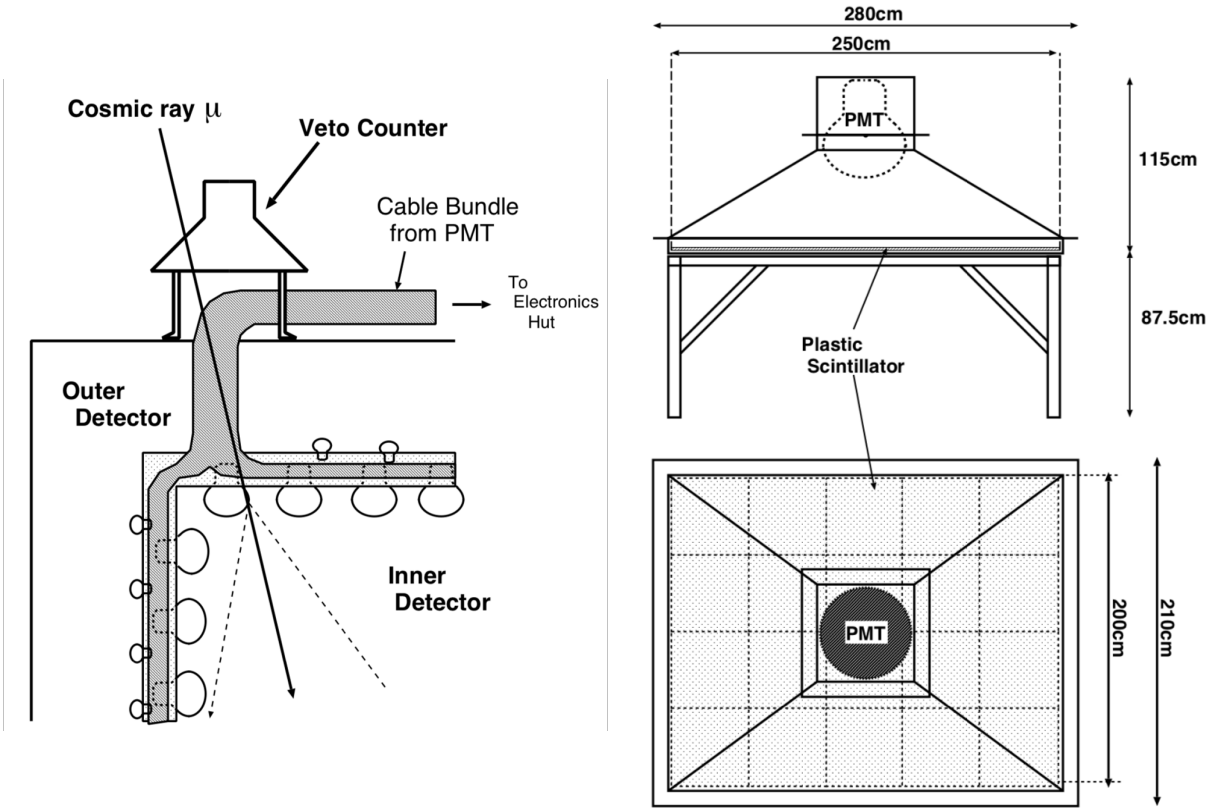

Figure 5.9: Schematic view of the veto counter. It is composed of a plastic scintillator plate and 50 cm PMT. Taken from [107].

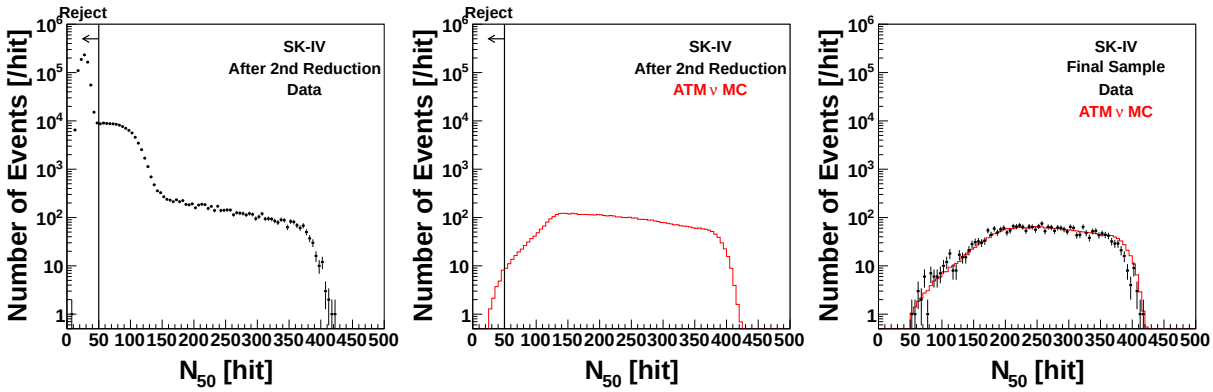

Figure 5.10: Reduction variable N_{50} distributions of events with less than 500 ID PMT hits in SK-IV. The atmospheric neutrino (ATM ν) MC histograms are normalized by SK-IV livetime and the two-flavor oscillation probability ($\Delta m^2 = 2.5 \times 10^{-3}$ eV^2, $\sin^2 2\theta = 1.0$). The term "Final Sample" refers to events after all the FC event selection criteria. Vertical error bars on the data points denote the statistical uncertainty.

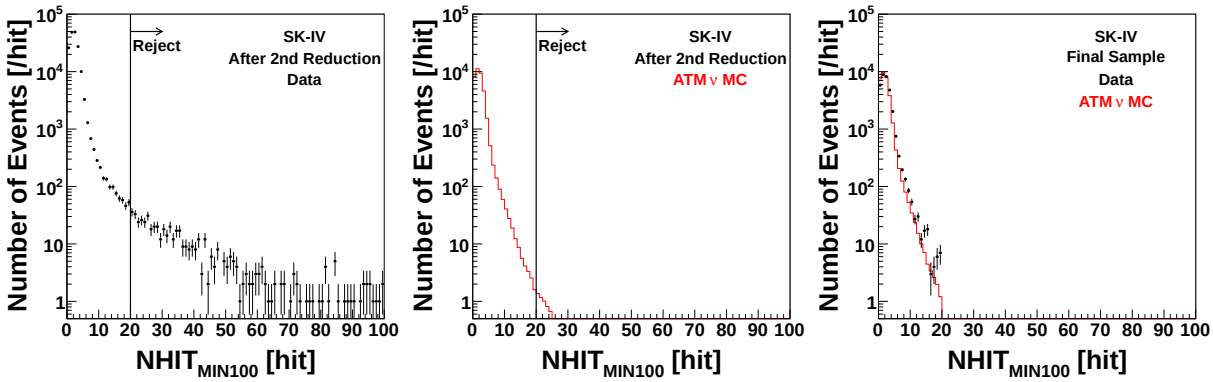

Figure 5.11: Reduction variable $\mathrm{NHIT}_{\mathrm{min100}}$ distributions in SK-IV. The atmospheric neutrino (ATM ν) MC histograms are normalized by SK-IV livetime and the two-flavor oscillation probability ($\Delta m^2 = 2.5 \times 10^{-3}$ eV^2, $\sin^2 2\theta = 1.0$). The term "Final Sample" refers to events after all the FC event selection criteria. Vertical error bars on the data points denote the statistical uncertainty.

For SK-II to -IV,

FC3-4-1′ $\mathrm{NHIT}_{\mathrm{min100}} \geq 20$.

The $\mathrm{NHIT}_{\mathrm{min100}}$ distributions are shown in Fig. 5.11.

Another flasher rejection criterion is applied to events with less than 250 ID PMT hits. Events whose low energy fit goodness defined in Eq. (5.3) is less than 0.4 are also removed as flasher events. The low energy fit goodness distributions of events with less than 250 ID PMT hits are shown in Fig. 5.12.

5.4.6 Accidental Coincidence Event Rejection

A cosmic-ray muon and low energy activity sometimes accidentally coincide. In case the cosmic-ray muon comes in the detector several hundred nsec after the low energy activity, the event trigger is issued by the low energy activity, and no obvious OD PMT hits are found around the trigger timing. Since the former event reduction steps search for OD PMT hits around the trigger timing, such events are not rejected. The event rejection criteria are as follows to prevent them from contaminating the data set:

FC3-5-1 $\mathrm{PE}_{\mathrm{LATE}} > 5000$ p.e.'s (2500 p.e.'s for SK-II),
where $\mathrm{PE}_{\mathrm{LATE}}$ is the total number of p.e.'s in the ID within a fixed 500 nsec timing window from +300 nsec to +800 nsec after the trigger timing.

FC3-5-2 $\mathrm{NHITA}_{\mathrm{LATE}} \geq 20$,
where $\mathrm{NHITA}_{\mathrm{LATE}}$ is the number of OD PMT hits within a fixed 500 nsec timing window from +300 nsec to +800 nsec after the trigger timing.

Events satisfying both criteria are removed. The two-dimensional $\mathrm{PE}_{\mathrm{LATE}}$ and $\mathrm{NHITA}_{\mathrm{LATE}}$ scatter plots and one-dimensional distributions of the final sample are shown in Fig. 5.13.

5.5 Fourth Reduction

At the fourth reduction step, a pattern matching method is used to reject flasher events because flasher events often occur repeatedly with a similar ID PMT hit profile. Typical flasher

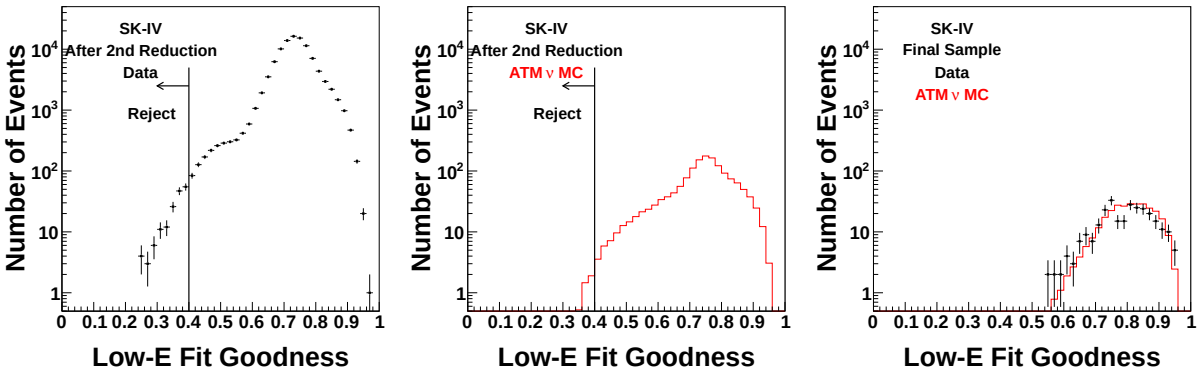

Figure 5.12: Low energy fit goodness distributions of events with less than 250 ID PMT hits in SK-IV. The atmospheric neutrino (ATM ν) MC histograms are normalized by SK-IV livetime and the two-flavor oscillation probability ($\Delta m^2 = 2.5 \times 10^{-3}$ eV^2, $\sin^2 2\theta = 1.0$). The term "Final Sample" refers to events after all the FC event selection criteria. Vertical error bars on the data points denote the statistical uncertainty.

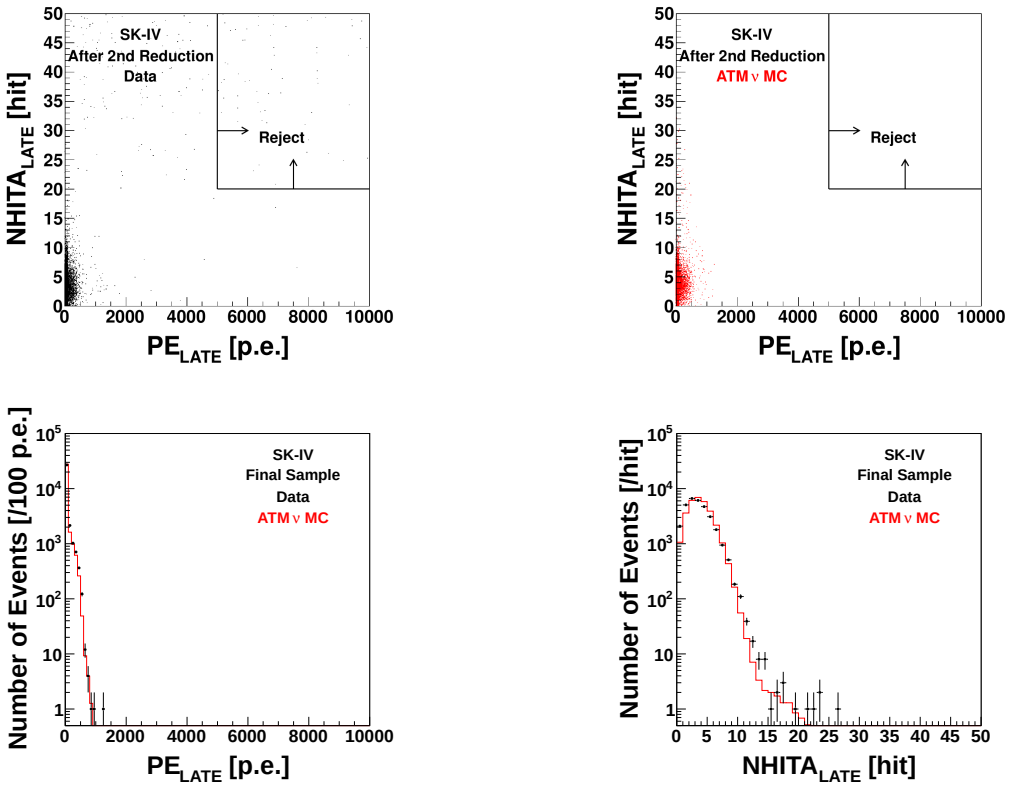

Figure 5.13: The top two plots show the two-dimensional $\mathrm{PE_{LATE}}$ and $\mathrm{NHITA_{LATE}}$ scatter plots in SK-IV. The bottom two plots show the one-dimensional distributions of the final sample in SK-IV. In the bottom plots, the atmospheric neutrino (ATM ν) MC histograms are normalized by SK-IV livetime and the two-flavor oscillation probability ($\Delta m^2 = 2.5 \times 10^{-3}$ eV^2, $\sin^2 2\theta = 1.0$). Vertical error bars on the data points denote the statistical uncertainty.

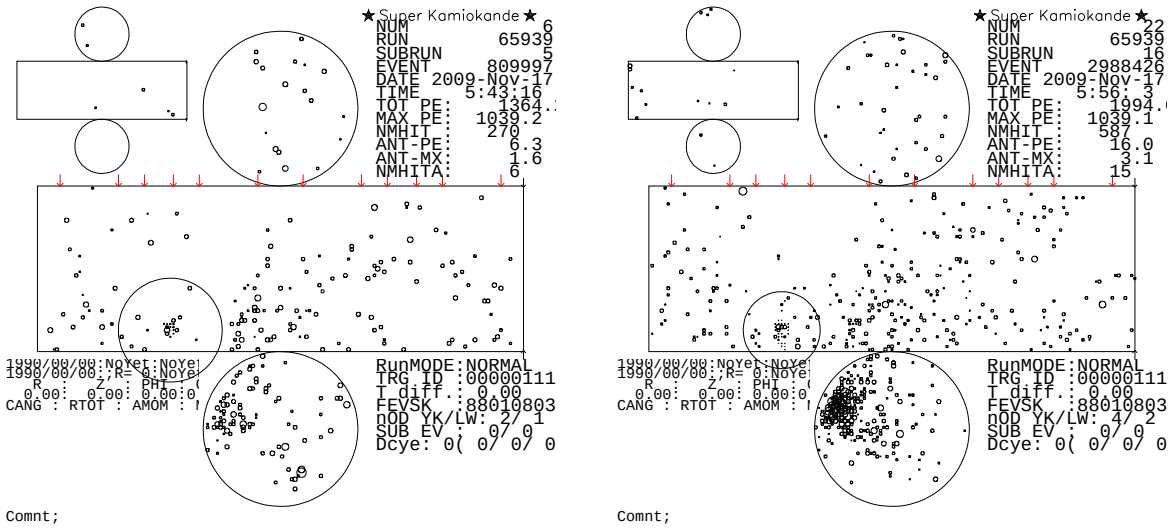

Figure 5.14: Typical flasher event displays. They are different events but caused by the same PMT which detects a large amount of photons (the large circle).

event displays are shown in Fig. 5.14. The algorithm tries to find two different events in which PMT hit (charge) patterns are similar. The ID is divided into 2 m × 2 m patches when comparing the PMT charge profiles in the two different events, event A and event B. Each patch has about 8 PMTs, and their charge sum is calculated. The following correlation coefficient, r, is defined:

$$r = \frac{1}{N} \sum_i \frac{(Q_i^{\mathrm{A}} - \langle Q^{\mathrm{A}} \rangle) \times (Q_i^{\mathrm{B}} - \langle Q^{\mathrm{B}} \rangle)}{\sigma_{\mathrm{A}} \sigma_{\mathrm{B}}}, \tag{5.4}$$

where N is the number of patches, Q_i^{A} (Q_i^{B}) is the ith patch's total observed charge in event A (B), $\langle Q^{\mathrm{A}} \rangle$ ($\langle Q^{\mathrm{B}} \rangle$) is the average charge over all patches in event A (B), and σ_{A} (σ_{B}) is the standard deviation of the observed charge in event A (B). For SK-I and -II, this single parameter r is used at this reduction step.

Since SK-III, a Kolmogorov-Smirnov test is performed for the accumulated charge distribution normalized by the total observed charge in each event. The maximum distance between the two accumulated charge distributions in event A and B, d_{KS}, is introduced. Furthermore, probability density functions are made using atmospheric neutrino MC events and these two parameters, r and d_{KS}, are combined into a single likelihood parameter. The combined likelihood value, *prob*, is used to select events at this reduction step. A higher *prob* value indicates "well-matched" event with another event, and events with more than 3 of *prob* are rejected. The *prob* distributions are shown in Fig. 5.15.

5.6 Fifth Reduction

There are miscellaneous selections at the last step to remove remaining background events.

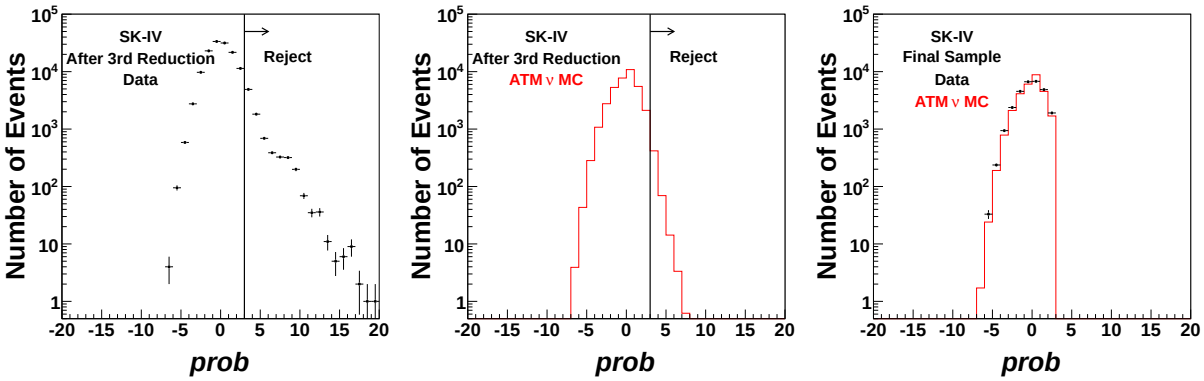

Figure 5.15: Reduction variable *prob* distributions in SK-IV. The atmospheric neutrino (ATM ν) MC histograms are normalized by SK-IV livetime and the two-flavor oscillation probability ($\Delta m^2 = 2.5 \times 10^{-3}$ eV^2, $\sin^2 2\theta = 1.0$). The term "Final Sample" refers to events after all the FC event selection criteria. Vertical error bars on the data points denote the statistical uncertainty.

5.6.1 Tight Stopping Muon Rejection

In order to further reject stopping muons, events satisfying at least one of the following criteria are thrown away:

FC5-1-1 Stopping muon fit goodness ≥ 0.5 and $\mathrm{NHITA_{in}} \geq 5$,

FC5-1-2 $\mathrm{NHITA_{in200}} \geq 4$,
where $\mathrm{NHITA_{in200}}$ is the maximum number of OD PMT hits located within 8 m from the reconstructed entering point in a sliding 200 nsec timing window.

FC5-1-3 The vertex reconstruction goodness *agood* < 0.77, the number of ID PMT hits is more than 7000 with more than 70000 p.e.'s deposited therein, and $\mathrm{NHITA_{in}} \geq 6$,
where *agood* is evaluated in the FC event reconstruction algorithm described in Section 6.1.1.

Criterion **FC5-1-1** criterion is the tighter condition of the stopping muon rejection criteria in the third reduction step (Section 5.4.2). The two-dimensional stopping muon fit goodness and $\mathrm{NHITA_{in}}$ scatter plots and one-dimensional distributions of the final sample are shown in Fig. 5.16. Criterion **FC5-1-2** rejects events in which OD PMT hits are localized in terms of time and location. The $\mathrm{NHITA_{in200}}$ distributions are shown in Fig. 5.17. Criterion **FC5-1-3** is introduced in the present analysis to reject high energy cosmic-ray muons which are mis-reconstructed in the fiducial mass region by the FC event reconstruction algorithm. The $\mathrm{NHITA_{in}}$ distributions after applying *agood*, the number of ID PMT hits, and total observed charge criteria are shown in Fig. 5.18.

5.6.2 Tight Cable Hole Muon Rejection

In the third reduction step, only criteria regarding the four cable holes with veto counters are applied (Section 5.4.3). To reject cosmic-ray muons passing through the other eight cable holes, events satisfying the following conditions are removed:

FC5-2-1 Stopping muon fit goodness ≥ 0.4,

FC5-2-2 $\mathrm{PE_{tot}} > 4000$ p.e.'s,

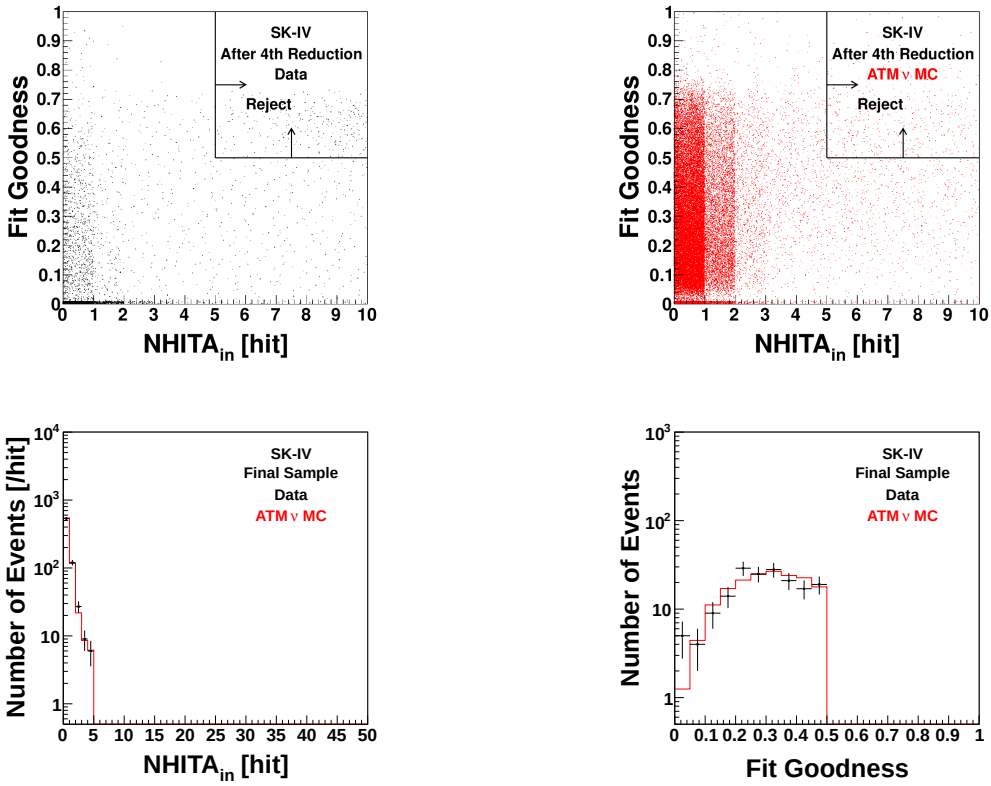

Figure 5.16: The top two plots show the two-dimensional stopping muon fit goodness and $\mathrm{NHITA_{in}}$ scatter plots in SK-IV. The bottom two plots show the one-dimensional distributions of the final sample in SK-IV. In the $\mathrm{NHITA_{in}}$ one-dimensional distribution, events with stopping muon fit goodness of 5 or more are filled. In the stopping muon fit goodness one-dimensional distribution, events with $\mathrm{NHITA_{in}}$ of 5 or more are filled. The atmospheric neutrino (ATM ν) MC histograms are normalized by SK-IV livetime and the two-flavor oscillation probability ($\Delta m^2 = 2.5 \times 10^{-3}$ eV^2, $\sin^2 2\theta = 1.0$). Vertical error bars on the data points denote the statistical uncertainty.

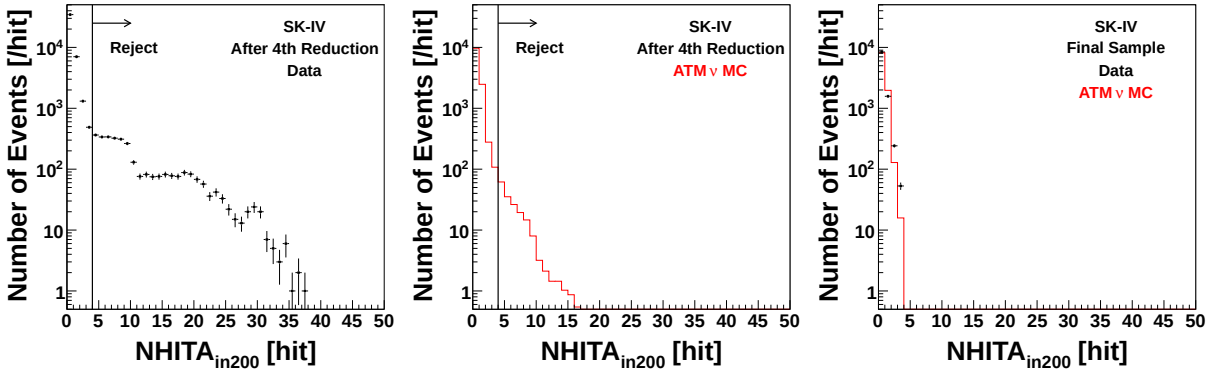

Figure 5.17: Reduction variable $\mathrm{NHITA_{in200}}$ distributions in SK-IV. The atmospheric neutrino (ATM ν) MC histograms are normalized by SK-IV livetime and the two-flavor oscillation probability ($\Delta m^2 = 2.5 \times 10^{-3}$ eV^2, $\sin^2 2\theta = 1.0$). The term "Final Sample" refers to events after all the FC event selection criteria. Vertical error bars on the data points denote the statistical uncertainty.

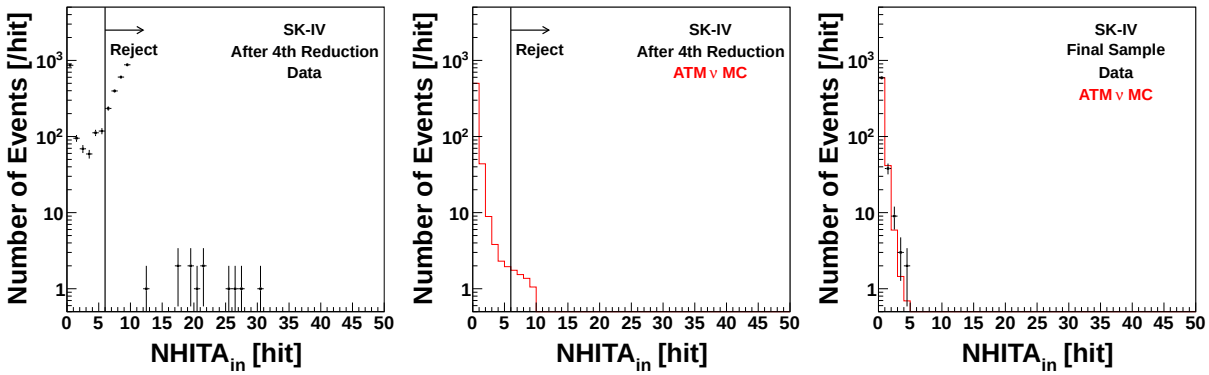

Figure 5.18: Reduction variable $\mathrm{NHITA_{in}}$ distributions in SK-IV. Events with less than $agood < 0.77$, more than 7000 ID PMT hits and more than 70000 p.e.'s of total observed charge are plotted. The atmospheric neutrino (ATM ν) MC histograms are normalized by SK-IV livetime and the two-flavor oscillation probability ($\Delta m^2 = 2.5 \times 10^{-3}$ eV^2, $\sin^2 2\theta = 1.0$). The term "Final Sample" refers to events after all the FC event selection criteria. Vertical error bars on the data points denote the statistical uncertainty.

FC5-2-3 $\cos\theta_z > 0.6$,
where $\cos\theta_z$ is the reconstructed muon direction, and $\cos\theta_z = 1.0$ is vertically downward-going.

FC5-2-4 $d_{\mathrm{hole}} < 250$ cm,
where d_{hole} is the distance between the reconstructed entering point and the closest cable hole position.

These criteria have been applied only to the SK-IV data in previous analyses but in the present work, they are applied to all of the SK data uniformly. The d_{hole} distributions after applying **FC5-2-1**, **FC5-2-2**, and **FC5-2-3** are shown in Fig. 5.19.

5.6.3 Invisible Muon Rejection

"Invisible muon" events are induced by Michel electrons from cosmic-ray muons which are below the Cherenkov threshold, invisible, and stop in the ID. A cluster of OD PMT hits, which are produced earlier than the ID trigger timing and are induced by the muon before its decay, are often found in such events. The ID event trigger is issued by the Michel electron from the muon decay. Events satisfying at least one of the following criteria are rejected as invisible muon events:

FC5-3-1 For events in which the total ID PMT charge, $\mathrm{PE_{tot}}$, is less than 1000 p.e.'s (500 p.e.'s for SK-II), $\mathrm{NHITA_{early200}} \geq 5$, and $\mathrm{NHITA_{sum}} \geq 10$,
where $\mathrm{NHITA_{early200}}$ is the maximum number of OD PMT hits in a sliding 200 nsec timing window from -9000 nsec to -200 nsec after the trigger timing, and $\mathrm{NHITA_{sum}}$ is:

$$\mathrm{NHITA_{sum}} = \begin{cases} \mathrm{NHITA_{early200}} + \mathrm{NHITA_{500}}, & (d_{\mathrm{OD}} < 500 \text{ cm}) \\ \mathrm{NHITA_{early200}}, & (\text{otherwise}) \end{cases} \tag{5.5}$$

where $\mathrm{NHITA_{500}}$ is the number of OD PMT hits in a fixed 500 nsec timing window from -200 nsec to +300 nsec after the trigger timing, and d_{OD} is the distance between the position of the OD PMT hit cluster in $\mathrm{NHITA_{early200}}$ and the position of the OD PMT hit cluster in $\mathrm{NHITA_{500}}$.

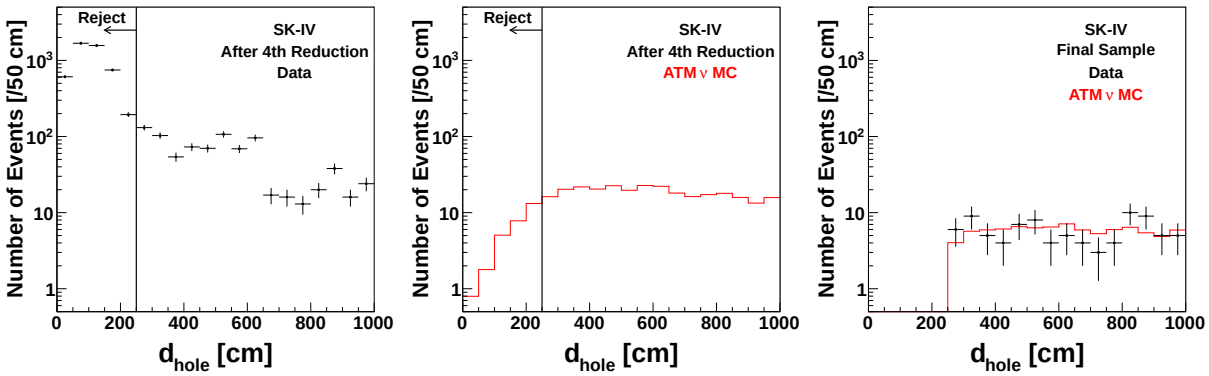

Figure 5.19: Distributions of the distance between the reconstructed entering point and the closest cable hole position, d_{hole}, in SK-IV. Events with more than 0.4 of stopping muon fit goodness, more than 4000 p.e.'s of total charge and $\cos\theta_z > 0.6$ are plotted. The atmospheric neutrino (ATM ν) MC histograms are normalized by SK-IV livetime and the two-flavor oscillation probability ($\Delta m^2 = 2.5 \times 10^{-3}$ eV^2, $\sin^2 2\theta = 1.0$). The term "Final Sample" refers to events after all the FC event selection criteria. Vertical error bars on the data points denote the statistical uncertainty.

FC5-3-2 $\text{NHITA}_{\text{early200}} \geq 50$ (55 for SK-IV).

Criterion **FC5-3-2** is newly implemented in this work and helps to reject remaining invisible muons. The two-dimensional $\text{NHITA}_{\text{early200}}$ and $\text{NHITA}_{\text{sum}}$ scatter plots and one-dimensional distributions of the final sample for events in which the total observed charge in the ID is less than 1000 p.e.'s are shown in Fig. 5.20. The $\text{NHITA}_{\text{early200}}$ distributions without any ID PMT conditions are shown in Fig. 5.21. The agreement between data and MC is not quite good but the cut point is far from the majority of the expected atmospheric neutrino events, and therefore the impact of this disagreement is small. This disagreement is caused by accidental OD PMT hits produced by uncorrelated low energy activities around the detector, which are not included in primary event MC.

5.6.4 Further Flasher Event Rejection

In order to further reject flasher events, there are flasher rejection criteria at the fifth reduction step. They use a vertex reconstruction tool, Point-fit, and the algorithm often returns bad fitting goodness in flasher events because of its broad timing distribution.

FC5-4-1 Point-fit goodness < 0.4 and $\text{NHIT}_{\text{MIN100}} \geq 6$,
where Point-fit goodness is described in Section 6.1.1.
For SK-II to -IV, there is an additional rejection criterion:

FC5-4-2 Point-fit goodness < 0.3 regardless of the $\text{NHIT}_{\text{MIN100}}$ value.

The two-dimensional Point-fit goodness and $\text{NHIT}_{\text{MIN100}}$ scatter plots and one-dimensional distributions of the final sample are shown in Fig. 5.22.

5.6.5 Tight Accidental Coincidence Event Rejection

Events satisfying the following criteria are removed from the data set as accidental coincidence events:

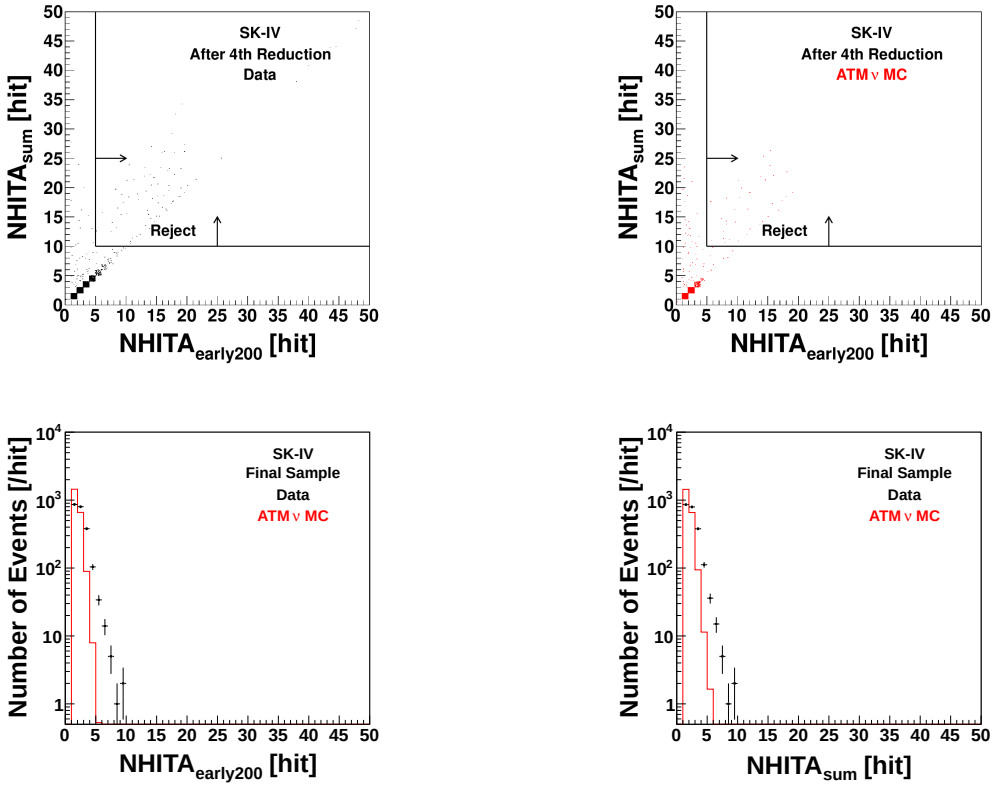

Figure 5.20: The top two plots show the two-dimensional $\mathrm{NHITA}_{\mathrm{early200}}$ and $\mathrm{NHITA}_{\mathrm{sum}}$ scatter plots in SK-IV. The bottom two plots show the one-dimensional distributions of the final sample in SK-IV. In the bottom plots, the atmospheric neutrino (ATM ν) MC histograms are normalized by SK-IV livetime and the two-flavor oscillation probability ($\Delta m^2 = 2.5 \times 10^{-3}$ eV^2, $\sin^2 2\theta = 1.0$). Only events with less than 1000 p.e.'s of total observed charge are plotted. Vertical error bars on the data points denote the statistical uncertainty.

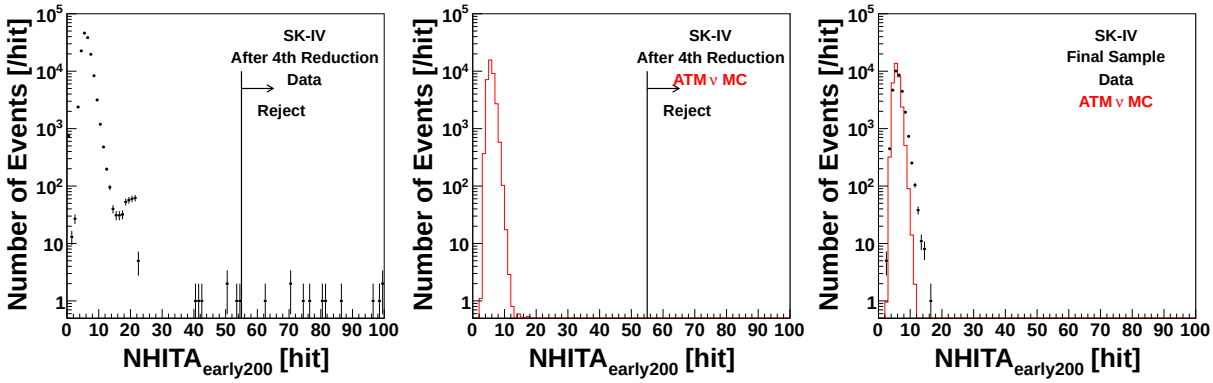

Figure 5.21: Reduction variable $\mathrm{NHITA}_{\mathrm{early200}}$ distributions without any ID PMT conditions in SK-IV. The atmospheric neutrino (ATM ν) MC histograms are normalized by SK-IV livetime and the two-flavor oscillation probability ($\Delta m^2 = 2.5 \times 10^{-3}$ eV^2, $\sin^2 2\theta = 1.0$). The term "Final Sample" refers to events after all the FC event selection criteria. Vertical error bars on the data points denote the statistical uncertainty.

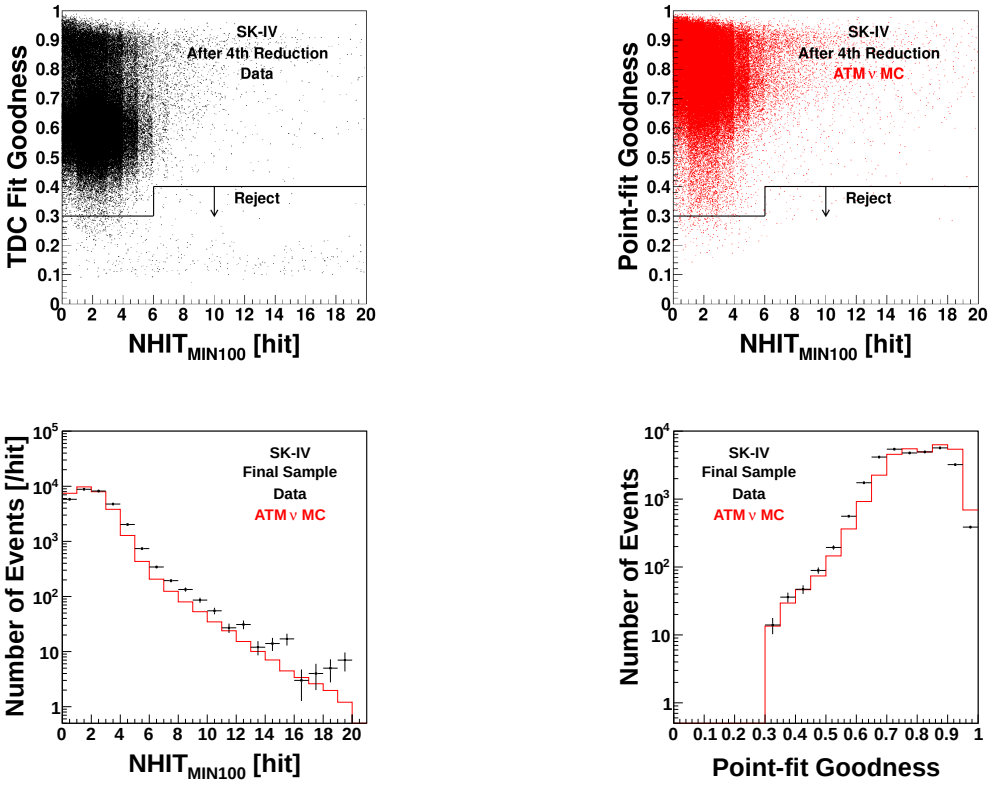

Figure 5.22: The top two plots show the two-dimensional Point-fit goodness and $\mathrm{NHIT}_{\mathrm{MIN100}}$ scatter plots in SK-IV. The bottom two plots show the one-dimensional distributions of the final sample in SK-IV. In the bottom plots, the atmospheric neutrino (ATM ν) MC histograms are normalized by SK-IV livetime and the two-flavor oscillation probability ($\Delta m^2 = 2.5 \times 10^{-3}$ eV^2, $\sin^2 2\theta = 1.0$). Vertical error bars on the data points denote the statistical uncertainty.

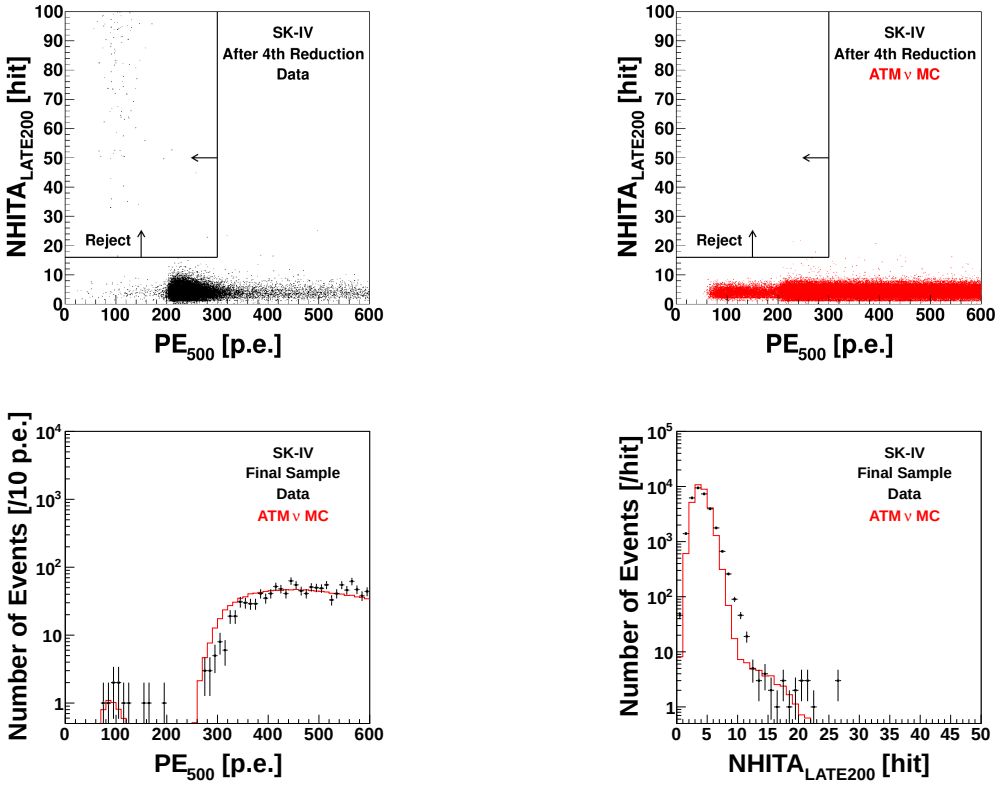

Figure 5.23: The top two plots show the two-dimensional PE_{500} and $NHITA_{LATE200}$ scatter plots in SK-IV. The bottom two plots show the one-dimensional distributions of the final sample in SK-IV. In the bottom plots, the atmospheric neutrino (ATM ν) MC histograms are normalized by SK-IV livetime and the two-flavor oscillation probability ($\Delta m^2 = 2.5 \times 10^{-3}$ eV^2, $\sin^2 2\theta = 1.0$). Vertical error bars on the data points denote the statistical uncertainty.

FC5-5-1 $PE_{500} < 300$ p.e.'s (150 p.e.'s for SK-II),
where PE_{500} is the total number of p.e.'s in a fixed 500 nsec timing window from -200 nsec to +300 nsec after the trigger timing.

FC5-5-2 $NHITA_{LATE200} \geq 20$ (16 for SK-IV),
where $NHITA_{LATE200}$ is the maximum number of OD PMT hits in a 200 nsec sliding timing window from +300 nsec to +1500 nsec after the trigger timing.

The two-dimensional PE_{500} and $NHITA_{LATE200}$ scatter plots and one-dimensional distributions of the final sample are shown in Fig. 5.23.

5.7 Event Reduction Summary

After the FC event reduction algorithm, the following event selection criteria are applied to select FC events at the analysis stage:

FC_{final}-1 NHITAC < 16 (10 for SK-I),
where NHITAC is the number of OD PMT hits in the highest charge OD cluster.

FC_{final}-2 $E_{vis} > 30$ MeV,
where E_{vis} is the visible (electron equivalent) energy which is defined as the energy of an electromagnetic shower producing the same amount of Cherenkov photons.

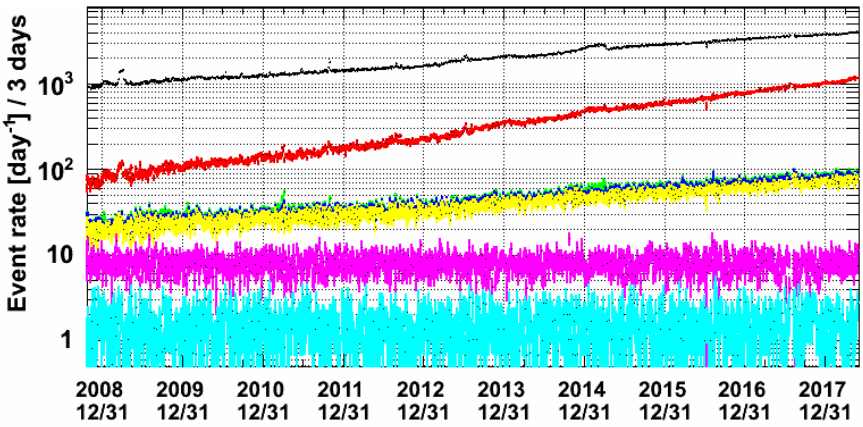

Figure 5.24: Event rate at each reduction step during SK-IV as a function of date. The 1st, 2nd, 3rd, 4th, and 5th reduction output rates are plotted in black, red, green, blue, and yellow, respectively. The purple (cyan) one corresponds to the event rate of the final sample with *dwall* greater than 200 cm (in between 100 and 200 cm).

FC$_{\text{final}}$-3 *dwall* $>$ 100 cm,
where *dwall* is the distance between the reconstructed event vertex position and the closest ID wall.

As for **FC$_{\text{final}}$-3**, called fiducial volume cut, in the previous analysis [27], the cut boundary was 200 cm, giving a 22.5 kton of water fiducial mass. However, the fiducial volume in this analysis is enlarged up to 100 cm from the ID wall, which gives an additional 4.7 kton of water fiducial mass. The non-neutrino background contamination level around the fiducial volume boundary is discussed in Section 5.7.2. The event reconstruction performance inside the new fiducial mass region is presented in Chapter 6. In the following, the term "conventional" fiducial volume (or fiducial mass region) refers to the region with *dwall* greater than 200 cm, and "additional" fiducial volume (or fiducial mass region) refers to the region in between *dwall* 100 cm and 200 cm. Terms representing each fiducial volume (mass region) are summarized in Table 5.1. The "Outside" region is not used in the proton decay analysis but it is used to evaluate the non-neutrino background contamination level and event reconstruction performance. Moving the fiducial mass boundary from 200 cm to 100 cm from the ID wall increases the total detector exposure from 372 kton·years to 450 kton·years.

Table 5.1: Terms representing each fiducial volume (mass region). Exposure is water mass times livetime.

Term	*dwall*	Water mass	Exposure
Conventional	200 cm $<$ *dwall*	22.5 kton	372 kton·years
Additional	100 $<$ *dwall* $\leq$ 200 cm	4.7 kton	78 kton·years
Enlarged	100 cm $<$ *dwall*	27.2 kton	450 kton·years
Outside	50 $<$ *dwall* $\leq$ 100 cm	2.6 kton	43 kton·years

The event rate during SK-IV kept increasing as shown in Fig. 5.24 because of the increased ID PMT gain, which is shown in Fig. 3.26, and the increased number of dead OD PMTs as shown in Fig. 5.25. However, the event rate of the final sample is stable in both fiducial mass regions, and it is 8.2 (1.5) events per day in the conventional (additional) fiducial mass region in SK-IV. In SK-I, -II, and -III, it is 8.2 (1.4), 8.3 (1.4), and 8.4 (1.6) events per day in the conventional (additional) fiducial mass region, respectively.

There are several new event reduction criteria as presented in Sections 5.4.3, 5.6.1, 5.6.2,

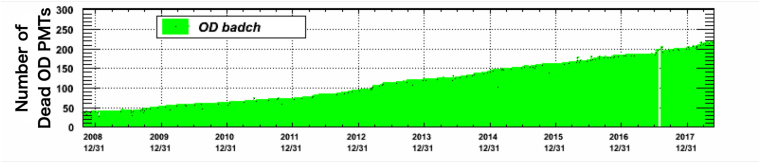

Figure 5.25: The number of dead OD PMTs as a function of date.

and 5.6.3. The SK-IV data has been reprocessed with the updated event selection algorithm from the raw data. On the other hand, the data in the other phases have been processed by just applying the new criteria to the final sample to save processing time. Although overall signal selection efficiencies for atmospheric neutrino MC and proton decay MC events are discussed in the next section, an additional signal selection efficiency loss for them by adopting the new criteria is estimated to be less than 0.01% in the enlarged fiducial mass region and is therefore negligible.

5.7.1 Event Selection Efficiency

Atmospheric neutrino and proton decay event selection efficiencies are evaluated using their MC events. Their value at each reduction step and the number of events in the final sample of the experimental data are summarized in Table 5.2. The reduction inefficiencies are estimated to be a few % level.

5.7.2 Non-neutrino Background Events

Non-neutrino backgrounds, which are not atmospheric neutrinos nor proton decay candidates, such as cosmic-ray muons and flasher events generically deteriorate SK physics analyses. For example, cosmic-ray muons may mimic proton decay signals in which a single non-showering track is left in the detector ($p \to \bar{\nu}K^+$ [103], $p \to \bar{\nu}\pi^+$ [104]), and also may bias atmospheric neutrino up-down ratios [64] because all of them are down-going. Flasher events may also contaminate proton decay search analyses but it is hard to estimate quantitatively. Furthermore, flasher events tend to produce similar topological events as shown in Fig. 5.14 and have similar event reconstruction results, such as reconstructed "particle direction". Thus, they may become unexpected backgrounds in atmospheric neutrino analyses and some exotic searches, e.g. search for neutrinos from WIMPs in the Earth's core [105]. Therefore, they must be minimized in the final sample.

They typically have a reconstructed vertex on the ID wall, *dwall* ~ 0 cm, but some of them are reconstructed inside the fiducial volume due to the limited vertex reconstruction resolution, and more of them were anticipated to exist in the region closer to the ID wall. Therefore, all events in the final sample with *dwall* greater than 50 cm were eye-scanned to evaluate the background contamination level around the fiducial volume boundary using a graphical event display as shown in Figures 5.1, 5.2, or 5.14. No events are rejected based on the scanning results. The remaining background distribution as a function of *dwall* is shown in Fig. 5.26. As predicted, more backgrounds have been found in the region closer to the ID wall. The fraction of the non-neutrino backgrounds to the total number of events in the final sample is about 0.5% (0.1%) in the additional (conventional) fiducial mass region, and it is tolerably worse than that in the conventional fiducial mass region. However, in the region between *dwall* of 50 cm and 100 cm, it increases to about 2.0% and restricts further expansion of the fiducial mass. The main component of the remaining non-neutrino backgrounds is flasher event that occurred during detector initial phases. When a flashing PMT is identified in daily event reduction processes, its HV is turned off and such flasher event rate decreases over time.

Events in the final sample are divided into the following sub-samples in SK standard analyses:

Table 5.2: Atmospheric neutrino and proton decay event selection efficiencies at each reduction step in units of % and the number of events in the final sample in SK-I to -IV. In the efficiency calculation, only events satisfying the final FC criteria presented in Section 5.7, NHITAC < 16, $E_{\rm vis} > 30$ MeV, and *dwall* > 100 cm, are considered for the numerator, while events which are satisfying NHITAC < 16 and $E_{\rm vis} > 30$ MeV and generated within the enlarged fiducial volume are used for the denominator. Atmospheric neutrino MC is normalized by livetime and includes reweighting to the latest SK oscillation fit result [64] described in Section 4.2.

Atmospheric neutrino MC

SK phase	SK-I	SK-II	SK-III	SK-IV
1st reduction	99.1	99.1	99.4	99.3
2nd reduction	99.0	99.0	99.4	99.3
3rd reduction	98.5	98.7	99.1	99.0
4th reduction	97.8	98.3	97.7	98.0
5th reduction	97.4	98.0	97.5	97.8

$p \to e^+\pi^0$ MC

SK phase	SK-I	SK-II	SK-III	SK-IV
1st reduction	99.3	99.3	99.6	99.6
2nd reduction	99.3	99.2	99.5	99.5
3rd reduction	99.0	98.9	99.1	99.2
4th reduction	98.7	98.6	97.2	97.6
5th reduction	97.7	97.9	96.2	96.9

$p \to \mu^+\pi^0$ MC

SK phase	SK-I	SK-II	SK-III	SK-IV
1st reduction	99.5	99.4	99.6	99.5
2nd reduction	99.5	99.3	99.6	99.5
3rd reduction	99.2	99.1	99.4	99.3
4th reduction	98.9	98.9	98.8	98.8
5th reduction	98.5	98.6	98.4	98.6

Number of events in the final sample

SK phase	SK-I	SK-II	SK-III	SK-IV
Data	14286	7740	5182	31317
Atmospheric neutrino MC	14164.7	7655.3	5035.2	30907.3

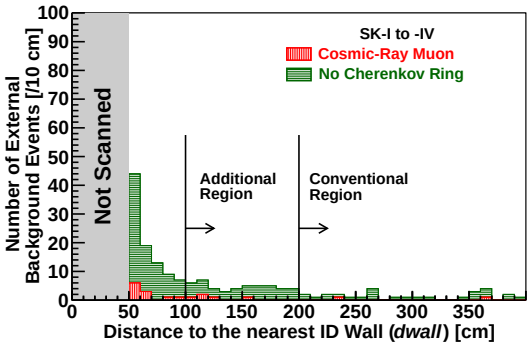

Figure 5.26: Remaining non-neutrino background distribution as a function of *dwall*. Cosmic-ray muons and no Cherenkov ring events are stacked. No Cherenkov ring events are dominated by flasher events described in the text.

- Sub-GeV single-ring e-like,
- Sub-GeV single-ring μ-like,
- Multi-GeV single-ring e-like,
- Multi-GeV single-ring μ-like,
- Multi-ring e-like,
- Multi-ring μ-like,

where Sub-GeV (Multi-GeV) stands for $E_{\rm vis}$ less (more) than 1.33 GeV, e-like (μ-like) stands for the reconstructed particle type of the most energetic particle is electron (muon). The "contamination rate" for each sub-sample is conservatively evaluated as follows:

$$\text{contamination rate} = \begin{cases} (N_{\rm non\nu BG} + \sqrt{N_{\rm non\nu BG}})/N_{\rm all}, & (N_{\rm non\nu BG} > 0) \\ 1/N_{\rm all}, & (N_{\rm non\nu BG} = 0) \end{cases} \tag{5.6}$$

where $N_{\rm non\nu BG}$ is the number of non-neutrino background events, and $N_{\rm all}$ is the total number of events in each sub-sample. The contamination rates in different fiducial volume boundary cases, *dwall* = 200, 100, and 50 cm for reference, are summarized in Table 5.3. In the case of the *dwall* boundary at 100 cm, they are kept within the consistent level with the conventional fiducial mass analysis for every detector phase and sub-sample. Therefore, in terms of the event quality, enlarging the fiducial mass up to 100 cm from the ID wall does not significantly deteriorate physics analyses in which this FC data set is used. The numbers in SK-IV are relatively small because of the stable data taking, longest live days, and reduced flasher event rate as described above.

Table 5.3: Non-neutrino background contamination rate in each sub-sample in units of %. Different *dwall* columns show the nun-neutrino background contamination rates in different fiducial volume boundary cases, i.e. numbers in the "*dwall* Boundary" column are evaluated using all events with *dwall* greater than 200, 100, or 50 cm.

		dwall Boundary		
Phase	Sub-sample	200 cm	100 cm	50 cm
SK-I	Sub-GeV single-ring e-like	0.1	0.2	0.2
	Sub-GeV single-ring μ-like	0.6	0.7	1.2
	Multi-GeV single-ring e-like	0.2	0.2	0.2
	Multi-GeV single-ring μ-like	0.1	0.1	0.5
	Multi-ring e-like	0.2	0.4	1.0
	Multi-ring μ-like	0.2	0.1	0.2
SK-II	Sub-GeV single-ring e-like	0.2	0.3	0.3
	Sub-GeV single-ring μ-like	0.3	0.4	0.4
	Multi-GeV single-ring e-like	0.3	0.2	0.2
	Multi-GeV single-ring μ-like	0.3	0.2	0.2
	Multi-ring e-like	0.4	0.4	2.8
	Multi-ring μ-like	0.3	0.5	1.4
SK-III	Sub-GeV single-ring e-like	0.2	0.4	0.5
	Sub-GeV single-ring μ-like	0.3	0.4	0.7
	Multi-GeV single-ring e-like	0.4	0.3	0.3
	Multi-GeV single-ring μ-like	0.4	0.7	1.1
	Multi-ring e-like	0.6	0.5	0.5
	Multi-ring μ-like	0.4	0.4	0.4
SK-IV	Sub-GeV single-ring e-like	< 0.1	< 0.1	< 0.1
	Sub-GeV single-ring μ-like	< 0.1	< 0.1	< 0.1
	Multi-GeV single-ring e-like	0.1	0.1	0.1
	Multi-GeV single-ring μ-like	0.1	0.1	0.1
	Multi-ring e-like	0.1	0.1	0.1
	Multi-ring μ-like	0.1	0.1	0.1

Chapter 6

Event Reconstruction

For events passing the FC event selection algorithm described in Chapter 5, charged particles above the Cherenkov threshold inside the ID are reconstructed with ID PMT timing and charge information to extract physics quantities, such as interaction (production) vertex position, number of Cherenkov rings (charged particles), particle type, and particle momentum. To tag neutrons emitted in a primary FC event, there is also an independent neutron tagging algorithm, which searches for a faint signature of 2.2 MeV gamma ray from neutron capture on hydrogen. In this Chapter, the FC event reconstruction algorithm and neutron tagging algorithm are described [108, 97, 106]. One of the most important reconstruction items in this study is the energy reconstruction, and the energy scale uncertainty is also discussed in this Chapter.

6.1 FC Event Reconstruction

The FC event reconstruction algorithm is divided into the following steps:

1. Vertex Reconstruction $\cdots$ The charged particle production vertex point is reconstructed mainly using PMT timing information.

2. Ring Counting $\cdots$ The number of Cherenkov rings projected on the ID wall is counted with a ring pattern recognition technique.

3. Particle Identification (PID) $\cdots$ Each Cherenkov ring is identified as either a showering (e-like) particle ($e^{\pm}$, γ) or non-showering (μ-like) particle ($\mu^{\pm}$, $\pi^{\pm}$) based on the pattern of PMT hits.

4. Precise Vertex Reconstruction $\cdots$ The event vertex position is redetermined using PMT charge information. This is applied only to single-ring events.

5. Ring Separation $\cdots$ For multi-ring events such as $p \to e^{+}\pi^{0}$ and $p \to \mu^{+}\pi^{0}$ signal events, the observed charge at each PMT is separated into the contribution from each Cherenkov ring.

6. Momentum Determination $\cdots$ Each ring momentum is determined using the total observed charge associated with the ring taking into account the water attenuation length, PMT acceptance as well as indirect light effects.

7. Ring Number Correction $\cdots$ If the momentum of one of the reconstructed rings is too small, or if the ring direction is too close to another, that ring is discarded as a fake ring.

8. Michel Electron Search $\cdots$ Clusters of PMT hits produced by subsequent Michel electrons from muon decays are searched for in the time-of-flight subtracted residual time distribution.

The algorithm proceeds step by step, and the later reconstruction steps use results obtained in the former steps.

6.1.1 Vertex Reconstruction

The vertex reconstruction algorithm consists of three steps, Point-fit, ring edge finding, and TDC-fit. Since this step is prior to the ring counting algorithm described later, the following calculation assumes a single-ring event and focuses on the most energetic ring.

Point-fit

An initial vertex position is estimated by maximizing the following estimator (G), assuming all photons are emitted at the same time and position:

$$G = \frac{1}{N}\sum_i \exp\left(-\frac{(t'_i - t_0)^2}{2\times(\langle\sigma\rangle\times 1.5)^2}\right), \tag{6.1}$$

where N is the number of hit PMTs, $\langle\sigma\rangle$ is fixed to 2.5 nsec here, and t'_i is the ith PMT's time-of-flight subtracted residual time for an assumed vertex position:

$$t'_i = t_i - \frac{n}{c}|\mathbf{P}_i - \mathbf{vtx}|, \tag{6.2}$$

where t_i is the ith PMT's photon detection time, $\mathbf{P}_i$ is the ith PMT position vector, and **vtx** is the vertex position vector. The factor of 1.5 in Eq. (6.1) has been determined to optimize performance, and t_0 is chosen so that G is maximized at each test vertex position. The vertex position is searched for by changing the assumed vertex position. The reconstructed vertex position in this step is the point with the highest G value, i.e. the residual time distribution becomes most peaked.

Using the reconstructed vertex position, the Cherenkov ring (particle) direction of the most energetic one is also estimated by taking the following vector sum:

$$\mathbf{dir} = \sum_i q_i^{\mathrm{obs}} \times \frac{\mathbf{P}_i - \mathbf{vtx}}{|\mathbf{P}_i - \mathbf{vtx}|}, \tag{6.3}$$

where **dir** is the ring direction vector, and q_i^{obs} is the ith PMT's observed charge.

Ring Edge Finding

The edge position (opening angle) and direction of the most energetic Cherenkov ring are redetermined using the following estimator, $Q(\theta_{\mathrm{edge}})$:

$$Q(\theta_{\mathrm{edge}}) = \frac{\int_0^{\theta_{\mathrm{edge}}} \mathrm{PE}^{\mathrm{cor}}(\theta)d\theta}{\sin\theta_{\mathrm{edge}}} \times \left(\frac{d\mathrm{PE}^{\mathrm{cor}}(\theta)}{d\theta}\bigg|_{\theta=\theta_{\mathrm{edge}}}\right)^2 \times \exp\left(-\frac{(\theta_{\mathrm{edge}} - \theta_{\mathrm{exp}})^2}{2\sigma_\theta^2}\right), \tag{6.4}$$

where θ_{edge} is the tested Cherenkov opening angle from the particle direction, and θ_{exp} and σ_θ are the expected Cherenkov opening angle and its resolution estimated by the total observed charge within a cone whose half opening angle is 70 degrees from the particle direction, respectively. Here, $\mathrm{PE}^{\mathrm{cor}}(\theta)$ is the observed charge distribution as a function of the angle from the particle direction, where the observed charge is corrected with the water attenuation length and PMT acceptance. A typical corrected charge distribution, $\mathrm{PE}^{\mathrm{cor}}(\theta)$, is shown in Fig. 6.1. The ring direction of the most energetic Cherenkov ring is reconstructed by searching for the direction which gives the highest $Q(\theta_{\mathrm{edge}})$.

Using the reconstructed ring direction, the ring edge (Cherenkov opening) angle of the ring (θ_{edge}) which satisfies the following conditions is determined:

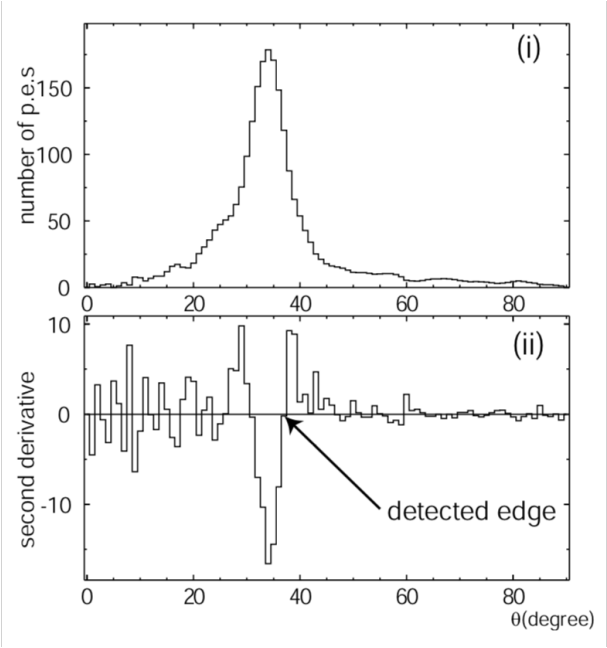

Figure 6.1: Typical observed charge distribution as a function of the opening angle (top), $\mathrm{PE}^{\mathrm{cor}}(\theta)$. The bottom plot is the second derivative distribution of the top plot. Taken from [108].

1. $\theta_{\mathrm{edge}} > \theta_{\mathrm{peak}}$,
2. $\left.\frac{d^2\mathrm{PE}^{\mathrm{cor}}}{d\theta^2}\right|_{\theta=\theta_{\mathrm{edge}}} = 0$,

where θ_{peak} is the peak position of the $\mathrm{PE}^{\mathrm{cor}}(\theta)$ distribution. If multiple angles satisfy the above conditions, the angle closest to the peak angle (θ_{peak}) is chosen. Some PMTs around the edge position are tagged, and they are used in the following TDC-fit step.

For events with *dwall* less than 400 cm, the opening angle and direction of the most energetic Cherenkov ring are determined using the same algorithm for particle identification described in Section 6.1.3. In the calculation for particle identification, the ring direction and Cherenkov opening are optimized using observed charge information.

TDC-fit

In TDC-fit, the track length of the particle and effects from scattered photons are taken into account.

First, the most energetic ring direction is tuned using the tagged PMTs, which are defined at the last step, so that the following estimator ($\chi(\mathbf{dir})$) is minimized:

$$\chi(\mathbf{dir}) = \sum_i \sqrt{q_i^{\mathrm{obs}}} \times \frac{(\theta_i - \langle\theta\rangle)^2}{(70\ \mathrm{cm}/|\mathbf{P}_i - \mathbf{vtx}|)^2}, \tag{6.5}$$

where q_i^{obs} is the ith tagged PMT's observed charge, θ_i is the opening angle of the ith tagged PMT position from an assumed ring direction, $\langle\theta\rangle$ is the average of θ_i for the tagged PMTs, and 70 cm corresponds to the size of the gaps between individual ID PMTs. The summation is performed for all of the tagged PMTs, and the ring direction which gives the minimum $\chi(\mathbf{dir})$ is used in the later steps. At the same time, the Cherenkov opening angle (θ_C) is determined as follows:

$$\theta_C = \langle\theta\rangle, \tag{6.6}$$

with the determined ring direction.

The total track length of the particle is estimated with the total observed charge within a cone whose half opening angle is 70 degrees from the particle direction and an assumed particle energy loss, $dE/dx = 3$ MeV/cm. This value is chosen to optimize performance. Time-of-flight subtracted residual time for PMTs located inside the reconstructed Cherenkov edge is recalculated as follows:

$$t'_i = t_i - \frac{1}{c} \times \left| \mathbf{X}_i - \mathbf{vtx} \right| - \frac{n}{c} \times \left| \mathbf{P}_i - \mathbf{vtx} \right|, \tag{6.7}$$

where $\mathbf{X}_i$ is the position where Cherenkov photons detected by the ith PMT are emitted, and it is deduced with the total track length, ring direction, and Cherenkov opening angle.

In TDC-fit, a vertex fitting estimator, *agood*, is calculated for PMTs inside the Cherenkov edge and for those outside separately. For PMTs inside the Cherenkov edge, the estimator (G_I) is defined as follows:

$$G_I = \sum_i \frac{1}{\sigma^2(q_i^{\rm obs})} \exp\left(-\frac{(t'_i - t_0)^2}{2 \times (\langle \sigma' \rangle \times 1.5)^2} \right), \tag{6.8}$$

where $\sigma(q_i^{\rm obs})$ is the ith PMT timing resolution which is tabulated as a function of observed charge, $\langle \sigma' \rangle$ is the average timing resolution for hit PMTs. For PMTs outside the Cherenkov edge, t_0 is modified to take into account the late timing PMT hits:

$$t'_0 = t_0 + \sigma_i \times (0.8 - 1.5 \times R_{\rm out}), \tag{6.9}$$

where the factors of 0.8 and 1.5 have been empirically determined, and $R_{\rm out}$ is the fractional charge outside the Cherenkov edge,

$$R_{\rm out} = 1 - \frac{\sum_{\theta < \theta_C + 3} q_i^{\rm obs}}{\sum_{\theta < 70^\circ} q_i^{\rm obs}}. \tag{6.10}$$

For PMTs outside the Cherenkov edge with $t'_i < t'_0$, the fitting estimator (G_{O1}) is revised as:

$$G_{O1} = \sum_i \frac{1}{\sigma^2(q_i^{\rm obs})} \left(2 \times \exp\left(-\frac{(t'_i - t'_0)^2}{2 \times (\langle \sigma' \rangle \times 1.5)^2} \right) - 1 \right), \tag{6.11}$$

and for PMTs outside the Cherenkov edge with $t'_i > t'_0$, the fitting estimator (G_{O2}) is corrected to consider effects from scattered photons:

$$G_{O2} = \sum_i \frac{1}{\sigma^2(q_i^{\rm obs})} \left(2 \times \max\left(G_{O1}, C_A \times G_{O1} + C_B \times \exp\left(-\frac{(t'_i - t'_0)}{60 \text{ nsec}} \right) \right) - 1 \right), \tag{6.12}$$

$$C_A = 1 - C_B, \tag{6.13}$$

$$C_B = (0.8 - 1.5 \times R_{\rm out}) + (0.2 + 1.5 \times R_{\rm out}) \times (1 - 1/1.5^2). \tag{6.14}$$

Finally, *agood* is defined by summing up these three estimators:

$$agood = \frac{G_I + G_{O1} + G_{O2}}{\sum_i 1/\sigma^2(q_i^{\rm obs})}. \tag{6.15}$$

At each tested vertex position, t_0 is chosen so that *agood* becomes maximal, and the reconstructed vertex position is the point with the highest *agood*. The vertex position reconstructed here is used for multi-ring events but for single-ring events, the vertex position is redetermined at the later step, Section 6.1.4.

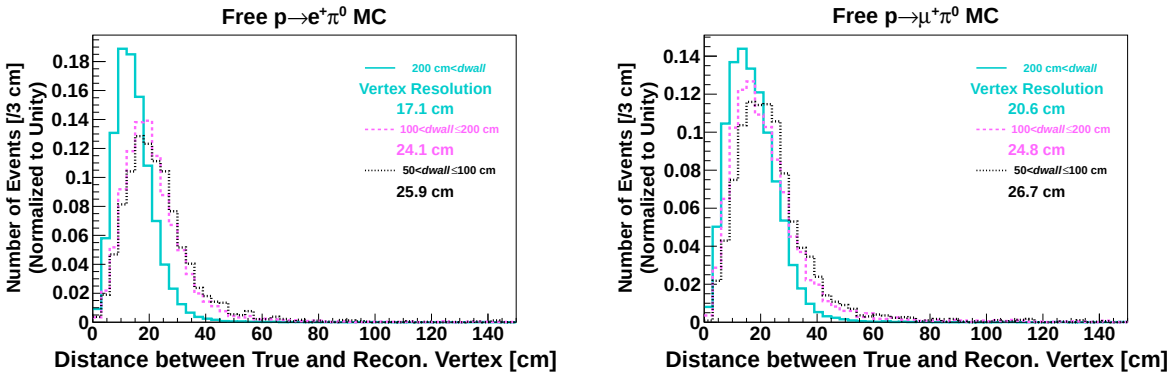

Figure 6.2: Distributions of the distance between the reconstructed vertex and true vertex position on free proton decay MC events. The left plot shows $p \to e^+\pi^0$ and the right shows $p \to \mu^+\pi^0$ MC events, and they are livetime-weighted combined from SK-I to -IV. The solid cyan histogram shows events reconstructed in the conventional fiducial mass region, the pink dashed histogram shows that for the additional fiducial mass region, and the black dotted histogram is for the region between *dwall* of 50 cm and 100 cm. Vertex resolution indicates 68 percentile.

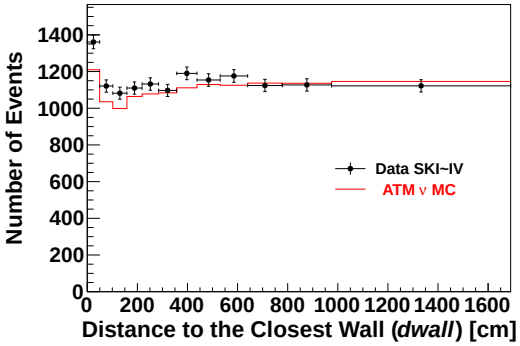

Figure 6.3: Reconstructed *dwall* distribution of Sub-GeV multi-ring events in SK-I to -IV. The black dots show the data and the red histogram shows the atmospheric neutrino MC (ATM ν MC) events. Atmospheric neutrino MC is normalized by livetime and includes reweighting to the latest SK oscillation fit [64]. Vertical error bars denote the statistical uncertainty.

Performance of Vertex Reconstruction

Figure 6.2 shows the distributions of the distance between the reconstructed vertex and true vertex position on free proton decay MC events. Only free proton decay events are used to remove the influence of nuclear effects. In the additional fiducial mass region, the number of PMT hits tends to be smaller when the charged particle travels toward the ID wall. In $p \to e^+\pi^0$ and $p \to \mu^+\pi^0$ decay events in which they produce back-to-back event topologies, at least one of the particles in the final state often has a small distance to the wall, and the number of PMT hits associated with its Cherenkov ring also becomes small. Since the vertex reconstruction performance depends on the number of hit PMTs associated with the most energetic ring, the performance is degraded outside the conventional fiducial mass region when the most energetic ring travels toward the wall. The vertex resolution for the $p \to e^+\pi^0$ ($p \to \mu^+\pi^0$) mode is 17.1 cm (20.6 cm) in the conventional fiducial mass region, and it is 24.1 cm (24.8 cm) in the additional fiducial mass region. Figure 6.3 shows the distributions of the distance between the reconstructed vertex and the closest ID wall (*dwall*) of Sub-GeV multi-ring events for data and atmospheric neutrino MC events.

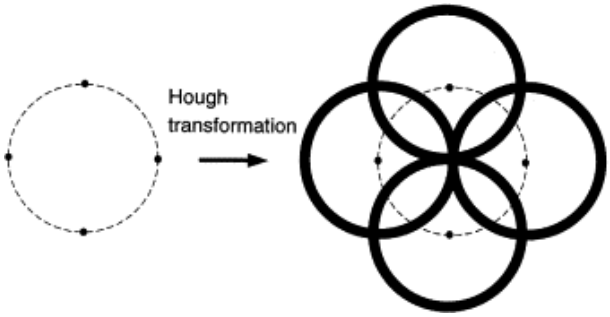

Figure 6.4: The Hough transformation. Suppose there are four hit PMTs on in a ring with a radius of r (left). The observed charge is transformed into the Hough space as a circle with a radius of r (right), and the resulting circles are overlapped at the center of the original ring, i.e. the original ring center manifests as a peak in the Hough space. Taken from [108].

6.1.2 Ring Counting

After reconstructing the vertex position with the most energetic ring, the total number of Cherenkov rings projected on the ID wall is counted. This process is divided into two steps, ring candidate selection and ring candidate test using a likelihood method.

Ring Candidate Selection

Cherenkov rings other than the one used for the previous vertex estimation are searched for using a ring pattern recognition algorithm based on the Hough transformation [109]. The principle of the Hough transformation is illustrated in Fig. 6.4. Suppose there are four hit PMTs in a ring with a radius of r as shown in the left figure, each PMT's observed charge is transformed into the Hough space as a circle with a radius of r. The amplitude of the circle in the Hough space is weighted by the observed charge which is corrected with the water attenuation length and PMT acceptance. The resulting circles in the Hough space are overlapped at the center of the original ring as shown in the right figure, and the original ring center manifests as a peak in the Hough space. Before this transformation, contributions from other Cherenkov rings, which are already identified, are subtracted to make the algorithm find a potential ring more easily.

The Hough space is defined as two-dimensional polar coordinates (Θ, Φ), which are calculated from the reconstructed vertex position. An actual Cherenkov image does not have sharp ring edges as shown in Fig. 6.4, and therefore a charge distribution template as a function of opening angle, which has been obtained using 500 MeV/c electron MC events in advance, is used as a weight in the transformation to diffuse the resulting circle edges in the Hough space. An example of the resulting Hough space is shown in Fig. 6.5, and peaks are identified as Cherenkov ring candidates. However, if the direction of the ring candidate is too close (less than 15 degrees) to another ring, which is already identified, that ring is not selected.

Ring Candidate Test

The ring candidates identified in the previous candidate selection are tested if they are real Cherenkov rings or not using a likelihood method. Given that N rings are already identified as real Cherenkov rings, and there is an $(N+1)$th ring candidate, the following likelihood for

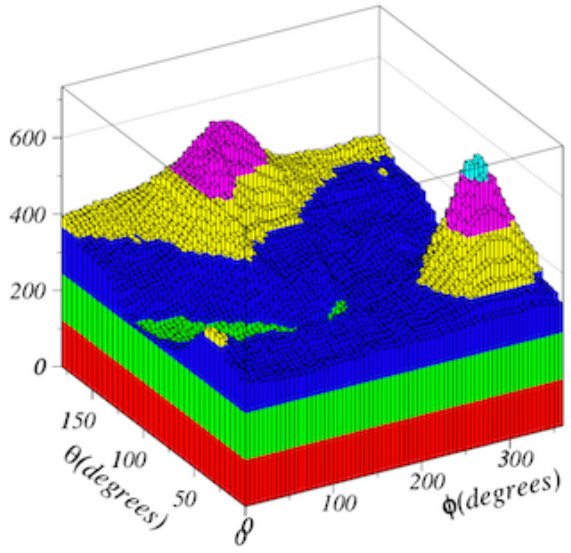

Figure 6.5: Example of the resulting Hough space for a two-ring event. The peaks correspond to their Cherenkov ring centers. Taken from [108].

either the $(N+1)$ ring or N ring assumption is defined:

$$L^{N+1} = \sum_{i}^{\exists n \in N+1, \theta_{i,n} < 1.2 \times \theta_{C,n}} \log\left(P\left(q_i^{\text{obs}}, \sum_{n}^{N+1} \alpha_n \times q_{i,n}^{\text{exp}}\right)\right) \tag{6.16}$$

$$L^{N} = \sum_{i}^{\exists n \in N+1, \theta_{i,n} < 1.2 \times \theta_{C,n}} \log\left(P\left(q_i^{\text{obs}}, \sum_{n}^{N} \alpha_n \times q_{i,n}^{\text{exp}}\right)\right) \tag{6.17}$$

where $\theta_{C,n}$ is the Cherenkov opening angle of the nth ring, $\alpha_n \times q_{i,n}^{\text{exp}}$ is the ith PMT expected charge given by the nth ring, and $P\left(q_i^{\text{obs}}, \sum_n^{N+1(N)} \alpha_n \times q_{i,n}^{\text{exp}}\right)$ is the probability density function of observing q_i^{obs} with an expectation of $\sum_n^{N+1(N)} \alpha_n \times q_{i,n}^{\text{exp}}$. The probability density function is tabulated based on the convolution of the single p.e. distribution and a Poisson distribution for the low charge region, and it is obtained from a Gaussian distribution for the high charge region. The summation is performed for all PMTs whose angle to the direction of one of the $(N+1)$ rings $(\theta_{i,n})$ is within 1.2 times its Cherenkov opening angle $(\theta_{C,n})$, and the same PMTs are used for both likelihoods. The expected charge given by the $(N+1)$th ring in each PMT, $\alpha_{N+1} \times q_{i,N+1}^{\text{exp}}$, is deduced by the total observed charge within a cone whose half opening angle is 70 degrees from the $(N+1)$th ring direction. The expected charge given by the other already identified N rings is obtained by the ring separation algorithm detailed in [108]. Both likelihoods are maximized by tuning α_n. For the $(N+1)$th ring candidate which satisfies $L^{N+1} \geq L^N$, the likelihood formula is modified by incorporating the following components:

- The average observed charge deposited around the edge of the $(N+1)$th ring candidate, Q_{edge}. If it is large, the $(N+1)$th ring candidate is regarded as a more probable ring candidate.
- The average observed charge deposited around outside the edge of the $(N+1)$th ring candidate. If it is smaller than Q_{edge}, the $(N+1)$th ring candidate is regarded as a more probable ring candidate.
- The residual observed charge, which is the sum of the observed charge associated with none of the identified N rings, in the N ring assumption. If it is large, the $(N+1)$th ring candidate is regarded as a more probable ring candidate.

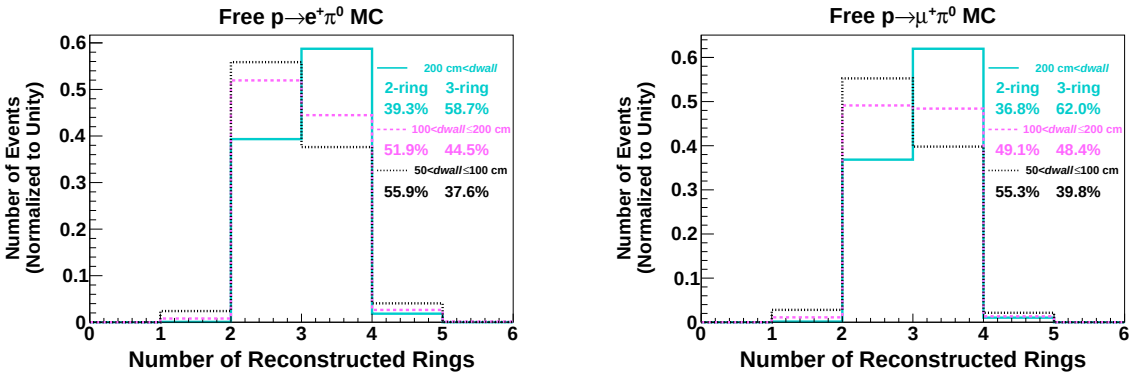

Figure 6.6: Distributions of the number of reconstructed rings of free proton decay MC events. The left plot shows $p \to e^+\pi^0$ and the right shows $p \to \mu^+\pi^0$ MC events, and they are livetime-weighted combined from SK-I to -IV. The solid cyan histogram shows events reconstructed in the conventional fiducial mass region, the pink dashed histogram shows that for the additional fiducial mass region, and the black dotted histogram is for the region between *dwall* of 50 cm and 100 cm.

Weights used to combine the above components into a final ring counting likelihood are optimized using atmospheric neutrino MC events.

Once the $(N+1)$th ring is judged as a real Cherenkov ring, the algorithm goes back to the ring candidate selection step to find another ring candidate. This procedure continues until no more candidates are found or the 5th ring is found.

Performance of Ring Counting

The distributions of the number of reconstructed rings of free proton decay MC events are shown in Fig. 6.6. Ideally, they should be reconstructed as three-ring events for both the $p \to e^+\pi^0$ and $p \to \mu^+\pi^0$ modes but a Cherenkov ring associated with one of the gamma rays from the π^0 decay sometimes overlaps with other rings, and thus such events are reconstructed as two-ring events. Although the full proton decay event selection criteria are discussed in Section 7.1.1, two-ring events are allowed as signal events. Besides, since hit PMTs in events in the additional fiducial mass region are more localized than those in the conventional fiducial mass region, the fraction of two-ring events becomes higher. Figures 6.7 and 6.8 show the distributions of the number of reconstructed rings and ring counting likelihood distributions, respectively, of Sub-GeV events for data and atmospheric neutrino MC events.

6.1.3 Particle Identification

The particle type of each identified Cherenkov ring is determined using the pattern of hit PMTs in the ring. As shown in Figures 3.9 and 3.10, the difference between showering (e-like) and non-showering (μ-like) particles manifests in their PMT hit (charge) profile. The following algorithm calculates the expected charge distribution for each particle assumption and compares it to the observed charge distribution. Therefore, the calculation of the expected PMT charge is essential. Furthermore, the reconstructed Cherenkov opening angle is also useful information to separate between the two particle types, especially in single-ring events.

Expected charge table for each particle type assumption

Expected charge distributions in the showering (electron) assumption have been tabulated using electron MC events. However, because some discrepancies between the old expected charge

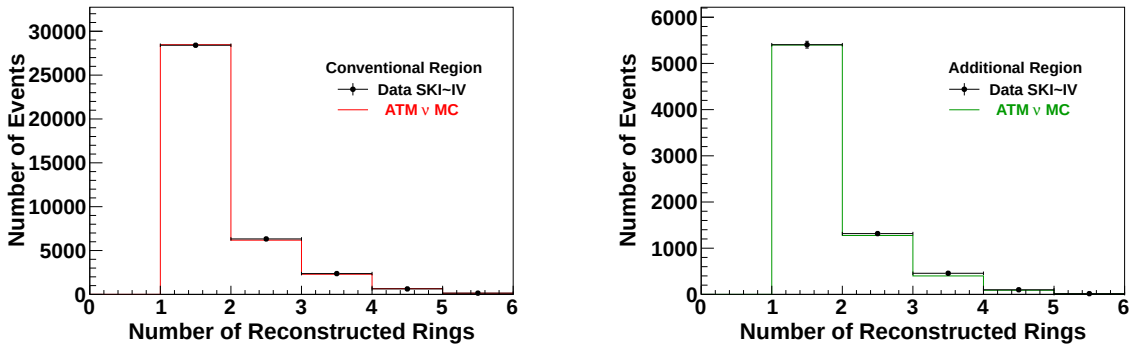

Figure 6.7: Distributions of the number of reconstructed rings of Sub-GeV events for data and atmospheric neutrino MC events (SK-I to -IV combined). The left plot corresponds to the conventional fiducial mass region and the right plot to the additional fiducial mass region. Atmospheric neutrino MC is normalized by livetime and includes reweighting to the latest SK oscillation fit [64]. Vertical error bars on the data points denote the statistical uncertainty.

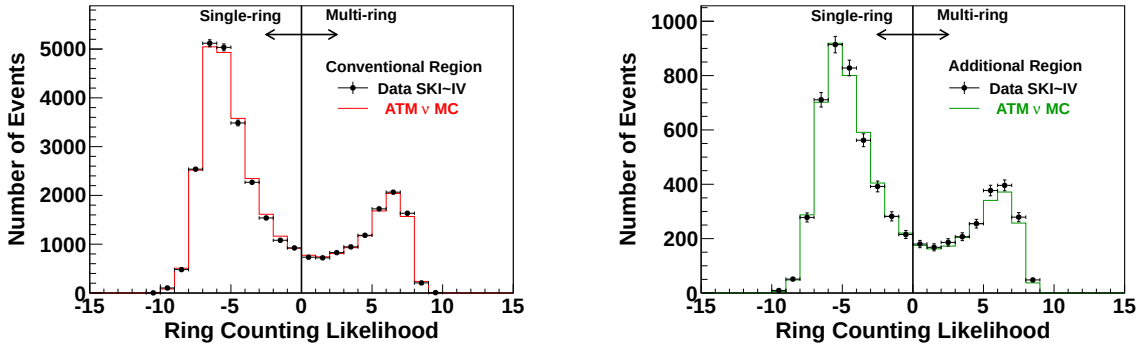

Figure 6.8: Ring counting likelihood distributions of Sub-GeV events for data and atmospheric neutrino MC events (SK-I to -IV combined). The left plot corresponds to the conventional fiducial mass region and the right plot to the additional fiducial mass region. Atmospheric neutrino MC is normalized by livetime and includes reweighting to the latest SK oscillation fit [64]. Vertical error bars on the data points denote the statistical uncertainty.

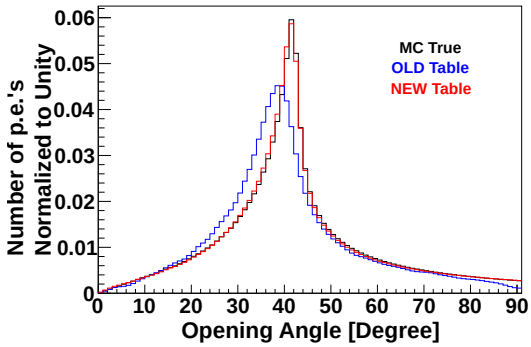

Figure 6.9: PMT charge distributions as a function of the opening angle from the electron direction. The Black histogram shows MC truth observed charge distribution, and the blue (red) histogram shows the expected charge distribution before (after) the update described in the text.

tables and MC expectations have been found, new expected charge tables have been made using the latest detector simulation (SKDETSIM) and introduced in this work. Electron particle gun MC events with a momentum of 30, 100, 200, 300, 500, 700, 1000, 1500, 2000, 5000, 10000 MeV/c have been generated. In the generation, effects from water scattering and absorption were turned off. The new expected charge distributions, $Q^{\rm exp}(p,\theta,r)$, are tabulated as a function of particle momentum (p), the distance between the event vertex and PMT position (r), and the opening angle from the particle direction (θ). Necessary linear interpolations and extrapolations were made to cover the entire electron event phase space. Using them, the expected charge given by the nth ring at the ith PMT, $q_{i,n}^{\rm direct}(e)$, is calculated as follows to correct with the water attenuation length and PMT acceptance:

$$q_{i,n}^{\rm direct}(e) = \alpha_n(e) \times Q^{\rm exp}(p_n, \theta_{i,n}, r_i) \times \exp\left(-\frac{r_i}{L}\right) \times f(\Theta_i), \tag{6.18}$$

where $\alpha_n(e)$ is the normalization factor, p_n is the nth ring momentum deduced from the total observed charge in the nth ring, $\theta_{i,n}$ is the opening angle to the ith PMT position from the nth ring particle direction, r_i is the distance between the event vertex and ith PMT position, L is the water attenuation length introduced in Section 3.3.6, and $f(\Theta_i)$ is the PMT acceptance correction factor as a function of photon incident angle (Θ_i). Figure 6.9 compares the obtained $q_{i,n}^{\rm direct}(e)$ distributions as a function of opening angle with the updated $Q^{\rm exp}(p_n, \theta_{i,n}, r_i)$ and the old one for 500 MeV/c electron events. The MC output is also shown, and the updated expected charge distribution well reproduces the MC expectation. The impacts of this update are discussed later in this section.

On the other hand, the expected charge given by the nth ring at the ith PMT for the muon assumption, $q_{i,n}^{\rm direct}(\mu)$, is analytically calculated as:

$$q_{i,n}^{\rm direct}(\mu) = \left(\alpha_n(\mu) \times \left(r_i \times \left(\sin\theta_{x_{i,n}} + r_i \times \frac{d\theta}{dx}\bigg|_{x=x_{i,n}}\right)\right)^{-1} \times \sin^2\theta_{x_{i,n}}\right) \times \exp\left(-\frac{r_i}{L}\right) \times f(\Theta_i), \tag{6.19}$$

where $\alpha_n(\mu)$ is the normalization factor, x is the distance between the event vertex and particle position on its track, $x_{i,n}$ is the distance between the event vertex and point where Cherenkov photons to the ith PMT from the nth ring are emitted, $\theta_{x_{i,n}}$ is the opening angle from the nth ring direction at $x = x_{i,n}$. The change of $\theta_{x_{i,n}}$ on its track due to the particle energy loss is taken into account. The factor of $\sin^2\theta_{x_{i,n}}$ corresponds to the number of emitted Cherenkov photons

between x and $x+dx$, and the factor of $\left(r_i \times \left(\sin\theta_{x_{i,n}} + r_i \times \frac{d\theta}{dx}\Big|_{x=x_{i,n}}\right)\right)$ corresponds to the cross-section to which they are emitted.

In this algorithm, direct photons and indirect (scattered and reflected) photons are separately treated. They are separated using ith PMT's time-of-flight subtracted time, t'_i:

$$\text{direct photons} \cdots -30 < t'_i - t_0 < 2\sigma_i(q_i^{\text{obs}}) + 5 \text{ nsec}, \tag{6.20}$$

$$\text{indirect photons} \cdots 2\sigma_i(q_i^{\text{obs}}) + 5 \text{ nsec} < t'_i - t_0, \tag{6.21}$$

where t_0 is the peak of the time-of-flight subtracted time distribution. Then, the expected charge at each PMT, $q_{i,n}^{\text{exp}}(e,\mu)$, is revised:

$$q_{i,n}^{\text{exp}}(e,\mu) = q_{i,n}^{\text{direct}}(e,\mu) + q_{i,n}^{\text{indirect}}, \tag{6.22}$$

where $q_{i,n}^{\text{indirect}}$ is the indirect light (scattered and reflected photons) contribution at the ith PMT from the nth ring and is deduced from the total observed charge in the nth ring with an assumption that scattered photons and reflected photons are distributed isotropically from the scattered and reflected points, respectively. Photon scattering points are estimated using the water attenuation length and scattering coefficients described in Section 3.3.6, while photon reflection points are assumed to be on the PMT surfaces.

Particle Identification Likelihood

The following likelihood, L_n, is defined to determine the particle type of the nth ring:

$$L_n(e,\mu) = \begin{cases} \Pi_{\theta_{i,n}<1.5\times\theta_{C,n}} P\left(q_i^{\text{obs}}, q_{i,n}^{\text{exp}}(e,\mu) + \sum_{n'\neq n} q_{i,n'}^{\text{exp}}\right), \text{ (direct photons)} \\ \Pi_{\theta_{i,n}<1.5\times\theta_{C,n}} P\left(0, \left(q_{i,n}^{\text{exp}}(e,\mu) + \sum_{n'\neq n} q_{i,n'}^{\text{exp}} - q_i^{\text{obs}}\right) + \left(q_{i,n}^{\text{obs}} - q_{i,n}^{\text{indirect}}\right)\right) \\ \quad \times P\left(q_i^{\text{obs}}, q_{i,n}^{\text{indirect}} + q_i^{\text{obs}} - q_{i,n}^{\text{obs}}\right), \text{ (indirect photons)} \end{cases} \tag{6.23}$$

where $\left(\sum_{n'\neq n} q_{i,n'}^{\text{exp}}\right)$ is the expected contributions from other rings (except for the nth ring), $P(q_i^{\text{obs}}, q_i^{\text{exp}})$ is the probability density function of observing q_i^{obs} with an expectation of q_i^{exp}, and $q_{i,n}^{\text{obs}}$ is the separated observed charge at the ith PMT from the nth ring. The product is performed for all PMTs whose angle from the nth ring direction ($\theta_{i,n}$) is within 1.5 times the Cherenkov opening angle of the nth ring ($\theta_{C,n}$). In each assumption, $L_n(e,\mu)$ is maximized by changing the nth ring direction and Cherenkov opening angle. For multi-ring events, such as those from $p \to e^+\pi^0$ and $p \to \mu^+\pi^0$ decays, the difference in the two likelihood values, $\sqrt{-\log_{10} L_n(e)} - \sqrt{-\log_{10} L_n(\mu)}$, is defined as "PID Likelihood" and used for particle identification. The optimized ring directions and opening angles in this step are also used in the analysis.

In order to combine with another likelihood evaluated with the Cherenkov opening angle, $L_n(e,\mu)$ is transformed into a χ^2 parameter:

$$\chi_n^2(e,\mu) = (-\log_{10} L_n(e,\mu)) + \text{const.}. \tag{6.24}$$

The probability from the PMT hit pattern, $P_n^{\text{pattern}}(e,\mu)$, is defined as:

$$P_n^{\text{pattern}}(e,\mu) = \text{const.} \times \left(-\frac{1}{2}\left(\frac{\chi_n^2(e,\mu) - \min(\chi_n^2(e), \chi_n^2(\mu))}{\sqrt{2N_n}}\right)^2\right), \tag{6.25}$$

where N_n is the number of PMTs used in Eq. (6.23).

The probability from the Cherenkov opening angle, $P_n^{\rm angle}(e,\mu)$, is defined as:

$$P_n^{\rm angle}(e,\mu) = \text{const.} \times \left(-\frac{1}{2} \left(\frac{\theta_{C,n}(e,\mu) - \theta_n^{\rm exp}(e,\mu))}{\sigma_\theta^2} \right)^2 \right), \tag{6.26}$$

where $\theta_{C,n}(e,\mu)$ is the optimized Cherenkov opening angle in each assumption, σ_θ is its uncertainty, and $\theta_n^{\rm exp}(e,\mu)$ is the expected opening angle estimated from the total observed charge in the nth ring. Finally, the two probabilities are combined as follows:

$$P_n^{\rm total}(e,\mu) = P_n^{\rm pattern}(e,\mu) + P_n^{\rm angle}(e,\mu). \tag{6.27}$$

For single-ring events, the difference in the total probability in each assumption, $\sqrt{-\log P_n^{\rm total}(e)} - \sqrt{-\log P_n^{\rm total}(\mu)}$, is used for particle identification. However, because of the gamma ray conversion length, about 50 cm in water, including $P_n^{\rm angle}(e,\mu)$ degrades the performance of the Cherenkov opening angle reconstruction in $p \to e^+\pi^0$ and $p \to \mu^+\pi^0$ signal events, resulting in the worse PID capability. Therefore, only the probability from the PMT hit pattern is used in this analysis as described above.

Performance of Particle Identification

Figure 6.10 shows the multi-ring PID likelihood distributions of free $p \to e^+\pi^0$ decay events in both the conventional and additional fiducial mass regions. From the 1st to 3rd ring, each PID distribution is shown. In every distribution, more rings are correctly reconstructed as e-like after introducing the update of the expected charge calculation. Since the number of hit PMTs tends to be smaller in the additional fiducial mass region, giving a more precise expected charge to each PMT is more important. Therefore, the update results in a more significant improvement in the additional fiducial mass region than in the conventional fiducial mass region. The signal selection efficiencies for $p \to e^+\pi^0$ and $p \to \mu^+\pi^0$ events are improved by about 20% in the additional fiducial mass region compared to the previous reconstruction version. After adopting the update, the correct PID fraction of events which pass one of the proton decay signal criteria associated with PID out of all two- and three-ring events is 95.8% (87.7%) for $p \to e^+\pi^0$ and 96.2% (90.7%) for $p \to \mu^+\pi^0$ in the conventional (additional) region.

Figure 6.11 shows the mis-PID rate as a function of particle momentum for single-ring events. They are estimated with electron and muon particle gun MC events. For single-ring events, the mis-PID rates are reduced by 35% in the additional fiducial mass region by adopting the update.

The data and MC comparison for Sub-GeV multi-ring events is shown in Figure 6.12.

6.1.4 Precise Vertex Reconstruction

Using not only timing information but also charge information, the precise vertex reconstruction algorithm improves the vertex reconstruction performance only for single-ring events. In this step, the Cherenkov opening angle and particle type determined in the former step are used.

First, the vertex position is scanned so that the estimator defined in Eq. (6.15) is maximized. Here, the scanning direction is limited to the perpendicular direction to the ring direction. Then, the vertex position along the ring direction is searched for by maximizing the pattern PID estimator of the identified particle type assumption, Eq. (6.23). At the end of this step, the ring direction is also redetermined using the vertex position fixed in this step by maximizing the same estimator again, Eq. (6.23).

6.1.5 Ring Separation

Since a PMT detects the total number of photoelectrons from all Cherenkov rings observed in the ID, it needs to be separated into the contribution from each ring. In order to determine

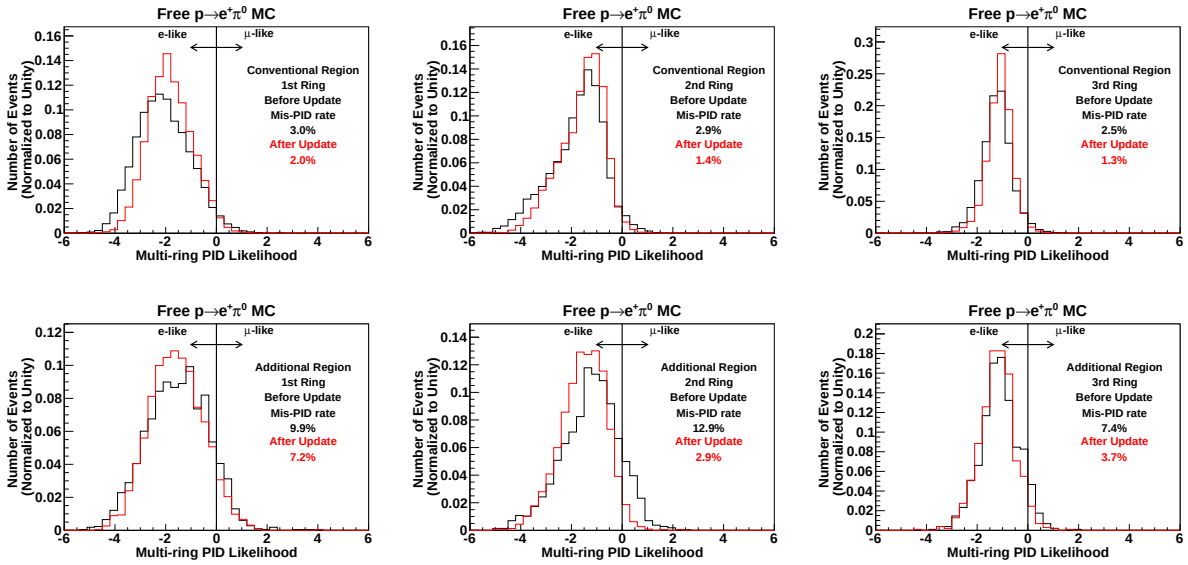

Figure 6.10: Multi-ring PID likelihood distributions of free $p \to e^+\pi^0$ decay events. The top three plots correspond to the conventional and the bottom three plots correspond to the additional fiducial mass region. The black (red) distributions are before (after) the expected charge table update described in the text. Here, Mis-PID rate indicates the fraction of Cherenkov rings which are reconstructed as μ-like. From left to right, the 1st to 3rd ring distributions are shown.

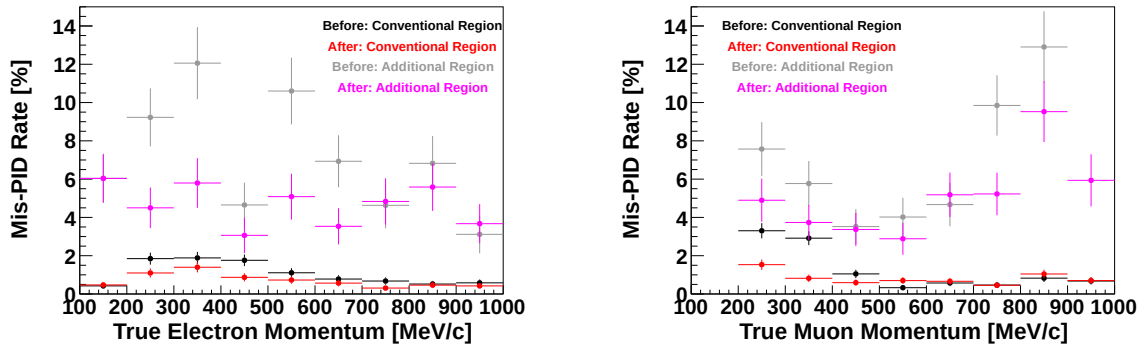

Figure 6.11: Mis-PID rate as a function of true particle momentum for single-ring events. The left plot shows the electron case and the right plot shows the muon case. Black and gray (red and magenta) points denote before (after) the updated of the expected charge table update described in the text. Vertical error bars denote the MC statistical uncertainty.

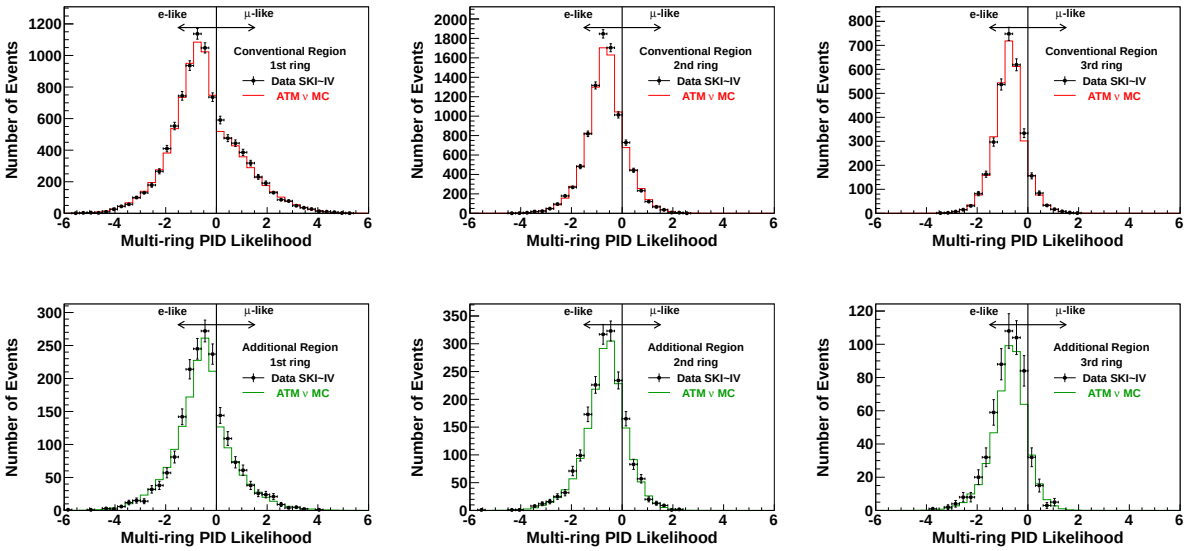

Figure 6.12: Multi-ring PID likelihood distributions of Sub-GeV multi-ring events for data and atmospheric neutrino MC events (SK-I to -IV combined). The top three plots correspond to the conventional and the bottom three plots correspond to the additional fiducial mass region. The black dots show the data and the red and green histograms show the atmospheric neutrino MC events. Atmospheric neutrino MC is normalized by livetime and includes reweighting to the latest SK oscillation fit [64]. From left to right, the 1st to 3rd ring distributions are shown. Vertical error bars denote the statistical uncertainty.

each ring's momentum in multi-ring events, this procedure is necessary. The separation of the observed charge is done using the expected charge distribution. The calculation of the expected charge for each PMT is almost the same as Equations (6.18) and (6.19). This calculation is done based on the identified particle type. Indirect light contributions, such as scattered and reflected photons, are also taken into account.

The following likelihood, L_n, is defined:

$$L_n = \sum_{\theta_{i,n}<70^\circ} \log\left(P\left(q_i^{\rm obs}, \sum_{n'} \alpha_{n'} \times q_{i,n'}^{\rm exp}\right)\right), \tag{6.28}$$

where $\alpha_{n'}$ is the normalization factor to be optimized, and $\alpha_{n'} \times q_{i,n'}^{\rm exp}$ is the expected charge given by the n'th ring at the ith PMT. The summation is performed for all PMTs inside the 70 degree half opening angle cone from the nth ring direction. The optimal $\alpha_{n'}$'s are searched for by maximizing L_n.

Then, the observed charge contribution from the nth ring at the ith PMT ($q_{i,n}^{\rm obs}$) is calculated as:

$$q_{i,n}^{\rm obs} = q_i^{\rm obs} \times \frac{\alpha_n \times q_{i,n}^{\rm exp}}{\sum_{n'} \alpha_{n'} \times q_{i,n'}^{\rm exp}}, \tag{6.29}$$

where $\alpha_{n'}$'s are optimized ones in the former likelihood calculation. This ring separation algorithm is also processed before identifying the particle types of the rings, such as in the ring counting and particle identification algorithms. In such cases, all rings are assumed to be e-like particles and the algorithm separates the observed charge at each PMT in a similar manner [108].

Figure 6.13 shows a two-ring event's event display. From left to right, the original event display, the separated first ring, and the second ring are shown as a result of the ring separation algorithm.

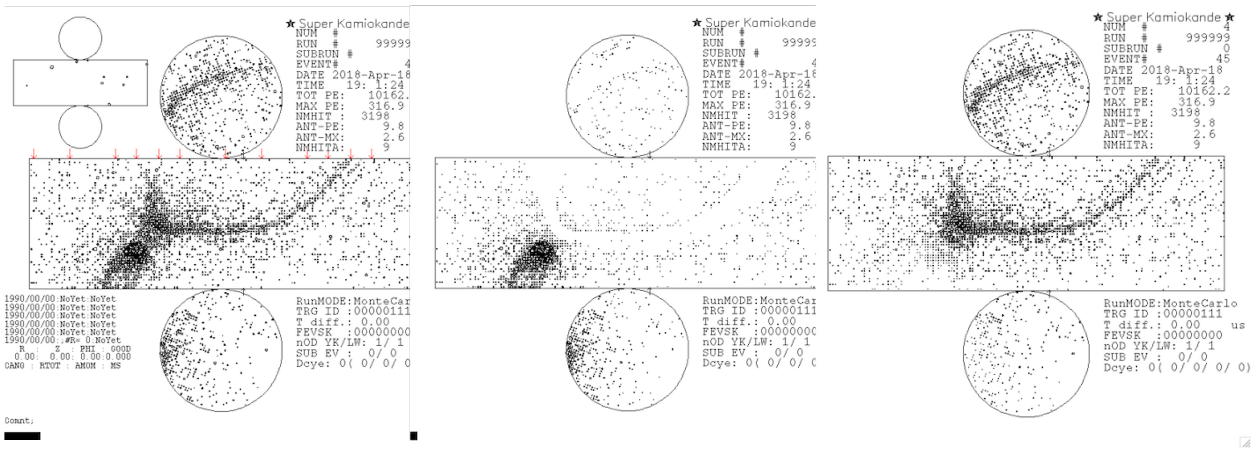

Figure 6.13: Event display of a two-ring event. The left one shows the original event display. The middle and right one show the separated first and second ring, respectively, after applying the ring separation algorithm.

6.1.6 Momentum Determination

The momentum of each Cherenkov ring is calculated with the total observed charge within a cone whose half opening angle is 70 degrees from the ring direction. When summing up the observed charge inside the cone, the following correction is applied to convert it to $RTOT_n$ taking into account effects from water scattering, absorption, PMT acceptance as well as reflected photons:

$$RTOT_n = \frac{G^{\mathrm{MC}}}{G^{\mathrm{data}}} \left(\alpha \times \sum_{\theta_{i,n}<70^\circ, t_1<t_i<t_2} \left(q_{i,n}^{\mathrm{obs}} \times \exp\left(\frac{r_i}{L}\right) \times \frac{\cos\Theta_i}{f(\Theta_i)} \right) - \sum_{\theta_{i,n}<70^\circ} (S_i + R_i) \right), \tag{6.30}$$

where G^{MC} is the gain factor in MC, G^{data} is the gain factor in data including its evolution over time discussed in Section 3.3.3, α is the normalization factor, $q_{i,n}^{\mathrm{obs}}$ is the observed charge at the ith PMT from the nth ring, r_i is the distance between the event vertex and ith PMT position, L is the water attenuation length discussed in Section 3.3.6, $\cos\Theta_i$ is the PMT density correction factor, $f(\Theta_i)$ is the PMT acceptance correction factor, and S_i and R_i are the contributions from scattered photons and reflected photons, respectively. The timing range (t_1, t_2) starts from $t_0 - 50$ nsec ($= t_1$) and ends at $t_0 + 250$ nsec ($= t_2$), where t_0 is the peak of the time-of-flight subtracted timing distribution. The relation between $RTOT_n$ and particle momentum has been tabulated in advance using MC for both the electron and muon assumptions, and the ring momentum is determined using it.

In the proton decay event selection, the total (invariant) mass (M_{tot}) and total momentum of the multi-ring kinematics (P_{tot}) are used, and they are defined as:

$$P_{\mathrm{tot}} = \left| \sum_n \vec{p}_n \right|, \tag{6.31}$$

$$E_{\mathrm{tot}} = \sum_n \sqrt{|p_n|^2 + m_n^2}, \tag{6.32}$$

$$M_{\mathrm{tot}} = \sqrt{E_{\mathrm{tot}}^2 - P_{\mathrm{tot}}^2}, \tag{6.33}$$

where p_n is the nth ring momentum, m_n is the electron (muon) mass in case the nth ring is reconstructed as an e-like (μ-like) ring, and E_{tot} is the total deposited energy.

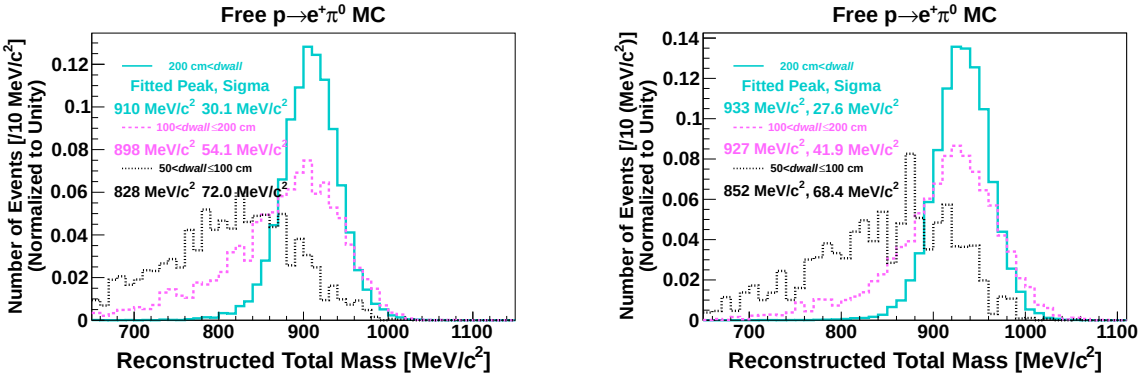

Figure 6.14: Reconstructed total mass distributions for free proton decays via $p \to e^+\pi^0$ MC events. The left (right) plot shows two-ring (three-ring) events. In each plot, the solid cyan histogram shows events reconstructed in the conventional fiducial mass region, the pink dashed histogram shows that for the additional fiducial mass region, and the black dotted histogram is for the region between *dwall* of 50 cm and 100 cm. The peak position and width of the distributions are obtained using Gaussian fits.

Performance of Momentum Reconstruction

The reconstructed total mass distributions of free proton decay MC events are shown in Figures 6.14 and 6.15. The distributions outside the conventional fiducial mass region have longer tails in the low mass region. This is because of the worse momentum resolution resulting from the lower number of hit PMTs in events occurring closer to the wall. Furthermore, particles generated in the region closer to the wall more often escape the ID and disable us to fully reconstruct their momenta. The data and MC agreement on the momentum reconstruction, the energy scale uncertainty, is discussed in Section 6.2.

6.1.7 Ring Number Correction

In this step, each reconstructed ring is tested if it is a real Cherenkov ring or not. There are two types of ring rejection criteria, and the first criteria are as follows:

Ring$_{\rm corr}$1-1 $E_{\rm visA} < E_{\rm visB}$,
where $E_{\rm visA(B)}$ is the visible (electron equivalent) energy of ring-A(B).

Ring$_{\rm corr}$1-2 $\theta_{\rm A-B} < 30°$,
where $\theta_{\rm A-B}$ is the angle between the ring-A and ring-B directions.

Ring$_{\rm corr}$1-3 $E_{\rm visA} \times \sin\theta_{\rm A-B} < 60$ MeV.

If ring-A satisfies the above conditions, it is discarded as a fake ring. The second criteria are as follows:

Ring$_{\rm corr}$2-1 $\frac{E_{\rm visA}}{E_{\rm vistot}} < 0.05$,
where $E_{\rm vistot}$ is the total visible energy in the event.

Ring$_{\rm corr}$2-2 $E_{\rm visA} < 40$ MeV

If ring-A satisfies the above conditions, it is also discarded as a fake ring. This process is applied only to multi-ring events. When at least one of the reconstructed rings is judged as a fake ring, the momenta of the remaining rings are redetermined.

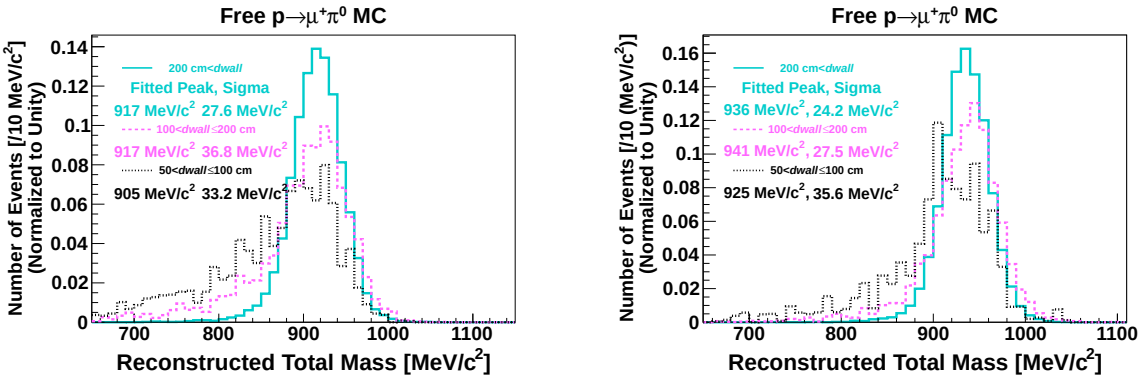

Figure 6.15: Reconstructed total mass distributions for free proton decays via $p \to \mu^+\pi^0$ MC events. The left (right) plot shows two-ring (three-ring) events. In each plot, the solid cyan histogram shows events reconstructed in the conventional fiducial mass region, the pink dashed histogram shows that for the additional fiducial mass region, and the black dotted histogram is for the region between *dwall* of 50 cm and 100 cm. The peak position and width of the distributions are obtained using Gaussian fits.

6.1.8 Michel Electron Search

Subsequent Michel electrons after muon decays are searched for using an independent low energy fitter, the same one used in Section 5.4.4. If a PMT hit cluster occurring after the primary event trigger timing satisfies the following criteria, it is tagged as a Michel electron:

Michel-$e_{\rm tag}$1 The time difference from the primary event is less than 20 μsec.

Michel-$e_{\rm tag}$2 The number of ID PMT hits in a fixed 1.3 μsec timing window around the hit cluster timing is greater than 50 (25 in SK-II).

Michel-$e_{\rm tag}$3 The total observed charge in a fixed 1.3 μsec timing window around the hit cluster timing is less than 2000 (1000 in SK-II) p.e.'s.

Michel-$e_{\rm tag}$4 Low energy fit goodness defined in Eq. (5.3) is greater than 0.5.

Michel-$e_{\rm tag}$5 The maximum number of ID PMT hits in a sliding 50 nsec timing window, N_{50} which is defined in Section 5.4.4, is greater than 30 (16 in SK-II).

For SK-I to -III, there are additional criteria:

Michel-$e_{\rm tag}$6 The time difference from the primary event (Δt) must satisfy, $0.1 < \Delta t < 0.8$ μsec or $1.2 < \Delta t < 20$ μsec.

Michel-$e_{\rm tag}$7 $N_{30} - N_{\rm BG} > 50$ (25 in SK-II).

where N_{30} is the number of ID PMT hits in a 30 nsec timing window around the hit cluster timing, and $N_{\rm BG}$ is the estimated number of ID PMT hits induced by other than the Michel electron in the same timing window. The value of $N_{\rm BG}$ is estimated with the number of ID PMT hits before the hit cluster timing. In this calculation, the time-of-flight subtracted residual timing is used with the primary vertex position. Due to effects from the PMT signal reflection in the cable, the time region between 800 and 1200 nsec after the primary event trigger is not used in the Michel electron search in SK-I to -III by applying **Michel-$e_{\rm tag}$6** as discussed in Section 3.2.5.

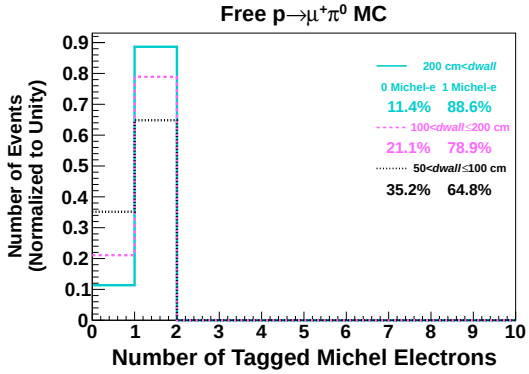

Figure 6.16: Distributions of the number of tagged Michel electrons for $p \to \mu^+\pi^0$ MC events. They are livetime-weighted combined from SK-I to -IV The solid cyan histogram shows events reconstructed in the conventional fiducial mass region, the pink dashed histogram shows that for the additional fiducial mass region, and the black dotted histogram is for the region between *dwall* of 50 cm and 100 cm.

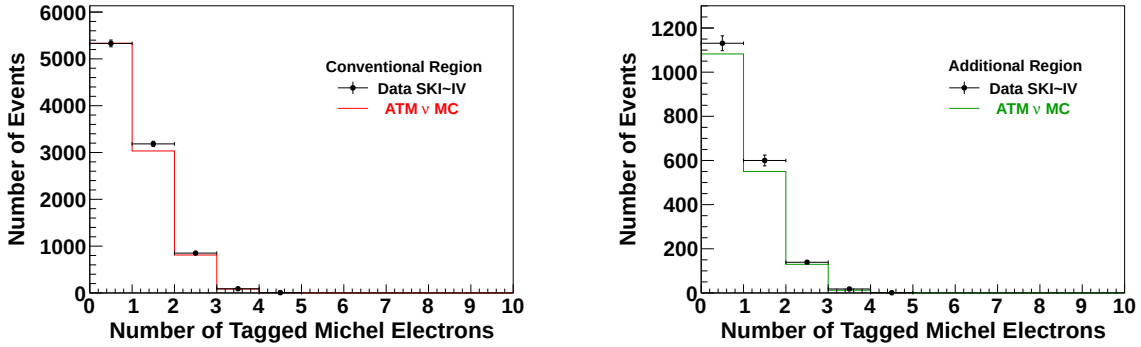

Figure 6.17: Distribution of the number of tagged Michel electrons of Sub-GeV multi-ring events for atmospheric neutrino MC and data in SK-I to -IV. The left plot corresponds to the conventional fiducial mass region and the right plot to the additional fiducial mass region. Atmospheric neutrino MC is normalized by livetime and includes reweighting to the latest SK oscillation fit [64]. Vertical error bars denote the statistical uncertainty.

Michel Electron Tagging Efficiency

The Michel electron tagging efficiency in cosmic-ray muon events is estimated to be about 73% in SK-I to -III. Because of the electronics upgrade described in Section 3.2.5, it improved to about 90% in SK-IV. The number of tagged Michel electron distribution of $p \to \mu^+\pi^0$ MC events is shown in Fig. 6.16. In the $p \to \mu^+\pi^0$ mode, an effect from muons escaping the ID manifests in the Michel electron tagging performance. A muon escaping from the ID disables us to tag the subsequent Michel electron, and therefore the tagging efficiency in the additional fiducial mass region (78.9%) is lower than that in the conventional fiducial mass region (88.6%). The data MC agreement is shown in Fig. 6.17 using Sub-GeV multi-ring events.

6.1.9 Reconstruction Performance on Proton Decay Events

The reconstruction performance on free $p \to e^+\pi^0$ and $p \to \mu^+\pi^0$ events is summarized in Table 6.1 among different ID regions. As described in each section, in events outside the conventional fiducial mass region, the number of hit PMTs tends to be small and they are more

localized than those inside. It is especially true for $p \to e^+\pi^0$ and $p \to \mu^+\pi^0$ decays because they produce back-to-back event topologies and one of the reconstructed rings generally has a small distance to the wall along its direction. These effects result in more two-ring events, worse particle identification, wider total mass distribution with longer tails on the low mass side, and lower Michel electron tagging efficiency. Although they are unavoidable and the signal selection efficiencies in the additional fiducial mass region are not as good as those in the conventional fiducial mass region due to them, the search sensitivity improvement by enlarging the fiducial mass is confirmed. It is discussed in Chapter 7, together with the concrete signal selection efficiencies and the expected number of atmospheric neutrino background events.

6.2 Energy Scale Uncertainty

In this section, the energy scale uncertainty used in this analysis is described. The obtained energy scale uncertainty is used as the source of the systematic uncertainty for the proton decay searches described in Chapter 7. The following three items are evaluated:

- Absolute energy scale uncertainty.
- Evolution of the energy scale over time.
- Zenith-angle-dependence of the energy scale.

For all items, the uncertainty is separately estimated in the conventional and additional fiducial mass region.

6.2.1 Absolute Energy Scale Uncertainty

The following control samples are used to evaluate the absolute energy scale uncertainty.

- Michel electrons from cosmic-ray muons.
- Neutral pions induced by atmospheric neutrinos.
- Sub-GeV stopping cosmic-ray muons.
- Multi-GeV stopping cosmic-ray muons.

The absolute energy scale uncertainty is estimated with the difference in reconstructed momenta or masses between data and MC for the above control samples in each SK phase. Among them, the event vertices of Michel electron and neutral pion events are almost uniformly distributed inside the ID and used to estimate the difference between data and MC for each fiducial mass of the detector separately. In the following, the uncertainty evaluation method for each control sample is described, and results are summarized at the end of this sub-Section.

Michel Electron Momentum

The Michel electron momentum spectrum from stopping cosmic-ray muons is used. The Michel electron event selection criteria are as follows:

Michel-e_{Escale}1 The time difference from the primary cosmic-ray event must be between 2 (1.2 for SK-IV) and 8 μsec.

Michel-e_{Escale}2 The maximum number of ID PMT hits in a sliding 50 nsec window for the Michel electron: $N_{50} > 60$ (30 for SK-II).

Michel-e_{Escale}3 The low energy fit goodness, the same one used in Section 6.1.8, > 0.5.

Table 6.1: Summary of reconstruction performance in different ID regions using only free proton decay MC events and weighted by the combined SK-I to -IV livetime. The particle identification (PID) efficiency is the fraction of events which pass the proton decay signal criterion associated with PID out of all two- and three-ring signal events. Here M_{π^0} ($M_{\rm tot}$) peak is the reconstructed neutral pion (total) mass distribution's peak position after applying all selections except the cut associated with M_{π^0} ($M_{\rm tot}$). The peak is determined using a Gaussian fit. Note that M_{π^0} peak values are evaluated for only three-ring events. The terms "Conventional", "Additional" and "Outside" stand for the conventional (200 cm $<$ *dwall*), additional fiducial volume (100 $<$ *dwall* $\leq$ 200 cm) and outside region (50 $<$ *dwall* $\leq$ 100 cm), respectively. The outside region is not used for the present analysis.

Decay Mode Region	Vertex resolution	2-ring fraction	3-ring fraction	PID efficiency	Michel electron tagging efficiency	M_{π^0} peak (3-ring)	$M_{\rm tot}$ peak (2-ring)	$M_{\rm tot}$ peak (3-ring)
$p \to e^+\pi^0$								
Conventional	17.1 cm	39.3%	58.7%	95.8%	N.A.	135 MeV/c^2	910 MeV/c^2	933 MeV/c^2
Additional	24.1 cm	51.9%	44.5%	87.7%	N.A.	134 MeV/c^2	898 MeV/c^2	927 MeV/c^2
Outside	25.9 cm	55.9%	37.6%	89.6%	N.A.	125 MeV/c^2	828 MeV/c^2	852 MeV/c^2
$p \to \mu^+\pi^0$								
Conventional	20.6 cm	36.8%	62.0%	96.2%	88.6%	135 MeV/c^2	917 MeV/c^2	936 MeV/c^2
Additional	24.8 cm	49.1%	48.1%	90.7%	78.9%	132 MeV/c^2	917 MeV/c^2	941 MeV/c^2
Outside	26.7 cm	55.3%	39.8%	82.6%	64.8%	125 MeV/c^2	905 MeV/c^2	925 MeV/c^2

Michel-e_{Escale}4 Fiducial volume cut using the reconstructed Michel electron vertex.

The Michel electron momentum spectra of data and MC are shown in Figure 6.18. The difference in the mean values between data and MC in each detector phase and fiducial mass region is used for the absolute energy scale uncertainty estimation.

Neutral Pion Mass

The neutral pion mass spectrum in atmospheric neutrino events is used. Neutral pions are mainly induced via NC meson production. Two-ring both e-like events are selected from the FC final sample, and the neutral pion mass is obtained based on Equations (6.31), (6.32), and (6.33). The π^0 mass distributions are shown in Figure 6.19. The difference in the peak values obtained by Gaussian fits between data and MC in each detector phase and fiducial mass region is used for the uncertainty estimation.

Sub-GeV Stopping Cosmic-ray Muon Momentum and Cherenkov Opening Angle

For this item, the following relation between particle momentum (p) and Cherenkov opening angle (θ_C) is utilized:

$$\cos\theta_C = \frac{1}{n\beta} = \frac{1}{n}\sqrt{1+\frac{m^2}{p^2}}. \tag{6.34}$$

As shown in Fig. 6.20, a Cherenkov opening angle depends on the muon momentum. Conversely, the muon momentum is calculated from the observed Cherenkov ring shape. Using Sub-GeV stopping cosmic-ray muon data and MC, the momentum derived from the total observed charge associated with the muon Cherenkov ring (P_{pe}) and the momentum derived from the Cherenkov opening angle (P_θ) are compared.

The Sub-GeV stopping cosmic-ray muon selection criteria are as follows:

STMU$_{\text{Escale}}$1-1 The reconstructed muon Z position must be greater than 1720 cm.

STMU$_{\text{Escale}}$1-2 The reconstructed muon direction $\cos\theta_z$ must be greater than 0.87, where $\cos\theta_z = 1.0$ is vertically downward-going.

STMU$_{\text{Escale}}$1-3 The muon fit goodness must be greater than 0.6.

STMU$_{\text{Escale}}$1-4 The total observed charge, PE_{tot}, in the ID must be $500 < \text{PE}_{\text{tot}} < 5000$ p.e.'s ($250 < \text{PE}_{\text{tot}} < 2500$ p.e.'s in SK-II).

STMU$_{\text{Escale}}$1-5 The reconstructed muon momentum derived from the Cherenkov opening angle must be $200 < P_\theta < 440$ MeV/c.

STMU$_{\text{Escale}}$1-6 There must be exactly one tagged Michel electron, and the time difference between the muon and Michel electron must be longer than 1.2 μsec.

The selected samples are divided into three groups with P_θ: $200 < P_\theta < 280$, $280 < P_\theta < 360$, and $360 < P_\theta < 440$ MeV/c. The P_{pe}/P_θ distributions in each P_θ region in SK-IV are shown in Fig. 6.21. The difference in the mean values between data and MC is assigned as the uncertainty for this control sample.

Multi-GeV Stopping Cosmic-ray Muon Momentum over Range

Multi-GeV stopping cosmic-ray muons are used for the highest energy region. The momentum divided by the range (track length) of muons (R_μ) is compared between data and MC. The following selection criteria are applied to select Multi-GeV stopping cosmic-ray muons:

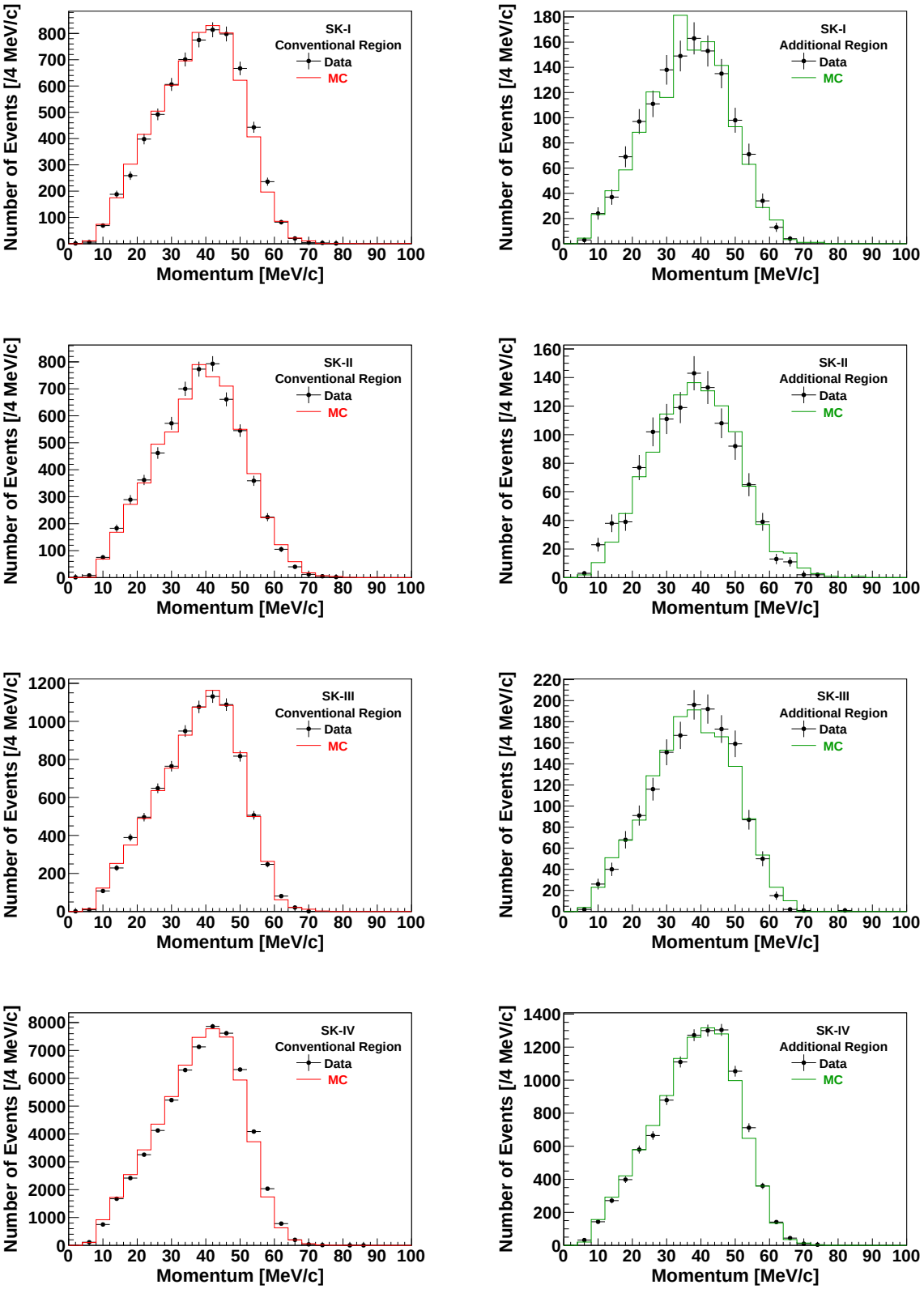

Figure 6.18: Michel electron momentum distributions. From top to bottom, SK-I to -IV plots are aligned. The left plots correspond to the conventional and the right plots correspond to the additional fiducial mass region. In each plot, the number of entries in the MC histogram is normalized to that of data. Vertical error bars denote the statistical uncertainty.

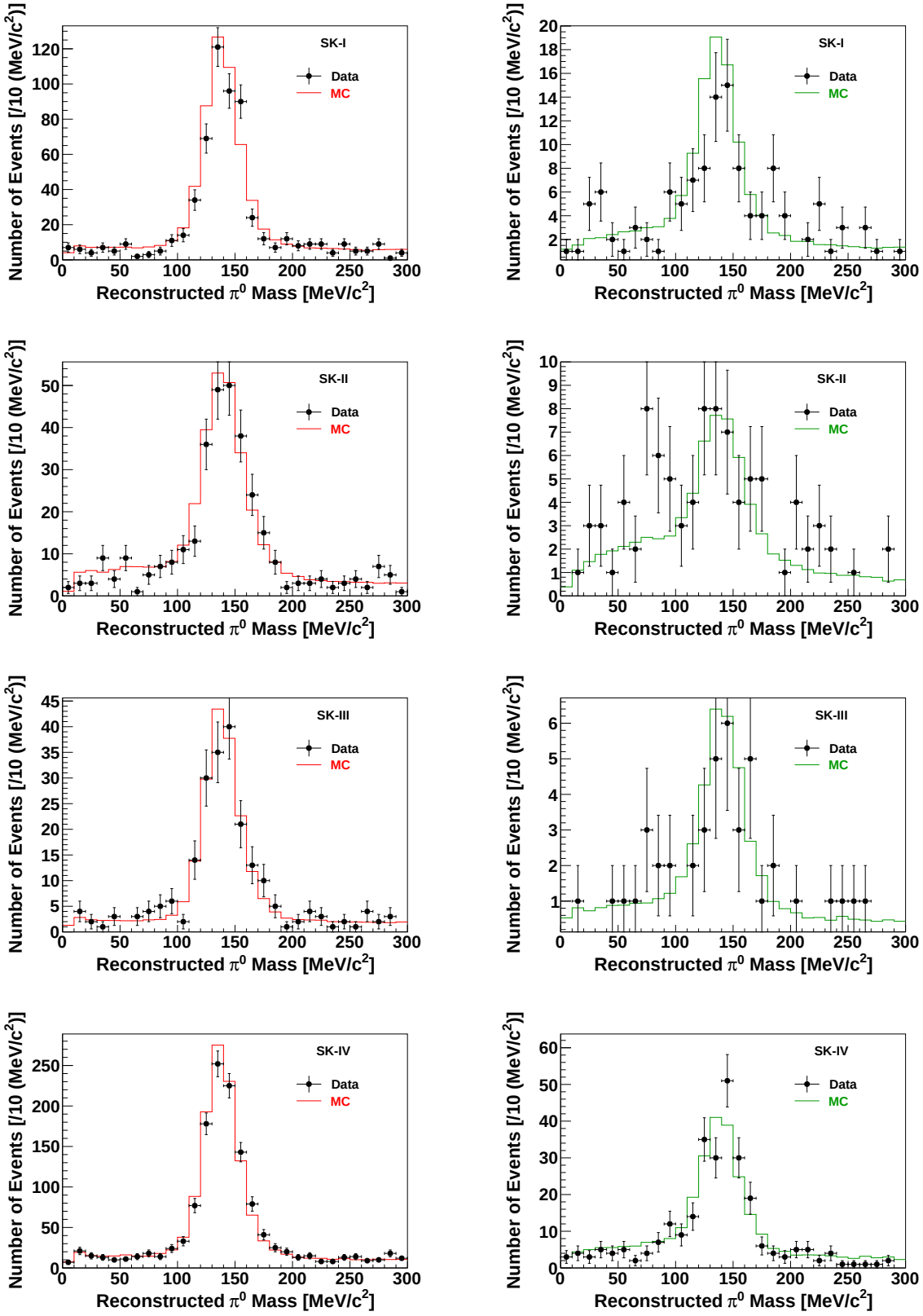

Figure 6.19: Neutral pion mass distributions. From top to bottom, SK-I to -IV plots are aligned. The left plots correspond to the conventional and the right plots correspond to the additional fiducial mass region. Atmospheric neutrino MC is normalized by livetime and the two-flavor oscillation probability ($\Delta m^2 = 2.5 \times 10^{-3}$ eV^2, $\sin^2 2\theta = 1.0$), here. Vertical error bars denote the statistical uncertainty.

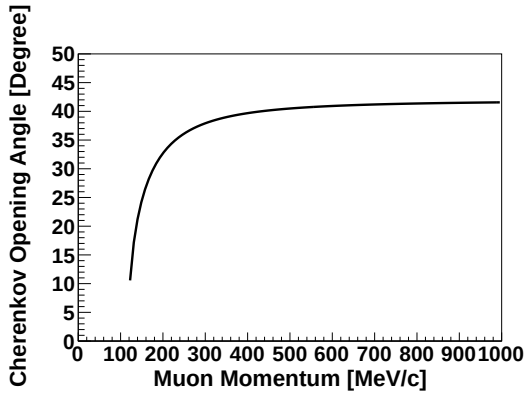

Figure 6.20: Cherenkov opening angle as a function of muon momentum.

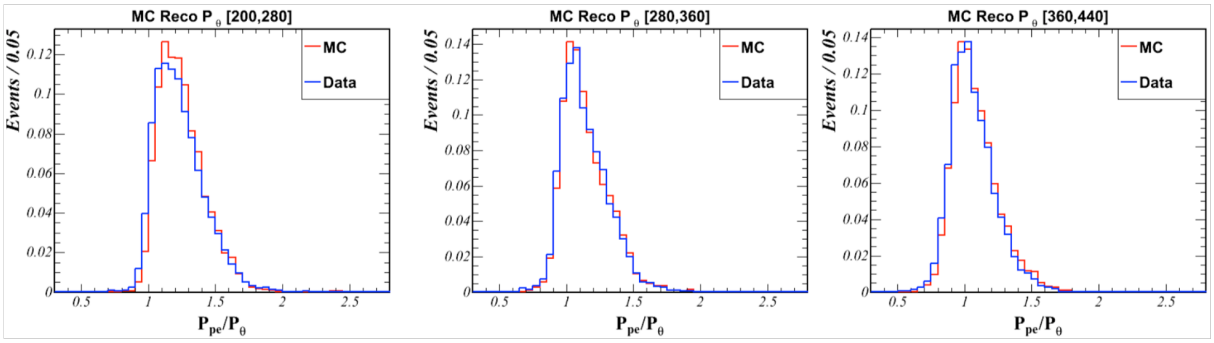

Figure 6.21: Distribution of the ratio of the momentum derived from the total observed charge (P_{pe}) to the momentum derived from the Cherenkov opening angle (P_θ) for SK-IV. The left plot corresponds to events with P_θ between 200 and 280 MeV/c. The middle plot corresponds to events with P_θ between 280 and 360 MeV/c. The right plot corresponds to events with P_θ between 360 and 440 MeV/c. In each plot, the blue histogram is data and the red is MC. Taken from [110].

Table 6.2: Summary of the absolute energy scale uncertainty for both the conventional and additional fiducial mass regions in units of %. The absolute scale uncertainty is taken to be the value of the most discrepant control sample, and cosmic-ray muon samples are considered for both fiducial mass regions to take the most discrepant one.

Absolute energy scale uncertainty				
Region	SK-I	SK-II	SK-III	SK-IV
Conventional	3.1	2.0	1.6	2.1
Additional	3.1	3.9	1.6	2.1

STMU$_{\text{Escale}}$2-1 The reconstructed muon entering point must be on the top of the detector.

STMU$_{\text{Escale}}$2-2 The muon fit is succeeded, fit goodness > 0 (0.5 in SK-IV).

STMU$_{\text{Escale}}$2-3 The reconstructed muon direction $\cos\theta_z$ must be greater than 0.94.

STMU$_{\text{Escale}}$2-4 There must be exactly one tagged Michel electron, and the time difference between the muon and the Michel electron must be longer than 1.2 μsec.

The selected samples are divided into five (six in SK-IV) groups with R_μ: 700 (500 in SK-IV) $< R_\mu <$ 1000, 1000 $< R_\mu <$ 1500, 1500 $< R_\mu <$ 2000, 2000 $< R_\mu <$ 2500, and 2500 $< R_\mu <$ 3000 cm(, and 3000 $< R_\mu <$ 3500 cm only in SK-IV). The muon momentum over range distributions for SK-IV are shown in Fig. 6.22. The difference in the peak values obtained by Gaussian fits between data and MC is taken as the uncertainty for this sample.

Summary of the Absolute Energy Scale Uncertainty

Figure 6.23 shows the absolute energy scale difference between data and MC for each of the control samples discussed above. Michel electrons and π^0 events are used to estimate the difference between data and MC for each fiducial mass region of the detector separately. The absolute scale uncertainty is taken to be the value of the most discrepant control sample in each SK phase and fiducial mass region and is summarized in Table 6.2. To take the most discrepant control sample, cosmic-ray muon samples are considered for both fiducial mass regions.

6.2.2 Evolution of the Energy Scale over Time

The evolution of the energy scale over time is estimated using the variation in the average reconstructed momentum of Michel electrons and the variation in the reconstructed momentum over range of Multi-GeV stopping cosmic-ray muons. The selection criteria for both two samples are the same as those described above. All Multi-GeV stopping cosmic-ray muons with R_μ between 700 (500 in SK-IV) and 3000 (3500 in SK-IV) cm are used. Figures 6.24 and 6.25 show the time variation of Michel electron momentum and momentum over range of Multi-GeV stopping cosmic-ray muons, respectively. As mentioned in Section 6.1.6, the evolution of the PMT gain and water attenuation length is corrected in the momentum reconstruction precess. The time variation is defined as the sample standard deviation of the data value over the run time in each SK phase and fiducial mass region. The larger value is taken as the uncertainty between the two samples. To take the larger value, the cosmic-ray muon sample is considered for both fiducial mass regions. The uncertainty due to the time variation of the energy scale is summarized in Table 6.3.

6.2.3 Zenith-angle-dependence of the Energy Scale

Particle directional dependence of the energy scale is estimated using Michel electrons because vertices and directions of Michel electrons are almost uniformly and isotropically dis-

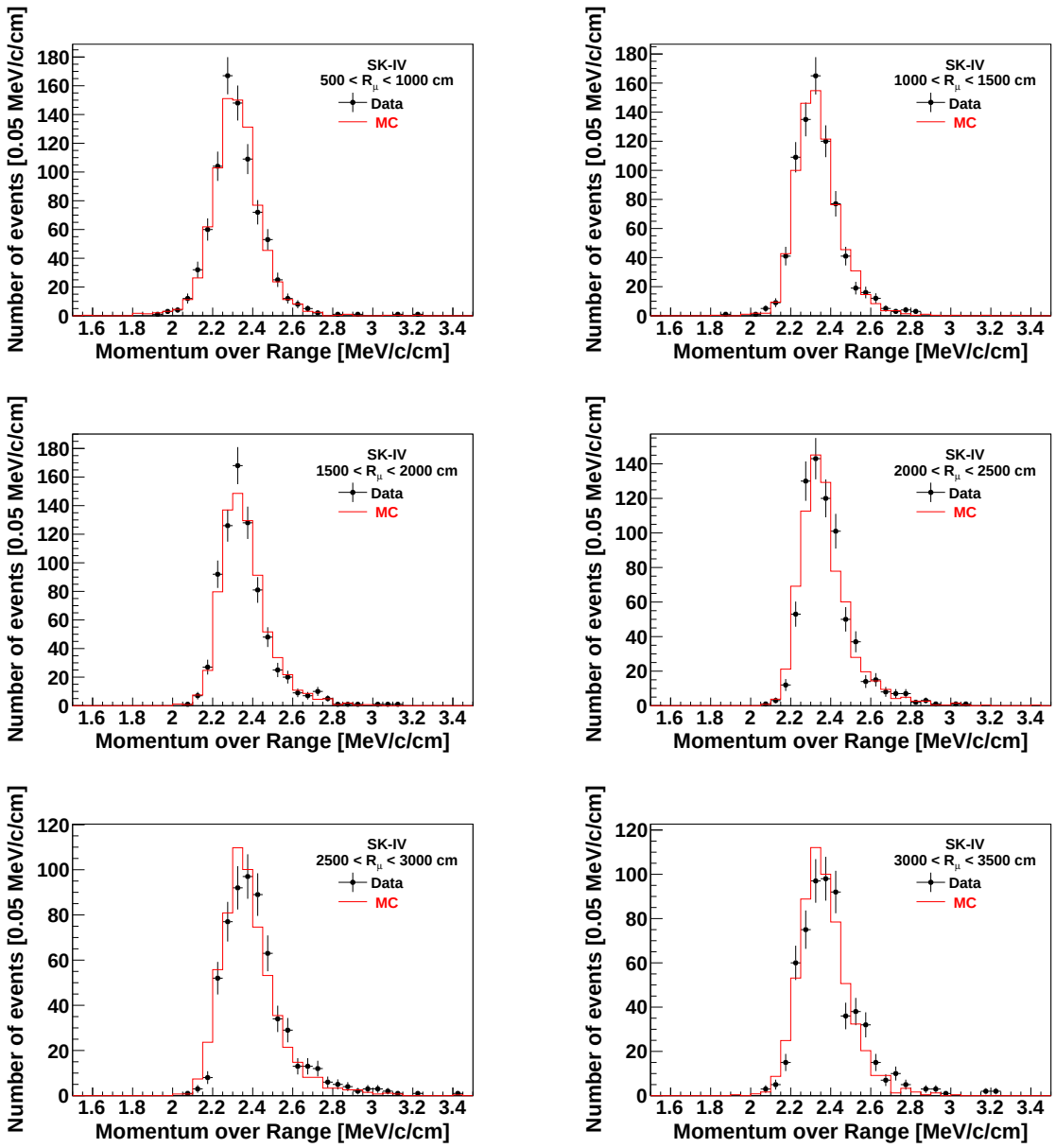

Figure 6.22: Muon momentum over range distributions for SK-IV. The Multi-GeV stopping cosmic-ray muons are divided into six group with their range, R_μ. In each plot, the number of entries in the MC histogram is normalized to that of data. Vertical error bars denote the statistical uncertainty.

Table 6.3: Summary of the time variation of the energy scale for both the conventional and additional fiducial mass regions in units of %. The time variation uncertainty is taken to be the larger value among the two control samples, and the cosmic-ray muon sample is considered for both fiducial mass regions to take the larger one.

Time variation of the energy scale				
Region	SK-I	SK-II	SK-III	SK-IV
Conventional	0.9	0.6	1.8	0.4
Additional	0.9	0.6	1.8	0.6

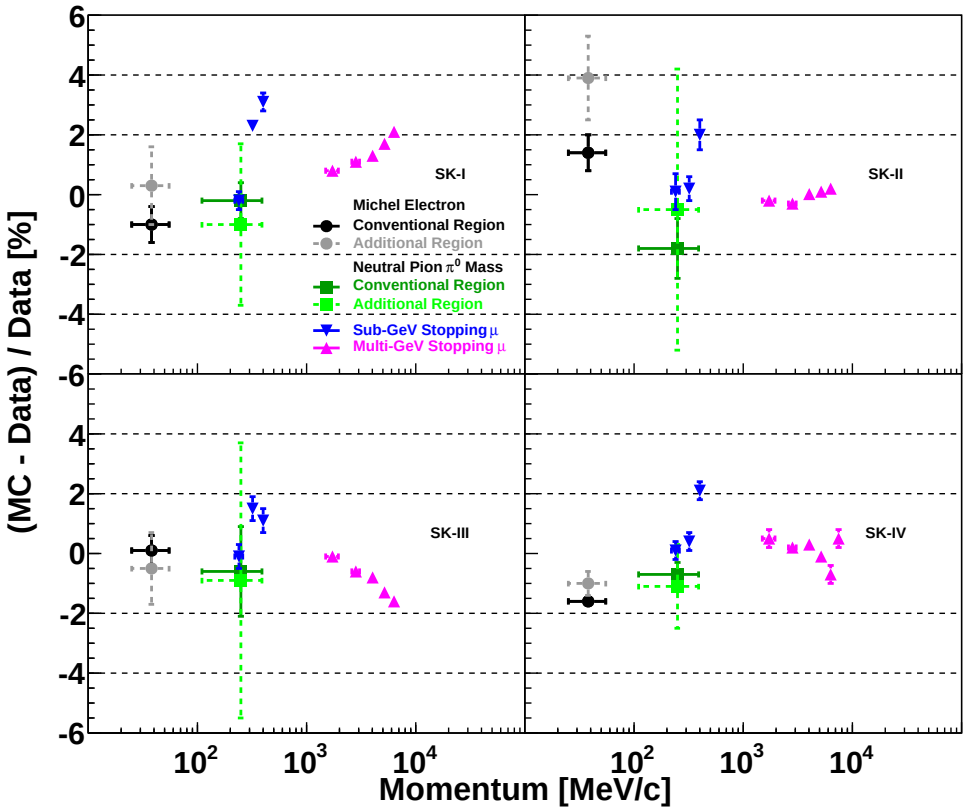

Figure 6.23: Absolute energy scale difference between data and MC control samples. Vertical error bars denote the statistical uncertainty, and horizontal error bars denote the momentum range for each control sample. For the Michel electron and π^0 samples, points with solid error bars correspond to the conventional fiducial mass region, and points with dashed error bars correspond to the additional fiducial mass region. Cosmic-ray muon samples are considered for both the conventional and additional fiducial mass regions to take the most discrepant control sample.

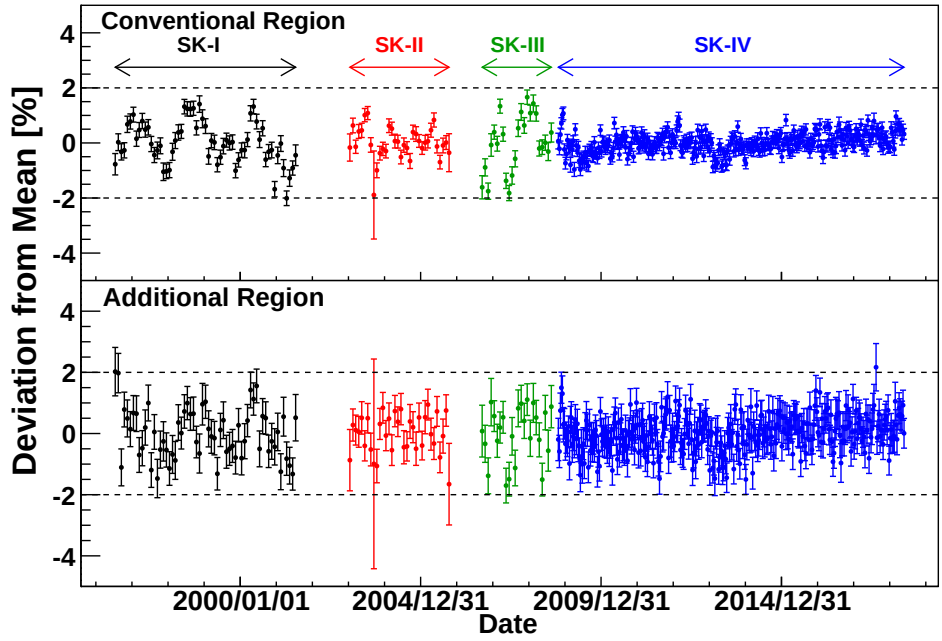

Figure 6.24: Time variation of the average momentum of Michel electrons as a function of date. For each fiducial mass region and SK phase, data points are normalized by their mean value. The upper (lower) plot corresponds to the conventional (additional) fiducial mass region. Vertical error bars denote the statistical uncertainty. For SK-I to -III, each data point corresponds to a one month average and for SK-IV, each data point corresponds to a 10 day average.

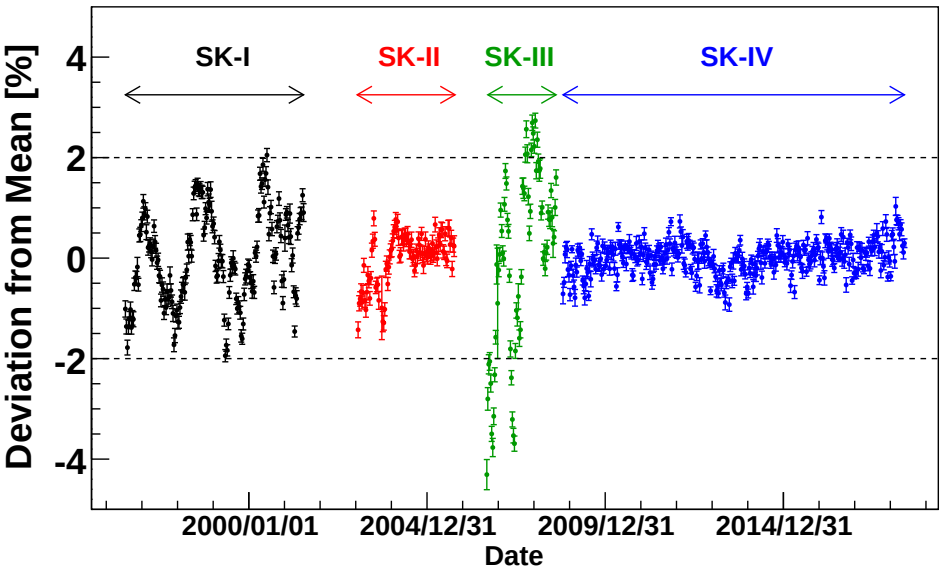

Figure 6.25: Time variation of the average momentum over range of Multi-GeV stopping cosmic-ray muons as a function of date. For each SK phase, data points are normalized by their mean value. Vertical error bars denote the statistical uncertainty. Each data point corresponds to a 10 day average.

Table 6.4: Summary of the zenith-angle-dependent non-uniformity of the energy scale for both the conventional and additional fiducial mass regions in units of %.

Zenith-angle-dependent non-uniformity				
Region	SK-I	SK-II	SK-III	SK-IV
Conventional	0.6	1.1	0.6	0.5
Additional	1.4	1.5	1.3	0.4

tributed in the ID. The Michel electron events are divided into five bins with their direction, $\cos\theta_z$. In each bin, the average Michel electron momentum is compared between data and MC. Figure 6.26 shows the ratio of the average momentum of MC to that of data as a function of particle direction (zenith angle), $\cos\theta_z$, in each SK phase and fiducial mass region. The MC over data ratio is normalized by the absolute difference derived in Section 6.2.1 using the Michel electron sample. The five bins' standard deviation is assigned as the uncertainty for SK-I to -III, and the most discrepant point is assigned as the uncertainty for SK-IV. The zenith-angle-dependent non-uniformity of the energy scale is summarized in Table 6.4.

Summarizing the above, data and MC agree within a few % level in both the conventional and additional fiducial mass regions for all items, the absolute energy scale (Table 6.2), time variation of the energy scale (Table 6.3), and zenith-angle-dependent non-uniformity of the energy scale (Table 6.4).

6.3 Neutron Tagging

Because of the data taking system upgrade presented in Section 3.2.5, neutrons emitted in a primary FC event can be counted in SK-IV by tagging 2.2 MeV gamma rays from neutron capture on hydrogen:

$$n + p \rightarrow d + \gamma \text{ (2.2 MeV)}. \tag{6.35}$$

In order to tag this faint gamma ray (Compton-scattered electron), an independent neutron tagging algorithm has been developed [97, 106]. The algorithm is composed of the following two steps:

1. Initial neutron candidate selection.
2. Final neutron candidate selection with Neural Network.

First, PMT hit clusters produced by such faint gamma rays are searched for as the initial selection. Then, 23 input variables associated with each initial neutron candidate are calculated and used as input variables to a dedicated neural network to identify it as either a neutron signal or background (fake signal).

6.3.1 Time-clustered PMT Dark Noise

About the SK PMT dark noise, besides random dark noise, which is uniformly distributed in time, another type of dark noise has been found recently [106]. That one clusters in time, and a typical waveform of such time-clustered noise hits is shown in Fig. 6.27. The source of these time-clustered noise hits has been identified to be the scintillation light in the SK PMT glass. Since a typical number of PMT hits induced by 2.2 MeV gamma ray (Compton-scattered electron) is less than 10, it is beneficial to identify a PMT hit as either a photon detection hit or dark noise hit and to effectively reduce the dark noise hits, which mimic a faint gamma ray signal. Therefore, a dedicated time-clustered noise cut is introduced in the initial selection and input variable calculations.

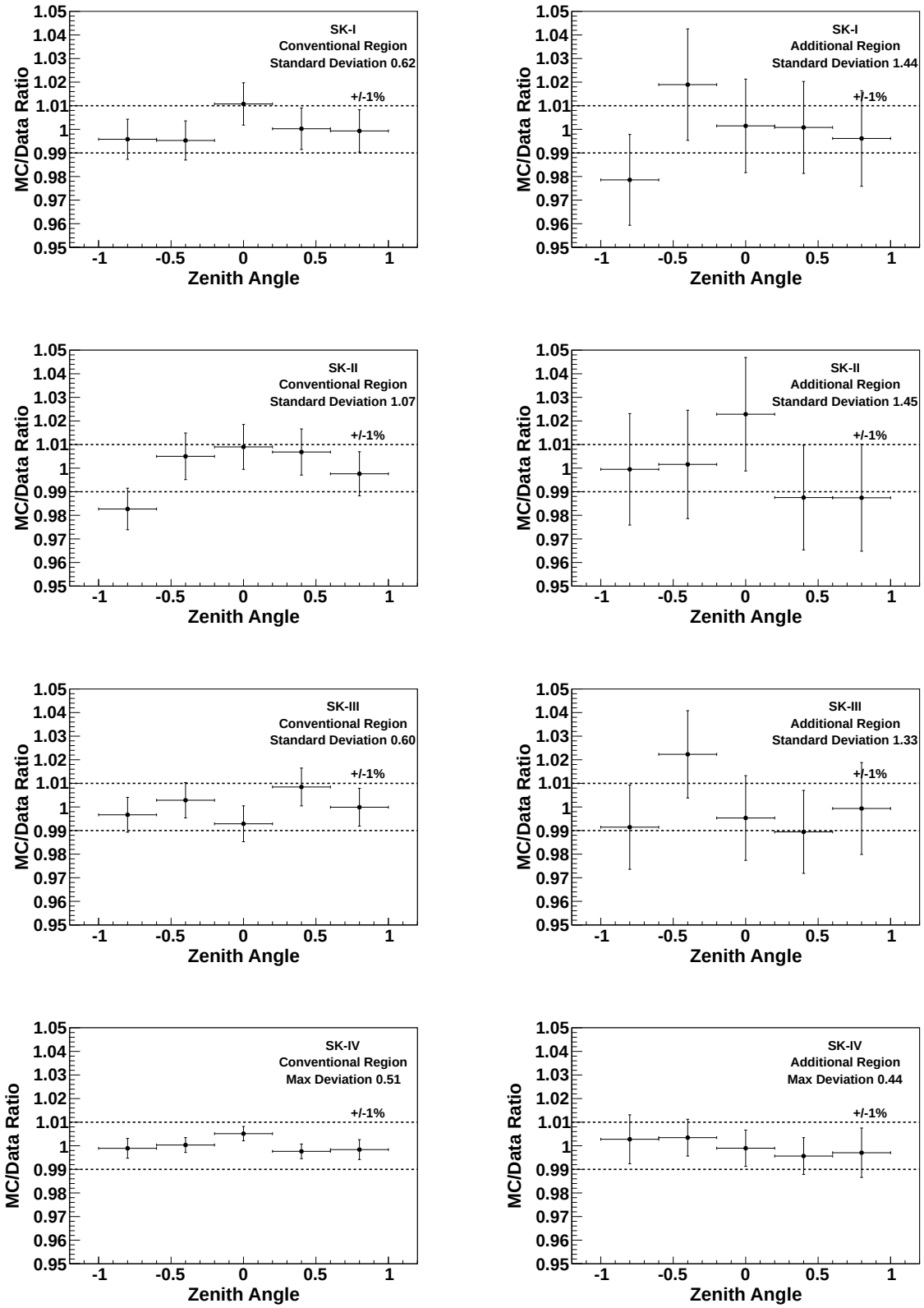

Figure 6.26: Ratio of the average momentum between data and MC as a function of Michel electron direction, zenith angle, $\cos\theta_z$. From top to bottom, SK-I to -IV plots are aligned. The left plots correspond to the conventional and the right plots correspond to the additional fiducial mass region. Vertical error bars denote the statistical uncertainty.

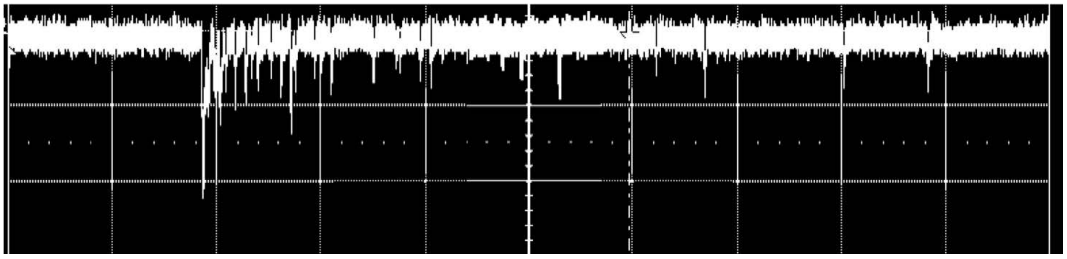

Figure 6.27: Typical waveform of time-clustered noise hits (1 μsec/div for the horizontal axis and 5 mV/div for the vertical axis). This sample PMT's dark noise is measured to be about 8 kHz in the measurement condition. Therefore, the expected number of dark noise hits per 10 μsec is about 0.08 if the dark noise is uniformly distributed in time. Taken from [106].

6.3.2 Initial Neutron Candidate Selection

As the initial selection, the number of PMT hits in a sliding 10 nsec timing window is counted, and PMT hit clusters produced by faint gamma rays are searched for. Each PMT hit timing is corrected with time-of-flight using the primary FC event vertex position (described in Section 6.1.1, and 6.1.4) in this calculation. The number of PMT hits in the sliding timing window is defined as N_{10}^{RAW}. If a cluster with N_{10}^{RAW} of more than four is found, that cluster is identified as a possible neutron candidate. If N_{10}^{RAW} is more than 50, or the number of PMT hits in a 200 nsec timing window around the cluster timing (N_{200}) is more than 200, that cluster is rejected as a background.

The time-clustered noise cut is introduced here, and N_{10}^{RAW} is redefined to be N_{10}. If there are multiple hits in the same PMT within X μsec, these hits are removed. The value of X depends on the value of N_{10}^{RAW}. For hit clusters with N_{10}^{RAW} of less than 7, X is set to 12 μsec, while for hit clusters with N_{10}^{RAW} of 7 or more, X is set to 6 μsec. They have been determined to optimize performance, and hit clusters with the remaining number of PMT hits (N_{10}) of more than four are selected as initial neutron candidates.

6.3.3 Final Neutron Candidate Selection with Neural Network

Before calculating the input variables to the neural network used in this analysis, the vertex position of the initial neutron candidate (Compton-scattered electron) is reconstructed using Neut-Fit. Neut-Fit searches for the vertex position so that the RMS of the time-of-flight subtracted residual timing distribution of the initial candidate is minimized. The RMS of the residual timing distribution is defined as follows:

$$t'_{\mathrm{rms}} = \sqrt{\frac{\sum_i^{N_{10\mathrm{n}}} (t'_i - t'_{\mathrm{mean}})^2}{N_{10\mathrm{n}}}}, \tag{6.36}$$

$$t'_{\mathrm{mean}} = \sum_i^{N_{10\mathrm{n}}} \frac{t'_i}{N_{10\mathrm{n}}}, \tag{6.37}$$

where t'_i is the ith PMT's time-of-flight corrected residual time for an assumed vertex position, and $N_{10\mathrm{n}}$ is the number of PMT hits in a 10 nsec timing window in residual timing for an assumed vertex position. Neut-Fit is executed twice: first, the reconstructed vertex position is forced to be within 200 cm from the primary FC event vertex position, and second, the vertex position is reconstructed without any constraints. In the following, the Neut-Fit vertex position denotes the result from the first attempt unless otherwise noted.

Input Variables to Neural Network

For each initial neutron candidate, the following 23 input variables are defined:

1. **Number of hits in 10 nsec, N_{10}:**
   The same variable used in the initial selection. Initial neutron candidates with larger N_{10} are regarded as more signal-like candidates.

2. **Mean opening angle, θ_{mean}:**
   The direction of each initial candidate is reconstructed by calculating the vector sum of the hit PMT directions from the Neut-Fit vertex position. Then, an opening angle to each hit PMT in the 10 nsec window is calculated from the obtained direction. The mean value of the opening angles is defined as θ_{mean}. Initial neutron candidates with θ_{mean} around 42 degrees are regarded as more signal-like candidates.

3. **Hit vector RMS, ϕ_{rms}:**
   An azimuthal angle to each hit PMT is also calculated using the reconstructed direction and Neut-Fit vertex position. The azimuthal angle differences between two consecutive hits in azimuth are calculated. Then, the RMS of the differences is used as an input variable, ϕ_{rms}. Initial neutron candidates with small ϕ_{rms} are regarded as more signal-like candidates because Cherenkov photons are expected to be distributed uniformly in azimuth.

4. **Number of spatially clustered hits, N_{c}:**
   PMT hits induced by radioactive products (background) are often spatially localized. Multiple hits within an opening angle of 14.1 degrees are counted as clustered-hits, N_{c}. If there are three spatially clustered hits or more, N_{c} is set to the number of these spatially clustered hits, otherwise 0. The difference between $N_{10\mathrm{n}}$ and N_{c}, $N_{10\mathrm{n}} - N_{\mathrm{c}}$, is used. Backgrounds are expected to have lower $N_{10\mathrm{n}} - N_{\mathrm{c}}$.

5. **Number of hits in 300 nsec, N_{300}:**
   In order to reject other possible higher energy backgrounds, the number of PMT hits in a 300 nsec timing window around the initial neutron candidate timing is calculated, N_{300}. The difference between N_{300} and $N_{10\mathrm{n}}$, $N_{300} - N_{10\mathrm{n}}$, is used, and initial neutron candidates with larger $N_{300} - N_{10\mathrm{n}}$ are regarded as more background-like candidates.

6. **Root-Mean-Square of hit timing, t'_{rmsFC}:**
   Initial neutron candidates from true neutrons should have a narrower peak in the residual timing distribution. In order to separate a gamma ray signal from backgrounds with this feature, the RMS of the residual timing distribution is used as an input variable. Here, the primary FC event vertex position is used for the calculation of the RMS of the residual timing distribution, t'_{rmsFC}:

$$t'_{\mathrm{rmsFC}} = \sqrt{\frac{\sum_i^{N_{10}} (t'_i - t'_{\mathrm{meanFC}})^2}{N_{10}}}, \tag{6.38}$$

$$t'_{\mathrm{meanFC}} = \sum_i^{N_{10}} \frac{t'_i}{N_{10}}. \tag{6.39}$$

   Initial neutron candidates with smaller t'_{rmsFC} are regarded as more signal-like candidates.

7, 8. **Minimum RMS of hit timing, $\min(t^3_{\mathrm{rms}})$ and $\min(t^6_{\mathrm{rms}})$:**
   The minimum RMS of hit timing for 3 and 6 consecutive hits in time is defined as $\min(t^3_{\mathrm{rms}})$ and $\min(t^6_{\mathrm{rms}})$, respectively, using Equations (6.36) and (6.37). In a similar manner to t'_{rmsFC}, initial neutron candidates with smaller $\min(t^3_{\mathrm{rms}})$ and $\min(t^6_{\mathrm{rms}})$ are regarded as more signal-like.

9, 10. BONSAI fit variables, $\mathrm{BS_{wall}}$ and $\mathrm{BS_{energy}}$:
The low energy reconstruction tool developed for solar neutrino analyses in SK, BONSAI [111], is used to reconstruct the Compton-scattered electron vertex position and energy. Vertex positions for backgrounds from radioactive products in the PMT components, such as PMT cases, and PMT cables, are localized in the edge of the detector. The distance between the BONSAI vertex position and the closest ID wall is defined as $\mathrm{BS_{wall}}$, and backgrounds are expected to have smaller $\mathrm{BS_{wall}}$. The reconstructed energy with BONSAI, $\mathrm{BS_{energy}}$, is expected to be around 2 MeV for true neutron candidates.

11, 12, 13. Neut-Fit variables, $\Delta t'_{\mathrm{rms}}$, ΔN_{10}, and $\mathrm{NF_{wall}}$:
The difference between t'_{rms} and t'_{rmsFC} is defined as $\Delta t'_{\mathrm{rms}}$. The former one is derived from the Neut-Fit vertex position, while the latter one is from the primary FC event vertex position. Similarly, $N_{10\mathrm{n}} - N_{10}$ is defined as ΔN_{10}.
The distance between the Neut-Fit vertex position and the closest ID wall is defined as $\mathrm{NF_{wall}}$. Here, the second Neut-Fit result is used. Vertex positions for backgrounds are expected to be localized in the small $\mathrm{NF_{wall}}$ region.

14, 15. Fit agreement variables: $(\mathrm{NF}-\mathrm{BS})_{\mathrm{dis}}$, and $(\mathrm{NF}-\mathrm{FC})_{\mathrm{dis}}$:
The distance between the two vertex positions from Neut-Fit and BONSAI is defined as $(\mathrm{NF}-\mathrm{BS})_{\mathrm{dis}}$. Furthermore, the difference between Neut-Fit and the primary FC event vertex positions, $(\mathrm{NF}-\mathrm{FC})_{\mathrm{dis}}$, is also used. True neutron candidates are more likely to be reconstructed consistently among the different tools. Initial neutron candidates with smaller $(\mathrm{NF}-\mathrm{BS})_{\mathrm{dis}}$ and $(\mathrm{NF}-\mathrm{FC})_{\mathrm{dis}}$ are regarded as more signal-like candidates.

16. Acceptance parameter, $P_{\mathrm{Acceptance}}$:
The probability to detect photons from a Compton-scattered electron at each PMT depends on the distance between the PMT and electron position as well as the PMT acceptance (effective coverage). On the other hand, it is not the case for dark noise hits. To differentiate neutron signals and backgrounds using this feature, the photon detection probability of each PMT (P_i) and the final acceptance parameter ($P_{\mathrm{Acceptance}}$) are defined as follows:

$$A_i = \frac{f(\Theta_i)}{r_i^2} \times \exp\left(-\frac{r_i}{L}\right), \tag{6.40}$$

$$A_{\mathrm{total}} = \sum_i A_i, \tag{6.41}$$

$$P_i = \frac{A_i}{A_{\mathrm{total}}}, \tag{6.42}$$

$$P_{\mathrm{Acceptance}} = \frac{\sum_i^{N_{10\mathrm{n}}} \log P_i}{N_{10\mathrm{n}}}, \tag{6.43}$$

where $f(\Theta_i)$ is the PMT acceptance correction factor as a function of photon incident angle (Θ_i), r_i is the distance between the ith PMT and Neut-Fit vertex position, and L is the water attenuation length. Initial neutron candidates with larger $P_{\mathrm{Acceptance}}$ are regarded as more signal-like candidates.

17. Cherenkov angle likelihood parameter, $L_{\mathrm{Cherenkov}}$:
Cherenkov photons are distributed around 42 degrees of opening angle from the Compton-scattered electron direction. This variable uses that feature. First, a cone is defined using three hit PMTs in $N_{10\mathrm{n}}$ to define the base, and the Neut-Fit vertex position is considered as the apex. There are ${}_{N_{10\mathrm{n}}}\mathrm{C}_3$ of combinations to select three hit PMTs. The opening angle of the cone for the jth three PMT combination is defined as θ_j. The probability density functions for the signal and background assumptions, P_{bkg}, and P_{sig}, are tabulated as a

function of θ_j, $N_{10\mathrm{n}}$, and products of photon detection probabilities defined in Eq. (6.42) for three hits using a 150-year equivalent exposure of atmospheric neutrino MC events. Then, the Cherenkov angle likelihood parameter, $L_{\mathrm{Cherenkov}}$, is defined as follows:

$$L_{\mathrm{Cherenkov}} = \sum_{j}^{{}_{N_{10\mathrm{n}}}\mathrm{C}_3} \left(\log P_{\mathrm{bkg}}(N_{10\mathrm{n}}, \theta_j, \prod_{k=1}^{3} P_k) - \log P_{\mathrm{sig}}(N_{10\mathrm{n}}, \theta_j, \prod_{k=1}^{3} P_k) \right) \tag{6.44}$$

Initial neutron candidates with negative $L_{\mathrm{Cherenkov}}$ are regarded as more signal-like candidates.

18∼22. Isotropy parameters, $\beta_{1\sim5}$:
Isotropy parameters, β's, are defined to further utilize the spatial distribution of hit PMTs:

$$\beta_l = \frac{2}{N_{10\mathrm{n}}(N_{10\mathrm{n}}-1)} \sum_{i=1}^{N_{10\mathrm{n}}-1} \sum_{j=i+1}^{N_{10\mathrm{n}}} P_l(\cos\theta_{ij}), \tag{6.45}$$

where l is the index ($l = 1 \sim 5$), θ_{ij} is the opening angle difference between the ith and jth hit PMTs, and P_l is lth Legendre polynomial.

23. Distance to the ID wall along Compton-scattered electron direction, *towall*:
The distance between the Neut-Fit vertex position and the ID wall along the reconstructed direction is defined as *towall*. Spatial parameters introduced above have *towall* dependence, and in order to efficiently train the neural network including such dependence, *towall* is included as an input variable.

Figure 6.28 (6.29) shows the 23 input variable distributions of initial neutron candidates associated with the primary FC events in the conventional (additional) fiducial mass region.

All 23 variables are fed into a neural network, which is a machine-learning-based tool used in various particle physics experiments. The ROOT class TMLP is employed to implement a feed-forward Multi-Layer Perceptron [112]. The neural network has been trained on a 250-year equivalent exposure of atmospheric neutrino MC events, and another 250-year atmospheric neutrino MC events have been used for testing the trained neural network.

Neutron Tagging Performance

The resultant distributions of the neural network output are shown in Figures 6.30 for neutron candidates associated with the primary FC events. Because the separation performance depends on the value of N_{10}, the threshold values on the neural network output to select a signal candidate have been also determined depending on the value of N_{10}. The threshold value is set to 0.920 for initial neutron candidates with $N_{10} = 5$, 0.908 for initial neutron candidates with $N_{10} = 6$, and 0.874 with N_{10} of 7 or more. The final neutron tagging efficiency and fake neutron tagging (false-positive) probability for the primary FC events in the conventional (additional) fiducial mass region are estimated using a 500-year equivalent exposure of atmospheric neutrino MC events, and they are 25.9% (22.7%) and 0.016 (0.029) per primary FC event, respectively (Table 6.5). The reason for the lower neutron tagging efficiency in the additional fiducial mass region is similar to the case in the particle momentum reconstruction. Because neutrons produced by primary FC events often travel more than 100 cm before thermalizing (the mean value of the neutron travel distance is about 160 cm), about 5% of neutrons produced in the additional fiducial mass region escape the ID, resulting in the lower tagging efficiency. Furthermore, as shown in the $\mathrm{BS}_{\mathrm{wall}}$ and $\mathrm{NF}_{\mathrm{wall}}$ distributions in Figure 6.29, backgrounds from radioactive products in the detector components are localized in the region closer to the ID wall. It results in the higher fake neutron tagging probability in the additional fiducial mass region.

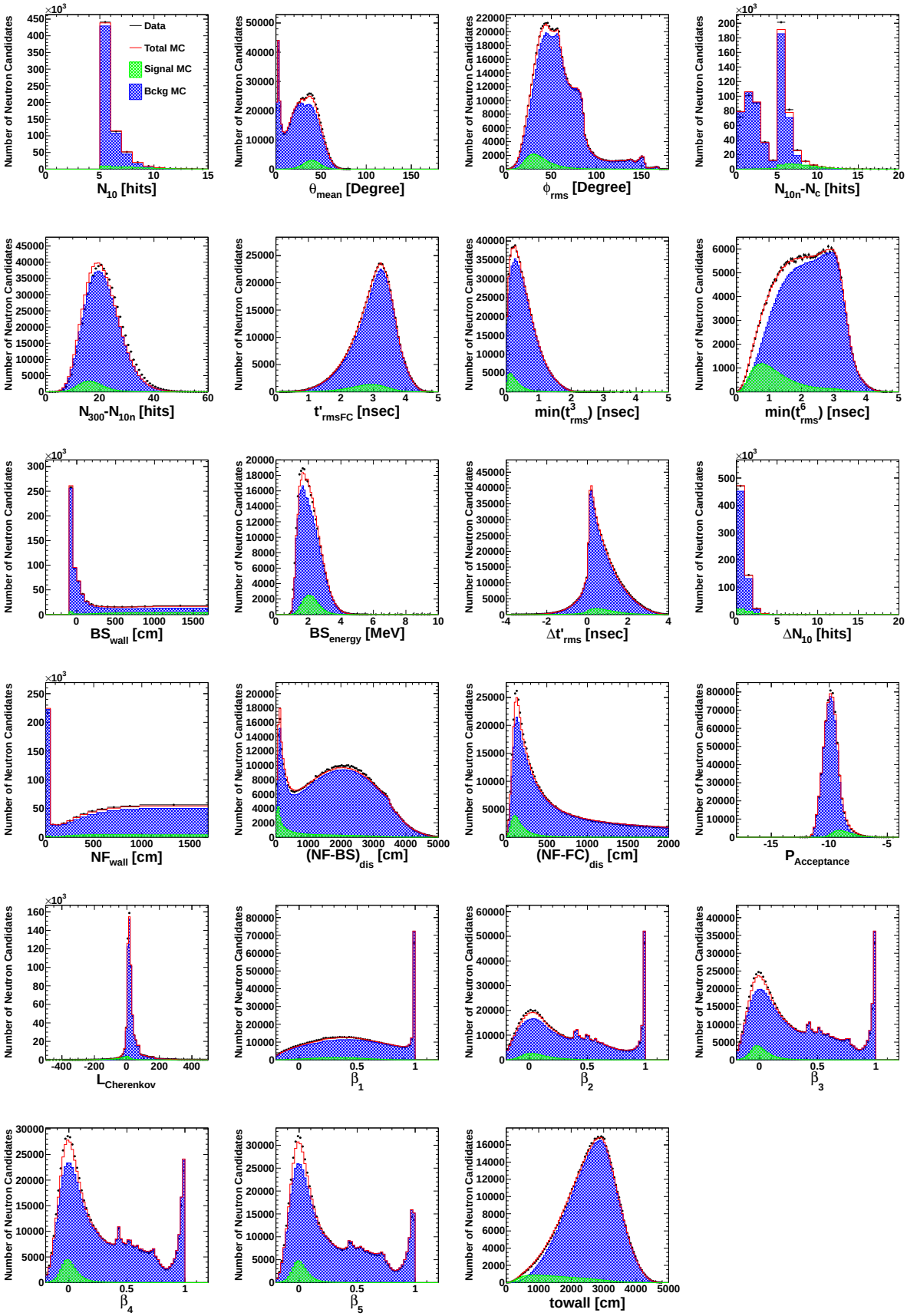

Figure 6.28: 23 input variable distributions of initial neutron candidates associated with the primary FC events in the conventional fiducial mass region. The black dots show the data in SK-IV. The red histograms show the atmospheric neutrino MC events and are normalized by livetime and the two-flavor oscillation probability ($\Delta m^2 = 2.5 \times 10^{-3}$ eV^2, $\sin^2 2\theta = 1.0$). True neutron candidates (green) and fake neutron candidates (blue) are also separately shown.

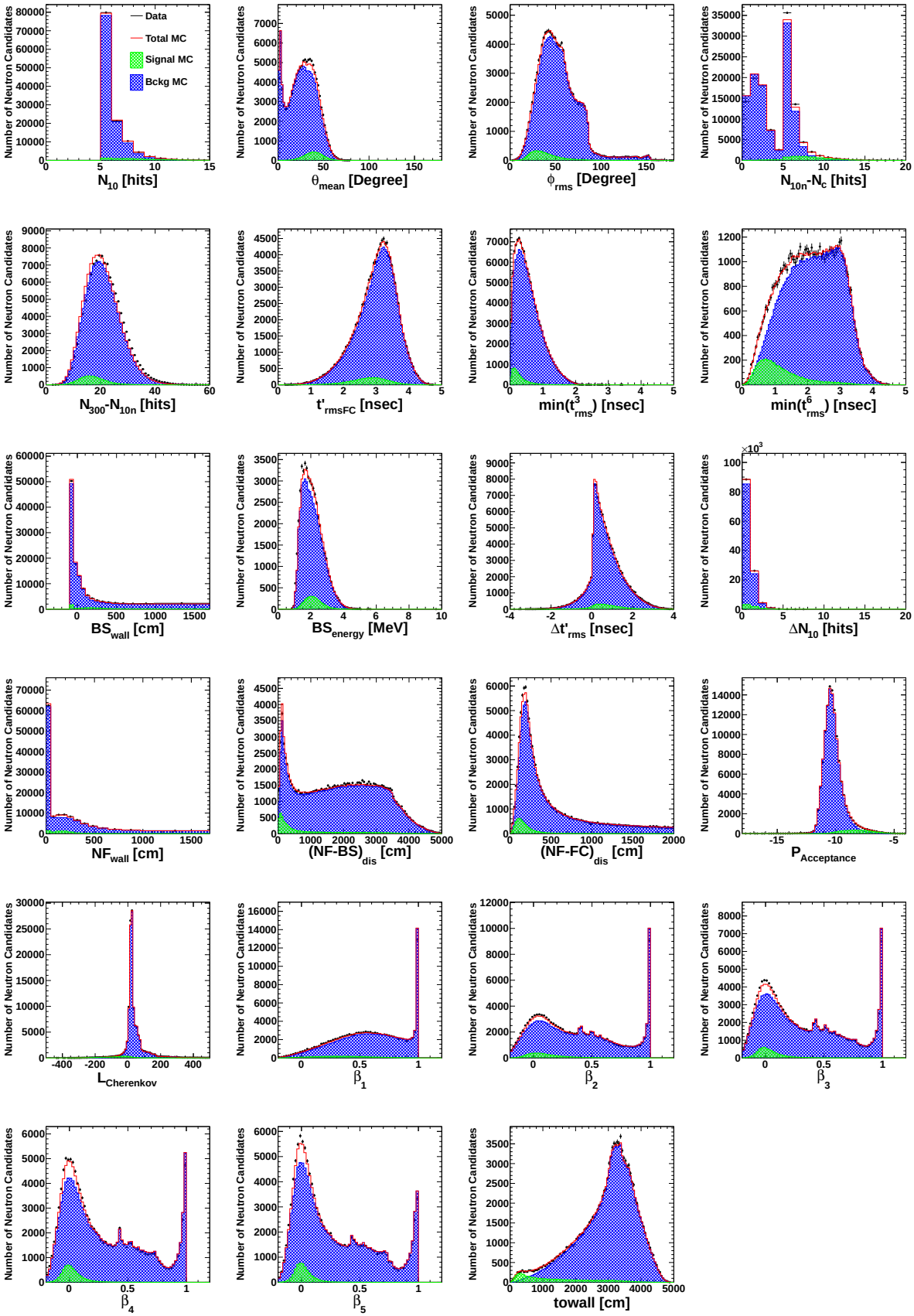

Figure 6.29: 23 input variable distributions of initial neutron candidates associated with the primary FC events in the additional fiducial mass region. The black dots show the data in SK-IV. The red histograms show the atmospheric neutrino MC events and are normalized by livetime and the two-flavor oscillation probability ($\Delta m^2 = 2.5 \times 10^{-3}$ eV^2, $\sin^2 2\theta = 1.0$). True neutron candidates (green) and fake neutron candidates (blue) are also separately shown.

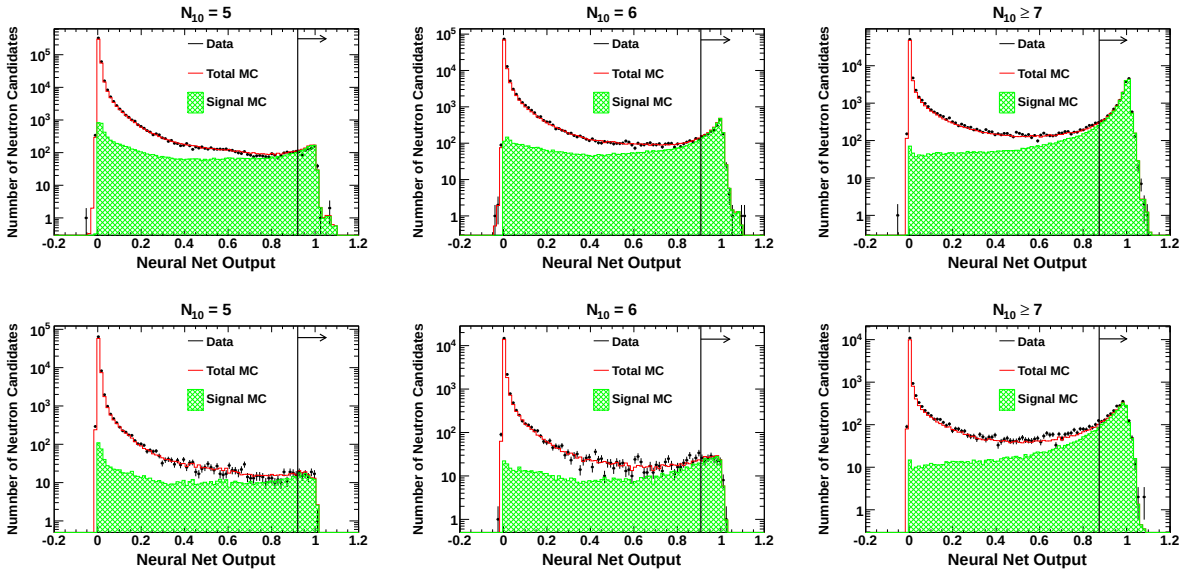

Figure 6.30: Neural network output distributions. The black dots show the data in SK-IV. The red histograms show the atmospheric neutrino MC events and are normalized by livetime and the two-flavor oscillation probability ($\Delta m^2 = 2.5 \times 10^{-3}$ eV^2, $\sin^2 2\theta = 1.0$). True neutron candidates are shown in green. The top (bottom) three plots correspond to neutron candidates associated with the primary FC events within the conventional (additional) fiducial mass region. Neutron candidates with $N_{10} = 5$ are shown in left, and those with $N_{10} = 6$ are shown in middle, and those with N_{10} of 7 or more are shown in right. The bold lines and arrows denote the neutron signal selection thresholds.

Table 6.5: Summary of the neutron tagging performance.

Region	Neutron Tagging Efficiency	False-positive Rate
Conventional	25.9%	0.016 per primary event
Additional	22.7%	0.029 per primary event

The neutron capture time and multiplicity distributions are shown in Fig. 6.31. A neutron capture time constant has been obtained by fitting the neutron capture time distribution to an exponential plus a constant. It is 217.5 ± 8.6 μsec (214.5 ± 23.5 μsec) in the conventional (additional) fiducial mass region for data, while it is 205.7 ± 7.6 μsec (205.0 ± 22.3 μsec) for MC. They are consistent with the previous result of 204.8 ± 0.5 μsec [113]. The neural network performance is validated in the following americium-beryllium (Am-Be) source calibration.

6.3.4 Am-Be Calibration

Calibration Setup

An americium-beryllium source is used to take neutron tagging calibration data. An ^{241}Am emits an α particle, and it interacts with ^{9}Be, and eventually emits a neutron as follows:

$$\alpha + {}^9\mathrm{Be} \rightarrow {}^{12}\mathrm{C}^* + n, \tag{6.46}$$

$$ {}^{12}\mathrm{C}^* \rightarrow {}^{12}\mathrm{C} + \gamma\ (4.43\ \mathrm{MeV}), \tag{6.47}$$

or

$$\alpha + {}^9\mathrm{Be} \rightarrow {}^{12}\mathrm{C}\ (\text{ground state}) + n. \tag{6.48}$$

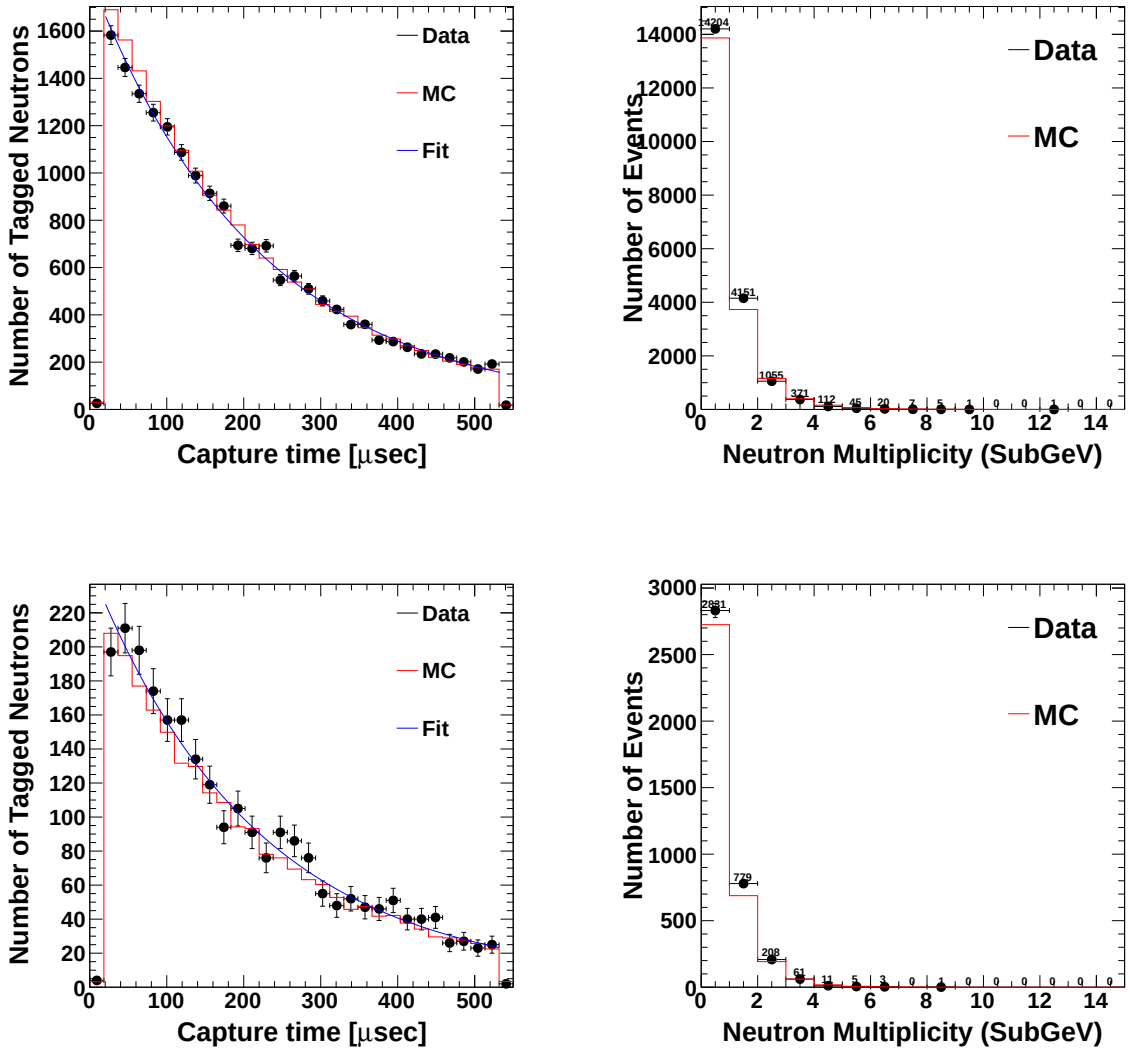

Figure 6.31: Neutron capture time (left) and multiplicity (right) distributions. The top (bottom) two plots correspond to tagged neutrons associated with the primary FC events in the conventional (additional) fiducial mass region. The black points shows the data in SK-IV, and the red histograms the atmospheric neutrino MC events and are normalized by livetime and the two-flavor oscillation probability ($\Delta m^2 = 2.5 \times 10^{-3}$ eV^2, $\sin^2 2\theta = 1.0$). The blue curves in the left plots are the best fit functions of the data histograms. $t = 0$ corresponds to the primary FC event timing. For the multiplicity distributions, only Sub-GeV primary FC events are used. Vertical error bars denote the statistical uncertainty.

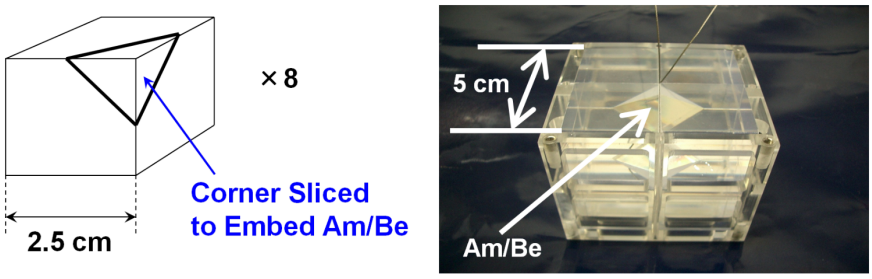

Figure 6.32: The Am-Be source used for the calibration. The source is embedded in a 5 cm cube of BGO scintillator and it is held in an acrylic case. Taken from [97].

The Am-Be source is embedded in a 5 cm cube of bismuth germanium oxide (BGO) scintillator as shown in Fig. 6.32. The scintillation light induced by the 4.43 MeV gamma ray in the BGO scintillator is used for triggering as "a primary FC event". In this calibration, the recorded timing width is extended from 535 μsec to 835 μsec. The Am-Be source was placed at three different points in the detector: (35.3, -70.7, 0.0) cm (Center), (35.3, -1201.9, 0.0) cm (Y12), and (35.3, -70.7, 1500.0) cm (Z15). The selection criteria for the primary event induced by the scintillation light are different depending on the source position, and they are as follows:

$$\text{Center} : 750 < \text{PE}_{\text{tot}} < 1050 \text{ p.e.'s}, \tag{6.49}$$

$$\text{Y12} : 850 < \text{PE}_{\text{tot}} < 1150 \text{ p.e.'s}, \tag{6.50}$$

$$\text{Z15} : 900 < \text{PE}_{\text{tot}} < 1150 \text{ p.e.'s}, \tag{6.51}$$

where PE_{tot} is the total deposited charge in the detector in a 1.3 μsec timing window around the trigger timing.

Am-Be Data Analysis

The same neural network algorithm trained on the atmospheric neutrino MC events is applied to both calibration data and MC. The difference in the neutron tagging efficiencies obtained in this calibration between data and MC is taken as a systematic uncertainty.

Neutron particle gun MC events have been generated as Am-Be calibration MC using the energy spectrum of the neutron from the α-Be reaction [114]. After combining with the random trigger data taken with the Am-Be source inside the detector (as background data), the same neural network is applied to the generated MC events.

The systematic uncertainties on the initial selection and final neural network selection are estimated separately. First, the systematic uncertainty on the initial selection is estimated by comparing the N_{10} distributions between calibration data and MC. In order to extract N_{10} distributions of true neutron candidates, the background component is statistically subtracted from the calibration data. The background component is obtained from the random trigger data. Figure 6.33 shows the N_{10} distributions of the calibration data, MC, and background data taken with the Am-Be source at Center. They are after the application of the initial selection ($N_{10} \geq 5$). Since the value of N_{10} has strong dependence on the photon detection efficiency (QE), various neutron MC predictions have been generated by varying the overall QE factor in SKDETSIM. For each MC prediction, a χ^2 test has been conducted on the N_{10} distribution of the calibration MC against the N_{10} distribution of the calibration data after the background subtraction, which is shown in the right plot in Figure 6.33. Figure 6.34 shows the χ^2 vs. relative QE change distribution. From the fitting result using a quadratic function, the 1 sigma error on the QE factor is estimated to be a 2.2% change. The 2.2% QE change corresponds to a 1.7% change in the number of initial neutron candidates. Therefore, the systematic uncertainty of 1.7% is assigned to the initial selection.

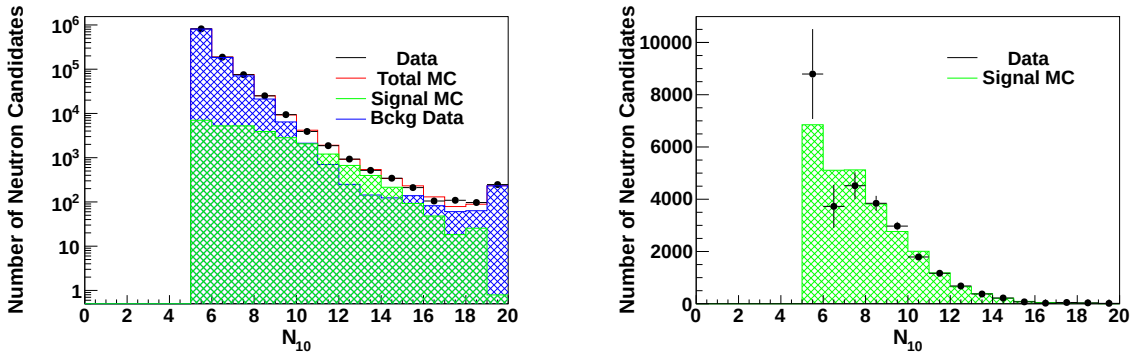

Figure 6.33: N_{10} distributions of the calibration data, MC, and background data taken with the Am-Be source at Center. The black dots in the left plot shows the calibration data, the red histogram shows the generated neutron MC (green) plus the background data (blue). The black dots in the right plot shows the calibration data after the subtraction of the background data (blue). Vertical error bars denote the statistical uncertainty. Entires with N_{10} of more than 20 are filled in the last bin. The green histograms are the standard MC outputs (without any QE changes).

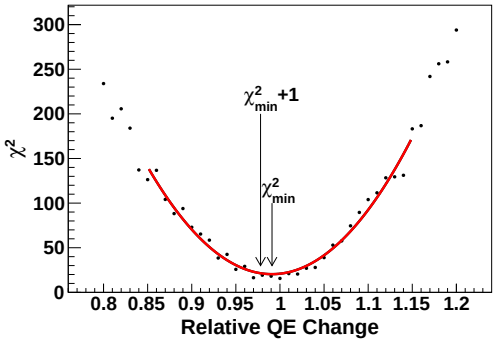

Figure 6.34: Chi-square test results as a function of relative QE change. The red curve is the best fit quadratic function. The χ^2 minimum corresponds to a 0.9% QE change, and the χ^2+1 point corresponds to a 2.2% QE change. The discrepancy between the standard MC prediction and χ^2+1 point is taken as a systematic uncertainty on the QE factor in MC.

Table 6.6: Summary of relative neutron tagging efficiency $\epsilon_{\rm NN}/\epsilon_{\rm IS}$ in units of %.

Am-Be Position	Data	MC	(MC-Data)/Data
Center	62.7	60.0	-4.5
Z15	62.5	67.0	8.8
Y12	68.1	65.9	-3.2

As for the neural network selection, the neural network neutron tagging efficiencies relative to the initial selection efficiencies are compared between data and MC for all three Am-Be source points. The neutron capture time distributions after applying the initial selection and after applying the neural network selection are fitted with an exponential plus a constant. Figure 6.35 shows neutron capture time distributions for Center data and MC. The obtained capture time values (τ's) are shown in Equations (6.54) $\sim$ (6.57). The relative neutron tagging efficiency ($\epsilon_{\rm NN}/\epsilon_{\rm IS}$) has been calculated by integrating the best fit exponential functions:

$$\epsilon_{\rm NN}/\epsilon_{\rm IS} = \frac{\int_{t=18\ \mu{\rm sec}}^{t=835\ \mu{\rm sec}} f_{\rm NN}(t)}{\int_{t=18\ \mu{\rm sec}}^{t=835\ \mu{\rm sec}} f_{\rm IS}(t)}, \tag{6.52}$$

$$f_{\rm IS,NN}(t) = A_{\rm IS,NN} \times \exp\left(-\frac{t}{\tau_{\rm IS,NN}}\right), \tag{6.53}$$

$$\tau_{\rm IS,Data} = 204.8 \pm 4.0\ \mu{\rm sec}, \tag{6.54}$$

$$\tau_{\rm IS,MC} = 204.7 \pm 4.0\ \mu{\rm sec}, \tag{6.55}$$

$$\tau_{\rm NN,Data} = 209.8 \pm 2.8\ \mu{\rm sec}, \tag{6.56}$$

$$\tau_{\rm NN,MC} = 198.3 \pm 2.6\ \mu{\rm sec}, \tag{6.57}$$

where A's are obtained by the fit, IS stands for the initial selection, and NN stands for the neural network selection. The estimated relative neutron tagging efficiencies are summarized in Table 6.6. The most discrepant value of 8.8% (Z15) is taken as the uncertainty on the neutral network selection. The combined systematic uncertainty on the neutron tagging efficiency is estimated to be 9.0%. This is used as the source of the systematic uncertainty for the proton decay searches described in Chapter 7.

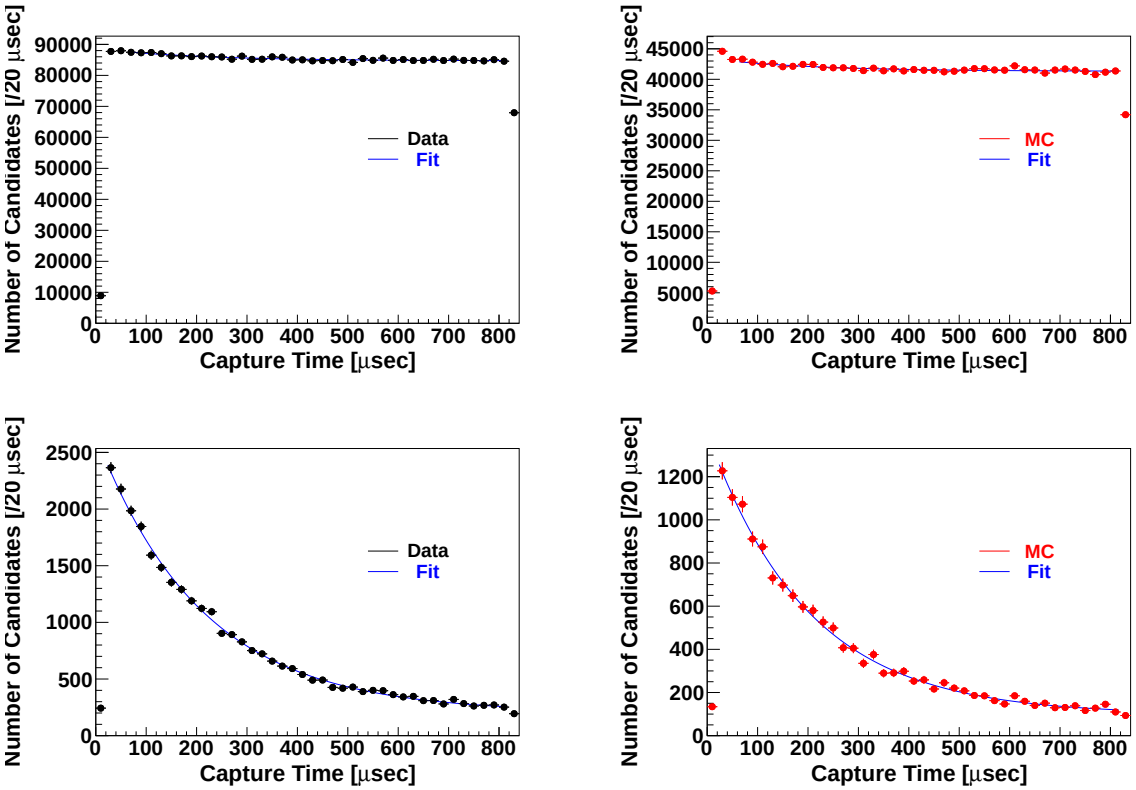

Figure 6.35: Neutron capture time distributions. The top two plots shows events after the initial selection. The bottom two plots shows events after the neural network selection. The left plots correspond to the calibration data taken with the Am-Be source at Center, while the right plots correspond to the neutron MC plus the background data. The blue curves are the best fit exponential plus constant functions. Vertical error bars denote the statistical uncertainty.

Chapter 7

Proton Decay Search Analysis

An analysis of the proton decay search via $p \to e^+\pi^0$ and $p \to \mu^+\pi^0$ with all SK-I to -IV enlarged fiducial mass FC data, which is described in Chapter 5 and corresponds to 450 kton·years exposure, is presented in this Chapter. First, the event selection criteria for the search for these modes as well as plots of variables used in the analysis are presented. The signal selection efficiency and the expected number of atmospheric neutrino background events for each mode are obtained by applying the same event selection criteria to the signal MC and atmospheric neutrino MC events, respectively, introduced in Chapter 4. Then, the unblinded data results are presented. As no proton decay signal has been found, lifetime limits together with the systematic uncertainties on the signal selection efficiency and the expected number of atmospheric neutrino background events are discussed. At last, the implications of the results and future prospects are discussed.

7.1 Proton Decay Search Performance

7.1.1 Proton Decay Signal Selection Criteria

The event selection criteria for the search for $p \to e^+\pi^0$ and $p \to \mu^+\pi^0$ are as follows:

C1 Events must pass the FC event selection criteria with a vertex within the fiducial mass region.

C2 Events must have two or three reconstructed Cherenkov rings.

C3 All rings must be reconstructed as showering (e-like) for $p \to e^+\pi^0$, and exactly one ring must be a non-showering (μ-like) for $p \to \mu^+\pi^0$.

C4 There must be no tagged Michel electrons for $p \to e^+\pi^0$ and exactly one for $p \to \mu^+\pi^0$.

C5 For events with three rings, the reconstructed π^0 mass must be $85 < M_{\pi^0} < 185$ MeV/c^2.

C6 The total reconstructed mass must be $800 < M_{\rm tot} < 1050$ MeV/c^2.

C7 The total momentum must be $P_{\rm tot} < 250$ MeV/c.

C8 For the SK-IV data, there must be no tagged neutrons.

The vertex resolution for the $p \to e^+\pi^0$ ($p \to \mu^+\pi^0$) MC events including proton decays within ^{16}O nuclei (bound proton decays) is 20.1 cm (22.5 cm) in the conventional fiducial mass region, and it is 26.3 cm (26.6 cm) in the additional.

The distributions of the number of reconstructed rings after applying **C1** are shown in Fig. 7.1. The π FSI effects discussed in Section 4.1 manifest in the number of reconstructed rings. When a neutral pion from the proton decay is absorbed or changes to a charged pion

with a momentum below the Cherenkov threshold, only a charged lepton from the proton decay is visible in the detector, and that event is reconstructed as a single-ring event. Since hit PMTs are more spatially localized in events closer to the ID wall, the two-ring event fraction in the additional fiducial mass region is higher than that in the conventional fiducial mass region.

The multi-ring PID distributions of the $p \to e^+\pi^0$ MC, atmospheric neutrino MC events, and data after applying **C1** $\sim$ **C2** are shown in Fig. 7.2. Although the signal selection efficiency for both modes has been improved by about 20% using the updated particle identification algorithm as described in Section 6.1.3, the PID performance in the additional fiducial mass region is still inferior to that in the conventional due to fewer PMT hits. As for the data and MC comparison, good agreement is confirmed with the new expected charge table.

Since there are no particles which decay to a Michel electron in $p \to e^+\pi^0$ decay events, events with at least one Michel electron are rejected in the $p \to e^+\pi^0$ selection. On the other hand, one Michel electron is expected from the muon decay for the $p \to \mu^+\pi^0$ mode. The distributions of the number of tagged Michel electrons after applying **C1** $\sim$ **C3** are shown in Fig. 7.3. Since it is easier for muons from the $p \to \mu^+\pi^0$ decays in the additional fiducial mass region to escape the ID, the Michel electron tagging efficiency in the additional fiducial mass region is lower than that in the conventional.

Criterion **C5** is applied to only three-ring events. The π^0 mass is calculated with every pair of rings for the $p \to e^+\pi^0$ mode. The pair giving the π^0 mass closest to 135 MeV/c^2 is considered to be two gamma rays from the π^0 decay. The π^0 mass distributions of three-ring events for the signal MC, atmospheric neutrino MC events, and data after applying **C1** $\sim$ **C4** are shown in Fig. 7.4.

The total reconstructed mass and total momentum distributions after applying all the selection cuts except cuts on the plotted variables are shown in Fig. 7.5. The kinematics of bound proton decays which experience π FSI scattering or correlated decay is distorted and is often reconstructed out of **C6** and **C7**. Furthermore, because of fewer PMT hits and particles escaping the ID, the total mass and total momentum distributions of the proton decay MC events in the additional fiducial mass region are wider than those in the conventional.

As presented in Section 6.3, the neutron tagging technique is applicable to only SK-IV data. The neutron emission probability in the proton decay MC events is expected to be less than 10%, while atmospheric neutrino events are often accompanied by neutrons. Figure 7.6 shows the distributions of the true number of produced neutrons per primary event after applying **C1** $\sim$ **C5**. No tagged neutrons are required at **C8**, and this criterion reduces the atmospheric neutrino backgrounds by about 50%. The distributions of the number of tagged neutrons after applying **C1** $\sim$ **C5** are shown in Fig. 7.7.

7.1.2 Search Performance

The signal selection efficiencies and the expected number of atmospheric neutrino background events for both the conventional and additional fiducial mass regions are estimated by applying the same selection criteria to the signal and atmospheric neutrino MC events. Their values at each event selection step are shown in Figure 7.8. The expected number of atmospheric neutrino background events is estimated using a 500-year equivalent exposure of atmospheric neutrino MC events for each SK phase (2000 years in total) and is normalized to detector livetime and the latest oscillation fit result [64] (oscillation parameters are mentioned in Section 4.2). The signal selection efficiency for both modes in the additional fiducial mass region has been improved by about 20% by the improvement of the event reconstruction algorithm as mentioned in Section 6.1.3. However, because of fewer ID PMT hits and escaping particles from the ID, signal selection efficiencies in the additional fiducial mass region are still lower than those in the conventional, especially in **C3** (PID) and **C6** (energy leakage due to escaping particles) for $p \to e^+\pi^0$, and **C3** (PID) and **C4** (muon escaping the ID) for $p \to \mu^+\pi^0$. For the $p \to e^+\pi^0$ ($p \to \mu^+\pi^0$) mode, the livetime-weighted total signal selection efficiency and the total expected

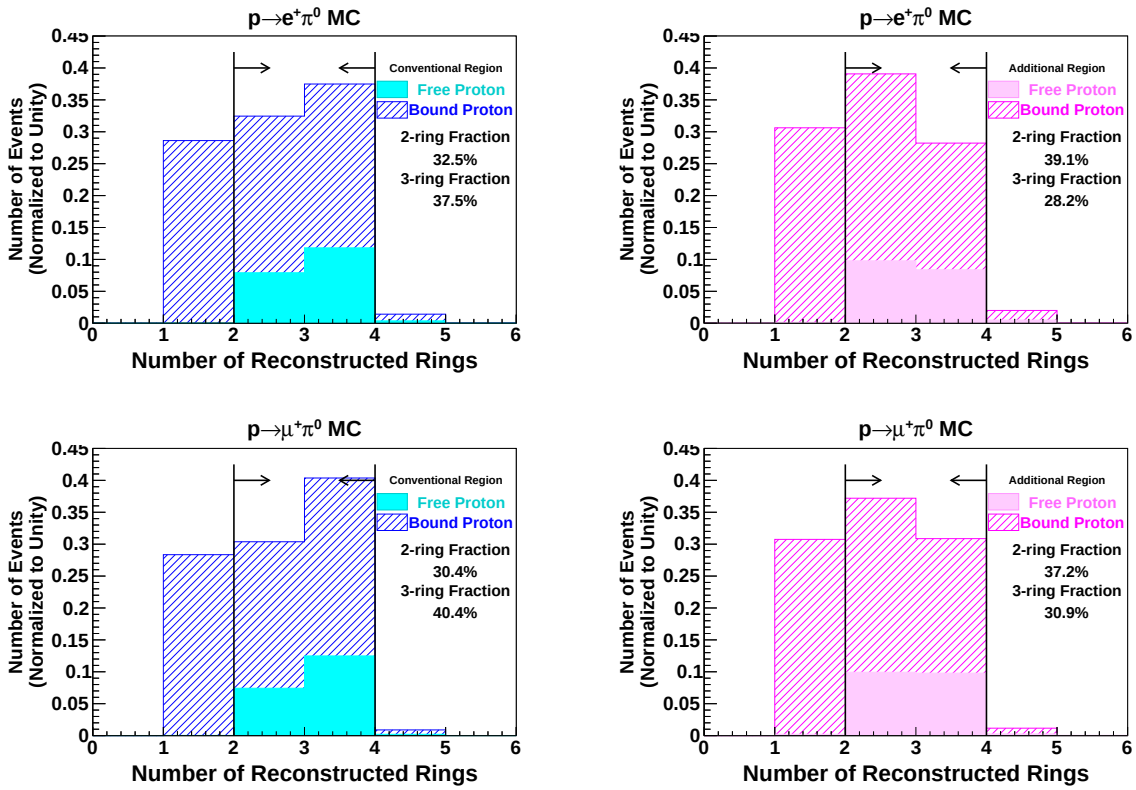

Figure 7.1: Distributions of the number of reconstructed rings after applying **C1**. They show the $p \to e^+\pi^0$ and $p \to \mu^+\pi^0$ MC events (SK-I to -IV are combined). Free proton decay events (light color) and bound proton events (dark color, hatched) are stacked. The left plots correspond to the conventional fiducial mass region, and the right plots to the additional. The distributions for the data in SK-I to -IV and atmospheric neutrino MC events are shown in Figure 6.7.

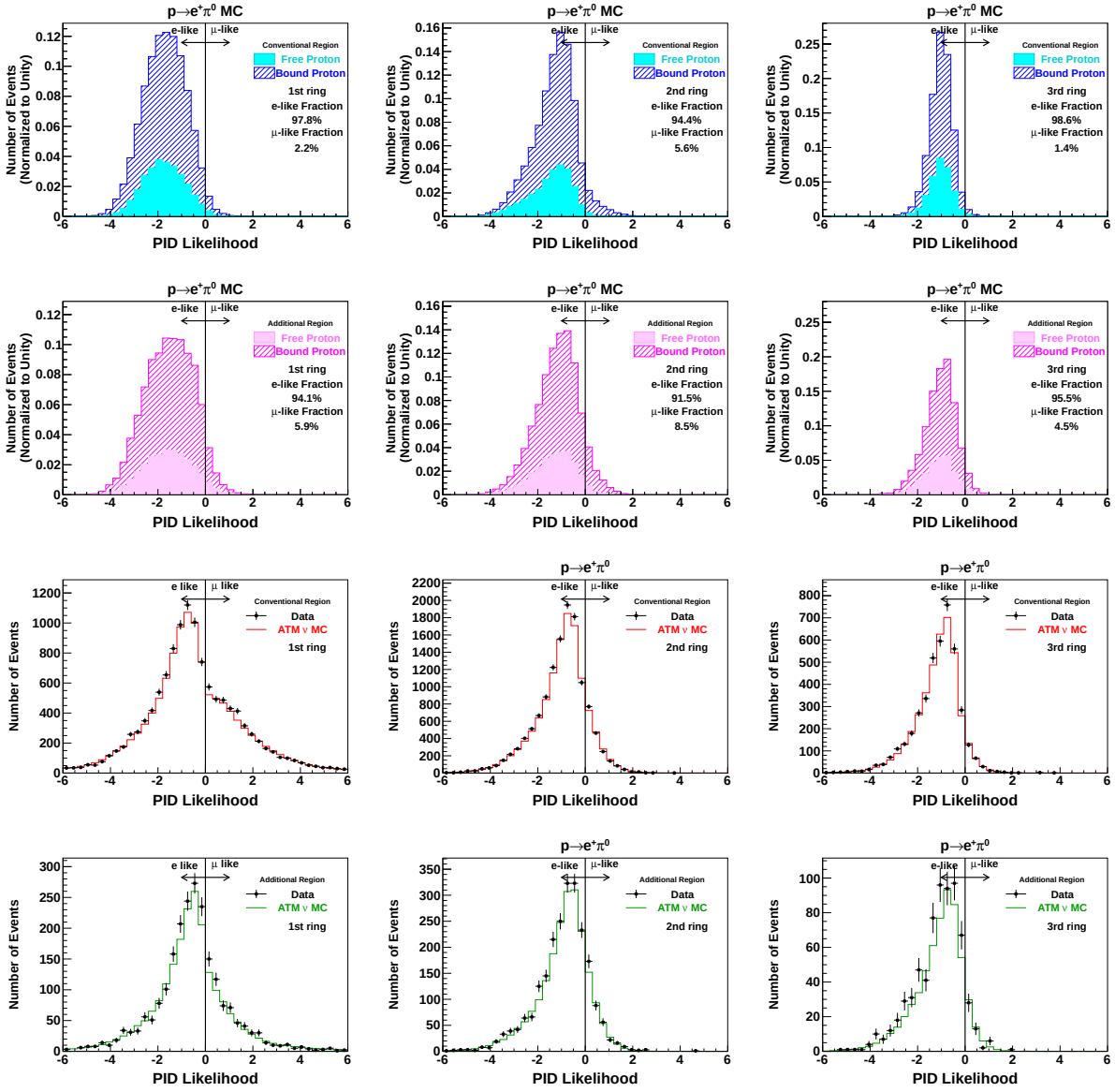

Figure 7.2: Multi-ring PID distributions after applying **C1** $\sim$ **C2**. The top six plots show the $p \to e^+\pi^0$ MC events (SK-I to -IV are combined). Free proton decay events (light color) and bound proton events (dark color, hatched) are stacked. The black dots show the data in SK-I to -IV, and the red and green histograms show the atmospheric neutrino MC events. Atmospheric neutrino MC is normalized by livetime and includes reweighting to the latest SK oscillation fit [64]. From left to right, the 1st to 3rd ring distributions are shown. The first and third plots from top correspond to the conventional fiducial mass region, and the second from top and bottom plots correspond to the additional. Vertical error bars on the data points denote the statistical uncertainty.

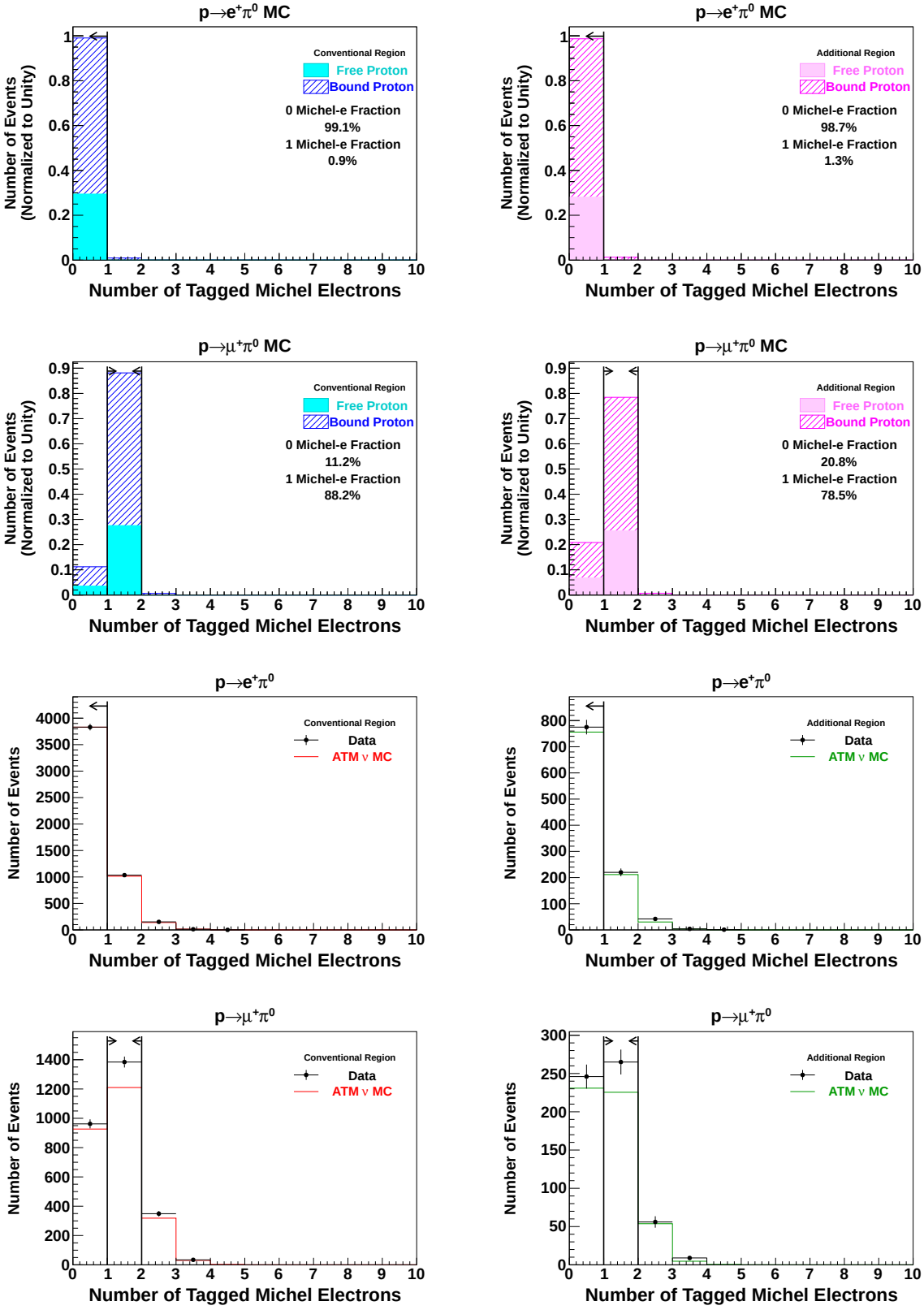

Figure 7.3: Distributions of the number of tagged Michel electrons after applying **C1** $\sim$ **C3**. The top four plots show the $p \to e^+\pi^0$ and $p \to \mu^+\pi^0$ MC events (SK-I to -IV are combined). Free proton decay events (light color) and bound proton events (dark color, hatched) are stacked. The black dots show the data in SK-I to -IV, and the red and green histograms show the atmospheric neutrino MC events. Atmospheric neutrino MC is normalized by livetime and includes reweighting to the latest SK oscillation fit [64]. Vertical error bars on the data points denote the statistical uncertainty. The event rate discrepancy between data and MC in the second bin for $p \to \mu^+\pi^0$ is within the systematic uncertainty associated with the physics modeling described in Section 7.3.1. The left plots correspond to the conventional fiducial mass region, and the right plots to the additional. 118

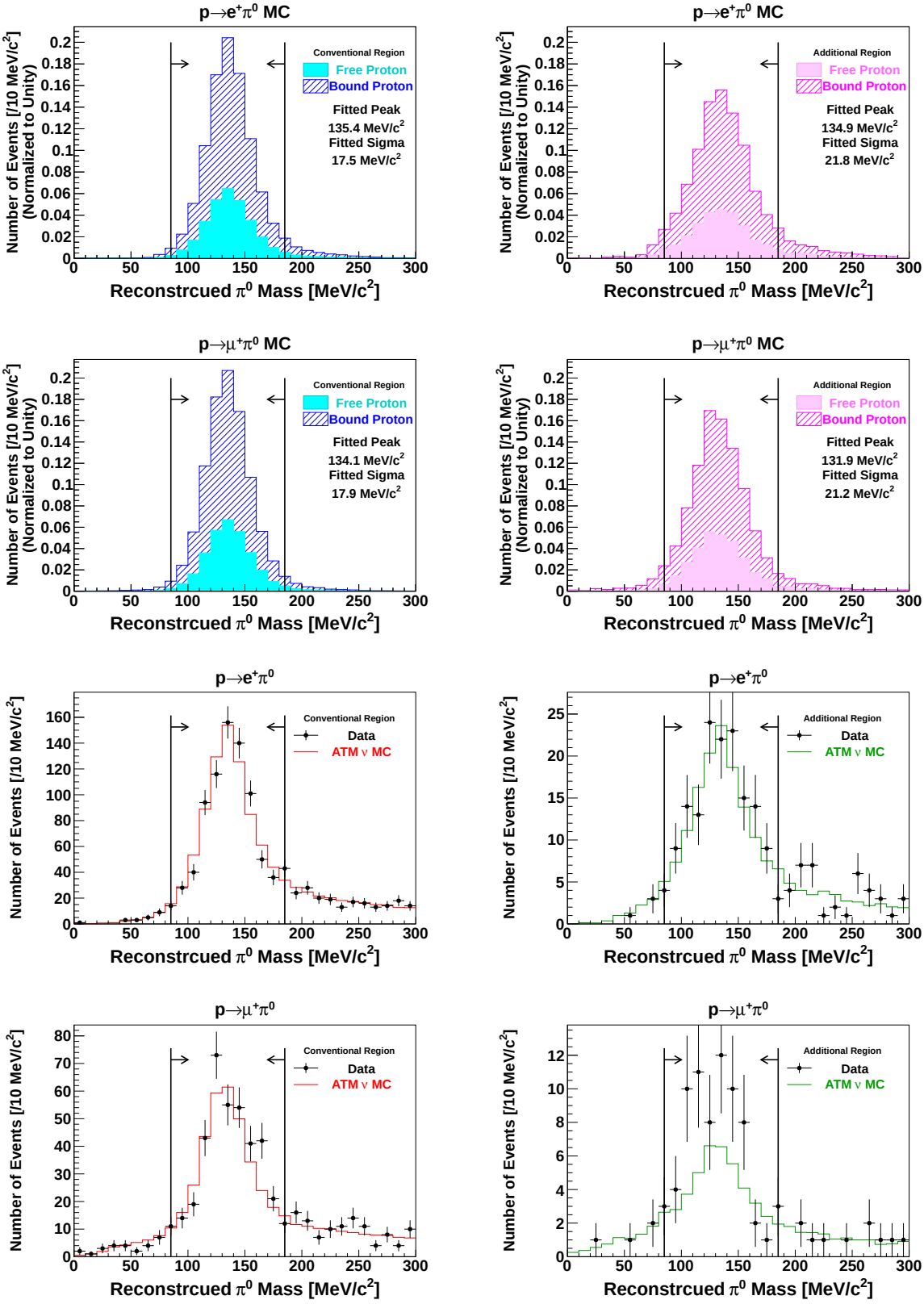

Figure 7.4: Neutral pion mass distributions of three-ring events after applying **C1** $\sim$ **C4**. The top four plots show the $p \to e^+\pi^0$ and $p \to \mu^+\pi^0$ MC events (SK-I to -IV are combined). Free proton decay events (light color) and bound proton events (dark color, hatched) are stacked. Gaussian fits have been used to determine the π^0 mass peak and width for the signal MC events. The black dots show the data in SK-I to -IV, and the red and green histograms show the atmospheric neutrino MC events. Atmospheric neutrino MC is normalized by livetime and includes reweighting to the latest SK oscillation fit [64]. Vertical error bars on the data points denote the statistical uncertainty. The left plots correspond to the conventional fiducial mass region, and the right plots to the additional.

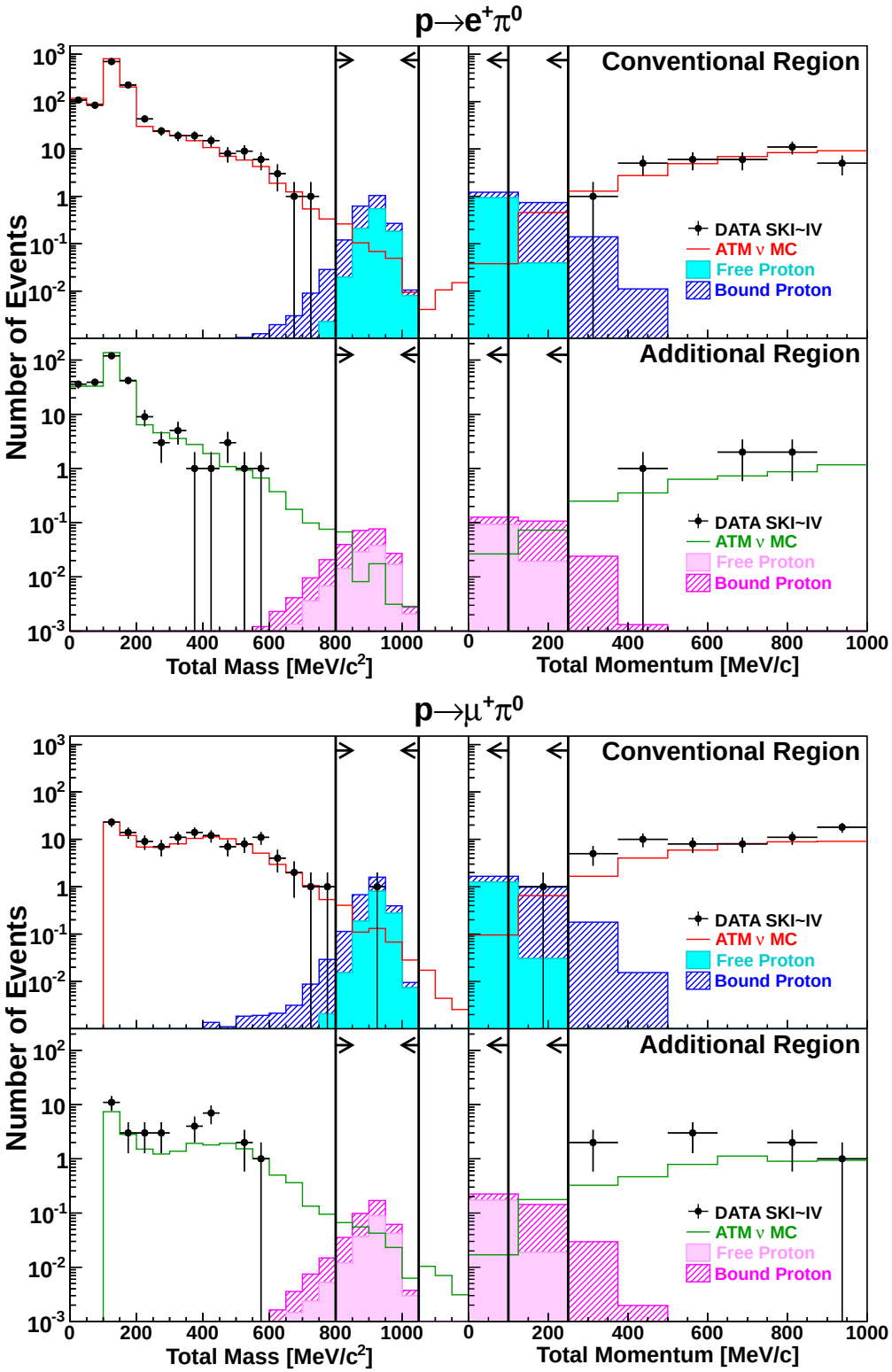

Figure 7.5: Reconstructed total mass and total momentum distributions for $p \to e^+\pi^0$ (top plot) and $p \to \mu^+\pi^0$ (bottom plot) after all the selection cuts except those on the plotted variables. In each plot, the top panels show the conventional, and the bottom panels show the additional fiducial mass region. The left panels show the reconstructed total mass, and the right panels show the reconstructed total momentum distributions. The signal MC histograms are stacked, showing free proton decay events (light color) and bound proton decay events (dark color, hatched), and they are normalized by the 90% C.L. upper limit on the signal derived in this work. Atmospheric neutrino MC (red and green) is normalized by livetime and includes reweighting to the latest SK oscillation fit [64]. Vertical error bars on the data points denote the statistical uncertainty. Bold lines and arrows show the signal region.

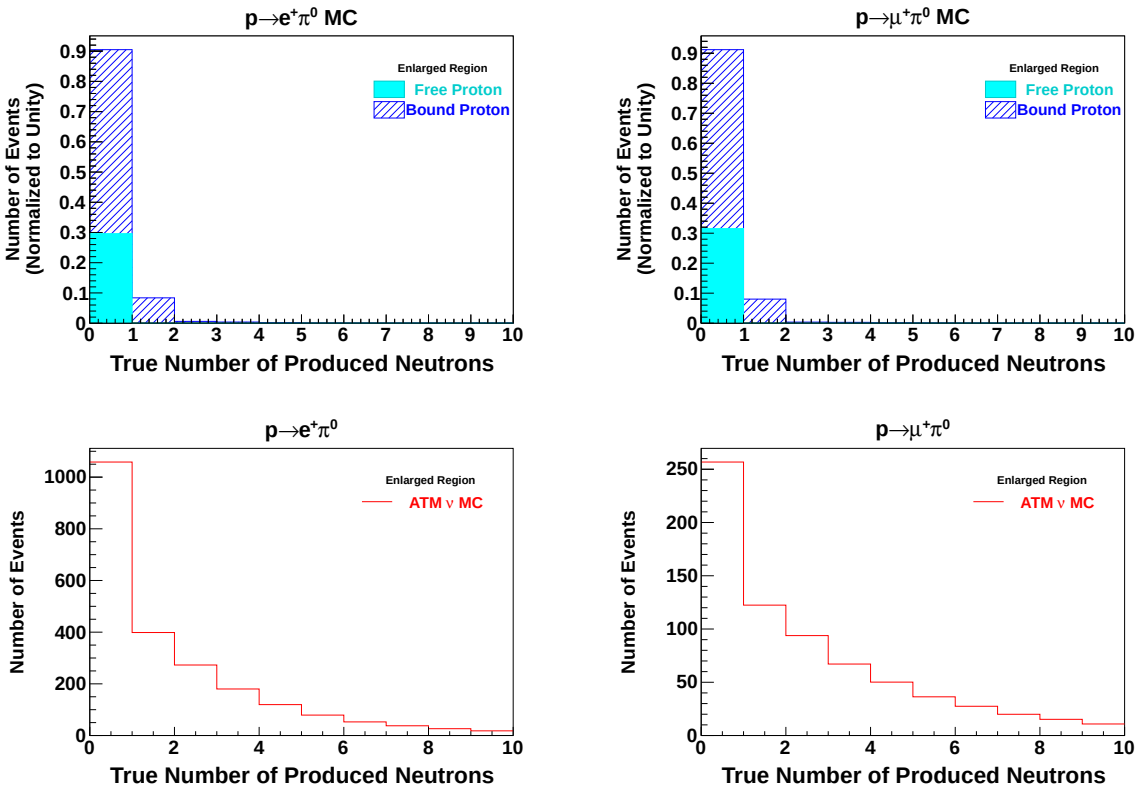

Figure 7.6: Distributions of the true number of produced neutrons after applying **C1** $\sim$ **C5**. All plots show the enlarged fiducial mass region (100 cm $< dwall$). The top two plots show the SK-IV $p \to e^+\pi^0$ (left) and $p \to \mu^+\pi^0$ (right) MC events. Free proton decay events (light color) and bound proton events (dark color, hatched) are stacked. As discussed in Section 4.1, neutrons are emitted only in bound proton decay events. Atmospheric neutrino MC is normalized by livetime and includes reweighting to the latest SK oscillation fit [64] and is shown in the bottom two plots.

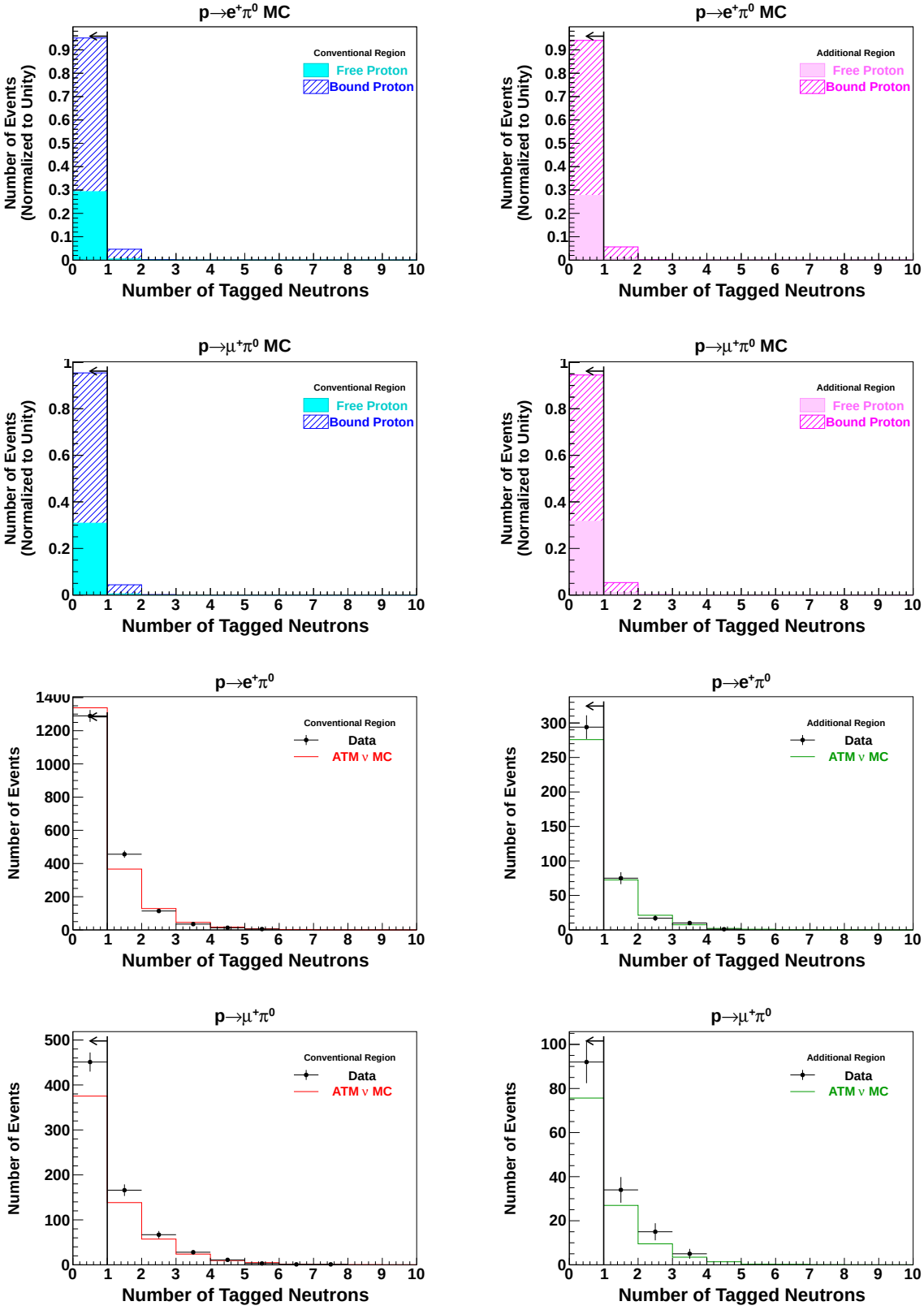

Figure 7.7: Distributions of the number of tagged neutrons after applying **C1** $\sim$ **C5**. The top four plots show the SK-IV $p \to e^+\pi^0$ and $p \to \mu^+\pi^0$ MC events. Free proton decay events (light color) and bound proton events (dark color, hatched) are stacked. The black dots show the data in SK-IV, and the red and green histograms show the atmospheric neutrino MC events. Atmospheric neutrino MC is normalized by livetime and includes reweighting to the latest SK oscillation fit [64]. Vertical error bars on the data points denote the statistical uncertainty. The overall event rate discrepancy between data and MC for $p \to \mu^+\pi^0$ is within the systematic uncertainty associated with the physics modeling described in Section 7.3.1. The left plots correspond to the conventional fiducial mass region, and the right plots to the additional.

Table 7.1: Summary of the livetime-weighted total signal selection efficiency and the total expected number of background events. The "Enlarged" row shows results for the enlarged 27.2 kton fiducial mass region. Detector phase by phase difference is shown in Table 7.3.

Region	Livetime-weighted total signal selection efficiency (%)	Total expected number of background events (events)
$p \to e^+\pi^0$		
Conventional	39.8	0.49
Additional	25.8	0.10
Enlarged	37.6	0.59
$p \to \mu^+\pi^0$		
Conventional	36.3	0.74
Additional	25.2	0.19
Enlarged	34.5	0.94

Table 7.2: Breakdown of interaction modes for background events remaining in the signal region for the $p \to e^+\pi^0$ and $p \to \mu^+\pi^0$ searches in units of %. Here, CC and NC stand for charged-current and neutral-current, respectively, and QE, 1π and DIS stand for quasi-elastic scattering, single π production and deep inelastic scattering, respectively.

Region	CCQE	CC1π	CCDIS	NC1π	NCDIS
$p \to e^+\pi^0$					
Conventional	18	63	10	1	8
Additional	21	62	14	0	3
$p \to \mu^+\pi^0$					
Conventional	13	65	18	0	4
Additional	7	60	17	0	16

number of background events in the additional fiducial mass region are 25.8% (25.2%) and 0.10 (0.19), respectively, while in the conventional fiducial mass region, they are 39.8% (36.3%) and 0.49 (0.74). They are summarized in Table 7.3 including the performance in the combined (enlarged) fiducial mass region.

The incoming neutrino energy distributions of the remaining backgrounds are shown in Fig. 7.9. Atmospheric neutrinos of about 1 to 3 GeV are the main background component in both fiducial mass regions. A breakdown of the remaining atmospheric neutrino background events by neutrino interaction mode is shown in Table 7.2. As mentioned in Section 4.2, the dominant interaction mode is the charged current single π production interaction, and there are no significant differences between the two fiducial mass regions. The expected background rate for $p \to e^+\pi^0$ without **C8** is 1.83 /Mt·years and is consistent with previous estimations by the K2K 1 kton water Cherenkov detector of $1.63^{+0.42}_{-0.33}$ (stat)$^{+0.45}_{-0.51}$ (sys) /Mt·years [115].

In order to improve the search sensitivity, the signal region is further divided into two regions: a lower total momentum region ($P_{\rm tot} < 100$ MeV/c) and a higher total momentum region ($100 \leq P_{\rm tot} < 250$ MeV/c). The final signal selection efficiencies and expected number of atmospheric neutrino background events for each SK phase are summarized in Table 7.3. Figure 7.10 shows the reconstructed total mass vs. total momentum distributions for the signal MC, atmospheric neutrino MC and all data from SK-I to -IV after all the selection cuts except the cuts on the plotted variables. In the lower $P_{\rm tot}$ signal region, most free proton decay events are reconstructed, and a nearly background-free search can be performed in both fiducial mass regions. Bound proton decays reconstructed outside the signal region in Fig. 7.10 are mainly due to the effects of π FSI scattering in the remaining nucleus and correlated decay.

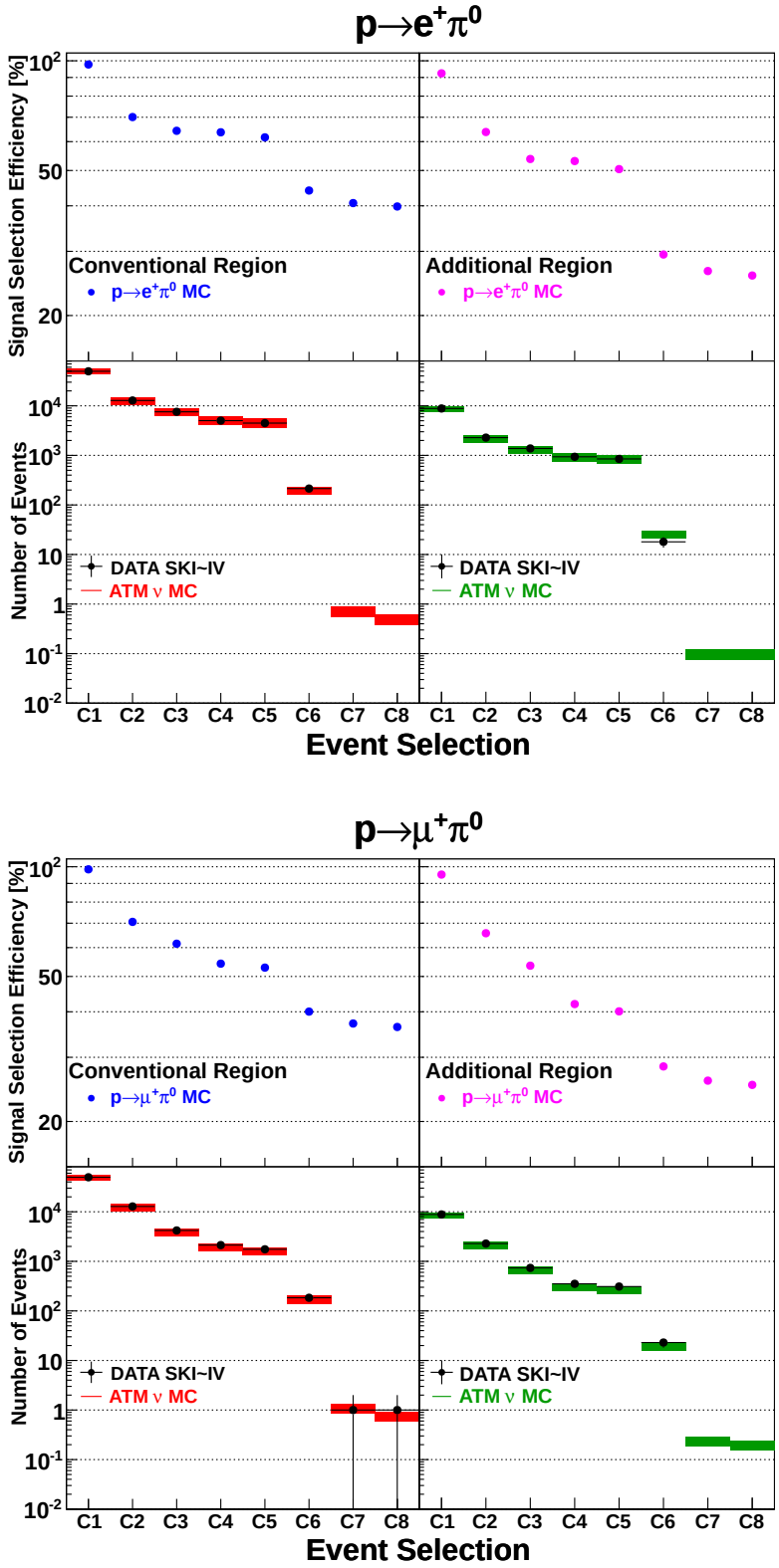

Figure 7.8: The signal selection efficiencies (blue and magenta dots) and the expected number of atmospheric neutrino background events (red and green histograms) and data candidates (black dots) for $p \to e^+\pi^0$ (top plot) and $p \to \mu^+\pi^0$ (bottom plot). Vertical error bars on the data points denote the statistical uncertainty. In each plot, the left panel corresponds to the conventional fiducial mass region and the right panel to the additional. Atmospheric neutrino MC is normalized by livetime and includes reweighting to the latest SK oscillation fit [64]. Vertical bands on the atmospheric neutrino MC points denote the sum in quadrature of the systematic uncertainties associated with the physics modeling described in Section 7.3.1. The combined data from SK-I to -IV is shown along with the combined signal and background MC.

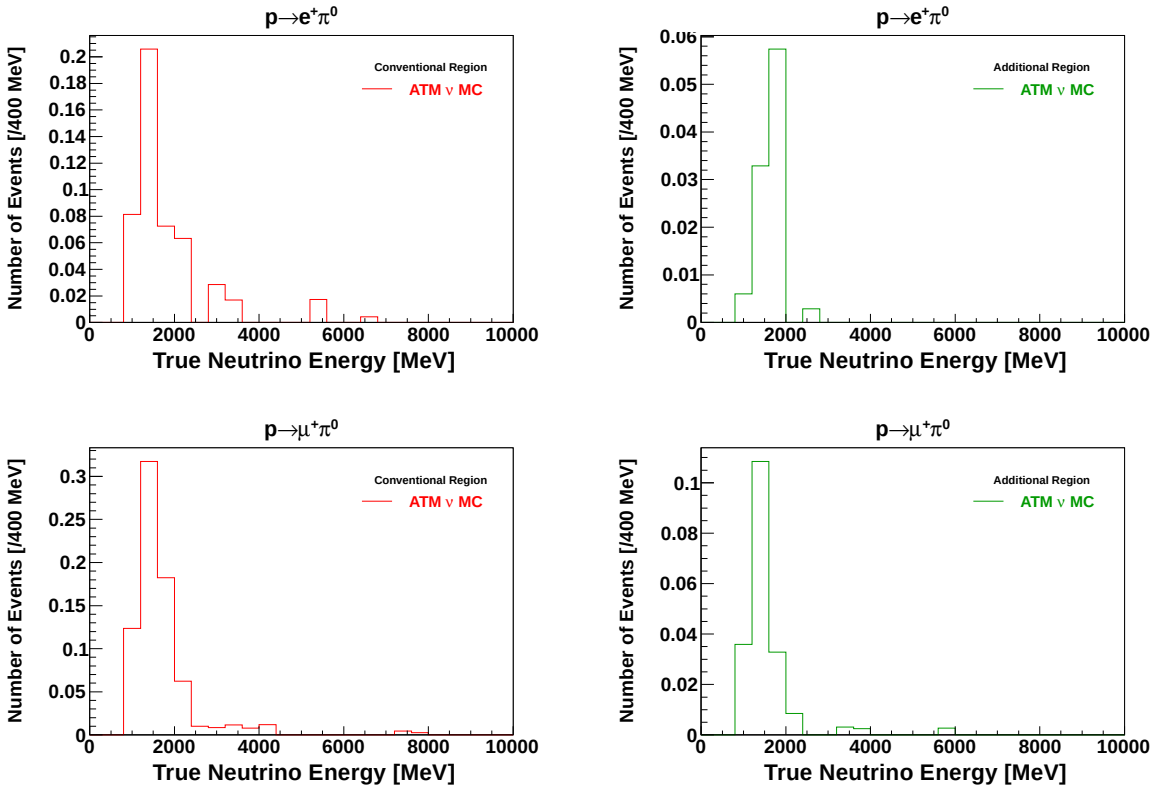

Figure 7.9: Incoming neutrino energy distributions of the remaining backgrounds (SK-I to -IV are combined). The upper (lower) two plots show the atmospheric neutrino MC events in the signal region for $p \to e^+\pi^0$ ($p \to \mu^+\pi^0$). These histograms are normalized by livetime and include reweighting to the latest SK oscillation fit [64]. The left plots correspond to the conventional fiducial mass region, and the right plots to the additional.

Table 7.3: Summary of the signal selection efficiencies, the expected number of background events and the number of data candidates for 92.1 (19.3), 49.1 (10.3), 31.9 (6.7) and 199.5 (41.8) kton·years exposures from the conventional (additional) fiducial mass region of SK-I, -II, -III, and -IV, respectively. The "Enlarged" row shows results for the enlarged 27.2 kton fiducial mass region. Here "Lower" and "Upper" indicate $P_{\rm tot} < 100$ MeV/c and $100 \leq P_{\rm tot} < 250$ MeV/c, respectively. Errors in the signal selection efficiency and the expected number of background events are the quadratic sum of MC statistical error and systematic errors.

Search Mode		Signal Selection Efficiency (%)				Atmospheric ν Background (events)					Candidate (events)			
Region		I	II	III	IV	I	II	III	IV	I to IV	I	II	III	IV
$p \to e^+\pi^0$														
Conventional	(Lower)	19.9±1.9	18.1±1.8	20.3±1.8	19.6±1.6	< 0.01	0.01±0.01	< 0.01	< 0.01	0.01±0.01	0	0	0	0
	(Upper)	21.0±3.5	20.2±3.2	21.1±3.5	19.8±3.3	0.13±0.05	0.11±0.04	0.05±0.02	0.20±0.09	0.48±0.21	0	0	0	0
Additional	(Lower)	9.6±1.5	8.8±1.4	9.9±1.7	11.0±1.5	0.01±0.01	< 0.01	< 0.01	< 0.01	0.01±0.01	0	0	0	0
	(Upper)	14.5±2.9	14.9±2.7	16.4±2.8	15.9±2.6	0.02±0.01	< 0.01	0.02±0.01	0.05±0.04	0.09±0.05	0	0	0	0
Enlarged	(Lower)	18.3±1.7	16.6±1.7	18.7±1.7	18.2±1.5	0.01±0.01	0.01±0.01	< 0.01	< 0.01	0.02±0.02	0	0	0	0
	(Upper)	20.0±3.3	19.4±3.0	20.3±3.3	19.2±3.1	0.15±0.06	0.11±0.04	0.07±0.03	0.25±0.11	0.57±0.23	0	0	0	0
$p \to \mu^+\pi^0$														
Conventional	(Lower)	17.0±1.6	16.2±1.5	17.5±1.6	19.9±1.9	0.03±0.02	< 0.01	0.01±0.01	< 0.01	0.04±0.03	0	0	0	0
	(Upper)	16.7±3.1	16.5±2.8	16.8±3.0	18.9±3.7	0.19±0.06	0.10±0.04	0.06±0.02	0.34±0.12	0.70±0.24	0	0	0	1
Additional	(Lower)	11.1±1.5	8.8±1.2	11.0±1.4	12.7±1.2	< 0.01	< 0.01	< 0.01	< 0.01	0.01±0.01	0	0	0	0
	(Upper)	12.0±2.3	12.6±2.3	12.5±2.2	14.7±2.6	0.02±0.02	0.03±0.01	0.02±0.01	0.12±0.06	0.19±0.08	0	0	0	0
Enlarged	(Lower)	16.0±1.5	14.9±1.4	16.4±1.5	18.7±1.7	0.03±0.02	0.01±0.01	0.01±0.01	< 0.01	0.05±0.03	0	0	0	0
	(Upper)	16.0±2.9	15.8±2.7	16.1±2.9	18.2±3.4	0.21±0.07	0.14±0.04	0.08±0.03	0.46±0.15	0.89±0.29	0	0	0	1

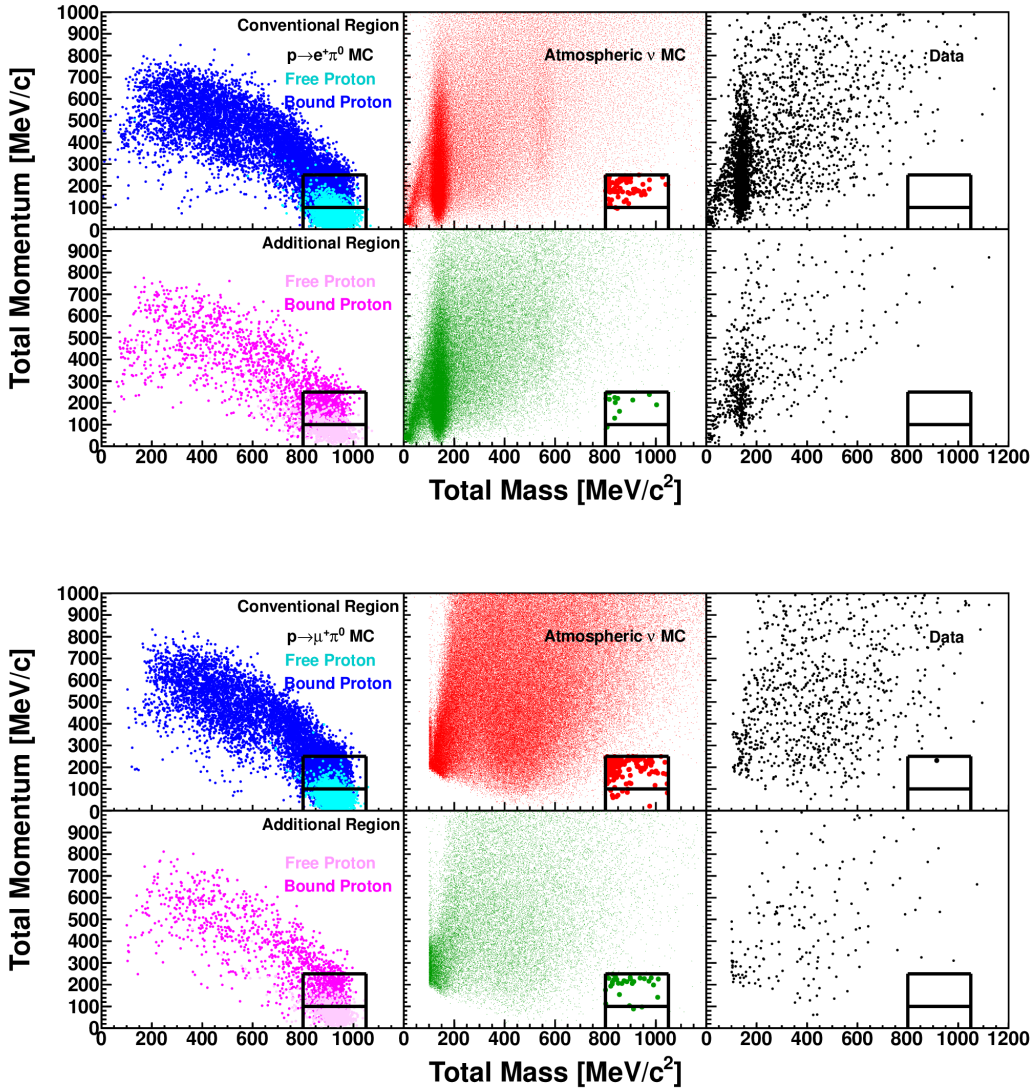

Figure 7.10: Reconstructed total mass shown against the total momentum distributions for $p \to e^+\pi^0$ (top) and $p \to \mu^+\pi^0$ (bottom) after all cuts except those on these variables. In each plot, the top panels correspond to the conventional and the bottom panels correspond to the additional fiducial mass region. The left panels show the signal MC (SK-I to -IV are combined), where lighter colors show free proton decays and dark colors show bound proton decays. The middle panels show the 2000-year equivalent atmospheric neutrino MC. The right panels show all the combined data from SK-I to -IV. The black box shows the signal region, and for the middle and right panels, the markers in the signal region have been enlarged for visibility.

Table 7.4: Summary of the search sensitivities (expected lifetime limit at 90% confidence level). "Conventional" denotes the conventional fiducial mass case (22.5 kton, 372 kton·years exposure), and "Enlarged" denotes the enlarged fiducial mass case (27.2 kton, 450 kton·years exposure).

Region	$p \to e^+\pi^0$	$p \to \mu^+\pi^0$
Conventional	1.7×10^{34} years	1.4×10^{34} years
Enlarged	1.9×10^{34} years	1.6×10^{34} years

7.1.3 Search Sensitivity Improvement by Enlarging the Fiducial Mass

The search sensitivity (expected lifetime limit at 90% confidence level, $\tau_{\rm exp}$) is calculated as follows:

$$\Gamma_{\rm exp} = \sum_{n=0}^{\infty} \frac{{\rm e}^{-b} b^n}{n!} \times \Gamma_{\rm limit}(b, n), \tag{7.1}$$

$$\tau_{\rm exp}/B = \frac{1}{\Gamma_{\rm exp}}, \tag{7.2}$$

where $\Gamma_{\rm exp}$ is the expected decay rate, b is the expected number of background events, n is the number of candidate events, and B is the branching ratio of a particular decay mode. Here, $\Gamma_{\rm limit}(b, n)$ is an upper limit of the decay rate with a candidate of n and a background of b, and the derivation of $\Gamma_{\rm limit}(b, n)$ is detailed in Section 7.4. Using the signal selection efficiencies, expected number of backgrounds, exposure in Table 7.3, and their systematic uncertainties described in Section 7.3, the search sensitivity is calculated for both the conventional fiducial mass (22.5 kton, 372 kton·years exposure) case and enlarged (27.2 kton, 450 kton·years exposure) case. Although the signal selection efficiencies in the additional fiducial mass region are lower than those in the conventional fiducial mass region, the search sensitivity for $p \to e^+\pi^0$ ($p \to \mu^+\pi^0$) is improved from 1.7×10^{34} years (1.4×10^{34} years) to 1.9×10^{34} years (1.6×10^{34} years) at 90% confidence level by enlarging the fiducial mass. For both modes, the search sensitivity improves by about 12% (Table 7.4).

7.2 Search Results

By applying the same proton decay selection criteria to a 450 kton·years exposure of the SK-I to -IV enlarged fiducial mass data, proton decay search results have been obtained. In the $p \to e^+\pi^0$ mode, no signal candidates have been observed in either the conventional or additional fiducial mass region. On the other hand, a single candidate is found for the $p \to \mu^+\pi^0$ mode, which is the same candidate event reported in the last published analysis [27]. The one candidate is in the higher $P_{\rm tot}$ signal region and the conventional fiducial mass region. No new candidates have been observed in the updated dataset. The number of observed candidates is consistent with the total atmospheric neutrino backgrounds, 0.59 events for $p \to e^+\pi^0$, and 0.94 events for $p \to \mu^+\pi^0$. For $p \to \mu^+\pi^0$, the Poisson probability to observe 1 event or more with a mean value of 0.94 is 61%. The data distributions are consistent with the atmospheric neutrino MC predictions. The event rate discrepancy between data and MC for the $p \to \mu^+\pi^0$ mode is covered by the systematic uncertainties associated with the physics modeling described in Section 7.3.1.

The event display of the single candidate event for the $p \to \mu^+\pi^0$ mode is shown in Fig. 7.11. It is a two-ring event, and there is one μ-like ring with a momentum of 559 MeV/c and one e-like ring with a momentum of 377 MeV/c. The distance between the vertex position and the closest ID wall is 458 cm, in the conventional fiducial mass region. The reconstructed total mass is 917 MeV/c^2, and the reconstructed total momentum is 233 MeV/c, in the higher $P_{\rm tot}$ signal region.

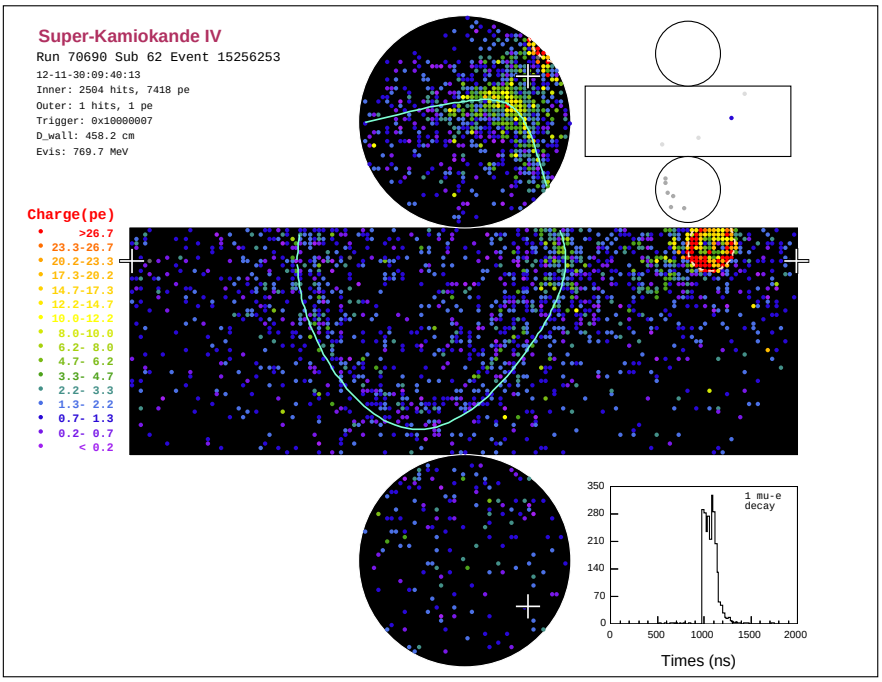

Figure 7.11: Run:70690, SubRun:62, Event:15256253. Event display of the $p \to \mu^+\pi^0$ candidate event. Two-ring event. The orange circle denote the μ-like ring and the cyan circle denote the e-like ring.

7.3 Systematic Uncertainty

Systematic uncertainties for the signal selection efficiencies and the expected number of atmospheric neutrino events have been estimated. Uncertainties on the expected number of atmospheric neutrino events have been evaluated combining the higher and lower P_{tot} signal regions because there are only a few events remaining in the lower P_{tot} signal region.

Uncertainties of the physics modeling as well as the reconstruction performance are considered. As systematic uncertainties associated with the physics modeling, the following three items are taken into account for the signal selection efficiency:

- correlated decay,
- the Fermi momentum,
- π FSI,

and the following three are for the expected number of atmospheric neutrino events:

- neutrino flux,
- neutrino interaction,
- π FSI and SI.

Since particles in the final state of proton decay $p \to e^+\pi^0$ and $p \to \mu^+\pi^0$ events are gamma rays and a charged lepton, the hadron secondary interaction in water (SI) is not considered for the signal selection efficiency. For the reconstruction part, systematic uncertainties associated with the following items are commonly considered for both the signal selection efficiencies and expected number of atmospheric neutrino events:

- fiducial volume,
- vertex position,
- number of identified Cherenkov rings,
- identified particle type,
- number of tagged Michel electrons,
- energy scale,
- non-uniformity of the energy scale,
- number of tagged neutrons.

Unless otherwise noted, the systematic uncertainty for each item is evaluated as follows:

$$\text{systematic uncertainty} = \begin{cases} \frac{\epsilon_{\mathrm{sys}} - \epsilon_{\mathrm{def}}}{\epsilon_{\mathrm{def}}}, & \text{(signal selection efficiency)} \\ \frac{\mathrm{Bkg}_{\mathrm{sys}} - \mathrm{Bkg}_{\mathrm{def}}}{\mathrm{Bkg}_{\mathrm{def}}}, & \text{(expected number of atmospheric neutrino events)} \end{cases} \tag{7.3}$$

where ϵ_{def} ($\mathrm{Bkg}_{\mathrm{def}}$) is the central value of the signal selection efficiency (expected number of atmospheric neutrino events) shown in Table 7.3, and ϵ_{sys} ($\mathrm{Bkg}_{\mathrm{sys}}$) is the changed signal selection efficiency (expected number of atmospheric neutrino events) by introducing the source uncertainty of each item. The systematic uncertainties are estimated in each (either conventional, additional, or enlarged) fiducial mass region separately. In the following, the evaluation method for each item is described, and a summary of the evaluated systematic uncertainties is presented in Section 7.3.3.

7.3.1 Physics Modeling

First, the systematic uncertainties associated with the physics modeling, which is introduced in Chapter 4, for the signal selection efficiency are discussed, and then those for the atmospheric neutrino events are described.

Correlated Decay

The probability of the correlated decay in proton decays within ^{16}O is predicted to be about 10% [46]. The changed signal selection efficiency is estimated by reweighting the correlated decay probability to 0% or 20%:

$$\epsilon_{\rm sys} = \frac{n_{\rm free}}{N_{\rm tot}} + \frac{(N_S + N_P \mp \alpha N_{\rm corr})}{(N_S + N_P)} \times \frac{(n_S + n_P)}{N_{\rm tot}} + (1 \pm \alpha) \times \frac{n_{\rm corr}}{N_{\rm tot}}, \tag{7.4}$$

where n is the number of signal MC events passing the signal selection criteria, N is the number of generated proton decay MC events in the fiducial volume, "free" stands for free proton decays, S (P) stands for proton decays in the S (P) state in ^{16}O, and "corr" stands for correlated decays. Using this notation, the central value of the signal selection efficiency is expressed as:

$$\epsilon_{\rm def} = \frac{(n_{\rm free} + n_S + n_P + n_{\rm corr})}{N_{\rm tot}}. \tag{7.5}$$

A factor of α is taken to be 1 (the correlated decay probability is twice) or -1 (no correlated decays), and a factor of $\frac{(N_S+N_P\mp\alpha N_{\rm corr})}{(N_S+N_P)}$ is introduced to conserve the total number of generated events. The more discrepant $\epsilon_{\rm sys}$ between the $\alpha = 1$ and $\alpha = -1$ cases is used for the uncertainty estimation.

The Fermi Momentum

The difference in the initial proton momentum distributions between the proton decay MC and atmospheric neutrino (NEUT) MC is considered to be the source of this item. The two plots are shown in Fig. 4.10. The changed signal selection efficiency is calculated by reweighting to fit the initial proton momentum distribution to that in NEUT:

$$\epsilon_{\rm sys} = \frac{n_{\rm free}}{N_{\rm tot}} + \sum_{i=1}^{11} \frac{n_i}{N_{\rm tot}} \times \frac{N_{{\rm NEUT},i}}{N_{{\rm PDK},i}}, \tag{7.6}$$

where i is the index of each initial momentum bin, $N_{{\rm PDK},i}$ ($N_{{\rm NEUT},i}$) is the number of generated events with an initial proton momentum of between $(25 \times (i-1))$ MeV/c and $(25 \times i)$ MeV/c in the proton decay (NEUT) MC. In order to conserve the total number of generated events, $N_{{\rm NEUT},i}$ is normalized to $N_{{\rm PDK},i}$:

$$\sum_{i=1}^{11} N_{{\rm PDK},i} = \sum_{i=1}^{11} N_{{\rm NEUT},i}. \tag{7.7}$$

Pion FSI and SI

The π FSI and SI probabilities in MC are calculated with six internal parameters, and they are determined based on π scattering experiment results as described in Section 4.1. For the six internal parameters, 16 different parameter sets are prepared so that the possible parameter space, which is suggested by the π scattering experiments, can be covered [49]. The signal selection efficiency ($\epsilon_{\rm sys}$) and expected number of atmospheric neutrino backgrounds (Bkg$_{\rm sys}$) are recalculated based on different π FSI and SI probabilities using the 16 parameter sets. For this item, the standard deviation of 16 $\epsilon_{\rm sys}$'s and Bkg$_{\rm sys}$'s over each mean value is assigned as the uncertainty.

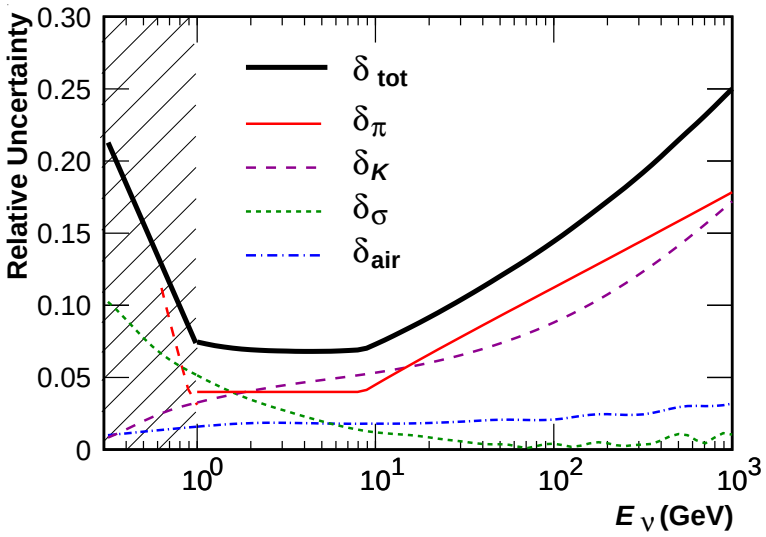

Figure 7.12: Uncertainty on the absolute flux normalization as a function of neutrino energy. The black line shows the total uncertainty. The red, purple, green, and blue lines show the uncertainty associated with the π production modeling, K production modeling, hadronic interaction cross-sections, and atmospheric density profile, respectively. Taken from [54].

Neutrino Flux

The uncertainty on the atmospheric neutrino flux is divided into various components and is summarized in Table 7.5. The dominant uncertainty source is the absolute flux normalization. It is provided by [54] and is the sum of the uncertainties on the π, K production modeling (δ_π, δ_K), hadronic interaction cross-sections (δ_σ), and atmospheric density profile (δ_{air}). The absolute normalization uncertainty as a function of neutrino energy is shown in Fig. 7.12.

Neutrino Interaction

The uncertainty on the atmospheric neutrino interaction (cross-section) is also divided into different items depending on the interaction mode. The estimated uncertainties are summarized in Table 7.6.

The dominant uncertainty source is the single meson production interaction as is expected from the interaction mode breakdown of the remaining backgrounds shown in Table 7.2. This is estimated by varying the new form factors, which are introduced in Section 4.3.3, by their error size. Furthermore, the cross-section ratios $\bar{\nu}/\nu$ and (π^0 production)/($\pi^\pm$ production) are taken into account by comparing the NEUT model and another model by E. Hernández *et al.* [116].

The sub-dominant component is the quasi-elastic scattering. The uncertainties on the absolute total cross-section as well as the cross-section ratios $\bar{\nu}/\nu$ and $(\nu_\mu + \bar{\nu}_\mu)/(\nu_e + \bar{\nu}_e)$ are estimated from the difference between the NEUT prediction and another model prediction by J. Nieves *et al.* [117]. Besides, an uncertainty of 20% is assigned to the axial vector mass.

7.3.2 Reconstruction

Fiducial Volume

The uncertainty associated with the fiducial volume is estimated to be 1.2% by comparing the number of events between data and MC. For this item, FC Sub-GeV multi-ring events are used. The number of atmospheric neutrino MC events within the conventional fiducial volume (200 cm $<$ *dwall*) is normalized to that of data for this calculation. The systematic uncertainty for this item is defined to be the difference in the number of events between data and normalized

Table 7.5: Summary of systematic uncertainties on the expected number of atmospheric neutrino background events for each fiducial mass region in units of %. They are associated with the atmospheric neutrino flux model. The "Enlarged" row shows the result for the combination of the two fiducial mass regions.

Region	Absolute Normalization	ν and $\bar{\nu}$ Flux Ratios	Up-down Ratio	K-π Ratio	Neutrino Path Length	Solar Activity	Relative Normalization in Multi-GeV Region	Matter Effect	Total
$p \to e^+\pi^0$									
Conventional	7.0	2.2	0.1	0.2	< 0.1	0.5	< 0.1	< 0.1	7.3
Additional	7.0	1.7	0.4	0.3	< 0.1	0.3	< 0.1	< 0.1	7.2
Enlarged	7.0	2.2	0.2	0.2	< 0.1	0.4	< 0.1	< 0.1	7.3
$p \to \mu^+\pi^0$									
Conventional	6.8	1.9	0.1	0.4	0.4	0.4	1.5	0.1	7.2
Additional	7.0	2.2	0.3	0.4	0.5	0.4	1.2	0.1	7.3
Enlarged	6.9	1.9	0.1	0.4	0.4	0.4	1.5	0.1	7.3

Table 7.6: Summary of systematic uncertainties on the expected number of atmospheric neutrino background events for each fiducial mass region in units of %. They are associated with the neutrino interaction model (cross-section). The "Enlarged" row shows the result for the combination of the two fiducial mass regions.

Region	Quasi-elastic Scattering	Single Meson Production	Deep Inelastic Scattering	CC and NC Ratio	Total
$p \to e^+\pi^0$					
Conventional	11.7	16.7	5.2	1.9	21.2
Additional	10.4	12.6	5.8	0.6	17.3
Enlarged	11.6	15.1	5.3	1.6	19.8
$p \to \mu^+\pi^0$					
Conventional	6.7	16.9	5.6	0.9	19.0
Additional	3.6	13.7	8.5	3.2	16.8
Enlarged	6.1	16.1	6.0	1.3	18.3

MC within the enlarged fiducial volume (100 cm $< dwall$):

$$\text{systematic uncertantiy}_{\text{fiducail volume}} = \frac{N_{\text{Normalized MC}} - N_{\text{Data}}}{N_{\text{Data}}}, \tag{7.8}$$

where N is the number of events within the enlarged fiducial volume. The evaluated systematic uncertainty is 1.2%, and Figure 6.3 confirms good agreement between data and MC.

Vertex Position

A systematic vertex reconstruction bias between data and MC does not manifest in the overall vertex distribution such as Fig. 6.3. Since the vertex reconstruction step is the first reconstruction step (Section 6.1), this possible fitting bias affects later reconstruction results. In order to estimate impacts of the vertex fit bias, an alternative reconstruction tool, in which an artificial vertex shift of ±20 cm along the most energetic ring direction is introduced after the vertex reconstruction calculation, has been applied to the same proton decay MC and atmospheric neutrino MC events. 20 cm is a comparable size to the accuracy of the timing calibration (Section 3.3.5) and vertex resolution for proton decay events. Then, ϵ_{sys} and Bkg_{sys} are estimated by applying the same proton decay event selection criteria, which are presented in Section 7.1.1. The more discrepant ϵ_{sys} (Bkg_{sys}) between the +20 cm shift and −20 cm shift cases is taken as the uncertainty.

Ring Counting and Particle Identification

The source uncertainties for ring counting and particle identification are evaluated by comparing their likelihood distributions between data and MC such as shown in Figures 6.8 and 7.2. FC Sub-GeV multi-ring events are used for these items again. The likelihood distribution of MC (L) is fitted to that of data by shifting and smearing as:

$$L' = a \times L + b, \tag{7.9}$$

where a is a scale parameter, b is a shift parameter, and L (L') stands for either ring counting likelihood or multi-ring PID likelihood. A log-likelihood shape test [118] has been conducted to search for the best-fit parameter pair, $(a_{\text{best}}, b_{\text{best}})$, for each SK phase and fiducial mass region. By artificially shifting and smearing the likelihood values with $(a_{\text{best}}, b_{\text{best}})$, ϵ_{sys} and Bkg_{sys} are estimated. As for the uncertainty associated with ring counting, similarly to the uncertainty associated with the vertex position, the best-fit two parameters are introduced in

the reconstruction tool, and the same proton decay MC and atmospheric neutrino MC events have been reprocessed because the ring counting result also affects later reconstruction outputs. When propagating the best-fit parameters, those obtained in the conventional and additional fiducial mass region are applied to the proton decay and atmospheric neutrino MC events within the conventional and additional fiducial mass region, respectively. Then, combining the two results gives the systematic uncertainty in the enlarged fiducial mass region.

Michel Electron Tagging

Atmospheric neutrino MC and FC data events passing **C1** $\sim$ **C3** are used (shown in Figure 7.3). After normalizing the number of MC events to that of data, the number of events in the no (one) Michel electron bin is compared between data and normalized MC for $p \to e^+\pi^0$ ($p \to \mu^+\pi^0$). This is done for each fiducial mass region separately, and the discrepancy between data and normalized MC is assigned as the uncertainty. Furthermore, the uncertainties for (SK-I to -III) and SK-IV are separately estimated because the Michel electron tagging performance is different among the SK phases.

Energy Scale

As the source uncertainty (δE), the sum in quadrature of the absolute energy scale (Table 6.2) and the time variation of the energy scale (Table 6.3) is used. By scaling the reconstructed π^0 mass (M_{π^0}), total mass ($M_{\rm tot}$), and total momentum ($P_{\rm tot}$) by $\pm\delta E$, $\epsilon_{\rm sys}$ and $\mathrm{Bkg_{sys}}$ are estimated for each SK phase and fiducial mass region, where the value of $\pm\delta E$ depends on the SK phase and fiducial mass region as shown in Tables 6.2 and 6.3. In a similar manner to the uncertainty associated with ring counting and particle identification, combining the two fiducial mass results gives the systematic uncertainty in the enlarged fiducial mass region. The more discrepant $\epsilon_{\rm sys}$ ($\mathrm{Bkg_{sys}}$) between the $+\delta E$ scale and $-\delta E$ scale cases is taken as the uncertainty.

Non-uniformity of the Energy Scale

The source uncertainty ($\delta E_{\rm nonuni}$) for this item is the zenith-angle-dependent non-uniformity of the energy scale (Table 6.4). Since the target proton decays produce back-to-back event topologies, the non-uniformity of the energy scale affects the reconstructed total momentum ($P_{\rm tot}$). By scaling it by $\pm 2\delta E_{\rm nonuni}$, $\epsilon_{\rm sys}$ and $\mathrm{Bkg_{sys}}$ are estimated for each SK phase and fiducial mass region, where the value of $\pm\delta E_{\rm nonuni}$ depends on the SK phase and fiducial mass region as shown in Table 6.4. The uncertainty in the enlarged fiducial mass region is obtained by the combination of the two fiducial mass results. The more discrepant $\epsilon_{\rm sys}$ ($\mathrm{Bkg_{sys}}$) between the $+2\delta E_{\rm nonuni}$ scale and $-2\delta E_{\rm nonuni}$ scale cases is taken as the uncertainty.

Neutron Tagging

The uncertainty on the neutron tagging efficiency is estimated to be 9.0% in Section 6.3.4. The 9.0% change of the neutron tagging efficiency corresponds to a 5.4% change of the number of remaining atmospheric neutrino backgrounds, and it is assigned to the expected number of atmospheric neutrino events in SK-IV as an additional uncertainty. This is deduced from the true number of produced neutrons in the remaining background MC events.

7.3.3 Summary of Systematic Uncertainties

Tables 7.7 and 7.8 show the summary of the evaluated systematic uncertainties on the signal selection efficiency and expected number of atmospheric neutrino background events, respectively. As for the signal selection efficiency, basically, the dominant uncertainty originates from

the physics modeling part. However, for the additional fiducial mass region, some of the uncertainties in the reconstruction part become comparable. Due to the degraded momentum resolution and the effects of escaping particles, more signal MC events in the additional fiducial mass region are reconstructed near the total mass and total momentum cut boundaries than in the conventional one as shown in Fig. 7.5. This has the effect of making the selection efficiency in the additional fiducial mass region more sensitive to uncertainties in the energy scale. The reconstructed momentum is also sensitive to the vertex position since in the momentum calculation, the observed PMT charge is corrected using the reconstructed vertex position as described in Section 6.1.6. Therefore, the effects from the vertex shift manifest more obviously in the additional fiducial mass region.

Systematic uncertainties associated with the neutrino interaction modeling and the energy scale are dominant for the expected number of atmospheric neutrino background events. As shown in the interaction mode breakdown table (Table 7.2) and kinetic distributions (Fig. 7.5), there are no major differences between the two fiducial mass regions, resulting in a similar size of uncertainties. For some of the items, the systematic uncertainty partially anticorrelates between the conventional and additional fiducial mass regions, and it leads to the smallest uncertainty after combining the two fiducial mass regions. The systematic uncertainties in the "Enlarged" rows are used in the following lifetime limit calculation. At last, the systematic uncertainty on the detector exposure is conservatively set to 1%.

7.4 Lifetime Limit

Since no significant data excess has been found in either decay mode, lower limits on the proton partial lifetime have been calculated using a Bayesian method [119]. In this calculation, numbers in the "Enlarged" rows in Tables 7.3, 7.7, and 7.8 and 450 kton·years have been used as the signal selection efficiency, expected number of background events, their systematic uncertainties, and exposure. Since the search performance varies depending on the SK phase, separate exposures from SK-I to -IV are taken into account. The expected number of background events is also different between the two P_{tot} signal regions, and therefore they are considered separately in the following calculation. The probability to detect n_i candidate events is calculated by Poisson statistics:

$$P_i(n_i|\Gamma\lambda_i\epsilon_i b_i) = \frac{\mathrm{e}^{-(\Gamma\lambda_i\epsilon_i+b_i)}(\Gamma\lambda_i\epsilon_i + b_i)^{n_i}}{n_i!}, \tag{7.10}$$

where i is the index of each signal region (SK-I to -IV, "Lower" and "Upper"), Γ is the true decay rate, λ_i is the true detector exposure, ϵ_i is the true signal selection efficiency, and b_i is the true number of backgrounds. According to Bayes' theorem, it is transformed as follows:

$$\begin{aligned} P_i(\Gamma\lambda_i\epsilon_i b_i|n_i)P_i(n_i) &= P_i(n_i|\Gamma\lambda_i\epsilon_i b_i)P(\Gamma\lambda_i\epsilon_i b_i) &(7.11)\\ &= P_i(n_i|\Gamma\lambda_i\epsilon_i b_i)P(\Gamma)P(\lambda_i)P(\epsilon_i)P(b_i), &(7.12)\end{aligned}$$

where $P(X)$ stands for the prior probability of X. The second equality holds because the decay rate, detector exposure, signal selection efficiency, and the number of backgrounds are independent.

In the eight signal regions (SK-I to -IV, "Lower" and "Upper"), each probability density function of the decay rate is defined as follows:

$$\begin{aligned} P_i(\Gamma|n_i) &= \iiint P_i(\Gamma\lambda_i\epsilon_i b_i|n_i)d\epsilon_i d\lambda_i db_i, &(7.13)\\ &= \frac{1}{A_i}\iiint \frac{e^{-(\Gamma\lambda_i\epsilon_i+b_i)}(\Gamma\lambda_i\epsilon_i + b_i)^{n_i}}{n_i!}P(\Gamma)P(\lambda_i)P(\epsilon_i)P(b_i)d\epsilon_i d\lambda_i db_i, &(7.14)\end{aligned}$$

Table 7.7: Summary of systematic uncertainties [%] on the signal selection efficiency for each fiducial mass region. SK-I to -IV are livetime-weighted combined. The "Enlarged" row shows the result for the combination of the two fiducial mass regions. Here, "Lower" and "Upper" show the $P_{\rm tot} < 100$ MeV/c and $100 \leq P_{\rm tot} < 250$ MeV/c signal regions, respectively. Besides, "FV", "RC", and "PID" stand for fiducial volume, ring counting, and particle identification, respectively.

Region		Correlated Decay	Fermi Momentum	π FSI	FV	Vertex Position	RC	PID	Michel-e Tagging	Energy Scale	Energy Non-uniformity	Total
$p \to e^+\pi^0$												
Conventional	(Lower)	1.7	7.2	2.8	1.2	1.1	0.3	0.4	1.5	2.5	1.0	8.6
	(Upper)	9.0	6.7	11.9	1.2	0.1	0.4	0.5	1.5	1.9	0.2	16.6
Additional	(Lower)	2.7	7.8	3.8	1.2	8.9	2.4	1.6	1.4	2.9	2.3	13.7
	(Upper)	8.4	1.0	10.6	1.2	4.4	2.5	1.3	1.4	8.3	0.3	16.8
Enlarged	(Lower)	1.9	7.2	2.9	1.2	1.8	0.3	0.3	1.5	2.5	1.1	8.8
	(Upper)	8.9	5.7	11.7	1.2	0.4	0.5	0.4	1.5	2.7	0.1	16.1
$p \to \mu^+\pi^0$												
Conventional	(Lower)	1.9	7.3	2.7	1.2	1.5	0.1	0.2	3.3	2.3	0.9	9.2
	(Upper)	9.3	8.3	13.3	1.2	0.3	0.2	0.2	3.3	1.8	0.2	18.7
Additional	(Lower)	2.0	6.8	2.9	1.2	3.8	0.7	1.2	4.5	2.8	2.0	10.4
	(Upper)	8.4	4.0	11.3	1.2	6.4	0.6	1.2	4.5	5.0	0.6	17.5
Enlarged	(Lower)	1.9	7.2	2.7	1.2	1.7	0.2	0.4	3.5	2.3	1.0	9.3
	(Upper)	9.2	7.7	13.0	1.2	1.1	0.3	0.4	3.5	2.3	0.2	18.2

Table 7.8: Summary of systematic uncertainties [%] on the expected number of atmospheric neutrino background events for each fiducial mass region. SK-I to -IV are livetime-weighted combined. They have been evaluated for the combined $P_{\rm tot} < 100$ MeV/c and $100 \leq P_{\rm tot} < 250$ MeV/c signal regions. Here, the "Enlarged" row shows the result for the combination of the two fiducial mass regions. Besides, "FV", "RC", and "PID" stand for fiducial volume, ring counting, and particle identification, respectively.

Region	ν Flux	ν Interaction	π FSI and SI	FV	Vertex Position	RC	PID	Michel-e Tagging	Energy Scale	Energy Non-uniformity	Neutron Tagging	Total
$p \to e^+\pi^0$												
Conventional	7.3	21.2	12.8	1.2	12.0	2.5	1.4	1.5	16.4	4.2	5.4	33.5
Additional	7.2	17.3	13.9	1.2	9.1	1.8	2.9	1.4	15.2	17.1	5.4	34.3
Enlarged	7.3	19.8	12.7	1.2	8.3	2.4	1.7	1.5	15.5	6.4	5.4	32.0
$p \to \mu^+\pi^0$												
Conventional	7.2	19.0	9.3	1.2	8.4	1.0	3.2	3.3	11.0	6.2	5.4	27.8
Additional	7.3	16.8	11.3	1.2	18.7	1.2	1.3	4.5	6.5	4.1	5.4	30.3
Enlarged	7.3	18.3	8.0	1.2	7.1	0.8	2.3	3.5	10.1	5.8	5.4	26.3

where A_i is the normalization factor representing the total integral of $P_i(\Gamma|n_i)$. The probability density function $P(\Gamma)$ is the prior probability of the decay rate and is assumed to be uniform, and $P(\lambda_i)$ and $P(\epsilon_i)$ stand for the prior probability of the exposure and the signal selection efficiency, respectively, defined by a Gaussian function:

$$P(\lambda_i) \propto \begin{cases} \exp\left(\frac{-(\lambda_i-\lambda_{0i})^2}{2\sigma^2_{\lambda_i}}\right), & (\lambda_i > 0) \\ 0, & (\text{otherwise}) \end{cases} \tag{7.15}$$

$$P(\epsilon_i) \propto \begin{cases} \exp\left(\frac{-(\epsilon_i-\epsilon_{0i})^2}{2\sigma^2_{\epsilon_i}}\right), & (\epsilon_i > 0) \\ 0, & (\text{otherwise}) \end{cases} \tag{7.16}$$

where λ_{0i} (σ_{λ_i}) and ϵ_{0i} (σ_{ϵ_i}) are the estimations (systematic uncertainties) of the exposure and signal selection efficiency, respectively. The prior probability of the expected number of background events, $P(b_i)$, is defined by the convolution of a Gaussian and Poisson distribution:

$$P(b_i) \propto \begin{cases} \int_0^\infty \frac{e^{-B}B^{n_{b_i}}}{n_{b_i}!} \exp\left(\frac{-(C_i b_i-B)^2}{2\sigma^2_{b_i}}\right) dB, & (b_i > 0) \\ 0, & (\text{otherwise}) \end{cases} \tag{7.17}$$

where n_{b_i} is the expected number of backgrounds in each 500 years atmospheric neutrino MC (not normalized by livetime), C_i is a constant factor to normalize MC livetime to the data livetime, and σ_{b_i} is the systematic uncertainty of the expected number of backgrounds. The systematic uncertainties described in Section 7.3 are considered as a standard deviation of each Gaussian function. With these prior probability distributions, confidence level (C.L.) is calculated as follows:

$$\text{C.L.} = \int_{\Gamma=0}^{\Gamma=\Gamma_{\text{limit}}} \prod_{i=1}^{8} P_i(\Gamma|n_i) d\Gamma. \tag{7.18}$$

As a consequence, the lower limits on the proton partial lifetime are obtained by calculating:

$$\frac{\tau_{\text{limit}}}{B} = \frac{1}{\Gamma_{\text{limit}}}, \tag{7.19}$$

where B is the branching ratio of each proton decay mode. From the above formulas, 90% confidence limits of the proton partial lifetime have been calculated, and they are:

$$\tau/B(p \to e^+\pi^0) > 2.4 \times 10^{34} \text{ years}, \tag{7.20}$$

and

$$\tau/B(p \to \mu^+\pi^0) > 1.6 \times 10^{34} \text{ years}. \tag{7.21}$$

7.5 Discussion

7.5.1 Implications of the Results

Compared to the previous results [27], the lifetime limit for the $p \to e^+\pi^0$ mode has improved by a factor of 1.5 as is expected from the increased exposure, from 306 kton·years to 450 kton·years. On the other hand, for the $p \to \mu^+\pi^0$ mode, the lifetime limit has improved by a factor of two because one of the two candidates reported in the last results moved out of the signal region after introducing a new gain correction method. In the new method, the PMT gain correction factor depends on the PMT production year as described in Section 3.3.3.

In comparison with theoretical predictions, the obtained lifetime limits are in the middle of the SO(10) GUT and SUSY GUT predictions, which are in the order of $\sim 10^{34}$ years or longer

and discussed in Chapter 2. Although the updated lifetime limits can not completely exclude them, they give the world's most stringent constraints for these decay modes.

According to [3], the proton lifetime and the mass of the mediator particle (GUT scale, M_X) is approximately connected as follows:

$$\tau_p \sim \frac{1}{\alpha_G}\frac{M_X^4}{m_p^5} \tag{7.22}$$

Assuming that α_G, the coupling constant at the unification scale (Figure 2.2), is about $\frac{1}{40}$, the obtained lifetime limit ($\tau/B(p \to e^+\pi^0) > 2.4 \times 10^{34}$ years) gives a constraint on the value of M_X:

$$M_X \gtrsim 5 \times 10^{15} \text{ GeV}. \tag{7.23}$$

7.5.2 Future Prospect

In order to further enhance the proton decay search sensitivity, a larger detector exposure and further atmospheric neutrino background reduction are essential. Because the update and data set presented in this thesis are generically applicable to every nucleon decay mode search (as well as atmospheric neutrino analysis), the search sensitivities for other decay modes will also improve using the enlarged fiducial mass. In the following, future proton decay searches, in which the neutron tagging technique becomes more important to reduce atmospheric neutrino backgrounds, are discussed.

In summer 2020, about 0.02% of Gadolinium (Gd) sulfate, $Gd_2(SO_4)_3$, by mass, i.e. about 0.01% of Gd has been dissolved in water of SK. After neutron capture on Gd, gamma rays with a total energy of about 8 MeV are emitted. Because of the higher energy deposition in the detector than neutron capture on hydrogen (2.2 MeV gamma ray), the neutron tagging efficiency is expected to increase from 25% to about 50%. The original goal of the "SKGd" project [120, 121] is to detect diffuse neutrinos from supernova explosions in the universe, but the higher neutron tagging efficiency is also beneficial to the proton decay search because more atmospheric neutrino backgrounds can be rejected with neutron information. By requiring no tagged neutrons for a proton decay signal, the expected number of atmospheric neutrino background rate is expected to be reduced by 65% (50%) in SKGd (SK-IV).

As a future project, the Hyper-Kamiokande (HK) detector [122] is being constructed, and it is expected to start its data taking in 2027. A schematic view of the HK detector is shown in Fig. 7.13. It is an upright cylinder in shape as SK, 68.0 m in diameter and 72.0 m in height, containing a total of 258 kton of water. The nominal fiducial volume is defined as the region more than 150 cm from the inner detector wall, and it gives a 188 kton of water fiducial mass. Suppose the fiducial volume boundary is extended to be 100 cm from the inner detector wall, the fiducial mass increases to 198 kton accordingly. Furthermore, a higher neutron tagging efficiency is expected to be achieved because of the new PMT with a higher photon detection efficiency. The expected neutron tagging efficiency in HK is estimated to be 70%. The expected number of atmospheric neutrino background rate in HK is reduced by 75% by requiring no tagged neutrons as a proton decay signal.

For both prospects, the proton decay $p \to e^+\pi^0$ search sensitivity is calculated using Equations (7.1) and (7.2), and it is plotted in Fig. 7.14. For both experiments, the fiducial volume is assumed to be defined as the region more than 100 cm from the inner detector wall, 27.2 kton for SKGd and 198 kton for HK, and the signal selection efficiency is assumed to be the same as the SK-IV performance in Table 7.3. As for the expected atmospheric neutrino background rate, it is assumed to be reduced to $\frac{2}{3}$ Mt·years in SKGd from that in SK-IV (about 1 /Mt·year) and it is assumed to be reduced by half in HK compared to that in SK-IV. The search sensitivity is expected to reach in the order of 10^{35} years after the HK detector accumulates about 15 years of livetime.

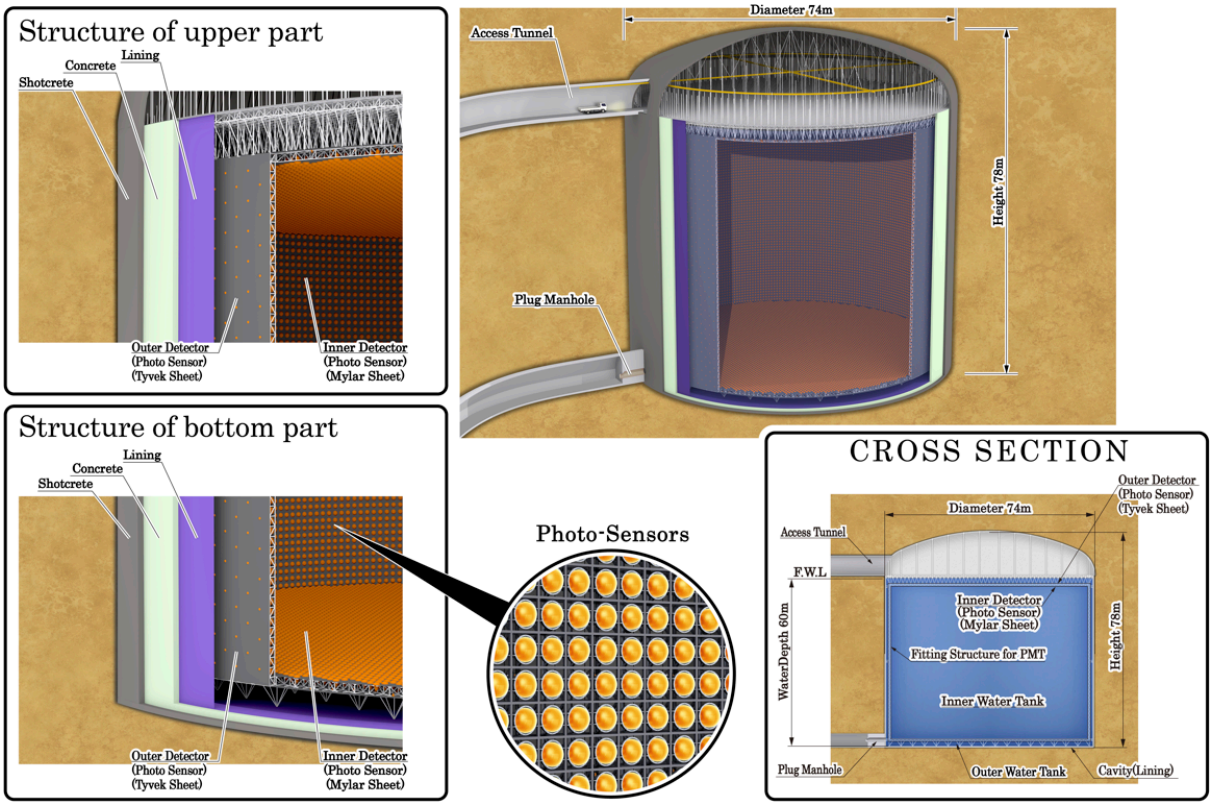

Figure 7.13: Schematic view of the HK detector. Taken from [122].

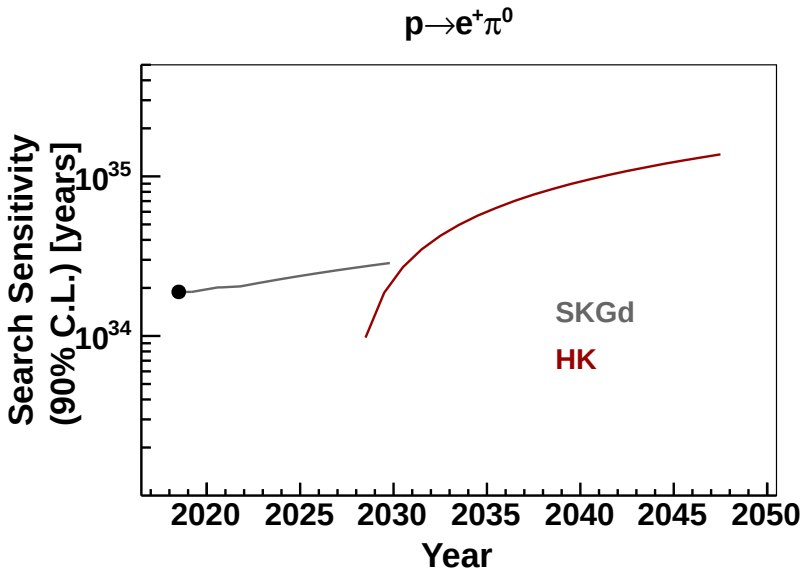

Figure 7.14: Proton decay $p \to e^+\pi^0$ search sensitivity as a function of time. Used signal selection efficiency and expected atmospheric neutrino background rate are described in the text. The black point corresponds to this work.

Chapter 8

Conclusion

We have performed searches for proton decay via $p \to e^+\pi^0$ and $p \to \mu^+\pi^0$ with the Super-Kamiokande enlarged fiducial mass data. In order to enlarge the fiducial mass from 22.5 kton to 27.2 kton for nucleon decay searches as well as atmospheric neutrino analyses, we have conducted the following comprehensive studies. First, we have introduced several tighter criteria in the event selection algorithm and quantified the non-neutrino background contamination rate in the additional fiducial mass region by event scanning. As a result of adopting the new selection criteria and the event scanning, we have demonstrated that the contamination rate is kept within 1%, tolerable level for SK analyses, while the selection efficiency for proton decay and atmospheric neutrino events is kept more than 96%. As for the event reconstruction performance, the particle identification algorithm has been improved by introducing new expected charge tables, resulting in the 20% higher signal selection efficiency in the additional fiducial mass region for both search modes. Furthermore, we have evaluated systematic uncertainties in the additional fiducial mass region and proved that the energy scale uncertainty, one of the most important error sources, is kept within a few percent level. Combining with the newly estimated systematic uncertainties, we confirm that enlarging the fiducial mass increases the proton decay search sensitivity by 12% for both modes.

Since the last publication [27], the detector has accumulated 25% more livetime and its fiducial mass has been enlarged by about 20%, resulting in a 50% larger exposure of SK-I to -IV full data, 450 kton·years. Using that updated data set, we have searched for proton decay via $p \to e^+\pi^0$ and $p \to \mu^+\pi^0$. No candidates have been found for the $p \to e^+\pi^0$ mode and one candidate has been found for the $p \to \mu^+\pi^0$ mode. They are not significant event excesses compared to the atmospheric neutrino background predictions, 0.59 for $p \to e^+\pi^0$, and 0.94 for $p \to \mu^+\pi^0$. Lower limits on the proton partial lifetime of $\tau/B(p \to e^+\pi^0) > 2.4 \times 10^{34}$ years and $\tau/B(p \to \mu^+\pi^0) > 1.6 \times 10^{34}$ years are set at 90% confidence level. These limits are a 1.5 times longer lifetime limit for the $p \to e^+\pi^0$ mode and two times longer for the $p \to \mu^+\pi^0$ mode than the previous results [27]. They do not completely rule out any prospective and remaining major GUT models such as SO(10) and SUSY GUT, but they are the world's most stringent constraints for these decay modes and should be referred to in building GUT models.

The analysis improvements and data set described above are applicable to other nucleon decay searches in Super-Kamiokande, and the search sensitivities for them are expected to improve using the enlarged fiducial mass.

Acknowledgments

I am grateful to all of the people who have contributed to this work. I express my sincere thanks to Prof. Masato Shiozawa for giving me this great opportunity to work on the Super-Kamiokande experiment. Without his many important suggestions and tireless support, this thesis could not have been completed. I would like to thank to Dr. Hidekazu Tanaka for his kind support throughout my master and Ph.D. courses, especially in the PMT calibration work and dataset preparation. I am grateful to Prof. Masayuki Nakahata, spokesperson of the Super-Kamiokande collaboration, for his helpful advice. I also thank all analysis group members, especially Ed Kearns, Yoshinari Hayato, Roger Wendell, Shunichi Mine, Makoto Miura, Kimihiro Okumura, Masahiro Kuze, Yosuke Kataoka, Mahdi Taani, and Yutaro Sonoda, for their many useful suggestions about the proton decay search analysis as well as FC data management. I would also like to take this opportunity to thank all calibration group members, especially Shigetaka Moriyama, Akira Konaka, Jun Kameda, Yasuhiro Nishimura, Motoyasu Ikeda, Yasuhiro Nakajima, Rika Sugimoto, Gianmaria Collazuol, Ali Ajmi, and Fabio Iacob. Thanks to all Kamioka staff and students, I could have a very enjoyable time in Kamioka.

This work is partially supported by Grant-in-Aid for JSPS Fellows. I also thank to the ALPS program in the University of Tokyo for its educational and financial support.

Finally, I would like to sincerely thank my family for their continuous support.

Appendix A

Detailed Calibration of 50 cm Diameter PMT Response and Impacts on Event Reconstruction

In this appendix, first, measurements of the photon incident position and ambient magnetic field dependence of the SK PMT response are described in Section A.1. Their impacts on the event reconstruction performance are estimated by implementing the obtained PMT response into SKDETSIM. The implementation and results are covered in Section A.3. Since it has been found in the PMT measurement that there is anisotropy of the PMT response with respect to the PMT dynode direction and a 100 mG level of the magnetic field has a sizable impact on the PMT response, the dynode directions of all of the PMTs and the residual magnetic field in the SK detector have been measured during the tank refurbishment work in 2018. These measurement results are described in Section A.2.

A.1 Detailed Calibration of SK PMT Response

A.1.1 Motivation of the Measurement

It has been demonstrated using SKDETSIM that Cherenkov photon incident positions on the SK PMT photocathode generically depend on the primary event topology, such as vertex position and particle direction. However, the photon incident position dependence of the SK PMT response was not fully understood in the previous measurement [32], and thus the PMT response in SKDETSIM is approximated to be uniform across the entire photocathode. Since events in the additional fiducial mass region have a smaller distance to the ID wall than those in the conventional and have not been actually used in SK analyses before, the size of the impact on the event reconstruction induced by this dependence needs to be understood in advance.

A.1.2 Measurement Method

Nine PMTs (R3600) were sampled from the SK detector, and their serial numbers are as follows:

- CE5817,
- CE5852,
- EF6453,
- FH5947,

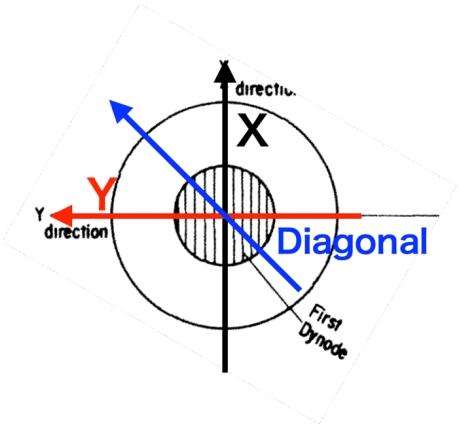

Figure A.1: SK PMT top view and coordinates. The X-axis is parallel to the PMT dynode major axis, the Y-axis is the perpendicular to X, and the D- (Diagonal) axis is in the middle of the other two.

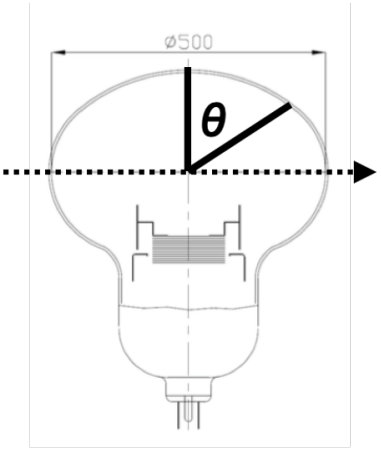

Figure A.2: SK PMT cross section and definition of PMT θ. The dotted black line stands for either the X-, Y-, or D-axis positive direction.

- FH5993,
- GH5655,
- GH5656,
- JM3213,
- LM7806.

The following items' position and magnetic field dependence has been measured:

- gain,
- photon detection efficiency,
- transit time.

Since the venetian blind dynode structure does not have rotational symmetry, the measurement point on the photocathode is defined along three different axes. The PMT coordinates are defined and are shown in Fig. A.1: the X-axis is parallel to the PMT dynode major axis, the Y-axis is perpendicular to X, and the D- (Diagonal) axis is in the middle of the other two. A photoelectron trajectory inside the PMT bulb depends on the photon incident position, and it produces a variation of the PMT response. Therefore, 11 optical fibers were put on the PMT photocathode to evaluate the variation: the PMT zenith angle θ = 0, 20, 40, 45, 50, 55, 60, 65, 70, 75, and 80 degrees. The definition of the PMT zenith angle θ is shown in Fig. A.2.

Figure A.3 shows the measurement setup. The PMT was placed at the center of Helmholtz coils, which are deployed to control the ambient magnetic field, and the room temperature was about 30°C. In order to measure magnetic field dependence of the PMT response, this PMT measurement has been conducted under the following magnetic field conditions in units of mG:

- $(BX, BY, BZ) = (0, 0, 0)$,
- $(BX, BY, BZ) = (50, 0, 0)$,
- $(BX, BY, BZ) = (-50, 0, 0)$,
- $(BX, BY, BZ) = (-100, 0, 0)$,

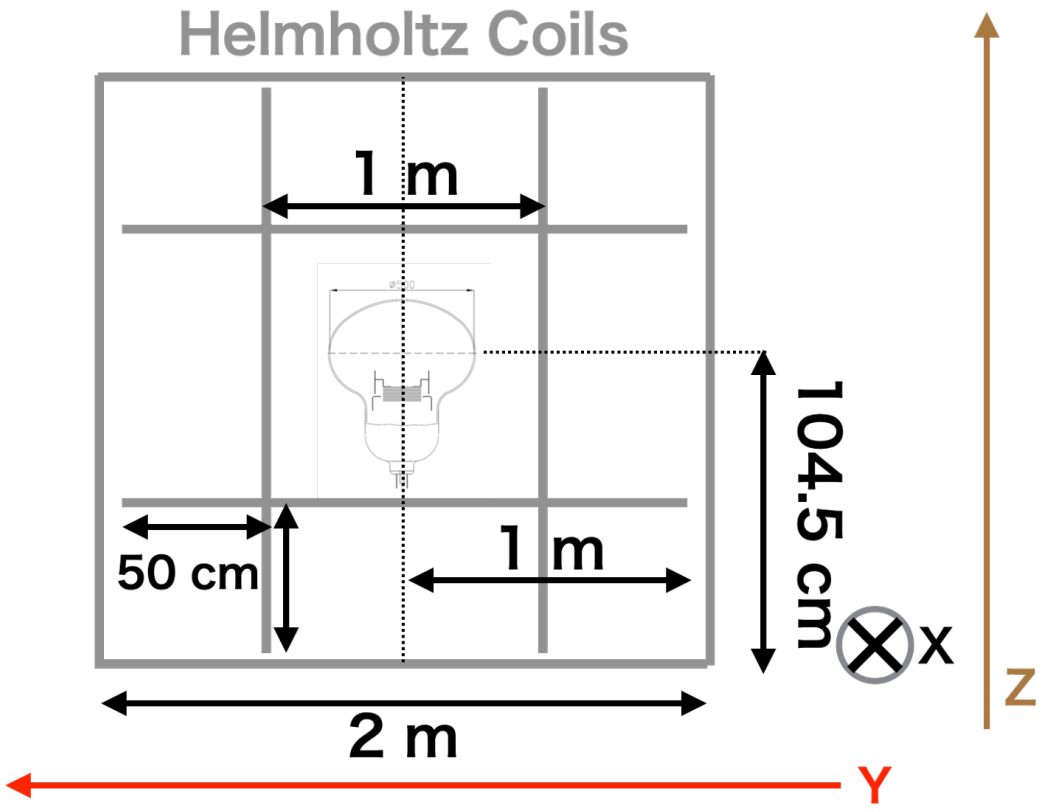

Figure A.3: Schematic view of the PMT measurement setup. The Helmholtz coils are deployed to control the ambient magnetic field.

- $(BX, BY, BZ) = (0, 50, 0)$,
- $(BX, BY, BZ) = (0, -50, 0)$,
- $(BX, BY, BZ) = (0, -100, 0)$,
- $(BX, BY, BZ) = (0, 0, 50)$,
- $(BX, BY, BZ) = (0, 0, 100)$,
- $(BX, BY, BZ) = (0, 0, -50)$,
- $(BX, BY, BZ) = (0, 0, -100)$,

where BX, BY, and BZ are defined as the magnetic field coordinates as shown in Fig. A.3, and the BX- and BY-axes are parallel to the X- and Y-axes in the PMT coordinate, respectively. A 7.5 cm diameter PMT was deployed a few meters away from the Helmholtz coils and split light from a light source is fed into the 7.5 cm PMT to monitor the light intensity variation during the measurement.

As a laser light source, a laser diode device produced by Hamamatsu Photonics, PLP-10, was used. Its laser pulse wavelength is 405.6 nm, and pulse width is 63.0 psec. Using a light attenuator (AQ-3105A), the incident light intensity was tuned so that the SK PMT counting rate was about 1%. PMT charge and timing information has been recorded with ADC (Lecroy: 1182) and TDC (CAEN: V1290) modules.

A.1.3 Measurement Results

The PMT gain value at each photon incident position was obtained by fitting a Gaussian function to the ADC single photoelectron distribution. The photon detection efficiency was calculated using the number of pulses whose height exceeds a certain threshold level. In this measurement, the threshold value was set to -1 mV, which is comparable to the SK configuration, and the photon detection efficiency at each incident position is normalized to the charge deposition at the 7.5 cm monitor PMT.

The signal transit time was calculated by fitting an asymmetric Gaussian function to the TDC distribution. A correction for the "time walk" effect has been applied to the TDC distribution in advance.

Figure A.4 shows the relative gain, relative photon detection efficiency, and relative transit time distributions at the $|B| = 0$ condition as a function of incident photon position on the photocathode for one of the sampled PMTs, EF6453. The black, red, and blue dots show the different photon incident points along the X-, Y-, and D-axes, respectively. These plots confirm that there is a $\pm 30\%$ variation in gain, a $\pm 25\%$ variation in detection efficiency, and a ± 3 nsec variation in transit time across the entire photocathode. An electron trajectory simulation by Hamamatsu Photonics suggests that the fall of the PMT gain seen around $\theta = \pm 60^\circ$ in the Y and D directions is caused by photoelectrons which pass through the gaps of the first dynode. The systematic uncertainty of this measurement is estimated from the measurement reproducibility. The same PMT was measured twice, and the reproducibility including fiber positioning is estimated to be better than 5% for the PMT gain and detection efficiency, 0.2 nsec for the PMT transit time measurement.

Figures A.5, A.6, and A.7 show the relative gain, relative photon detection efficiency, and relative transit time distributions of the same PMT at different magnetic field conditions along BX, BY, and BZ, respectively. The impact by applying the magnetic field along BX is most significant, and under the $BX = -100$ mG condition, the size of the deviation from the $|B| = 0$ condition is comparable to the size of the photon incident position dependence effect. Basically, these behaviors are also consistent with the electron trajectory simulation results by Hamamatsu Photonics.

Figure A.8 shows the average distributions of relative gain, relative photon detection efficiency, and relative transit time for the nine sampled PMTs at the $|B| = 0$ condition. Vertical bands denote the statistical uncertainty of the average value at each photon incident position, $\frac{(\text{standard deviation})}{\sqrt{9-1}}$, and correspond to the PMT by PMT individual differences. The PMT by PMT individual difference of relative gain, relative photon detection efficiency, and relative transit time is estimated to be less than 5%, 3%, and 0.5 nsec, respectively. The nine PMTs' average results are consistent with an assumption that the non-uniform PMT response is symmetric with respect to $\theta = 0$.

A.2 Measurement of PMT Dynode Direction and Residual Magnetic Field in the SK Detector

From the PMT response measurement, it has been found that there is anisotropy of the PMT response with respect to the PMT dynode direction, and about 100 mG level of the magnetic field also has a sizable impact on the PMT response. In order to estimate impacts on the event reconstruction by these detailed PMT responses, dynode directions of the PMTs and the magnetic field in the SK detector have been measured during the tank refurbishment work in 2018.

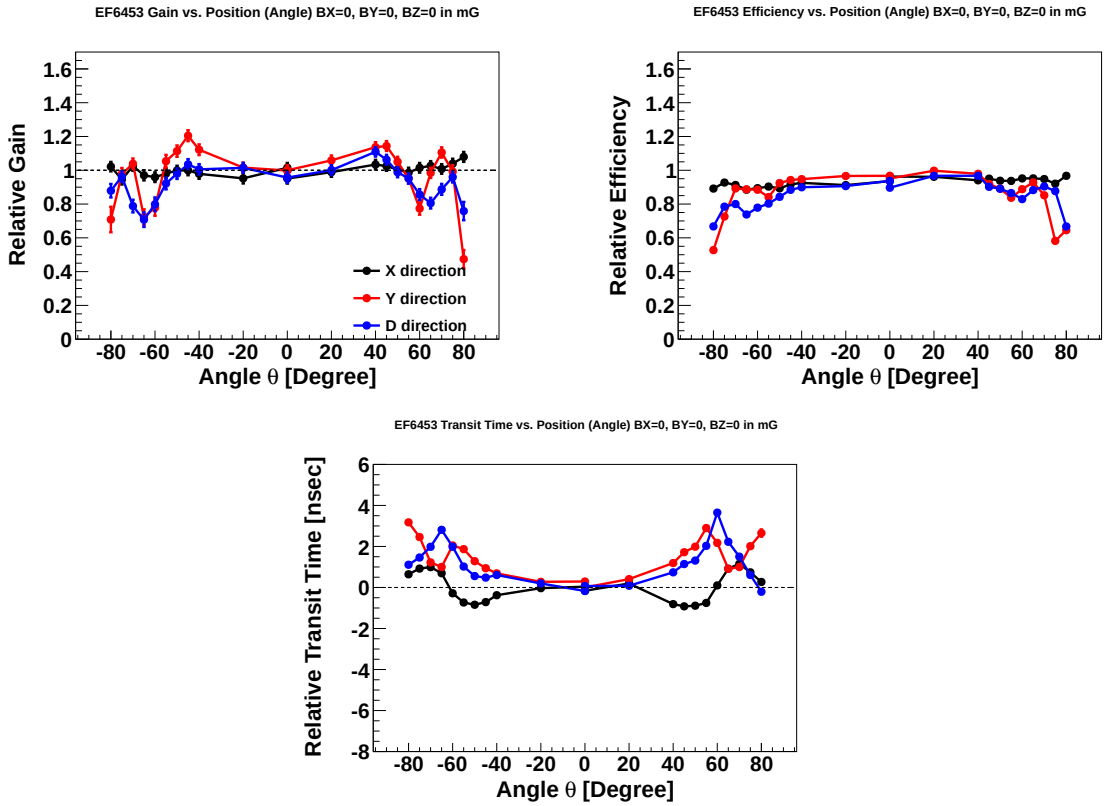

Figure A.4: Relative gain (top left), relative photon detection efficiency (top right), and relative transit time (bottom) distributions at the $|B| = 0$ condition as a function of incident photon position on the photocathode (θ) defined in Figure A.2. They are results for one of the sampled PMTs, EF6453. The black, red, and blue dots show the different photon incident points along the X-, Y-, and D-axes, respectively. For the relative gain distribution, the vertical axis values are normalized to the mean of $\theta = 0$ values. For the photon detection efficiency distribution, the vertical axis values are normalized to the charge deposition at the monitor PMT. For the relative transit time distribution, the vertical axis values correspond to the difference from the mean of $\theta = 0$ values. Vertical error bars on the data points shows the statistical uncertainty.

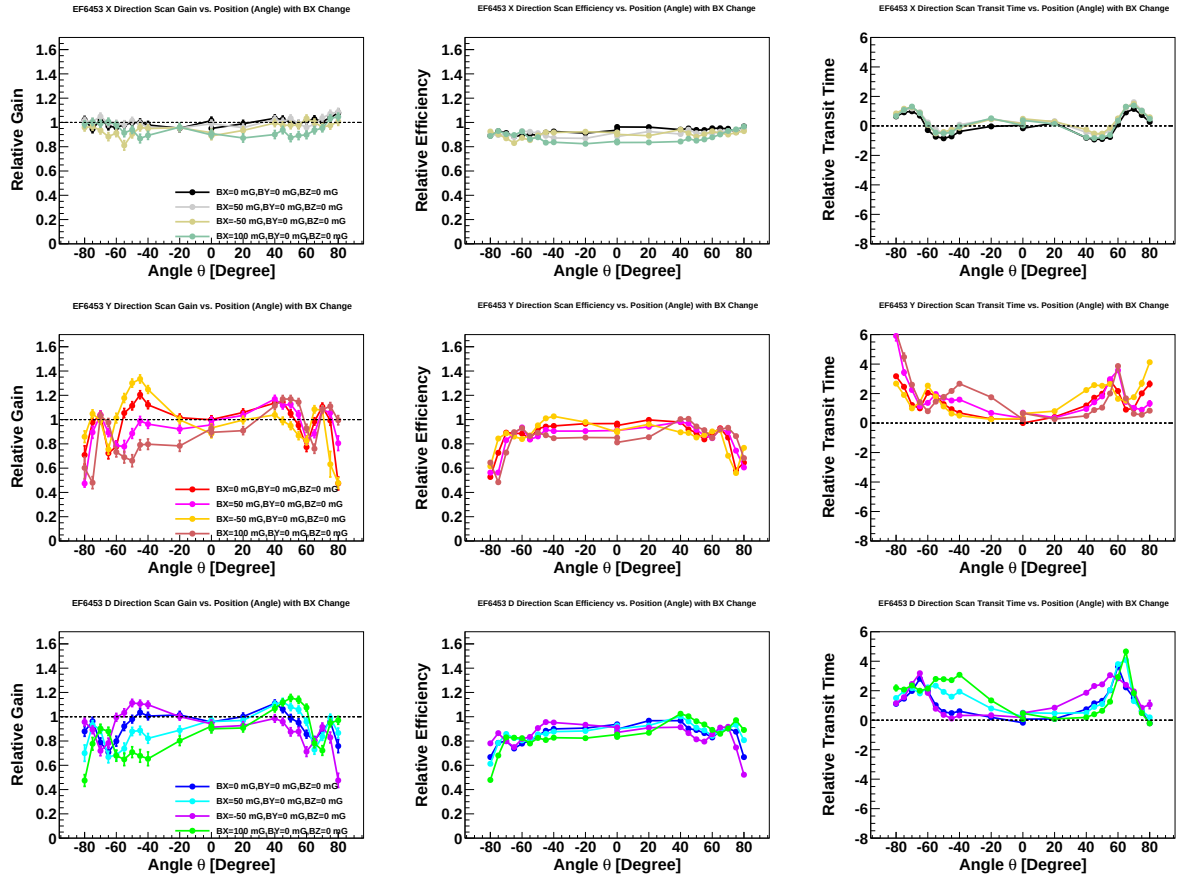

Figure A.5: Relative gain (left), relative photon detection efficiency (middle), and relative transit time (right) distributions at different magnetic field conditions along BX as a function of incident photon position on the photocathode (θ). They are results for one of the sampled PMTs, EF6453. Different colors correspond to the different magnetic field conditions. From top to bottom, X, Y, and D direction scanning results are shown. For the relative gain distribution, the vertical axis values are normalized to the mean of $\theta = 0$ values at the $|B| = 0$ condition. For the photon detection efficiency distribution, the vertical axis values are normalized to the charge deposition at the monitor PMT. For the relative transit time distribution, the vertical axis values correspond to the difference from the mean of $\theta = 0$ values at the $|B| = 0$ condition. Vertical error bars on the data points shows the statistical uncertainty.

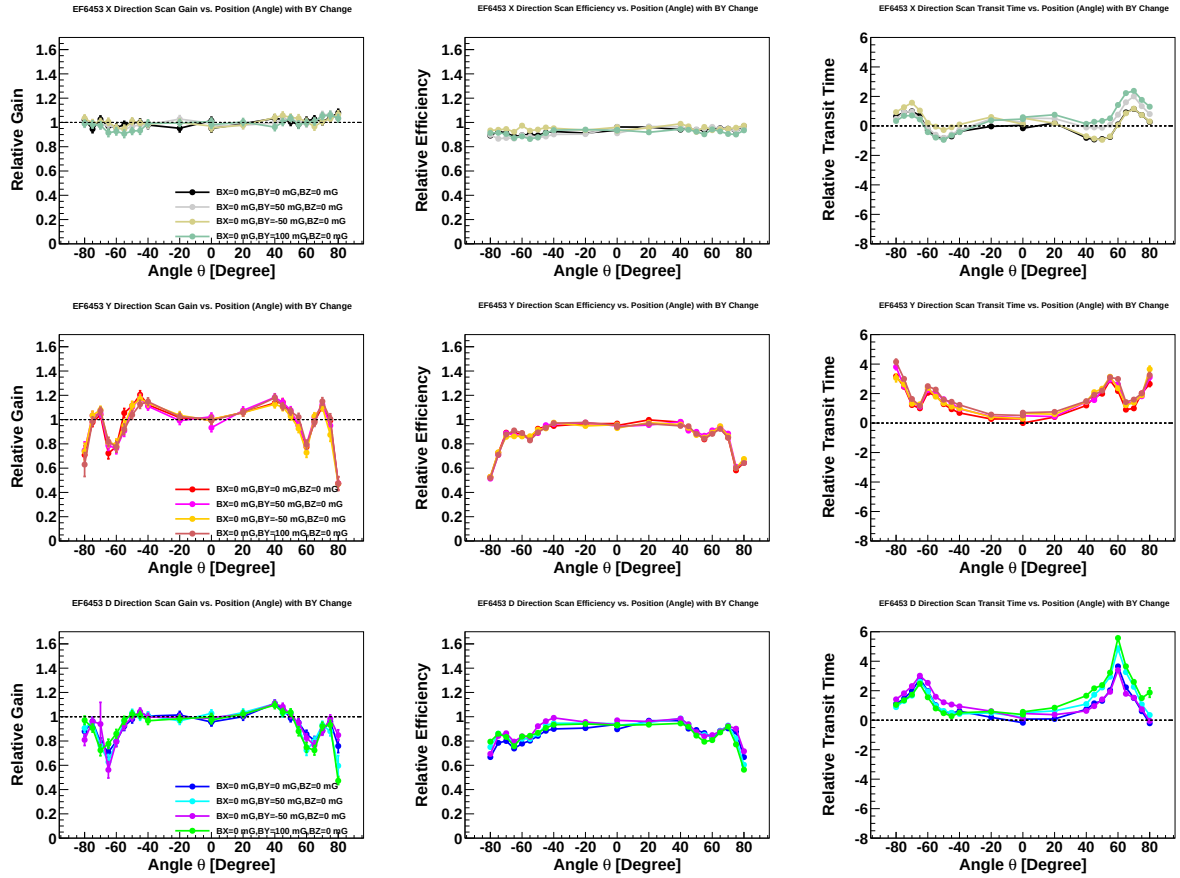

Figure A.6: Relative gain (left), relative photon detection efficiency (middle), and relative transit time (right) distributions at different magnetic field conditions along BY as a function of incident photon position on the photocathode (θ). They are results for one of the sampled PMTs, EF6453. Different colors correspond to the different magnetic field conditions. From top to bottom, X, Y, and D direction scanning results are shown. For the relative gain distribution, the vertical axis values are normalized to the mean of $\theta = 0$ values at the $|B| = 0$ condition. For the photon detection efficiency distribution, the vertical axis values are normalized to the charge deposition at the monitor PMT. For the relative transit time distribution, the vertical axis values correspond to the difference from the mean of $\theta = 0$ values at the $|B| = 0$ condition. Vertical error bars on the data points shows the statistical uncertainty.

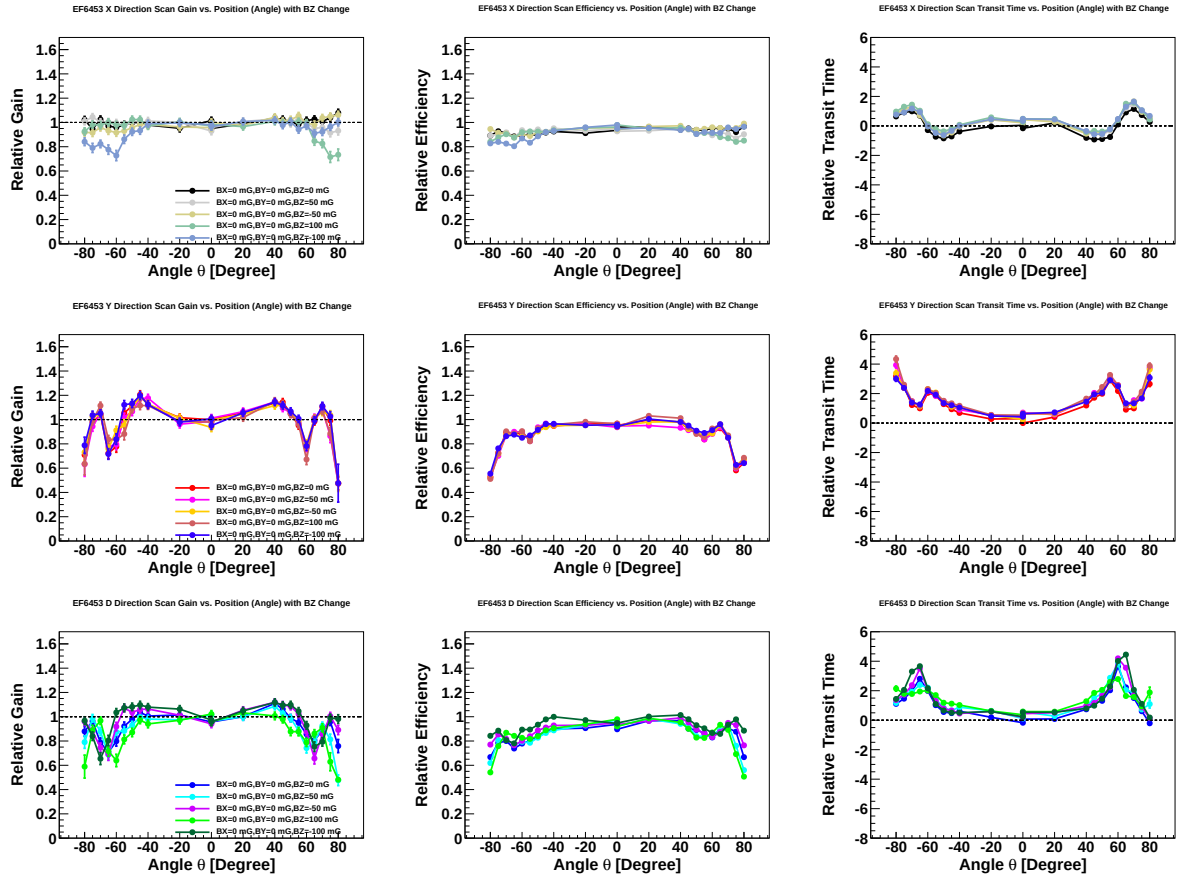

Figure A.7: Relative gain (left), relative photon detection efficiency (middle), and relative transit time (right) distributions at different magnetic field conditions along BZ as a function of incident photon position on the photocathode (θ). They are results for one of the sampled PMTs, EF6453. Different colors correspond to the different magnetic field conditions. From top to bottom, X, Y, and D direction scanning results are shown. For the relative gain distribution, the vertical axis values are normalized to the mean of $\theta = 0$ values at the $|B| = 0$ condition. For the photon detection efficiency distribution, the vertical axis values are normalized to the charge deposition at the monitor PMT. For the relative transit time distribution, the vertical axis values correspond to the difference from the mean of $\theta = 0$ values at the $|B| = 0$ condition. Vertical error bars on the data points shows the statistical uncertainty.

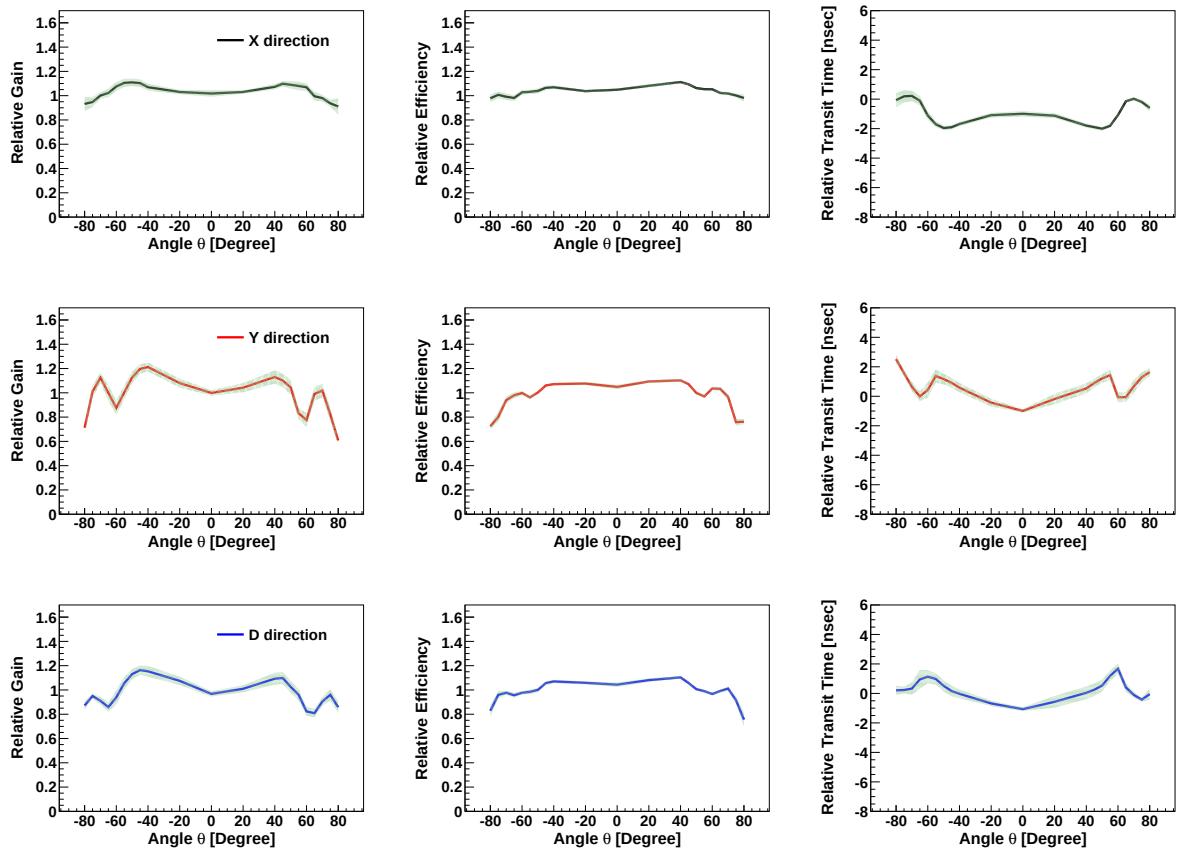

Figure A.8: Average distributions of relative gain, relative photon detection efficiency, and relative transit time of the nine sampled PMTs at the $|B| = 0$ condition as a function of incident photon position on the photocathode (θ). From top to bottom, X, Y, and D direction scanning results are shown. Vertical bands denote the statistical uncertainty of the average value at each photon incident position, $\frac{(\text{standard deviation})}{\sqrt{9-1}}$, and correspond to the PMT by PMT individual differences.

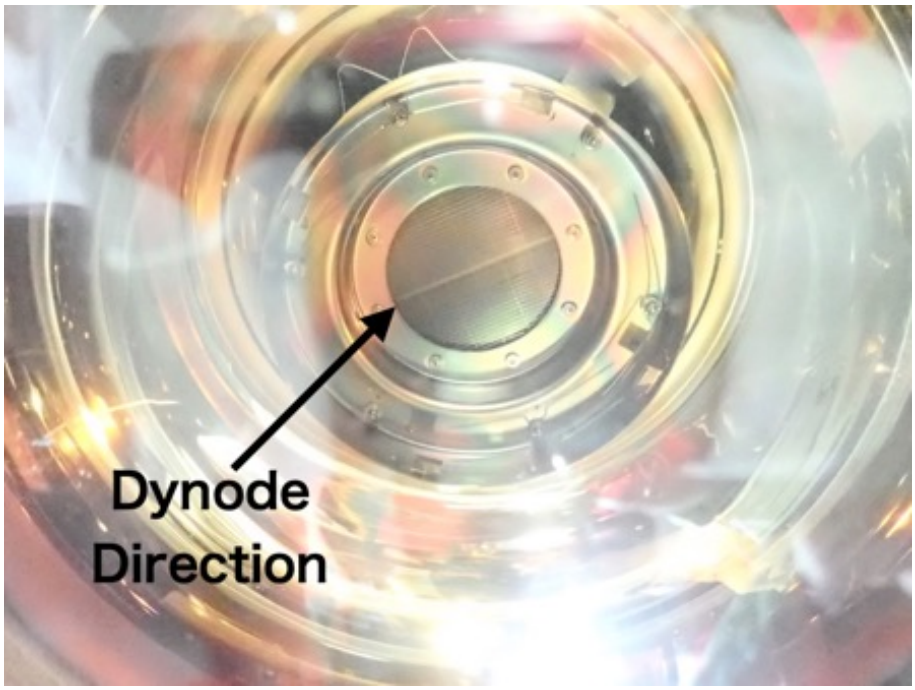

Figure A.9: Example of the dynode picture taken in the SK detector. The thin while lines correspond to the mesh on the dynode and the dynode direction has been estimated from their tilt.

A.2.1 PMT Dynode Direction

The dynode direction inside the PMT can be seen in front of the PMT photocathode by eye. Therefore, a digital camera, OLYMPUS TG-5, has been deployed in front of the PMTs and has recorded the dynode directions. An example of the dynode picture is shown in Fig. A.9. A mesh (thin white lines in the figure), which is deployed for fine-tuning the electric field inside the bulb, is tagged as a mark to estimate the dynode direction. A picture processing tool based on OpenCV [123] has been developed, and it calculates the mesh angle from the picture horizon with both ends of the mesh. The mesh end positions on the display were pointed out by workers.

Pictures of the dynode directions have been taken from the top to bottom of the detector. For the top, side, and bottom PMTs, the camera was placed so that the picture horizon is aligned with the y-axis, xy-plane, and x-axis in the SK coordinates, respectively. For the top PMTs, the camera was handled by hand, while for the side and bottom PMTs, the camera was fixed on a selfie stick as necessary. Some PMTs' dynode directions have been taken twice, and the measurement reproducibility is estimated to be 3 degrees.

Figure A.10 shows the dynode angle distributions. The left plot shows the PMTs produced in the 1990s, and the right shows those produced in the 2000s. The dynode angle is defined as the angle from the xy-plane in the SK coordinates for the side PMTs, while it is defined as the angle from the y-axis in the SK coordinates for the top and bottom PMTs. The dynode directions of PMTs produced in the 2000s were intended to distribute randomly. On the other hand, those produced in the 1990s were basically manufactured in almost the same manner.

A.2.2 Residual Magnetic Field

A magnetometer with a user interface functionality has been developed based on a nine-axes sensor module, LSM9DS0, in which an accelerometer, gyroscope, and magnetometer are integrated. Using the magnetometer, the residual magnetic field at more than 3,000 points in the entire detector has been measured while the compensation coils, which are described in

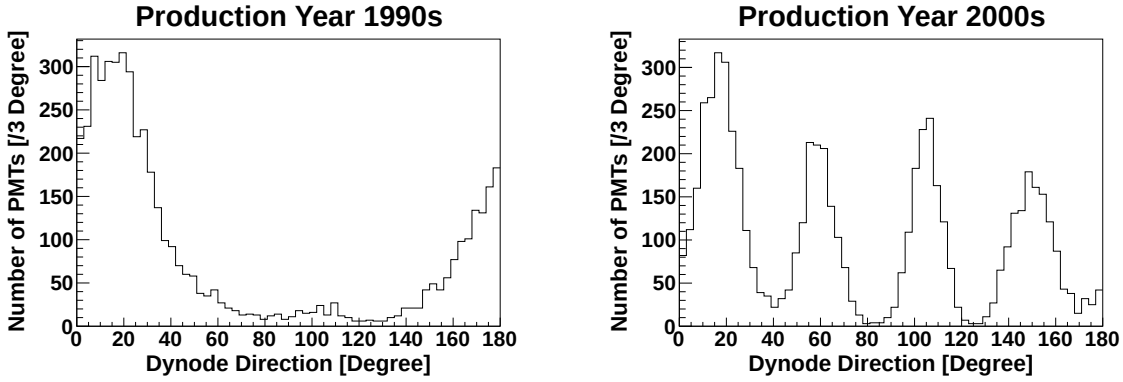

Figure A.10: Dynode angle distributions. The left plot shows the PMTs produced in the 1990s and the right shows those produced in the 2000s. The dynode angle is defined as the angle from the xy-plane in the SK coordinates for the side PMTs, while it is defined as the angle from the y-axis in the SK coordinates for the top and bottom PMTs.

Section 3.2.2, were on to reproduce the SK operation condition. The number of measurement points is more than six times larger than the previous measurement [42]. The magnetometer was handled by hand, and the tilt of the sensor is corrected with the accelerometer data. The measurement reproducibility is estimated to be better than 4 mG.

Figure A.11 shows the distribution of the residual magnetic field strength in the SK detector. In Figure A.11, the number of entries is 3,253 in total, and the number of measurement points in the detector top, side, and bottom region is 321, 2,700, and 232, respectively. Although the measurement points are not distributed uniformly inside the detector due to time constraints, the magnetic field strength has been measured to be less than 100 mG for more than 99% of the measurement points. The mean value is 33 mG, and the standard deviation is 16 mG. Figure A.12 shows the magnetic field maps. Color markers denote the measurement point and magnetic field strength value. The highest magnetic field region is localized in the detector bottom edge, where the dominant component is along the SK y-axis, and the highest value is 122 mG.

A.3 Impacts on Event Reconstruction

The results of the PMT response calibration and detector inspection confirm that an impact on a single PMT response by the photon incident position dependence is larger than that by the residual magnetic field effect for almost all the detector parts. Therefore, only the photon incident position dependence has been implemented into SKDETSIM to estimate impacts on the event reconstruction as a first-order approximation. Assuming that the PMT response is symmetric with respect to the center of the PMT photocathode, relative gain, photon detection efficiency, and transit time factors are calculated based on the PMT measurement results described in Section A.1. Figure A.13 shows the distributions of the implemented relative gain, relative photon detection efficiency, and relative transit time factors. The implemented factors are shown in the dotted lines, which are calculated by averaging the measurement results in the $\theta \geq 0$ and $\theta \leq 0$ regions. Bands show the mean$\pm 1\sigma$ regions plotted in Fig. A.8. The same factors have been implemented for all the ID PMTs in SKDETSIM uniformly. The dynode directions of the PMTs have been also implemented based on the measurement results. In the following, "implemented MC" refers to MC described above, and "standard MC" refers to conventional SKDETSIM MC.

After necessary parameter tuning to reproduce the calibration results presented in Sec-

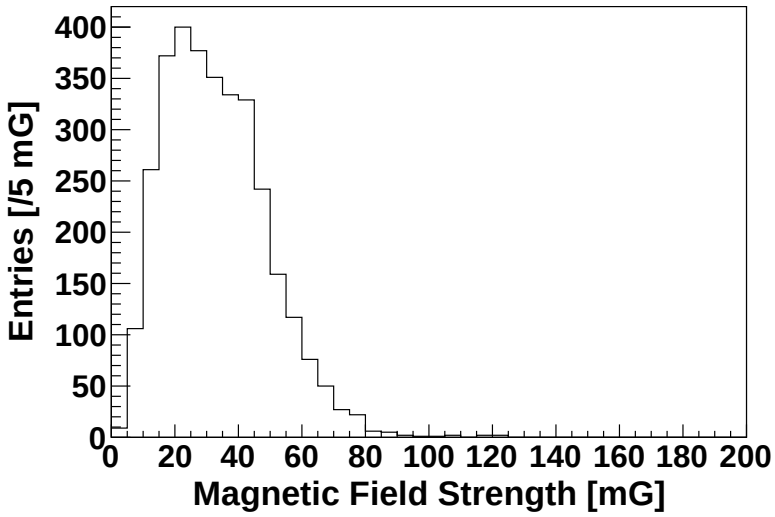

Figure A.11: Distribution of the residual magnetic field strength. The number of entries is 3,253 in total, and the number of measurement points in the detector top, side, and bottom region is 321, 2,700, and 232, respectively. The mean value is 33 mG, and the standard deviation is 16 mG.

tion 3.3, several types of MC events have been generated using implemented MC in the SK-IV detector configuration:

- 500 MeV/c electron,
- 500 MeV/c muon,
- 1000 MeV/c electron,
- 1000 MeV/c muon.

These events have been generated inside the entire detector with randomly distributed particle directions. The same reconstruction algorithm described in Section 6.1 has been applied to the generated events. Figures A.14 and A.15 show the distributions of the distance between the reconstructed vertex and true vertex position as well as reconstructed momentum distributions. The 500 MeV/c and 1000 MeV/c particle gun MC events are plotted in Fig. A.14 and A.15, respectively. The size of the vertex and momentum shifts between implemented MC and standard MC in the additional fiducial mass region is less than 1 cm and less than 0.3% and is much smaller than the vertex resolution ($20 \sim 30$ cm) and energy scale uncertainty discussed in Section 6.2 ($2 \sim 3\%$), respectively. No significant differences are observed in the ring counting and particle identification performances. Furthermore, proton decay $p \to e^+\pi^0$ MC events have been also generated using implemented MC. Applying the same event reconstruction and same signal selection criteria results in a 1% of signal selection efficiency change in the additional fiducial mass region, which is also smaller than the estimated systematic uncertainty associated with the detector (reconstruction) performance described in Section 7.3.2. These results confirm that the average impacts by the photon incident position dependence of the SK PMT response is limited on the event reconstruction performance, and the approximation in standard MC is tolerable for enlarging the fiducial mass. Since outputs of standard MC are well understood and calibrated with various control samples, standard MC is used in the analysis presented in this thesis, and implemented MC is not used.

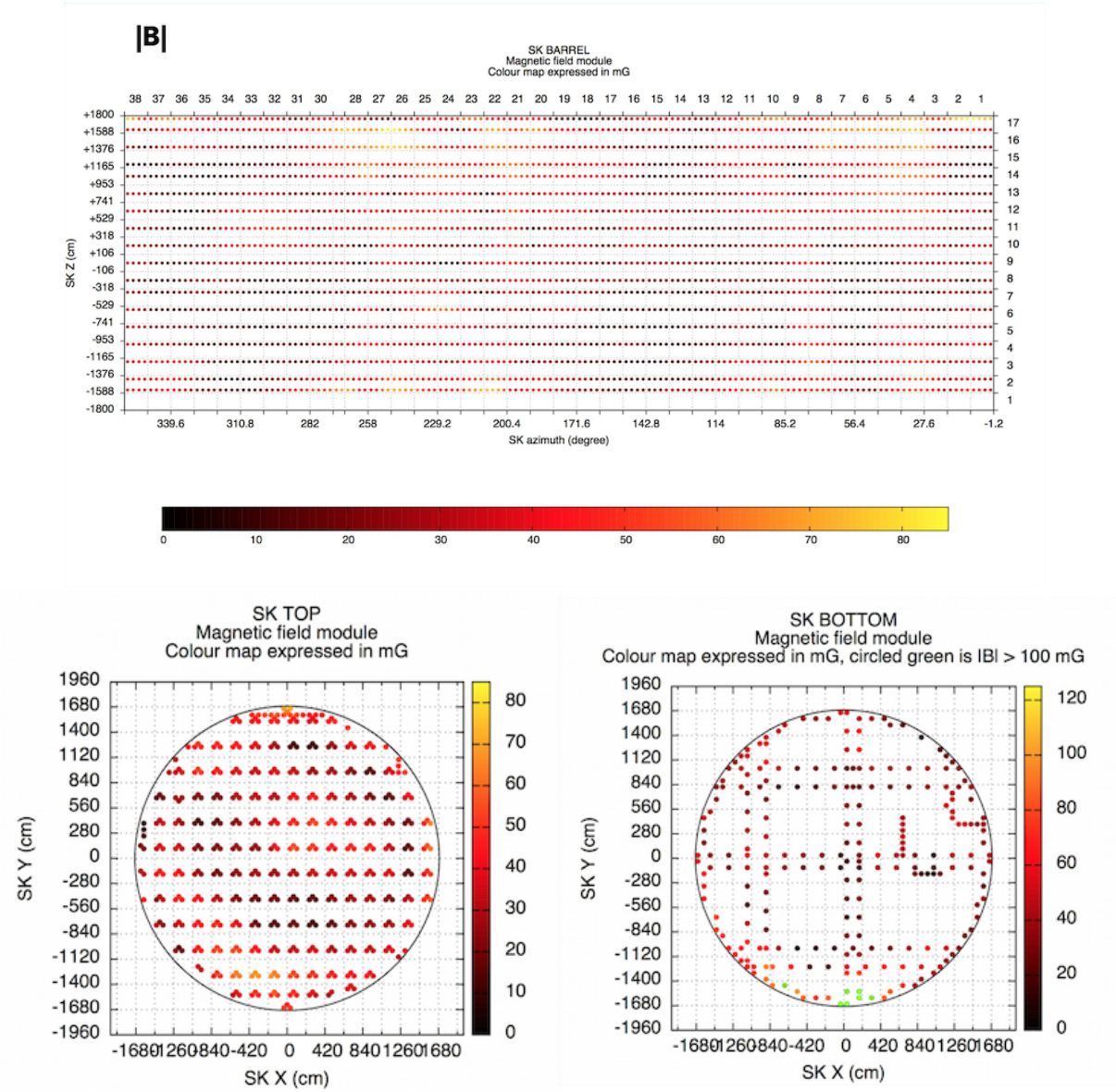

Figure A.12: Magnetic field maps. Color markers denote the measurement point and magnetic field strength value in units of mG. The upper plot shows the detector barrel (side) region and the horizontal axis is the azimuth angle from the SK x-axis. The lower left (right) plot shows the detector top (bottom) region. The highest magnetic field region is localized in the detector bottom edge, and the markers are highlighted in green. Due to time constraints, the number of measurement points in the detector bottom is lower than that in the detector top. Provided by [124].

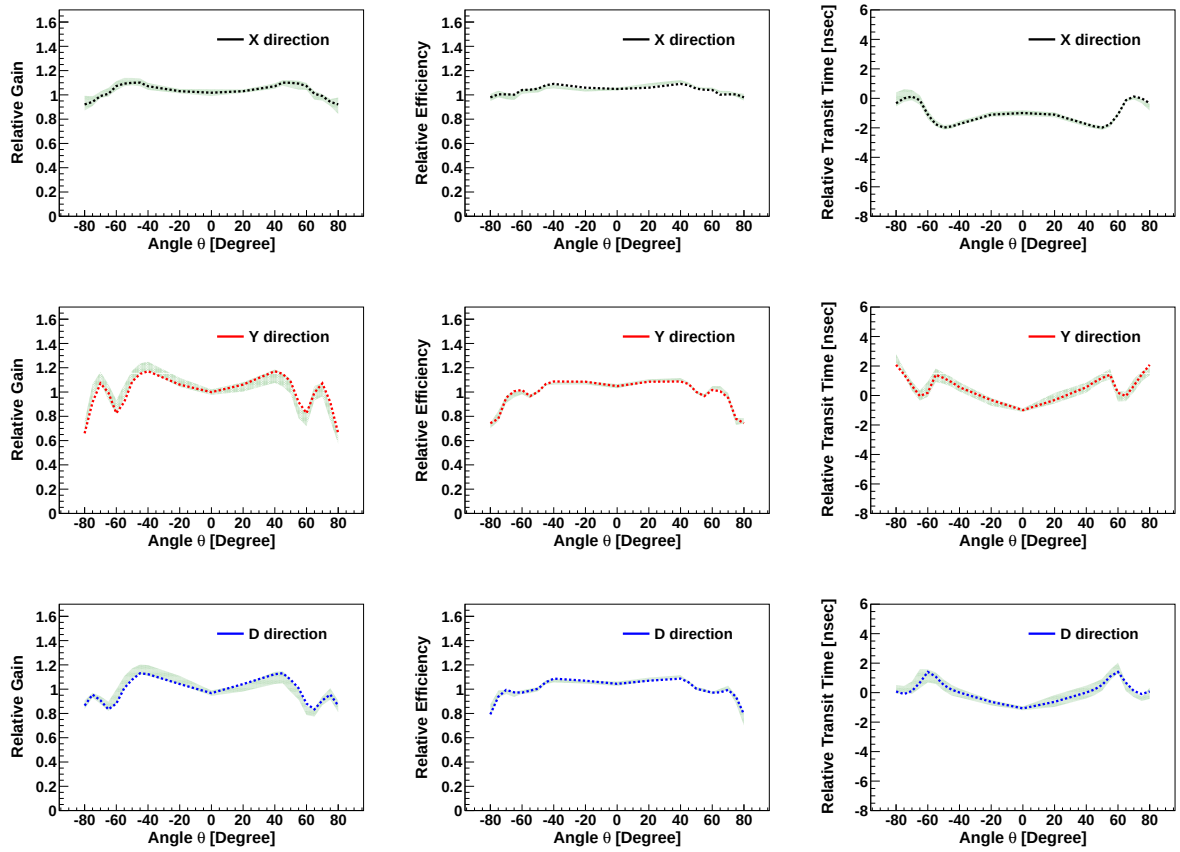

Figure A.13: Distributions of relative gain (left), relative photon detection efficiency (middle), and relative transit time (right) factors. The implemented factors are shown in the dotted lines. From top to bottom, implemented factors for the X, Y, and D directions are shown. Bands show the mean $\pm 1\sigma$ region plotted in Fig. A.8.

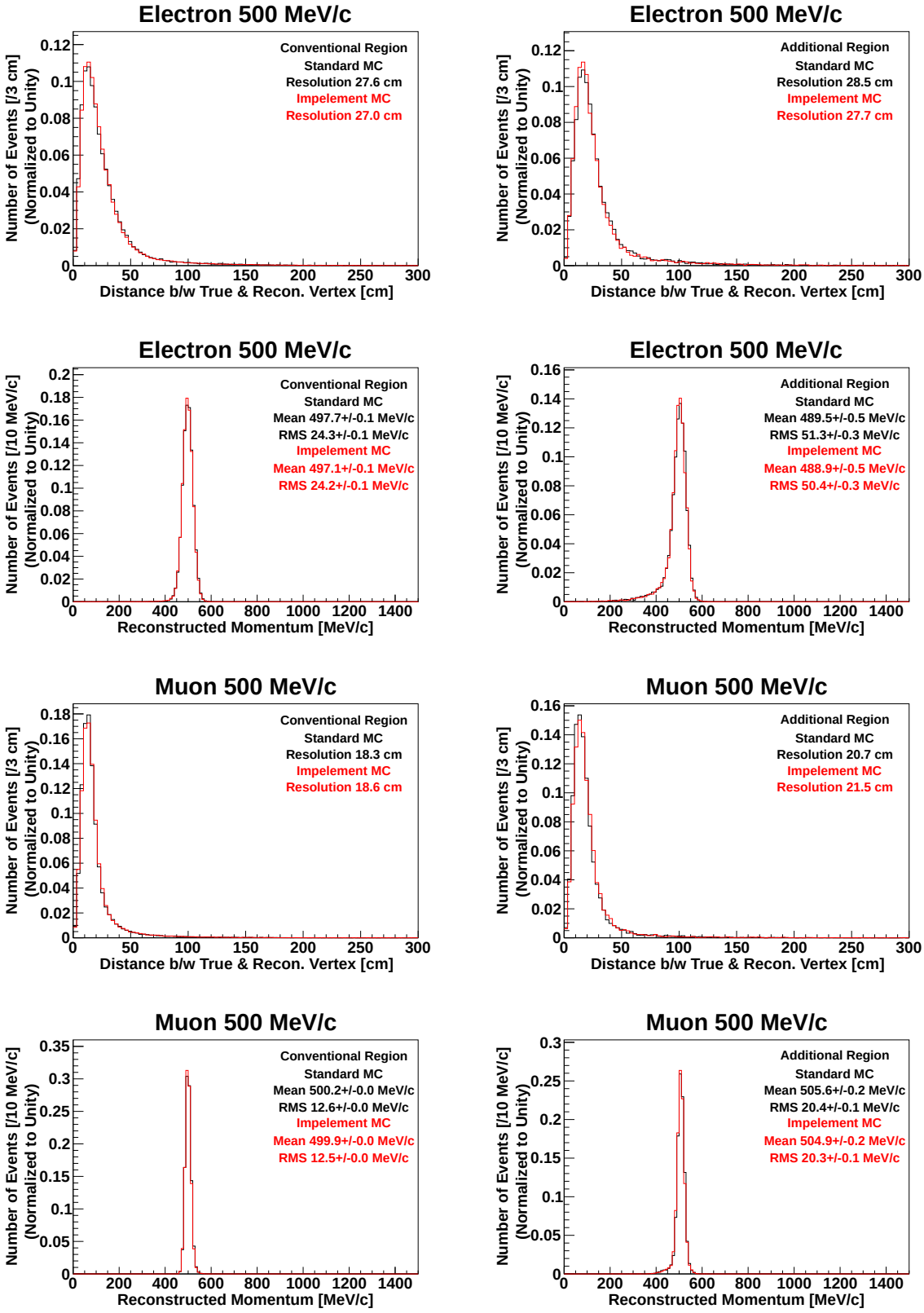

Figure A.14: Distributions the distance between the reconstructed vertex and true vertex position and reconstructed momentum. Implemented MC outputs are plotted in red, and standard MC outputs are in black. The top (bottom) four plot show the electron (muon) 500 MeV/c MC events. The left and right plots correspond to the conventional and additional fiducial mass regions, respectively.

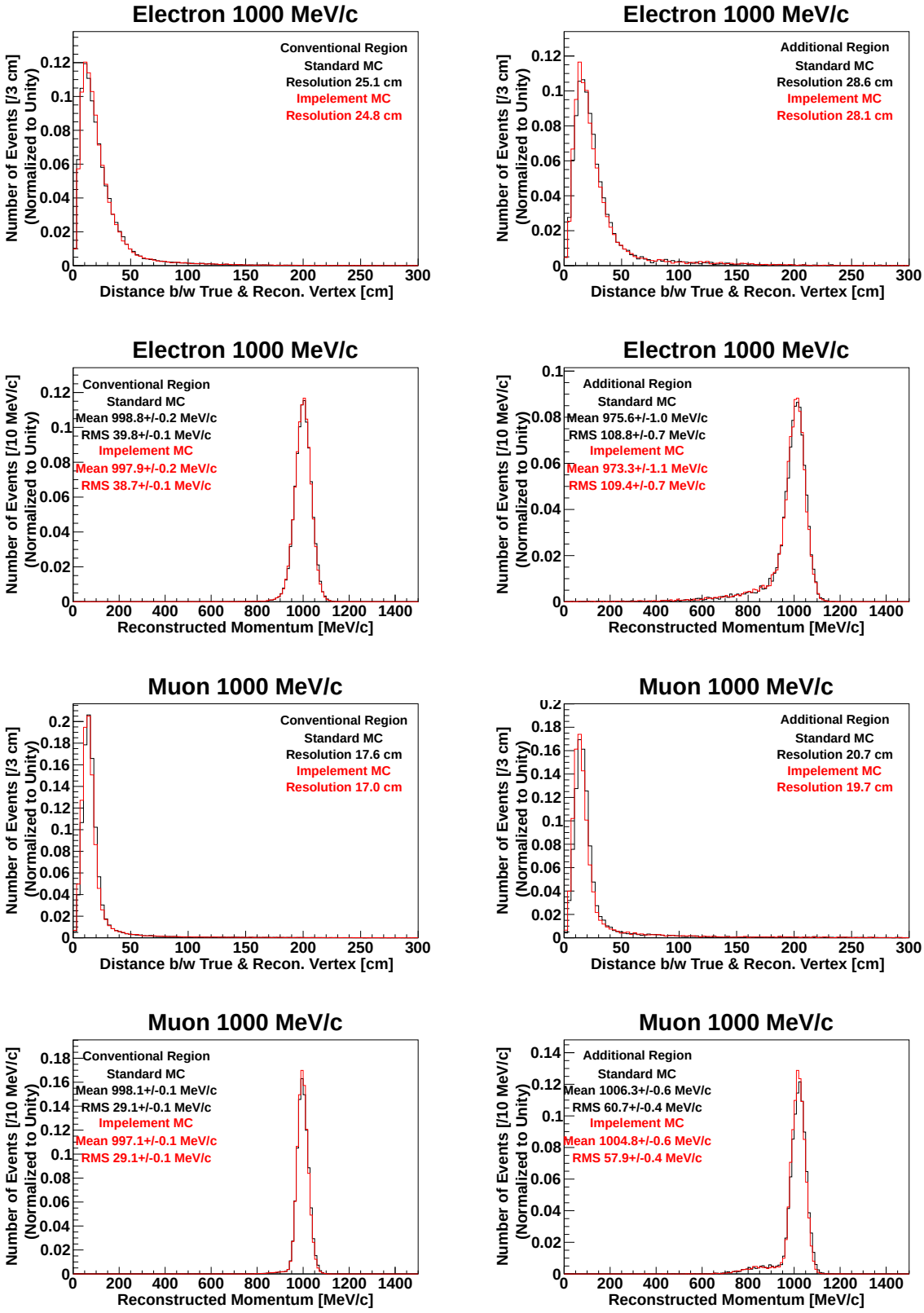

Figure A.15: Distributions the distance between the reconstructed vertex and true vertex position and reconstructed momentum. Implemented MC outputs are plotted in red, and standard MC outputs are in black. The top (bottom) four plot show the electron (muon) 1000 MeV/c MC events. The left and right plots correspond to the conventional and additional fiducial mass regions, respectively.

Bibliography

[1] A. Takenaka *et al.* (Super-Kamiokande Collaboration), Search for proton decay via $p \to e^+\pi^0$ and $p \to \mu^+\pi^0$ with an enlarged fiducial volume in Super-Kamiokande I-IV, Phys. Rev. D 102, 112011 (2020).

[2] M. E. Peskin and Daniel V. Schroeder, An Introduction to Quantum Field Theory, Westview, Boulder (1995).

[3] G. G. Ross, Grand Unified Theories, Westview, Boulder (1985), C. Patrignani *et al.* (Particle Data Group), Chin. Phys. C 40, 100001 (2016), W. de Boer, Grand Unified Theories and Supersymmetry in Particle Physics and Cosmology, Prog. Part. Nucl. Phys. 33, 201 (1994), D. H. Perkins, Proton Decay Experiments, Ann. Rev. of Nucl. and Part. Sci. 34, 1 (1984).

[4] G. Aad *et al.*, Observation of a new particle in the search for the Standard Model Higgs boson with the ATLAS detector at the LHC, Phys. Lett. B 716, 1 (2012), S. Chatrchyan *et al.*, Observation of a new boson at a mass of 125 GeV with the CMS experiment at the LHC, Phys. Lett. B 716, 30 (2012).

[5] Y. Fukuda *et al.* (Super-Kamiokande Collaboration), Evidence for Oscillation of Atmospheric Neutrinos, Phys. Rev. Lett. 81, 1562 (1998), Q. R. Ahmad *et al.* (SNO Collaboration), Direct Evidence for Neutrino Flavor Transformation from Neutral-Current Interactions in the Sudbury Neutrino Observatory, Phys. Rev. Lett. 89, 011301 (2002), K. Eguchi *et al.* (KamLAND Collaboration), First Results from KamLAND: Evidence for Reactor Antineutrino Disappearance, Phys. Rev. Lett. 90, 021802 (2003).

[6] R. Percacci, Gravity from a Particle Physicists' perspective, arXiv:0910.5167 (2009).

[7] L. Canetti, M. Drewes, M. Shaposhnikov, Matter and Antimatter in the Universe, arXiv:1204.4186 (2012).

[8] Stefano Profumo, Leonardo Giani, Oliver F. Piattella, An Introduction to Particle Dark Matter, arXiv:1910.05610 (2019).

[9] Anson Hook, TASI Lectures on the Strong CP Problem and Axions, arXiv:1812.02669 (2018).

[10] H. Georgi and S. L. Glashow, Unity of All Elementary-Particle Forces, Phys. Rev. Lett. 32, 438 (1974), P. Langacker, Grand unified theories and proton decay, Phys. Rept. 72, 185 (1981).

[11] H. Fritzsch and P. Minkowski, Unified interactions of leptons and hadrons, Annals Phys. 93, 193 (1975).

[12] F. Gursey, P. Ramond and P. Sikivie, A universal gauge theory model based on E_6, Phys. Lett. 60B, 177 (1976).

[13] C. McGrew *et al.* (IMB Collaboration), Search for nucleon decay using the IMB-3 detector, Phys. Rev. D 59, 052004 (1999), K. S. Hirata *et al.* (Kamiokande Collaboration), Experimental limits on nucleon lifetime for lepton + meson decay modes, Phys. Lett. B 220, 308 (1989), M. Shiozawa *et al.* (Super-Kamiokande Collaboration), Search for Proton Decay via $p \to e^+\pi^0$ in a Large Water Cherenkov Detector, Phys. Rev. Lett. 81, 3319 (1998), H. Nishino *et al.* (Super-Kamiokande Collaboration), Search for Proton Decay via $p \to e^+\pi^0$ and $p \to \mu^+\pi^0$ in a Large Water Cherenkov Detector, Phys. Rev. Lett. 102, 141801 (2009).

[14] T. Yanagida, in Proceedings of the Workshop on the Unified Theory and the Baryon Number of the Universe, eds. O. Sawada and A. Sugamoto, KEK report No. 79-18, Tsukuba, Japan, (1979).

[15] S. M. Barr, A new symmetry breaking pattern for SO(10) and proton decay, Phys. Lett. 112B, 219 (1982), I. Antoniadis, John Ellis, J. S. Hagelin and D. V. Nanopoulos, The Flipped SU(5) x U(1) String Model Revamped, Phys. Lett. B231, 65 (1989).

[16] J. Pati and A. Salam, Unified Lepton-Hadron Symmetry and a Gauge Theory of the Basic Interactions, Phys. Rev. D8, 1240 (1973).

[17] H. Kolesova and M. Malinsky, Proton lifetime in the minimal SO(10) GUT and its implications for the LHC, Phys. Rev. D 90, 115001 (2014), H. Kolesova and M. Malinsky, Flavor structure of GUTs and uncertainties in proton lifetime estimates, Phys. Rev. D 99, 035005 (2019).

[18] S. Weinberg, Implications of dynamical symmetry breaking, Phys. Rev. D 13, 974 (1976), S. Weinberg, Implications of dynamical symmetry breaking: An addendum, Phys. Rev. D 19, 1277 (1979), E. Gildener, Gauge-symmetry hierarchies, Phys. Rev. D 14, 1667 (1976), L. Susskind, Dynamics of spontaneous symmetry breaking in the Weinberg-Salam theory, Phys. Rev. D 20, 2619 (1979).

[19] A. Djouadi, J. L. Kneur and G. Moultaka, SuSpect: A Fortran code for the Supersymmetric and Higgs particle spectrum in the MSSM, Comp. Phys. Comm. 176, 426 (2007).

[20] J. Hisano, D. Kobayashi, N. Nagata, Enhancement of proton decay rates in supersymmetric SU(5) grand unified models, Phys. Lett. B 716, 406 (2012).

[21] J. Hisano, D. Kobayashi, T. Kuwahara and N. Nagata, Decoupling can revive minimal supersymmetric SU(5), J. High Energ. Phys. 2013, 38 (2013).

[22] F. Reines, C. L. Cowan, Jr., and M. Goldhaber, Conservation of the Number of Nucleons, Phys. Rev. 96, 1157 (1954).

[23] F. Reines, C. L. Cowan, and H. W. Kruse, Conservation of the Number of Nucleons, Phys. Rev. 109, 609 (1958), G. K. Backenstoss, H. Frauenfelder, B. D. Hyams, L. J. Koester and P. C. Marin, An investigation of the stability of nucleons, Nuovo Cim 16, 749 (1960), C. C. Giamati and F. Reines, Experimental Test of the Conservation of Nucleons, Phys. Rev. 126, 2178 (1962), W. R. Kropp, Jr. and F. Reines, Experimental Test of Baryon Conservation and Neutrino Flux Limits, Phys. Rev. 137, B740 (1965), H. S. Gurr, W. R. Kropp, F. Reines, and B. Meyer, Experimental Test of Baryon Conservation, Phys. Rev. 158, 1321 (1967), L. Bergamasco and G. Cini, Limits of the radiochemical and geochemical method for the test of nucleon stability, Nuovo Cimento C 1, 293 (1978), F. Reines and M. F. Crouch, Baryon-Conservation Limit, Phys. Rev. Lett. 32, 493 (1974), J. Learned, F. Reines, and A. Soni, Limits on Nonconservation of Baryon Number, Phys. Rev. Lett. 43, 907 (1979).

[24] G.Battistoni *et al.*, Fully contained events in the Mont Blanc nucleon decay detector, Phys. Lett. B 118, 461 (2012), M. R. Krishnaswamy *et al.*, Results from the KGF proton decay experiment, Nuovo Cimento C 9, 167 (1986), J. Bartelt *et al.*, Monopole-flux and proton-decay limits from the Soudan 1 detector, Phys. Rev. D 36, 1990 (1987), Ch. Berger *et al.*, Results from the Frejus experiment on nucleon decay modes with charged lepton, Z. Phys. C - Particles and Fields 50, 385 (1991).

[25] N. Maekawa and Y. Muramatsu, Nucleon decay via dimension-6 operators in anomalous $U(1)_A$ supersymmetric GUT, Phys. Rev. D 88, 095008 (2013), N. Maekawa and Y. Muramatsu, Flavor changing nucleon decay, Phys. Lett. B767, 398 (2017).

[26] J. Ellis *et al.*, Proton Decay: Flipped vs Unflipped SU(5), arXiv:2003.03285 (2020).

[27] K. Abe *et al.* (The Super-Kamiokande Collaboration), Search for proton decay via $p \to e^+\pi^0$ and $p \to \mu^+\pi^0$ in 0.31 megaton·years exposure of the Super-Kamiokande water Cherenkov detector, Phys. Rev. D 95, 012004 (2017).

[28] Y. Fukuda *et al.* (Super-Kamiokande Collaboration), The Super-Kamiokande detector, Nucl. Instrum. Meth. A501, 418-462 (2003).

[29] H. Nishino *et al.*, High-speed charge-to-time converter ASIC for the Super-Kamiokande detector, Nucl. Instrum. Meth. A 610, 710 (2009).

[30] S. Yamada *et al.*, Commissioning of the New Electronics and Online System for the Super-Kamiokande Experiment, IEEE Transactions on Nuclear Science, vol. 57, no. 2, pp. 428-432, (2010).

[31] H.Kume *et al.*, 20 inch diameter photomultiplier, Nucl. Instrum. Meth. 205, 443 (1983).

[32] A.Suzuki *et al.*, Improvement of 20 in. diameter photomultiplier tubes, Nucl. Instrum. Meth. A 329, 299 (1993).

[33] T. Yamaguchi, Observation of ^{8}B Solar Neutrinos from 300-day data at Super-Kamiokande, Ph.D thesis, Osaka University, (1998).

[34] Y.Takeuchi *et al.*, Development of high sensitivity radon detectors, Nucl. Inst. Meth. A, 421, 334 (1999).

[35] Y. Nakano *et al.*, Measurement of the radon concentration in purified water in the Super-Kamiokande IV detector, Nucl. Inst. Meth. A, 977, 164297 (2020).

[36] Y. Nakano, ^{8}B solar neutrino spectrum measurement using Super-Kamiokande IV, PhD thesis, University of Tokyo, 2016.

[37] T. K. Ohsuka *et al.*, KEK Report 85-10 (1985).

[38] T. Tanimori *et al.*, Design and performance of semi-custom analog IC including two TACs and two current integrators for 'Super-Kamiokande', IEEE Transactions on Nuclear Science, vol. 36, no. 1, pp. 497-501 (1989).

[39] H. Ikeda *et al.*, Front-end hybrid circuit for super-KAMIOKANDE, Nucl. Inst. and Meth. A 320, 310 (1992).

[40] J. George, Experimental Study of the Atmospheric ν_μ / ν_e Ratio in the Multi-GeV Energy Range, Ph.D. Thesis, University of Washington (1998).

[41] H. Nishino, Search for Nucleon Decay into Charged Antilepton plus Meson in Super-Kamiokande, Ph. D. thesis, University of Tokyo, (2009).

[42] K. Abe *et al.* (Super-Kamiokande Collaboration), Calibration of the Super-Kamiokande detector, Nucl. Instrum. Meth. A737, 253 (2014).

[43] D. Motta, S. Schönert, Optical properties of bialkali photocathodes, Nucl. Inst. Meth. A, 539, 217 (2005).

[44] K. Nakamura *et al.*, The reaction ^{12}C(e, e'p) at 700 MeV and DWIA analysis, Nucl. Phys. A268, 381 (1976).

[45] M. G. Mayer and J. H. D. Jensen, Elementary Theory of Nuclear shell structure, Wiley, Neu York (1955).

[46] T. Yamazaki and Y. Akaishi, Nuclear medium effects on invariant mass spectra of hadrons decaying in nuclei, Phys. Lett., B 453, 1 (2000).

[47] R. D. Woods and D. S. Saxon, Diffuse Surface Optical Model for Nucleon-Nuclei Scattering, Phys. Rev. 95, 577 (1954).

[48] Y. Hayato, NEUT, Nucl. Phys. B, Proc. Suppl. 112, 171 (2002), G. Mitsuka, NEUT, AIP Conf. Proc. 967, 208 (2007), AIP Conf. Proc. 981, 262 (2008).

[49] L. L. Salcedo, E. OsetM, J. Vicente-Vacas and C. Garcia-Recio, Computer simulation of inclusive pion nuclear reactions, Nucl. Phys. A 484, 557 (1988). P. de Perio, NEUT pion FSI, AIP Conf. Proc., 1405, 223, (2011). P. de Perio, Joint Three-Flavour Oscillation Analysis of ν_μ Disappearance and ν_e Appearance in the T2K Neutrino Beam, Ph. D. thesis, University of Toronto, (2014).

[50] R. A. Giannelli *et al.*, Multiproton final states in positive pion absorption below the Delta (1232) resonance, Phys. Rev. C 61, 054615 (2000), A. Saunders *et al.*, Reaction and total cross sections for low energy π^+ and π^- on isospin zero nuclei, Phys. Rev. C 53, 1745 (1996), I. Navon *et al.*, True absorption and scattering of 50 MeV pions, Phys. Rev. C 28, 2548 (1983), T. J. Bowles *et al.*, Inclusive ($\pi^\pm$, π^0) reactions in nuclei, Phys. Rev. C 23, 439 (1981), D. Ashery *et al.*, True absorption and scattering of pions on nuclei, Phys. Rev. C 23, 2173 (1981), D. Ashery *et al.*, Inclusive pion single-charge-exchange reactions, Phys. Rev. C 30, 946 (1984), S. M. Levenson *et al.*, Inclusive pion scattering in the $\Delta(1232)$ region, Phys. Rev. C 28, 326 (1983), M. K. Jones *et al.*, Pion absorption above the $\Delta(1232)$ resonance, Phys. Rev. C 48, 2800 (1993), P. Chavanon, M. Crozon, T. Leray, and J. Tocqueville, Determination of the pion neutral angular distribution in the reaction π^+, $p \to \pi^+$, p, π^0 in the energy range 600 to 1300 MeV (in French), Phys. Lett. B 28, 296 (1968), T. Takahashi *et al.*, π^--^{12}C elastic scattering above the Δ resonance, Phys. Rev. C 51, 2542 (1995), B. W. Allardyce *et al.*, Pion reaction cross sections and nuclear sizes, Nucl. Phys. A 209, 1 (1973), J. W. Cronin, R. Cool, and A. Abashian, Cross Sections of Nuclei for High-Energy Pions, Phys. Rev. 107, 1121 (1957), K. Aoki *et al.*, Elastic and inelastic scattering of π^+ and π^- on ^{12}C at 995 MeV/c, Phys. Rev. C 76, 024610 (2007), A. Rahav *et al.*, Measurement of the ^{12}C(π, 2π) reactions and possible evidence of a double-Δ excitation, Phys. Rev. Lett. 66, 1279 (1991).

[51] G. Rowe, M. Salomon, and R. H. Landau, Energy-dependent phase shift analysis of pion-nucleon scattering below 400 MeV, Phys. Rev. C 18, 584 (1978).

[52] R. A. Arndt, W. J. Briscoe, I. I. Strakovsky, R. L. Workman, and M. M. Pavan, Dispersion relation constrained partial wave analysis of πN elastic and $\pi N \to \eta N$ scattering data: The baryon spectrum, Phys. Rev. C 69, 035213 (2004).

[53] H. Ejiri, Nuclear deexcitations of nucleon holes associated with nucleon decays in nuclei, Phys. Rev. C 48, 1442 (1993).

[54] M. Honda, T. Kajita, K. Kasahara, and S. Midorikawa, Comparison of 3-dimensional and 1-dimensional schemes in the calculation of atmospheric neutrinos, Phys. Rev. D 64, 053011 (2001), M. Honda, T. Kajita, K. Kasahara, and S. Midorikawa, New calculation of the atmospheric neutrino flux in a three-dimensional scheme, Phys. Rev. D 70, 043008 (2004), M. Honda, T. Kajita, K. Kasahara, S. Midorikawa, and T. Sanuki, Calculation of atmospheric neutrino flux using the interaction model calibrated with atmospheric muon data, Phys. Rev. D 75, 043006 (2007), M. Honda, T. Kajita, K. Kasahara, and S. Midorikawa, Improvement of low energy atmospheric neutrino flux calculation using the JAM nuclear interaction model, Phys. Rev. D 83, 123001 (2011).

[55] G. Battistoni, A. Ferrari, T. Montaruli, P. R. Salad, The FLUKA atmospheric neutrino flux calculation, Astropart. Phys. 19, 269 (2003).

[56] G. D. Barr, T. K. Gaisser, P. Lipari, S. Robbins, and T. Stanev, Three-dimensional calculation of atmospheric neutrinos, Phys. Rev. D 70, 023006 (2004).

[57] J. Alcaraz *et al.* (AMS Collaboration), Cosmic protons, Phys. Lett. B 490, 27 (2000).

[58] T. Sanuki *et al.* (BESS Collaboration), Precise measurements of cosmic-ray hydrogen and helium spectra with BESS, Astrophys. J. 545, 1135, (2000), S. Haino *et al.* (BESS Collaboration), Measurements of primary and atmospheric cosmic-ray spectra with the BESS-TeV spectrometer, Phys. Lett. B 594, 35 (2004).

[59] NASA, U.S. Standard Atmosphere, 1976, NASA Technical Reports Server (1976).

[60] S. Roesler, R. Engel, and J. Ranft The Monte Carlo Event Generator DPMJET-III, Advanced Monte Carlo for Radiation Physics, Particle Transport Simulation and Applications. Springer, Berlin, Heidelberg.

[61] K. Niita, T. Sato, H. Iwase, H. Nose, H. Nakashima, and L. Sihver, PHITS-a particle and heavy ion transport code system, Radiation Measurements, 21, 1080 (2006).

[62] P. Achard *et al.* (L3 Collaboration), Measurement of the atmospheric muon spectrum from 20 to 3000 GeV, Phys. Lett. B 598, 15 (2004).

[63] T. Sanuki *et al.* (BESS Collaboration), Measurements of atmospheric muon spectra at mountain altitude, Phys. Lett. B 541, 234 (2002), K. Abe *et al.* (BESS Collaboration), Measurements of proton, helium and muon spectra at small atmospheric depths with the BESS spectrometer, Phys. Lett. B 564, 8 (2003).

[64] K. Abe *et al.*, Atmospheric neutrino oscillation analysis with external constraints in Super-Kamiokande I-IV Phys. Rev. D 97, 072001 (2018).

[65] C. H. Llewellyn Smith, Neutrino reactions at accelerator energies, Phys. Rept., 3, 261, (1972).

[66] R. A. Smith and E. J. Moniz, Neutrino reactions on nuclear targets, Nucl. Phys. B, 43, 605 (1972).

[67] R. Gran *et al.* (K2K Collaboration), Measurement of the quasielastic axial vector mass in neutrino interactions on oxygen, Phys. Rev. D 74, 052002 (2006).

[68] A. A. Aguilar-Arevalo *et al.* (MiniBooNE Collaboration), First measurement of the muon neutrino charged current quasielastic double differential cross section, Phys. Rev. D 81, 092005 (2010).

[69] S. J. Barish *et al.*, Study of neutrino interactions in hydrogen and deuterium: Description of the experiment and study of the reaction $\nu + d \to \mu^- + p + p_s$, Phys. Rev. D 16, 3103 (1977).

[70] N. J. Baker, A. M. Cnops, P. L. Connolly, S. A. Kahn, H. G. Kirk, M. J. Murtagh, R. B. Palmer, N. P. Samios, and M. Tanaka, Quasielastic neutrino scattering: A measurement of the weak nucleon axial-vector form factor, Phys. Rev. D 23, 2499 (1981).

[71] M. Pohl *et al.*, Experimental study of the reaction $\nu n \to \mu p$, Lett. Nuovo Cimento 26, 332 (1979). S. Bonetti, G. Carnesecchi, D. Cavalli, P. Negri, A. Pullia, M. Rollier, F. Romano, and R. Schira, Study of quasi-elastic reactions of ν and $\bar{\nu}$ in Gargamelle, Nuov Cim A 38, 260 (1977).

[72] S. V. Belikov *et al.*, Quasielastic Neutrino and Antineutrino Scattering Total Cross-Sections, Axial-Vector Form-Factor, Z Physik A 320, 625633 (1985).

[73] J. Brunner *et al.* (SKAT Collaboration), Quasielastic nucleon and hyperon production by neutrinos and antineutrinos with energies below 30 GeV, Z. Phys. C - Particles and Fields 45, 551 (1990).

[74] J. Nieves, I. R. Simo, and M. J. V. Vacas, Inclusive charged-current neutrino-nucleus reactions, Phys. Rev. C 83, 045501 (2011).

[75] D. Rein and L. M. Sehgal., Neutrino Excitation of Baryon Resonances and Single Pion Production, Annals Phys. 133, 79 (1981).

[76] K. M. Graczyk and J. T. Sobczyk., Form Factors in the Quark Resonance Model, Phys. Rev. D 77, 053001, Erratum: Phys. Rev. D 79, 079903 (2009).

[77] G. M. Radecky *et al.*, Study of single-pion production by weak charged currents in low-energy νd interactions, Phys. Rev. D 25, 1161 (1982), T. Kitagaki *et al.*, Charged-current exclusive pion production in neutrino-deuterium interactions, Phys. Rev. D 34, 2554 (1986).

[78] M. Derrick *et al.*, Properties of the hadronic system resulting from $\bar{\nu}_{mu}p$ interactions, Phys. Rev. D 17, 1 (1978), S. Barlag *et al.* (Amsterdam Bologna Padova Pisa Saclay Torino Collaboration), Charged hadron multiplicities in high energy $\bar{n}u_\mu n$ and $\bar{n}u_\mu p$ interactions, Z. Phys. C - Particles and Fields 11, 283 (1982).

[79] T. Sjostrand, PYTHIA 5.7 and JETSET 7.4 Physics and Manual, arXiv:hep-ph/9508391.

[80] M. Glück, E. Reya, and A. Vogt, Dynamical parton distributions revisited, Eur. Phys. J. C 5, 461 (1998).

[81] A. Bodek and U.K. Yang, Modeling Neutrino and Electron Scattering Cross Sections in the Few GeV Region with Effective LO PDFs, AIP Conf. Proc., 670, 110, (2003).

[82] P. S. Auchincloss *et al.*, Measurement of the inclusive charged-current cross section for neutrino and antineutrino scattering on isoscalar nucleons, Z. Phys. C - Particles and Fields 48, 411 (1990).

[83] P. Berge *et al.*, Total neutrino and antineutrino charged current cross section measurements in 100, 160, and 200 GeV narrow band beams, Z. Phys. C - Particles and Fields 35, 443 (1987).

[84] S. Ciampolillo *et al.*, Total cross section for neutrino charged current interactions at 3 GeV and 9 GeV, Phys. Lett. B 84, 281 (1979).

[85] J. V. Allaby (CHARM Collaboration) *et al.*, Total cross sections of charged-current neutrino and antineutrino interactions on isoscalar nuclei, Z. Phys. C - Particles and Fields 38, 403 (1988).

[86] D. C. Colley *et al.*, Cross sections for charged current ν and $\bar{\nu}$ interactions in the energy range 10 to 50 GeV, Z. Phys. C - Particles and Fields 2, 187 (1979).

[87] D. S. Baranov *et al.*, Measurement of the $\nu_\mu N$ total cross section at 230 GeV in a skat neutrino experiment, Phys. Lett. B 81, 255 (1979).

[88] V. B. Anikeev *et al.*, Total cross section measurements for $\nu_\mu, \bar{\nu}_\mu$ charged current interactions in 330 GeV energy range with IHEP-JINR neutrino detector, Z. Phys. C - Particles and Fields 70, 39 (1996).

[89] A. I. Mukhin, V. F. Perelygin, K. E. Shestermanov, A. A. Volkov, A. S. Vovenko, and V. P. Zhigunov, Energy Dependence of Total Cross-sections for Neutrino and Anti-neutrino Interactions at Energies Below 35 GeV, Sov.J.Nucl.Phys. 30, 528 (1979).

[90] D. B. MacFarlane *et al.*, Nucleon structure functions from high energy neutrino interactions with iron and QCD results, Z. Phys. C - Particles and Fields 26, 1 (1984).

[91] C. Zeitnitz and T. A. Gabriel, The GEANT-CALOR interface and benchmark calculations of ZEUS test calorimeters, Nucl. Instrum. Meth., A349, 106 (1994).

[92] HETC: Monte Carlo High-Energy Nucleon-Meson Transport Code, Oak Ridge National Laboratory RSIC Computer Code Collection CCC-178.

[93] A. Fassó *et al.*, FLUKA92, Proc. 1st Workshop on Simulating Accelerator Radiation Environments (1993).

[94] J. O. Johnson and T. A. Gabriel, A user's guide to MICAP: A Monte Carlo Ionization Chamber Analysis Package, ORNL/TM-10340 (1988).

[95] R. Brun, F. Bruyant, M. Maire, A. C. McPherson, P. Zanarini, GEANT 3 : user's guide Geant 3.10, Geant 3.11, CERN-DD-EE-84-01.

[96] K. Abe *et al.*, The T2K experiment, Nucl. Instrum. Meth. A659, 106 (2011).

[97] T. J. Irvine, Development of Neutron-Tagging Techniques and Application to Atmospheric Neutrino Oscillation Analysis in Super-Kamiokande, Ph.D. thesis, University of Tokyo, (2014),

[98] Y. Ashie *et al.* (Super-Kamiokande Collaboration), Measurement of atmospheric neutrino oscillation parameters by Super-Kamiokande I, Phys. Rev. D 71, 112005 (2005).

[99] K. Abe *et al.* (The Super-Kamiokande Collaboration), Indirect search for dark matter from the Galactic Center and halo with the Super-Kamiokande detector, Phys. Rev. D 102, 072002 (2020).

[100] K. Abe *et al.* (The Super-Kamiokande Collaboration), Neutron-Antineutron Oscillation Search using a 0.37 Megaton·Year Exposure of Super-Kamiokande, arXiv:2012.02607 (2020).

[101] Lee Ka Pik, Study of the neutrino mass hierarchy with the atmospheric neutrino data observed in Super-Kamiokande, Ph. D. thesis, University of Tokyo, (2012).

[102] M. Taani *et al.*, Private communication.

[103] K. Abe *et al.* (The Super-Kamiokande Collaboration), Search for proton decay via $p \to \nu K^+$ using 260 kiloton·year data of Super-Kamiokande, Phys. Rev. D 90, 072005 (2014).

[104] K. Abe *et al.* (The Super-Kamiokande Collaboration), Search for Nucleon Decay via $n \to \nu\pi^0$ and $p \to \nu\pi^+$ in Super-Kamiokande, Phys. Rev. Lett. 113, 121802 (2014).

[105] K. Frabkiewicz, Indirect Search for Dark Matter with the Super-Kamiokande Detector, Ph. D. thesis, National Centre For Nuclear Research, (2018).

[106] T. Mochizuki, Master thesis, University of Tokyo, (2019).

[107] J. Kameda, Detailed Studies of neutrino oscillation with atmospheric neutrinos of wide energy range from 100 MeV to 1000 GeV in Super-Kamiokande, Ph. D. thesis, University of Tokyo, (2002).

[108] M. Shiozawa, Reconstruction algorithms in the Super-Kamiokande large water Cherenkov detector, Nucl. Instrum. Methods Phys. Res., Sect. A 433, 240 (1999), M. Shiozawa, Ph. D. thesis, University of Tokyo, (1999).

[109] E. R. Davies, Machine Vision: Theory, Algorithms, Practicalities, Academic Press, San Diego (1997).

[110] J. Palomino, J. Hignight, and S. Mine, Private Communication.

[111] M. Smy, Low Energy Event Reconstruction and Selection in SuperKamiokandeIII, Proc. of the 30th ICRC, 5, 1279 (2007).

[112] R. Brun and F. Rademakers, ROOT — An object oriented data analysis framework, Nucl. Instrum. Meth., A389, 8186 (1997).

[113] D. Cokinos and E. Melkonian, Measurement of the 2200 m/sec neutron-proton capture cross section, Phys. Rev. C 15, 1636 (1977).

[114] J. E. Renner, High Pressure Xenon Detectors for Rare Physics Searches, Ph. D. Thesis, UC, Berkeley (2014).

[115] S. Mine *et al.* (K2K Collaboration), Experimental study of the atmospheric neutrino backgrounds for $p \to e^+\pi^0$ searches in water Cherenkov detectors, Phys. Rev. D 77, 032003 (2008).

[116] E. Hernández, J. Nieves, and M. Valverde, Weak pion production off the nucleon, Phys. Rev. D 76, 033005 (2007).

[117] J. Nieves, J. E. Amaro, and M. Valverde, Inclusive quasielastic charged-current neutrino-nucleus reactions, Phys. Rev. C 70, 055503 (2004), Erratum: Phys. Rev. C 72, 019902 (2005).

[118] F. C. Porter, Testing Consistency of Two Histograms, arXiv:0804.0380.

[119] C. Amsler *et al.* (Particle Data Group Collaboration), Review of particle physics, Phys. Lett. B 667, 1 (2008)., B. P. Roe and M. B. Woodroofe, Setting confidence belts, Phys. Rev. D 63, 013009 (2000).

[120] J. F. Beacom and M. R. Vagins, Antineutrino Spectroscopy with Large Water Cerenkov Detectors, Phys. Rev. Lett. 93, 171101 (2004).

[121] Ll. Marti *et al.*, Evaluation of gadolinium's action on water Cherenkov detector systems with EGADS, Nucl. Instrum. Methods Phys. Res., Sect. A 959, 11 (2020).

[122] K. Abe *et al.*, Hyper-Kamiokande Design Report, arXiv:1805.04163 (2018).

[123] G. Bradski, The OpenCV Library, Dr. Dobb's Journal of Software Tools (2000).

[124] F. Iacob, Primvate Communication.